Thermal Stress Analysis of

Automotive Disc Brakes

by

Saiprasit Koetniyom
BSc (Eng), MSc (Eng)

Submitted in accordance with the requirements for the degree of
Doctor of Philosophy

The University of Leeds
School of Mechanical Engineering

November 2000

The candidate confirms that the work submitted is his own and that appropriate credit has been given where reference has been made to the work of others.

ACKNOWLEDGEMENTS

This project would not have been completed without advice from Professor D. C. Barton and Dr P. C. Brooks of the Mechanical Engineering School at Leeds University. I truly appreciate their time and attention. I am also grateful for the technical support in the experimental work that was directed by T. Wiese of the Strength of Materials laboratory in the Mechanical Engineering School. Special thanks to the assistance of Rover/BMW in providing relevant information and sample brake discs. I also owe a debt of gratitude to my mother who passed away during my study. She provided the motivation and stimulation. Her contributions to my morale are immeasurable. Without her, I would never have pursued this study. Thanks to all brothers and sisters from Leeds International Church of Christ who warmly supported me while staying in the UK. Finally, I would like to thank the Thai government that provided the scholarship throughout my study.

วิทยานิพนธ์ฉบับนี้ ขอมอบให้แด่ คุณพ่อประจวบ คุณแม่วิไล และ ครอบครัว เกิดนิยม

ABSTRACT

A brake disc rotor forms part of a foundation brake and rotates with the wheel hub assembly. The main function of a foundation brake is to generate a retarding torque by converting mechanical energy to thermal energy by virtue of the frictional work done in relative sliding at the rotor-pad interface. In practice, most brake discs are made from cast iron and in use are sometimes subjected to high thermal stresses which can lead to permanent plastic deformation and occasionally rotor cracking. The aim of the present work is to investigate the thermal response of such a cast iron brake disc using the finite element (FE) method. One particular existing brake disc design for a medium passenger car was chosen for the investigation. This is a "back-vented" disc designed to minimise disc coning but the present work also includes an investigation of a conventional "front-vented" disc similar in dimension to the back-vented disc but with different detailed geometry. Experimental work was undertaken to derive the rotor material properties in tension and compression as a function of temperature. This data was used to generate suitable FE material model routines which accurately allow for the different temperature-dependent yield properties of cast iron in tension and compression. The modelling work highlights the role of the rotor geometry in controlling the thermal response of the structure but, more importantly, the necessity for an accurate material model is illustrated, particularly with regard to its ability to predict the accumulation of plastic strain which may lead to rotor cracking. Using the most accurate user-developed material subroutine, the thermal response of the back-and front-vented disc designs are compared: the back-vented disc suffers lower thermal distortion but at the expense of higher plastic strain accumulation, particularly near the point of attachment of the vanes.

CONTENTS

(All figures are grouped at the end of the Chapter in which they are first referenced)

LIST OF FIGURES

LIST OF TABLES

NOMENCLATURE

a	Vehicle deceleration
b	Parameter for cast iron material properties
c	Specific heat of material
k	Radius of gyration
m	Mass of rotating parts
q	Magnitude of heat input
dx	Length in x direction
k_c	Conductivity of material
n_p	Number of pads on front axle
q_x	Conduction heat rate in x direction
A	Total rubbing surface area per pad
I	Moment of inertia of rotating parts
K	Correction factor due to vehicle inertia
M	Vehicle mass
G	Plastic potential function
P	Hydrostatic stress
Q	The rate of thermal input per unit rotor rubbing area
R	Radius of rotating part
S	Deviatoric stress tensor
T	Temperature
U	Nodal displacement
V	Instantaneous velocity
W	External loads
F_t	Tensile yield function
F_c	Compressive yield function
F_x	Yield function at position x
K_d	Correction factor due to rolling resistance and drag force
K_p	Proportion of heat transferred to disc
V_f	Final vehicle velocity
V_i	Initial vehicle velocity
S_x	Principal deviatoric stress
X_f	Proportion of braking due to front wheels
J_x	Invariant of the deviatoric stress tensor
$\dot{E}_{st}$	Rate of heat increment in the volume
$\dot{E}_g$	Rate of internal heat generation

$[D]$	Elastic stiffness matrix
$[D_t]$	Jacobian matrix
γ	Parameter for cast iron material properties
θ	Location of the stress state
ω	Angular velocity of rotating parts
ρ	Density of material
ψ	Rate of heat generated per unit volume
α	Linear thermal expansion
Π	Potential energy
Λ	Strain energy
σ	Stress tensor
σ_x	Stress state at position x
ν	Poisson's ratio
ν_{pl}	Plastic Poisson's ratio
σ_c	Compressive yield stress
σ_e	Von Mises stress
σ_m	Mean elastic stress
σ_0	Yield stress
σ_t	Tensile yield stress
ΔS	Vehical distance travelled
Δt	Braking time
ΔT	Temperature increment
$\Delta\varepsilon$	Strain increment
$\Delta\varepsilon^{pl}$	Plastic strain increment
$\Delta\bar{\varepsilon}^{pl}$	Equivalent plastic strain increment
$\Delta\lambda$	Plastic strain multiplier
$\Delta\lambda_x$	Plastic strain multiplier at position x
ε	Thermal strain
$\bar{\varepsilon}^{pl}$	Equivalent plastic strain
$\dot{\varepsilon}^{pl}$	Plastic strain rate
$\dot{\varepsilon}_{vol}^{pl}$	Volumetric plastic strain rate
$\dot{\bar{\varepsilon}}_t^{pl}$	Equivalent plastic strain rate in tension
$\dot{\bar{\varepsilon}}_c^{pl}$	Equivalent plastic strain rate in compression
$d\{\varepsilon^{pl}\}$	Plastic strain increment
$d\bar{\varepsilon}^{pl}$	Equivalent plastic strain increment
$\dot{e}^{pl}$	Deviatoric plastic strain rate
$\dot{\bar{e}}_t^{pl}$	Equivalent deviatoric plastic strain rate in tension
$\dot{\bar{e}}_c^{pl}$	Equivalent deviatoric plastic strain rate in compression

CHAPTER 1

INTRODUCTION AND LITERATURE REVIEW

1.1 INTRODUCTION TO AUTOMOTIVE DISC BRAKES

A brake disc rotor is the rotating part of a disc brake assembly normally located on the front axle. It consists of a rubbing surface, a top-hat and a neck section. The rubbing surface is where a tangential friction force between the rotor and the stationary pad is generated that gives rise to the brake force in the tyre-ground plane which retards the vehicle. The top-hat section is mounted to the hub of the wheel. The connection between the rubbing surface and the hat is known as the neck. Brake discs are favoured by most manufacturers of passenger cars as the standard foundation brake at the front wheel. A drum brake, in contrast, is an internal expanding type of brake that uses a device for expanding two shoes against a rotating drum when the brake pedal is depressed. Typical disc and drum brakes are shown in Figure 1.1. Drum brakes are currently fitted to the rear axle of some vehicles because of lower manufacturing costs.

At the present time, the disc brake used in most high-specification cars has a vented rotor consisting of separate inboard and outboard rubbing surfaces (or cheeks) that are connected by fins (or vanes). Thus, air can flow between the rubbing surfaces for cooling the brake disc both during and after braking. In practice, the neck of the brake disc can be connected to either the outboard or inboard rubbing surface. The outboard connection design, known as a front-vented disc, is the most common. On the other hand, the inboard connection is used in a back-vented disc as shown in Figure 1.2. Both brake disc designs may use the same calipers to house the pistons that are used to press the pads of friction material against the rubbing surfaces of the brake disc and so generate the friction forces. Typically, brake calipers can be classified into two

categories: fixed calipers and floating calipers as shown in Figure 1.3. The fixed caliper is rigid and requires at least one piston located on each side of the rotor to push the pads against the rubbing surface. In the case of the floating caliper, a minimum of one piston is located on the inboard side. When the brake fluid applies a pressure to the piston, the reaction force in the opposite direction will cause the housing of caliper, known as the finger or paw, to move towards the pad on the outboard side of the caliper. The floating caliper then acts as a simple hydraulic clamp.

"Coning" is an axial distortion of the brake disc planar geometry which results in the disc taking up a conical shape. Generally, it occurs due to the different thermal expansions of the outboard and inboard cheeks as a result of the asymmetric radial constraint from the cooler top-hat and neck. The importance of reducing brake disc thermal displacements in general and "coning" in particular has been realised in order to control the pressure distribution between the pads and brake rotor. If brake disc coning occurs, high localised pressures and temperature distributions are developed, resulting in high pad wear rates. Metzler [1] reviewed brake disc development from the first disc brakes in the early 1950s and described many innovative brake disc designs introduced in order to control coning with different forms of rotor connection, hat size and machined undercut grooves at the neck.

In addition, other factors that are taken into account in the development of disc brakes are noise and self-excited vibration during operation. However, these are specialised problem areas that are not considered further in this thesis which concentrates on analysing the problems of thermal distortion and rotor cracking as outlined below.

1.1.1 ROTOR CRACKING

Rotor cracking is a problem that particularly affects vented discs subject to extreme loading conditions Angus et al. [2] reported that cracks on the rubbing surface as shown in Figure 1.4. arose from thermal energy input at the rubbing surfaces which became greater than the thermal energy output by convection. The degree of increase of surface temperature depended on the thermal conductivity of the brake disc material. If the material had low thermal conductivity, the temperature gradient across the brake disc thickness was high. As a result, the surface temperature rose faster than that of the brake disc body, resulting in different thermal expansions between the surface and body of the brake disc. Due to the constraints associated with the cooler brake disc body, compressive stresses were induced at the rubbing surfaces and tensile stresses occurred over the brake rotor interior. If these thermally induced stresses exceeded a certain magnitude or were repeated many times, brake disc cracking could occur.

In addition, Limpert [3] investigated the thermal characteristics of solid cast iron rotors that led to surface rupture and cracking. The temperature results obtained from his mathematical analyses, which assessed thermal partitioning between the pads and the rotor, were correlated with temperature measurements from experimental work. The results of the thermal stress analysis revealed that surface rupture occurred when the induced compressive stress exceeded the yield strength in compression in a single brake application. During repeated braking, the fatigue properties were a significant factor in determining the onset of brake disc cracking.

Rainbolt [4] investigated the effect of disc material selection on cracking in brake discs. The investigation was carried out for various test parameters and disc materials using a dynamometer. The experimental results revealed that the degree of surface cracking was

related to the carbon content which had a strong influence on the thermal conductivity of the cast iron brake disc material.

Ferdani and Holme [5] studied the influence of brake disc materials on cracking through the measurement of rotor temperatures during the brake application using an infra-red dual wavelength pyrometer. The results revealed that the cracking of the brake rotor was related to the maximum temperature generated at the rubbing surfaces. Also cast irons with high levels of carbon had fewer cracks in comparison with low carbon materials.

Although increasing the carbon content in cast iron has the effect of increasing thermal conductivity, the yield strength of the material decreases. For this reason, Jimbo et al. [6] introduced a new brake disc cast iron which had high carbon content, low silicon content and a molybdenum additive in order to improve the thermal conductivity whilst minimising the decline in strength. Furthermore, the influence of varying carbon content and chemical composition for several different brake discs was investigated. The experimental results revealed that the proposed material reduced the degree of cracking on the rubbing surfaces.

Apart from the influence of the disc material, the pad material is another factor to be considered in rotor cracking. Ellis [7] studied the influence of different pad materials on several brake discs where failures were experienced. Several brake disc materials, commonly used in Europe, were cyclically tested between surface temperatures of 100 °C and 600 °C using an inertia dynamometer against hard and soft pad materials. The results revealed that most brake disc materials suffered more cracking when tested against the hard pad material. However, the brake discs with the high carbon grade cast iron were able to withstand cracking against both pad materials.

1.2 CAST IRON MATERIAL

1.2.1 GENERAL ENGINEERING MATERIAL PROPERTIES

Cast iron is a material that has been commonly used to create components of varying complexity for a long time. This is because it is relatively inexpensive and easily formed into complex shapes. Normally, cast iron consists of two main substances: graphite (carbon) flakes and matrix ferrous metal. Both of these constituents have a significant influence on the stress-strain response of the material. This is because of the weak bonding between the graphite flakes and metal matrix which causing gaps or voids to open in the material under tension. Therefore, the compressive strength of cast iron is two or three times higher than its tensile strength. In order to capitalise on this anisotropy, the cast iron product should be designed to be loaded in compression wherever possible.

Gilbert [8] performed tests to obtain essential engineering material data that included tensile strength, Young's modulus, thermal conductivity, specific heat and thermal expansion on a variety of grey cast irons which were classified using tensile strengths according to the relevant British Standard [9]. The strong influence of carbon content on mechanical and physical properties is clearly seen in these results.

Hecht et al.[10] measured the specific heat and thermal conductivity at room and elevated temperatures of various cast iron materials used in brake discs. They found that carbon had a large influence on these properties. In addition, the longer the graphite flakes, the greater the thermal diffusivity (ratio of conductivity to the product of specific heat and density). However, elevated temperatures largely resulted in reduction of thermal diffusivity and conductivity.

1.2.2 MONOTONIC LOADING STRESS-STRAIN RESPONSE

The stress-strain curve for one direction of loading only in a uniaxial load test is called the monotonic stress-strain curve (MSSC). Even though cast iron is a brittle material (low strain to failure), there is evidence of inelastic behaviour at relatively low strains. Figure 1.5 shows typical stress-strain curves in tension and compression for low carbon cast iron in which the deviation from the limited initial linear region is obvious [11]. In tension, this deviation is due to the debonding of the graphite flakes in the material and subsequent plastic deformation due to high localised strains in the metal matrix.

To obtain the MSSC at elevated temperature, methods of heating the specimen are a vital key in controlling the temperature conditions. Van Leeuwen [12] reviewed a number of heating methods for metallic specimens such as combustion furnace heating, electric induction heating, electronic resistance heating in gas atmosphere, heating with incandescent lamps and with electric blankets. In practice, electric induction heating provides the fastest temperature response. However it is suitable only for metallic specimens tested under atmospheric conditions.

1.2.3 CYCLIC LOADING STRESS-STRAIN RESPONSE

A different stress-strain curve from the MSSC can exist if the material is subjected to a cyclic load. This is called the cyclic stress-strain curve (CSSC) and has a very important influence on the fatigue characteristics of a material as indicated in Figure 1.6. This is because the CSSC indicates the peaks during cyclic steady state loading. It also provides a more meaningful definition of the mechanical behaviour under cyclic loading at different strain levels.

In theory, if the vertices of stress decrease gradually with the number of cycles, the material will be experiencing cyclic softening. If the vertices of stress increase, cyclic hardening has occurred. This behaviour can also be investigated by comparing the CSSC with the MSSC. Cyclic hardening of a material occurs when the CSSC lies above the MSSC, and vice versa for the cyclic softening.

In practice, there are many procedures to determine the CSSC of a material as reviewed by Landgraf et al.[13]. For example, the multiple step test is used to determine the CSSC by connecting the tips of the stable hysteresis loops at each constant strain-controlled amplitude. The amplitude is increased after each hysteresis loop becomes stable, Figure 1.7 (a). Another technique is known as the incremental step test. In this test, the strain-controlled amplitude is increased gradually at each cycle and reduced gradually after reaching the desired maximum, Figure 1.7 (b). After a few blocks of load pattern have caused a stable superimposed hysteresis loop, the CSSC is determined in the same way as for the multiple step test. The great advantage of the incremental step test is that it is faster in determining the CSSC than the multiple step test.

In reality, the cyclic stress-strain response varies according to the load pattern, and the strain range, strain rate, and temperature. Koibuchi and Kotani [14] studied the cyclic stress-strain behaviour of 0.3 percent carbon steel under several constant amplitude tests that included the multiple step test and the incremental step test. As a result, the degree of cyclic softening from the incremental step test was found to be greater than that from the multiple step test. Furthermore, the CSSC can be expressed in the equation for the plastic strain and stress amplitudes that can be used to find the fatigue life of the material from the Manson-Coffin equation [15].

Gilbert [16] investigated the cyclic strain response of grade 300 cast iron. He found that the peak tensile stresses decreased gradually and the peak compression stresses increased with each strain cycle until failure. This was due to the effect of the repeated opening and closing of gaps between the graphite flakes and metal matrix. The vertices of stress at the given cycle numbers were used to plot the CSSC shown in Figure 1.8. This indicates that cyclic softening occurs in tension whilst cyclic hardening takes place in compression.

To apply and control external loads on specimens in cyclic testing, special grips must be designed to prevent or minimise backlash during load reversal. For this reason, grip designs and arrangements related to particular specimen designs have been developed for particular cyclic load tests. For example, Slot et al.[17] designed grips in order to have good alignment and rigidity as shown in Figure 1.9. This design minimised the likelihood of backlash during tests. However, the assembly of specimens within the grips was cumbersome. Another grip design that used a threaded end specimen was introduced [18]. As shown in Figure 1.10, this grip design could be also used with induction heating but the insertion and removal of specimens was again difficult.

1.3 FINITE ELEMENT (FE) METHOD

Before the age of computers, analytical methods were used as engineering tools for determining the integrity of a design. For example, Dike [19] illustrated that the mathematical equations for conduction of heat in an isotropic solid could be used to investigate the temperature response of brake disc designs by simplifying complicated parameters such as temperature dependent material properties, real brake disc geometry and complex boundary conditions. However, for real problems involving complex material properties and boundary conditions, a numerical method of analysis is more

suitable. The most popular of the various numerical methods that have been developed is the finite element (FE) method. Two types of FE analysis are widely used in brake design: heat transfer analysis to determine transient temperature distributions and thermal stress analysis to determine stresses and strains due to these non-uniform temperature distributions.

1.3.1 APPLICATION OF FE TO BRAKE DISC TEMPERATURE ANALYSIS

The nature of the engineering problem to be solved dictates the structure of the finite element model which could, for example, be axisymmetric or three dimensional. An axisymmetric model is based on the assumption that both the geometry and loading do not vary in the circumferential direction which implies that the measurements (temperature, stress, etc) are also invariant in the circumferential direction. Using complex three-dimensional models, a whole brake disc can be modelled in order to obtain such variables. However, one angular sector of a brake disc can also be modelled in three dimensions using the concept of cyclic symmetry.

After the brake disc geometry has been modelled, the boundary conditions, i.e. energy input and energy output, must be specified. Energy input is in the form of heat flux generated at the rubbing surfaces during the brake application. Energy output from the brake is defined as the rate of thermal energy transferring to the ambient air. Such thermal energy is lost from the structure by the processes of convection and radiation but also involves conduction to other parts of the vehicle e.g. the hub and wheel. Blot [20] defined several numerical procedures for the temperature analysis of brake discs and revealed that the FE technique was the fastest and most accurate for the investigation of brake disc performance. Furthermore, the time and cost of prototype manufacture and test could be significantly reduced.

Sheridan et al. [21] reviewed the techniques for modelling the thermal response of brake discs ranging from simple to complex three dimensional analyses including the methods to calculate the thermal boundary conditions. They suggested that more than 90% of all heat dissipated to ambient was transferred by convection for most braking conditions. Furthermore, the accuracy of thermal brake disc models was dependent on how the thermal boundary conditions were determined. As well as specifying the energy input and output accurately, the material properties (e.g. thermal conductivity, specific heat, etc.) had a great influence on the temperature response.

The heat flux generated at the rubbing surface can transfer to both the rotor and the pad. The amount of thermal energy transferred into the brake rotor depends on the specification of the friction and disc materials. Yano and Murata [22] performed experimental work to determine the amount of heat flow from the frictional interface into the rotor by conduction. The volume or quantity of heat transferring to the pads, the rotor and the ambient air was obtained from the measured temperature gradients and heat transfer coefficients. According to their experiments, the heat conduction from the rubbing surfaces to the rotor was approximately 72% of the heat generated.

Simple models assume the heat flux to be uniform over the contact region between the pad and rotor but in practice non-uniform heat flux occurs during brake application. The non-uniform heat flux on the brake disc can be calculated from the non-uniform pressure distribution, the local friction coefficient and local sliding velocity along the pad width [21].

Samie and Sheridan [23] investigated the effects of friction on the pressure distribution between the rotor and the pads with a floating caliper using the FE technique. The computational results without the friction forces (static case) revealed that the inboard and outboard pressure distributions varied because the locations of the normal forces acting on the pads were different on the piston and finger sides of the floating caliper. Furthermore, the pressure distributions with the friction forces taken into account were different from the static case due to the moment set up between the abutment and the friction interface.

Similarly, Lee et al.[24] studied the pressure distribution between the rotor and the pads including the friction force with a floating caliper in order to investigate the motion at the friction interface that could be used to determine the onset of disc brake squeal using the FE technique. The computed result revealed that the pressure distributions acting on the pads were different on the piston and finger sides of the floating caliper. Moreover, the axial displacements at the friction interface on the two sides were different.

Richmond et al. [25] studied the pressure distribution at the interface between the pad and the brake disc using the FE technique. The heat generation at the interface was calculated from the local sliding speed, friction coefficient, and contact pressure. The results revealed that the contact pressure peak moved along the pad as wear occurred at the interface.

Rinsdorf [26] studied the effect of parameters leading to the non-uniform pressure distribution that was a major factor causing high local energy input and, therefore, local brake disc cracking. These parameters included the thickness of the backing plate and the design of the shim between the piston and the backing plate. It was found that the

pressure distribution could be made more uniform by carefully designing and positioning the shim with respect to the piston. However, no major influence of the backing plate thickness was found.

Tirovic and Day [27] considered the influence of friction material compressibility, backing plate thickness, coefficient of friction, caliper configuration and disc stiffness in the axial direction on the pressure distributions using the FE technique. The results showed that the pressure distribution and contact area varied according to all of these factors except for the disc stiffness. However, it should be taken into account that the effect of thermal distortions such as brake disc coning also causes non-uniform heat flux across the rubbing surfaces. When attempting to analyse such gross thermal deformations, the assumption of a uniform heat flux over the rubbing surfaces is usually sufficiently accurate.

Limpert [28] investigated the temperature performance of a solid brake disc. The applied uniform heat flux was calculated from an assumed uniform pressure distribution, the coefficient of friction and the heat partitioning between the rotor and the pad. The maximum temperatures from calculation and experiment at the rotor surface were correlated during a series of brake applications.

Noyes and Vickers [29] predicted the temperature response on the rubbing surfaces of a brake disc, using the assumption of a uniform heat flux. The computational results were compared with the temperatures measured at the rotor surface on entry to and exit from the pad area. It was found that the measured temperature on exit from the pad was higher than the temperature calculated using the assumption of uniform heat flux by approximately 55°C. Moreover, the calculated temperature was 14°C higher than the

measured temperature on pad entry. However, for many applications, the effect of this circumferential temperature variation, the so-called "rotating heat source" effect, can be ignored.

As mentioned above, the majority of the heat generated at the rubbing surface is dissipated through the mechanism of convection, conduction and to some extent radiation under almost all braking conditions. Thus the definition of the appropriate convection heat transfer coefficient for each exterior surface of the brake disc model is extremely important.

Schwartz et al.[30] studied design improvements for a cast iron brake disc in order to achieve lower temperatures at the rubbing surfaces. To accomplish this objective, the predicted temperature responses at the rubbing surface were correlated with experimental results by the adjustment of the heat transfer coefficients over the brake disc surface. To obtain the heat transfer coefficients, they considered the brake disc geometry to consist of simple geometric shapes e.g. discs, cylinders, flat plates etc. Heat transfer coefficients could be estimated from the Nusselt number for these various geometric shapes using analytical expressions that were readily available within primary sources of literature.

Dennis et al. [31] studied the heat transfer coefficients from a rotating brake disc in an airstream. The brake disc was heated using an electronic heater located under the brake disc surface. The heat flows were calculated from temperature differences measured by thermocouples located in the brake disc. The relationship between the mean Nusselt number and Reynolds number was presented. Cobb and Saunders [32] performed a similar experiment in order to investigate the heat transfer from a rotating disc but this

time in still air. From the results, the Nusselt number and Reynolds number were correlated including the relationship between the measured velocity and the temperature profiles.

Daudi et al.[33] studied the influence of differing brake disc geometry and the type and number of fins on the cooling efficiency of a brake disc using CFD techniques and experimental airflow measurements. For the optimum design the resulting increased flow rate and air velocity through the vents led to increases of the Nusselt and Reynolds numbers which would increase the convective heat transfer coefficients.

1.3.2 APPLICATION OF FE TO BRAKE DISC THERMAL STRESS

A thermal stress analysis of a brake disc uses nodal temperatures as input that are firstly calculated in a preceding temperature analysis. Fukano and Matsui [34] applied this technique in order to investigate elastic thermal stresses in a brake disc with temperature dependent material properties. They found that the maximum calculated tensile stresses in brake discs exceeded the tensile strength of the actual brake disc material, resulting in cracking in the top-hat section close to the attachment holes which had high stress concentration. This prediction of cracking agreed with the experimental results.

Timtner [35] studied the influence of solid brake disc geometry on brake disc coning using linear elastic FE models. Nodal temperatures, derived from thermal FE analysis, again provided the input to the structural analysis. The effects of changes in the top-hat depth, hat thickness and the undercut depth were investigated. The computational results revealed that increases of the hat depth and the undercut depth both reduced the degree of brake disc coning. However, increases of the hat thickness had the greatest influence.

In contrast, Bailey et al.[36] applied the thermal imaging technique in order to obtain the temperature distributions as the data input to the thermal stress analysis. The procedure for using this technique was divided into a number of stages. Temperature data from a camera that recorded thermal images from the brake disc were used to generate the input heat flux on the rubbing surface. From a steady state FE temperature analysis using this heat flux, the nodal temperatures in the disc could be obtained. A similar FE model was then used for the calculation of thermal stress in which the effect of circumferential temperature variation was also taken into account. In this analysis, non linear stress-strain curves for cast iron in tension only were used. With the thermal imaging technique, estimations of the heat partitioning between the rotor and the pads and the effects of a non-uniform pressure distribution are unnecessary. However, its validity relies on the accuracy of the temperatures measured in the experiment.

In order to accurately predict the induced thermal stress and non-reversible (plastic) strain accumulation in a brake disc, it is necessary to improve the accuracy of the material model. For example, if cast iron is used, the material model should include differences in yield behaviour in tension and compression and also allow for temperature dependence. D'Cruz [37] investigated inelastic thermal stresses in a cast iron brake disc with a von Mises stress yield surface. The input data for the material model was obtained from the compressive stress-strain curve only based on the fact that the brake disc cheeks were mainly subjected to compressive thermal load. If plastic strain occurred under tension in other areas, the tensile thermal stress was calculated by hand from the tensile stress-strain curve and the predicted plastic strain.

In practice, a brake application induces both thermal and mechanical stress in a disc. As already stated, the induced thermal stress occurs from the non-linear temperature

gradient, potentially resulting in plastic strain accumulation. However, the mechanical loads (i.e. pressure normal to disc over pad area, friction braking drag load, centrifugal force, and inertia force due to the deceleration of the disc during the brake application) might also affect the overall stress levels. Medonos [38] investigated the mechanical and elastic thermal stresses using the FE technique with temperature dependent properties. A full three dimensional model was necessary in order to take the braking drag load and the circumferential variation of thermal stresses into account. The results revealed that the effect of mechanical stresses due to the braking pressure load, deceleration forces and centrifugal forces were minor and could be neglected. However, the friction braking drag load induced significant shear stress in the disc.

1.3.3 MATERIAL MODELLING

In inelastic stress analysis, a mathematical equation involving the three principal normal stresses, known as a yield function, is generated. If the calculated yield function is greater than the yield strength of a material, plastic straining and subsequent strain softening or hardening occurs. Generally, there are several yield functions available to check whether the stress state is beyond the elastic region. These include the von Mises stress criterion, the maximum shear stress criterion and the maximum normal stress criterion. If a material is subjected to stresses beyond the elastic region, change of the yield surface occurs due to the development of plastic strain. There are two basic types of change of the yield surface. One is based on the assumption that the centre of the yield surface remains fixed whilst, at the same time, the yield surface expands without changing shape. This is known as isotropic hardening. The other, known as kinematic hardening, is based on the assumption that the yield surface translates within the stress space but does not change size or shape.

Both the maximum shear stress and von Mises stress criteria are widely used to predict the yield surfaces of ductile materials because they have been found to fit the experimental results, Figure 1.11 [39]. In contrast, the maximum normal stress criterion is commonly used to predict fracture for brittle materials (e.g. grey cast iron) because their yield stresses occur at the low strain levels and are difficult to define. Grassi and Cornet [40] performed experimental work to investigate the fracture properties of grey cast iron and compared the results with the maximum principal stress criterion as shown in Figure 1.12. The fracture data are shown to be closely related to the maximum normal stress criterion in tension. This is because grey cast iron consists of graphic flakes inside a metal matrix and tensile normal stresses are expected to open voids between these substances which then acted as cracks. Thus tensile failure is expected to occur on the plane normal to the maximum tensile stress. Conversely, in compression the gaps between the substances are pressed together, resulting in high compressive strength. According to Grassi and Cornet, it seems that the failure of grey cast iron in compression occurs on planes inclined to the maximum compression stress. The data in fact lies close to the von Mises stress criterion.

Coffin and Schenectady [11] also studied the flow and fracture of a grey cast iron by applying biaxial loads to tube specimens. They reported that the effective stress in the iron matrix at the edge of the graphite flakes could be calculated using the maximum shear stress or von Mises stress yield criterion. Therefore the theory of generalised plastic stress-strain relationships and plastic flow of ductile metals could be applied to cast iron in tension.

Since cast iron is widely used in engineering designs, the commercial company who developed the well-known FE package ABAQUS (Hibbitt, Karlsson and Sorensen, Inc.)

decided to develop a special cast iron material model as a standard option [41]. The yield surface for this model utilises the maximum normal stress and von Mises stress criterion in tension and compression respectively. Details of this material model and its plastic flow criteria are discussed in Chapter 4. Although the maximum normal stress criterion may be used to describe fracture of a brittle solid, there is little evidence that this criterion is suitable for describing the yield behaviour of a relatively ductile matrix containing voids caused by debonding at the graphite flakes. In fact, yield for such a voided solid is usually assumed to be a function of the von Mises stress and current void volume fraction [42-43].

Josefson et al.[44] proposed an alternative material model for cast iron using the user-subroutine option in ABAQUS. To avoid using the maximum normal stress criterion, a modified von Mises yield criterion was specified in the tensile region by adding the tensile and compressive yield strengths in the yield function as defined in Equation 1.1:

$$\begin{aligned} F_t &= \frac{1}{2}S_{ij}S_{ij} - P(\sigma_c - \sigma_t) - \frac{1}{3}\sigma_c\sigma_t \;, \; P < -\frac{\sigma_c}{3} \\ F_c &= \frac{1}{2}S_{ij}S_{ij} - \frac{1}{3}\sigma_c^2 \qquad\qquad\qquad\quad \;, \; P \geq -\frac{\sigma_c}{3} \end{aligned} \tag{1.1}$$

where

F_t = Tensile yield function

F_c = Compressive yield function

S_{ij} = Deviatoric stress tensor

σ_t = Tensile yield stress

σ_c = Compressive yield stress

P = Hydrostatic pressure

Furthermore, the simple compressive von Mises yield criterion was used in the compression region. These two different yield surfaces are governed by the hydrostatic pressure and compressive yield strength. If the hydrostatic pressure is more than one third of the compressive yield strength, the compressive von Mises yield criterion is used; otherwise the modified tensile von Mises yield surface, Equation 1.1, is used. However, this particular cast iron material model is independent of temperature. It is considered extremely important to take account of the effect of temperature on the yield behaviour of cast iron in the analyses of brake rotors since the range of temperatures experienced is potentially large. Therefore a von Mises yield criterion with temperature dependence in both tension and compression, that is unique and different from Josefson's yield criterion [44], is implemented in Chapter 4.

1.4 SCOPE AND OBJECTIVES OF THESIS

Excessive thermal deformation of cast iron rotors is one of the most serious problems facing automotive brake designers as they try to enhance disc brake performance for faster and heavier vehicles within tight packaging constraints. In addition, cracking sometimes occurs as a result of repeated high speed stops when the brake rotor is subject to rapid and severe thermal cycling. It is postulated that this type of failure occurs from ductility exhaustion as a result of inelastic (plastic) cyclic strain accumulation in the cast iron rotor. Therefore, any attempt to understand or predict this mechanism of failure must include the non-linear stress-strain response of the cast iron material. Furthermore, the different yield behaviour of cast iron in tension and compression should be taken into account. Since temperatures vary considerably in a brake rotor under severe braking conditions, it is also necessary to allow accurately for the effect of temperature on the non-linear stress-strain response of cast iron. At present, the required data does not appear to be available in the literature. Therefore, it is

essential to generate such data and then embody it within a suitable analytical model of cast iron behaviour in order to accurately predict plastic strain accumulation in brake rotors. Thus, the overall aim of the thesis is to determine suitable material models for cast iron and to apply them in realistic analyses of typical brake disc designs. Accurate predictions of plastic strain accumulation, which may ultimately lead to disc cracking, can then be made.

The thesis begins with the literature review contained in this Chapter which has introduced automotive brake disc technology together along with a survey of cast iron material properties and FE analysis techniques applied to brake discs. The application of the FE technique to a back-vented disc design for both temperature and elastic thermal stress analysis is presented in Chapter 2. A corresponding front-vented disc design is also investigated. The mechanical response of the cast iron material for this particular brake disc under uniaxial and cyclic loads at various temperatures is explored in Chapter 3 and the techniques used to obtain the stress-strain response at elevated temperatures are introduced. Chapter 4 is devoted to the description and development of the material models for cast iron to be used in the inelastic thermal stress analysis. The applications of these material models to the back-and front-vented disc designs during the brake application and cooling period are presented in Chapter 5. In addition, the effect of further thermal cycles on both brake disc designs is presented. Discussion of results from the computational and experimental work is contained in Chapter 6 whilst Chapter 7 is devoted to the conclusions including suggestions for further work.

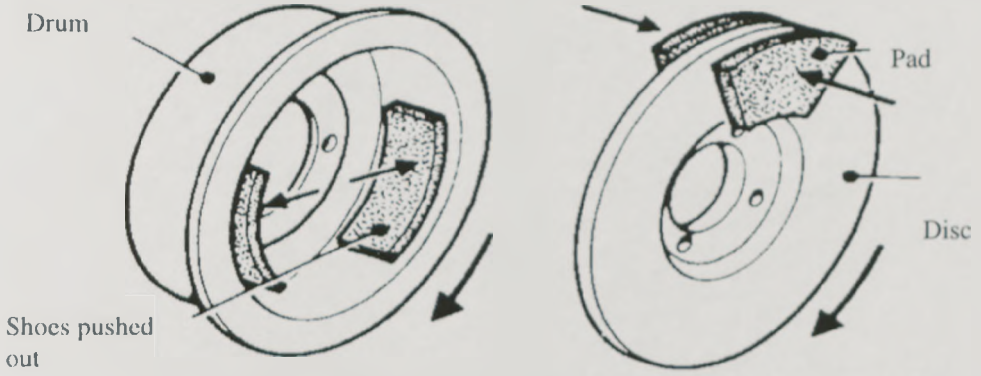

Figure 1.1: Basic types of foundation brake [45]

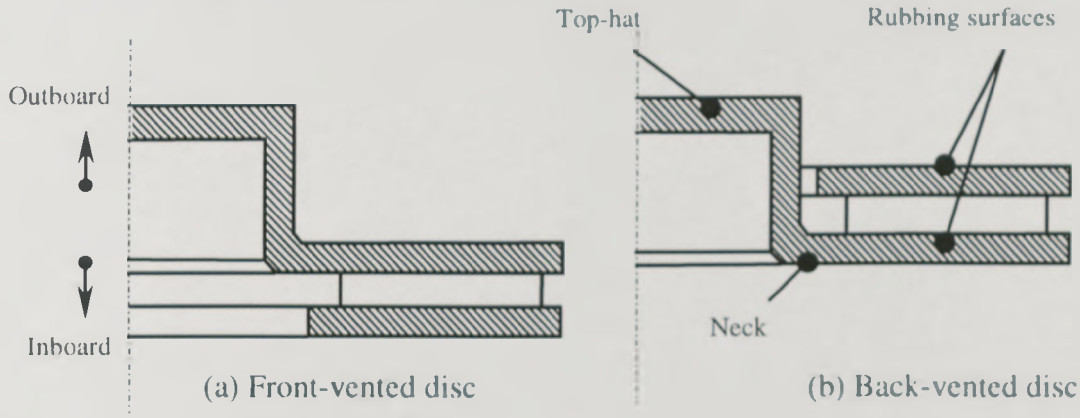

Figure 1.2: Typical front-and back-vented discs

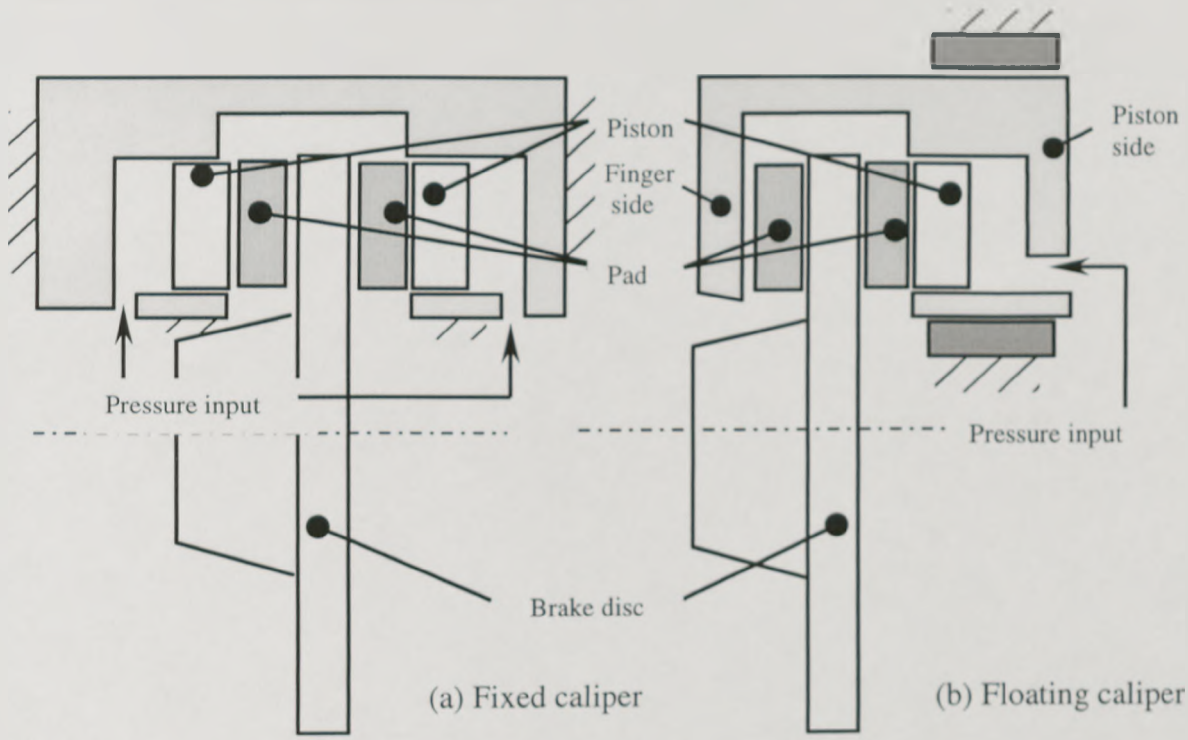

Figure 1.3: Schematics of typical fixed and floating calipers [46]

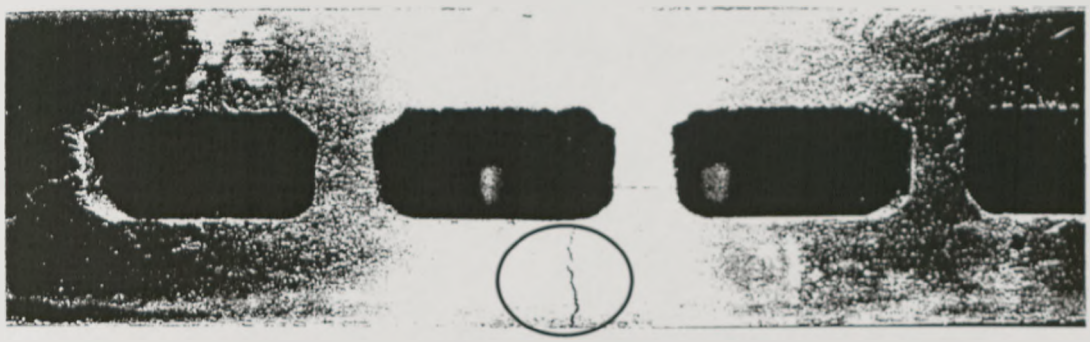

Figure 1.4: Cracking in a vented brake disc [4]

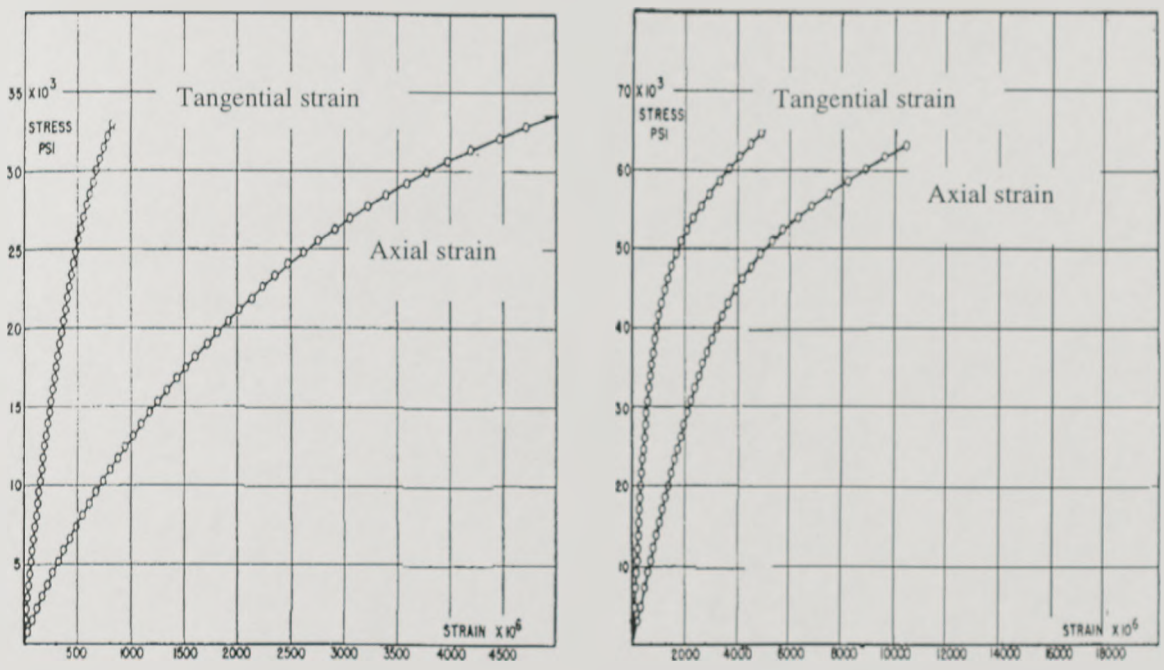

(a) Tension

(b) Compression

Figure 1.5: Monotonic stress-strain curves for grey cast iron [11]

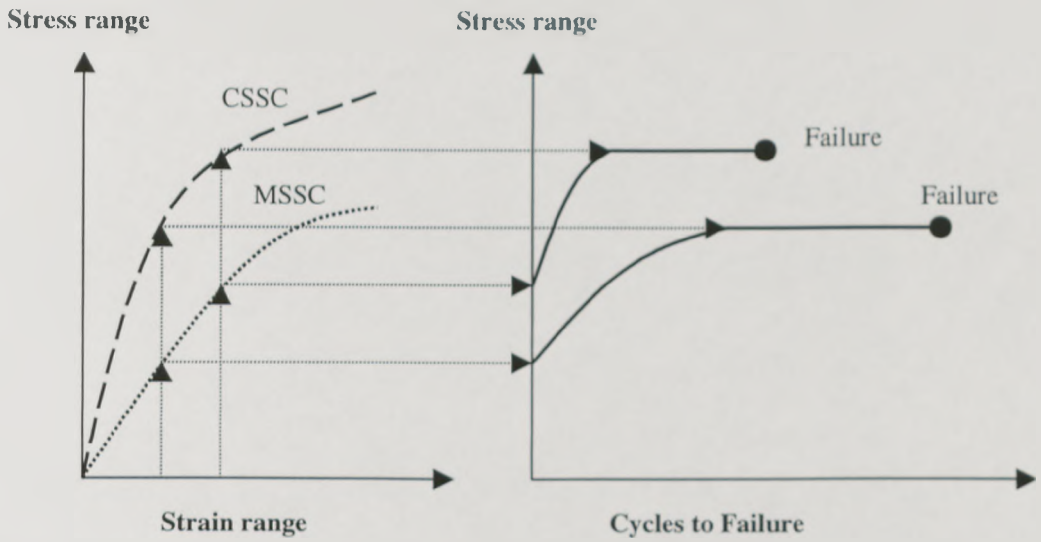

Figure 1.6: The relation between the CSSC and fatigue life [47]

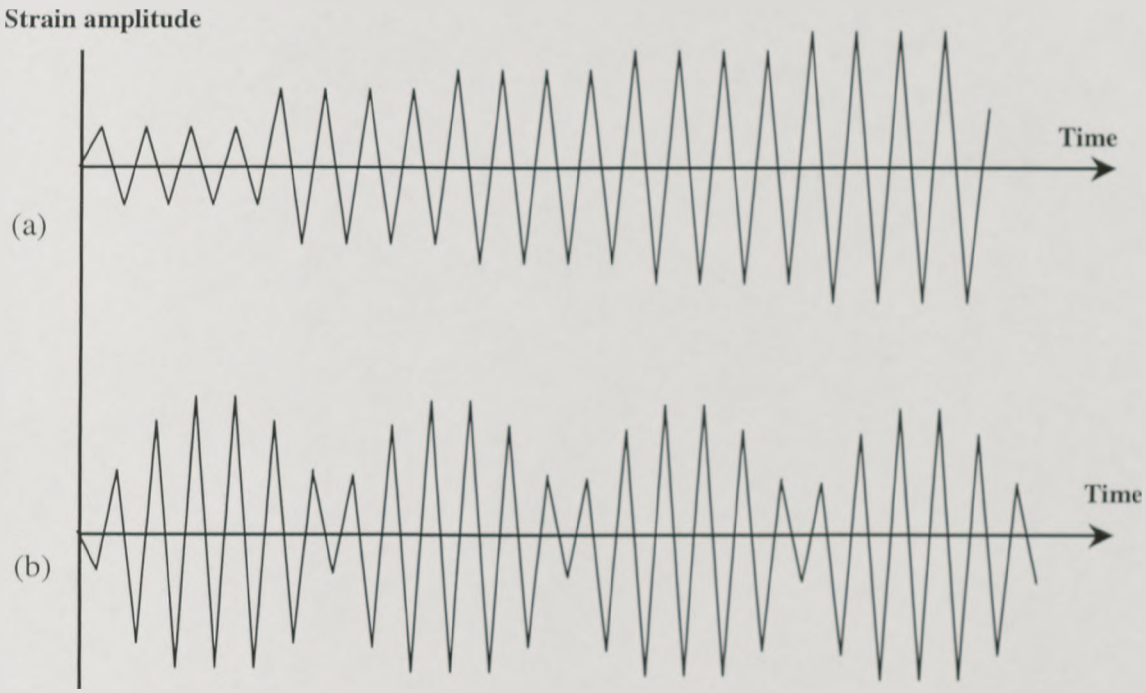

Figure 1.7: Strain time histories for (a) multiple step test, (b) incremental step test [13]

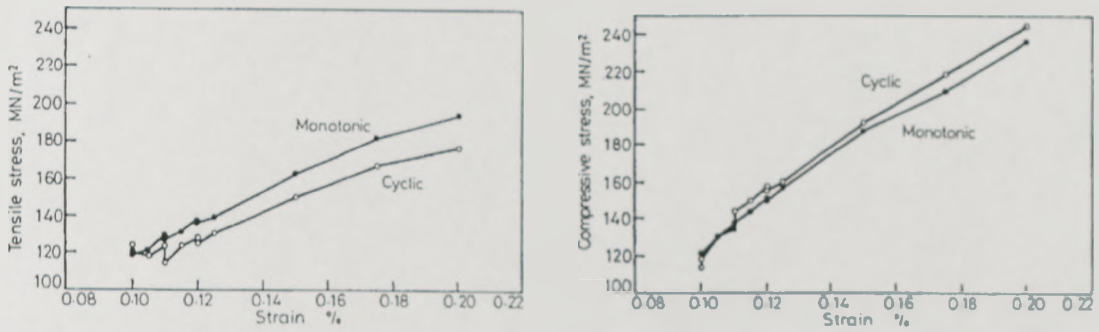

(a) Tension (b) Compression

Figure 1.8: Cyclic and monotonic stress-strain curves in tension and compression [16]

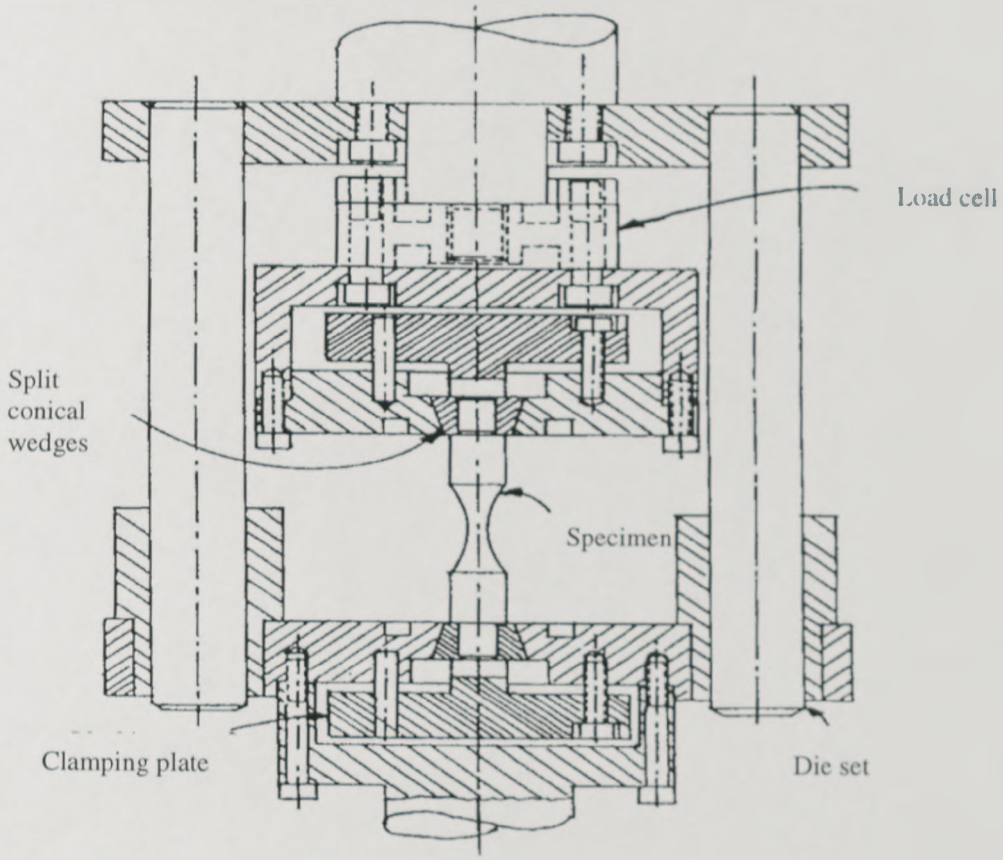

Figure 1.9: Grip design for fatigue testing [17]

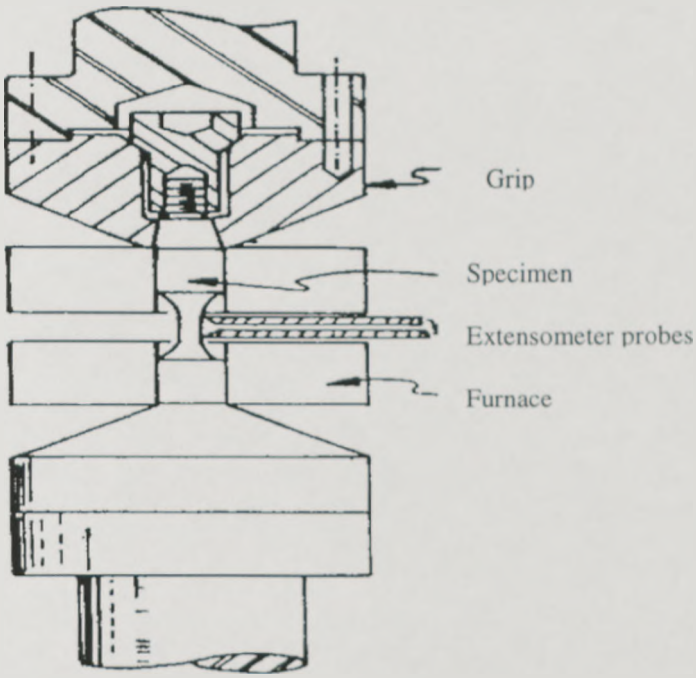

Figure 1.10: Grip design for fatigue testing [18]

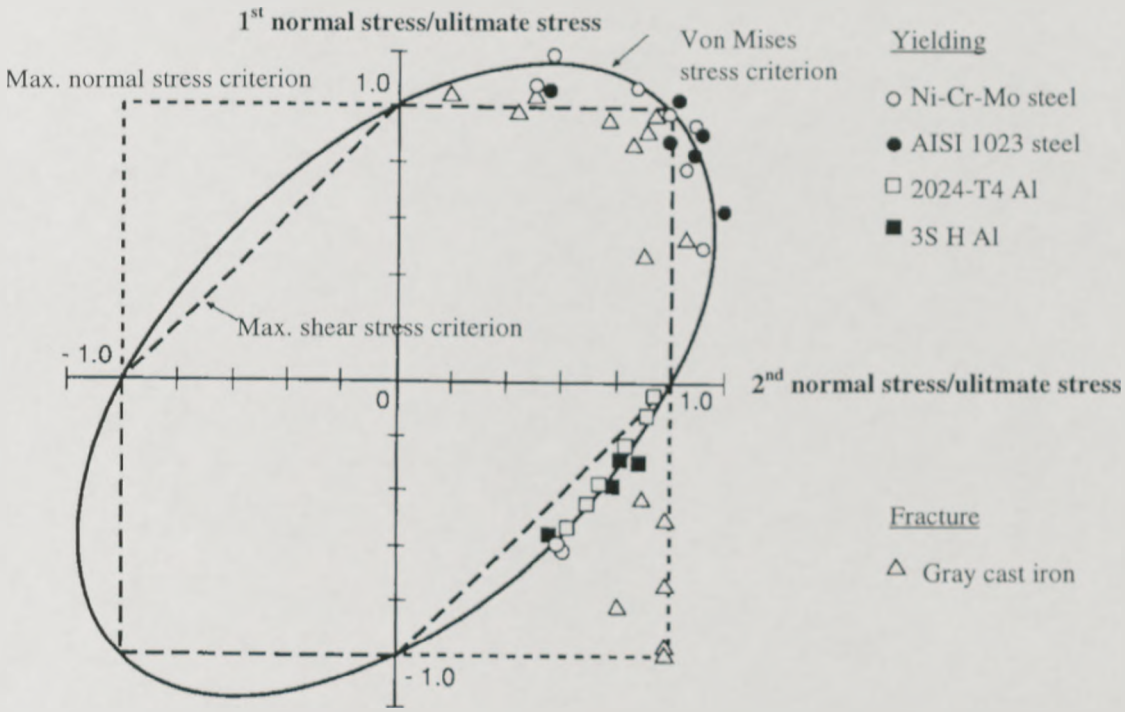

Figure 1.11: Biaxial yield stress data for Ni-Cr-Mo steel, AISI 1023 steel, 2024-T4 Al and 3S-H Al; and fracture stress data for grey cast iron with three different failure criteria shown [39]

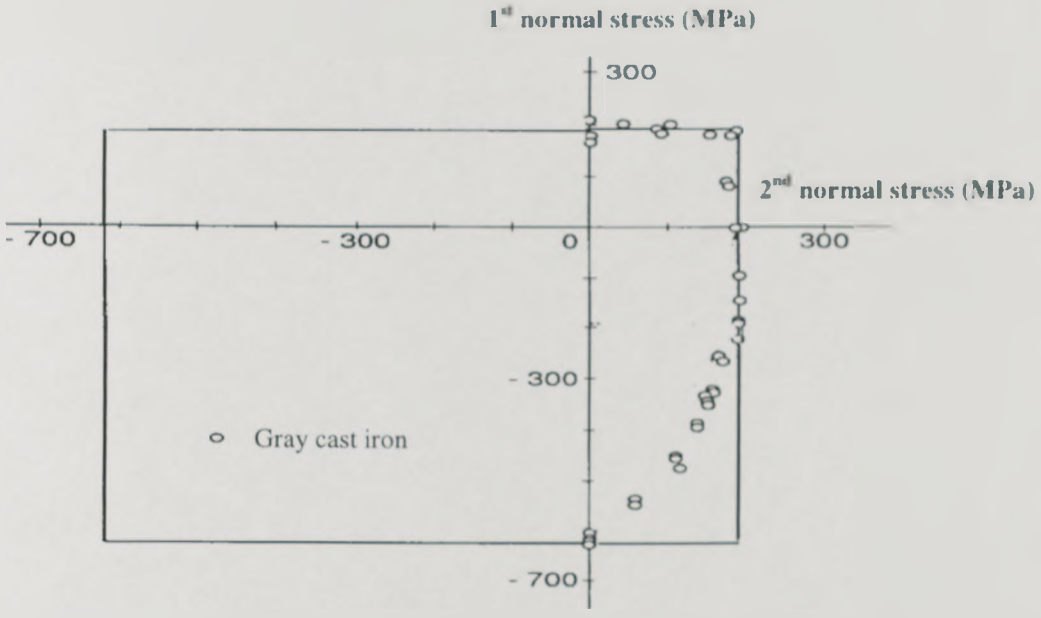

Figure 1.12: Biaxial fracture data for grey cast iron compared to the maximum normal stress failure criterion [40]

CHAPTER 2

INITIAL FINITE ELEMENT ANALYSIS OF BRAKE DISC

2.1 INTRODUCTION

This Chapter concentrates on a linear elastic thermal stress analysis of a new design of back-vented high carbon cast iron disc developed by Rover Cars for a medium size yet relatively high performance passenger car [48]. The purpose is to investigate disc performance and verify whether the maximum thermal stress is beyond the proportional limit under severe brake conditions. The transient temperature response of the brake disc is first required in order to be used as a load input for the thermal stress analysis. In this Chapter, an FE model of the Rover disc is subjected to severe thermal cycles using the commercial package ABAQUS [41]. The particular cycle chosen for the simulation involves successive high 'g' braking of the vehicle from high speed. The details of the thermal analysis procedure are firstly described followed by a description of the elastic thermal stress analysis. In a parallel study, these analyses are repeated to include the investigation of an equivalent front-vented disc design in order to compare the effect of brake disc geometry.

2.2 THERMAL ANALYSIS

To investigate the thermal stress behaviour of brake discs under cyclic thermal load, it is necessary to obtain typical temperature distributions in these brake discs as a function of time. Therefore, the objective of this section is to predict the temperature response of the back-vented brake disc design. The techniques and assumptions are introduced below.

2.2.1 METHODOLOGY

A basic principle underlying the finite element method applied to heat transfer analysis is derived from the variational approach that relies on the minimisation of a functional. In the field of heat transfer, the functional is derived from the governing differential equation for heat diffusion along with its boundary conditions. To obtain the differential equation, the conservation of heat energy is applied to a differential control volume (dx . dy . dz) that has heat conduction heat rates (q_x, q_y and q_z) perpendicular to each of the control surfaces in the x, y, and z co-ordinate directions respectively. The heat conduction rates into the control volume are illustrated in Figure 2.1. The conduction heat rates (q_{x+dx}, q_{y+dy} and q_{z+dz}) at the opposite surfaces can then be expressed as a Taylor series expansion:

$$
\begin{aligned}
q_{x+dx} &= q_x + \frac{\partial q_x}{\partial x} dx \\
q_{y+dy} &= q_y + \frac{\partial q_y}{\partial y} dy \\
q_{z+dz} &= q_z + \frac{\partial q_z}{\partial z} dz \\
q_x &= -k_c \cdot dy \cdot dz \cdot \frac{\partial T}{\partial x} \\
q_y &= -k_c \cdot dx \cdot dz \cdot \frac{\partial T}{\partial y} \\
q_z &= -k_c \cdot dx \cdot dy \cdot \frac{\partial T}{\partial z}
\end{aligned}
\tag{2.1}
$$

where

k_c = Conductivity
T = Temperature

For convenience, the conservation of energy can be expressed in rate form over the control volume as shown in Equation 2.2.

$$
\begin{aligned}
\text{Rate of heat increment in the volume } (\dot{E}_{st}) = {} & \text{ rate of heat transfer across its surfaces} \\
& + \text{rate of internal heat generation } (\dot{E}_g)
\end{aligned}
\tag{2.2}
$$

The rate of heat increment in the volume ($\dot{E}_{st}$) is a function of density (ρ), specific heat (c) and the rate of temperature increase ($\partial T/\partial t$):

$$\dot{E}_{st} = \rho c \frac{\partial T}{\partial t} dx\, dy\, dz \tag{2.3}$$

The rate of heat transfer across the surfaces is obtained from the sum of the conduction heat rates defined in Equation 2.1. The energy source within the volume can be defined as the rate of internal heat generation:

$$\dot{E}_g = \psi\, dx\, dy\, dz \tag{2.4}$$

where ψ is the rate at which energy is generated per unit volume.

Substituting Equation 2.1, 2.3 and 2.4 into Equation 2.2 gives:

$$-\frac{\partial q_x}{\partial x} dx - \frac{\partial q_y}{\partial y} dy - \frac{\partial q_z}{\partial z} dz + \psi\, dx\, dy\, dz = \rho c \frac{\partial T}{\partial t} dx\, dy\, dz \tag{2.5}$$

or

$$\frac{\partial}{\partial x}(k_c \frac{\partial T}{\partial x}) + \frac{\partial}{\partial y}(k_c \frac{\partial T}{\partial y}) + \frac{\partial}{\partial z}(k_c \frac{\partial T}{\partial z}) + \psi = \rho c \frac{\partial T}{\partial t} \tag{2.6}$$

To determine the temperature distribution from Equation 2.6, the physical conditions existing at the boundaries must be defined such as surface heat fluxes and convective heat transfer coefficients at free surfaces. By expressing this differential equation as a functional that is defined as some integral over the control volume and part of its boundary, the basic finite element method for heat transfer analysis can be derived using the variational approach [49].

The material properties required for the temperature analysis in brake discs include the density, specific heat capacity and thermal conductivity. Table 2.1 below shows the temperature dependent properties for the grade 150 cast iron used in the Rover disc design [8]. A constant density of 7050 kgm^{-3} was assumed.

Temperature (°C)	Conductivity ($W\ mm^{-1}\ °C^{-1}$)	Specific heat ($J\ kg^{-1}\ °C^{-1}$)
20	0.0533	103
100	0.0525	247
200	0.0515	427
300	0.0505	607
400	0.0495	697

Table 2.1: Material data for grade 150 grey cast iron [8]

2.2.2 FINITE ELEMENT MODEL

In order to accurately conduct the heat transfer and structural analysis of the vented rotor design chosen for this study, a 3D model of the brake disc and wheel hub was developed. Since the purpose is to predict typical temperature data for investigating the thermal stress behaviour, only the area where the brake disc is subjected to high thermal load was modelled in detail. Thus, a high mesh density around the vanes is essential to allow accurate predictions of both thermal and structural effects in this area. Many different models that included different levels of detail and mesh density were explored [50]. The final model contains a 15.65° segment of the brake disc and hub meshed using nearly three thousand 20 noded solid elements with a quadratic interpolation function as shown in Figure 2.2. Note that one complete long vane and two half short vanes have been included in the model which allows for the cyclic symmetry that exists in the disc (i.e. this segment is repeated 23 times to give the complete brake disc). However, the

undercut between the bell and the neck has been excluded from the model since the mesh density around this area will be high, resulting in the increase of time in analysis.

2.2.3 THERMAL LOADING CONDITIONS

The particular cycle chosen from autobahn driving conditions chosen for the simulation involved braking the vehicle from an initial velocity of 48 ms^{-1} (108 mph) to 16.7 ms^{-1} (37.5 mph) at a constant deceleration of 0.7g with the brake rotor at an initial uniform temperature of 80 °C. The vehicle is subsequently accelerated up to the same initial velocity and the rotor is allowed to cool again to 80 °C before the cycle is repeated up to seven times (the "Audi eight stop" test). The assumed relative air speed of vehicle in the present analysis is shown in Figure 2.3. For investigating the linear elastic thermal stresses in the back-vented disc, only a single cycle of braking and cooling is simulated since stresses and deformations are fully reversible and will simply be repeated for any subsequent cycle.

2.2.3.1 ENERGY INPUT

The heat flux generated by pressing the pad against the rubbing surface of the rotor is the only source of heat input to the model. The magnitude of this heat flux can be calculated from basic energy considerations. The assumption starts with a vehicle of mass, M (kg), that has an initial velocity of V_i (ms^{-1}) before the brakes are applied to give a constant deceleration of a (ms^{-2}) until the final vehicle velocity of V_f (ms^{-1}) is attained over braking time, Δt (s). If all the kinetic energy of the vehicle is converted to heat, conservation of energy dictates that for the entire vehicle:

$$\frac{(\frac{1}{2}MV_i^2+\frac{1}{2}I\omega_i^2)-(\frac{1}{2}MV_f^2+\frac{1}{2}I\omega_f^2)}{\Delta t}=\frac{q}{\Delta t} \qquad (2.7)$$

where:

ω = Angular velocity of rotating parts, ($rads^{-1}$)

I = Moment of inertia of rotating parts, (kgm^2)

q = Magnitude of heat input, (J)

Assuming $\omega = \frac{V}{R}$ where R (m) is the wheel rolling radius, and the moment of inertia, I, for the rotating parts is $I = mk^2$ where m = mass of rotating parts (kg), and k = radius of gyration (m) then:

$$\frac{(\frac{1}{2}MV_i^2 + \frac{1}{2}mk^2\frac{V_i^2}{R^2}) - (\frac{1}{2}MV_f^2 + \frac{1}{2}mk^2\frac{V_f^2}{R^2})}{\Delta t} = \frac{q}{\Delta t} \qquad (2.8)$$

Substituting $V_i^2 - V_f^2 = 2\,a\,\Delta S$, where ΔS = distance travelled (m), Equation 2.8 becomes:

$$\frac{a\,\Delta S}{\Delta t}(M + m\frac{k^2}{R^2}) = \frac{q}{\Delta t} \qquad (2.9)$$

Replacing the term $(M + m\frac{k^2}{R^2})$ with K M and $\frac{\Delta S}{\Delta t}$ with V , the instantaneous velocity (ms^{-1}), Equation 2.9 becomes :

$$K\,V\,M\,a = \frac{q}{\Delta t} \qquad (2.10)$$

For the purposes of the present analysis, the total mass of the rotating parts, i.e. the crankshaft of the engine, transmission system and road wheels, was assumed to be around 10 % of the gross vehicle weight although it will vary according to the exact vehicle specification. Therefore, as a ball-park figure, K was assumed to be 1.1.

Due to the effect of axial load transfer during the brake application, the friction forces between tyres and road at the front wheels will be higher than those at the rear wheels. This requires a higher front braking effort in order to get maximum deceleration.

Therefore, a pressure limiting or pressure reducing valve is often used to regulate the distribution of braking effort across the axles in order to optimise the system efficiency. For the temperature analysis in this Chapter, 70% of the braking effort was assumed to act at the front axle. This is a representative value of front axle braking effort found in a typical two axle road vehicle [51]. As a result, the correction factor (X_f) applied to the thermal input due to this braking ratio was set to 0.7 i.e. 70 % of the total thermal energy is dissipated at the front wheels.

The thermal energy generated at the brake friction interface can be transferred to both the brake rotor and the pads. This partitioning of the thermal energy is dependent on the relative thermal resistances of the pad and brake rotor that are functions of their respective material densities, heat capacities and thermal conductivities as well as of the presence of any transfer film or third body layer at the rubbing interface. Theoretically, the pad thermal resistance should be higher than the rotor thermal resistance in order to protect the brake fluid from high temperatures but the value of the thermal resistance varies from one pad material to another. For the present analysis, the partitioning factor (K_p) for thermal input to the brake disc was assumed to be 95% of the total thermal energy [3]. Therefore, Equation 2.10 becomes:

$$X_f \, K_p K \, V \, M \, a = \frac{q}{\Delta t} \tag{2.11}$$

Finally, all vehicles in motion are subjected to rolling resistance due to tyre losses and friction in the bearings of the rotating parts of the transmission. The rolling resistance is also augmented by engine braking if the vehicle is left in gear during the brake application. Moreover, aerodynamic drag forces act to further reduce the vehicle speed according to the frontal cross-sectional area of the vehicle and the square of the vehicle speed. The rolling resistance and aerodynamic drag therefore reduce the kinetic energy

that must be dissipated by the brakes. For the present analysis, the correction factor for the rolling resistance and drag force (K_d) was set at a constant 0.725 i.e. 27.5 % of the kinetic energy was assumed to be dissipated by the rolling resistance and the aerodynamic drag. This value was calculated from the drag power and the rolling resistance power required for a typical passenger vehicle on a concrete road surface [52]. Therefore, Equation 2.11 is further modified to obtain the rate of thermal input per unit rotor rubbing area ($\dot{Q}$) as shown in Equation 2.12:

$$\dot{Q} = K_d \frac{q}{\Delta t} \times \frac{1}{n_p A} = \frac{K_d X_f K_p K V M a}{n_p A} . (Wm^{-2}) \qquad (2.12)$$

where

K_d = correction factor due to rolling resistance and drag force (0.725)

X_f = proportion of braking due to front wheels (0.7)

K_p = proportion of heat transferred to disc (0.95)

K = correction factor due to vehicle inertia (1.1)

V = instantaneous velocity (ms^{-1})

M = total vehicle mass (1990 kg)

a = deceleration (0.7 g)

n_p = number of pads on front axle (4)

A = total rubbing surface area per pad (0.0392 m^2)

The last three parameter values defined above were supplied by Rover for the family saloon car for which the brake rotor was designed [48]. The heat flux rate defined in Equation 2.12 is a function of vehicle speed but was otherwise assumed to apply uniformly over both rubbing surfaces of the disc. In reality, the generated heat flux in a disc brake is non-uniform and time-dependent over the rubbing surface due to the effects of pad wear and disc deformation such as coning which cause a biased non-

uniform pressure distribution [23-27,53]. Also no account was taken of radial variations of sliding speed or spatial variations of heat flux over a single rotation cycle of the disc (the so-called "rotating heat" source effect). These assumptions were made in order to simplify the thermal analysis which was only intended to predict typical temperature distributions for input to the thermal stress analysis.

2.2.3.2 ENERGY OUTPUT

Heat loss by convection must be defined in the temperature analysis of the brake disc because the vehicle is travelling at high speed and with high rotational velocity of the brake discs, resulting in a high rate of heat transfer by convection. However, the heat loss by radiation was ignored in this analysis because its effects are only significant at very high temperatures. The convective heat loss was calculated from the Nusselt number that is itself a function of Reynolds number, Equation 2.14 [31]:

$$\text{Heat convection coefficient} = \frac{\text{Nusselt number} \times \text{Conductivity of air}}{\text{Rotor outer radius}} \tag{2.13}$$

$$\text{Nusselt number} = 0.037 \times \text{Reynolds number}^{0.8} \tag{2.14}$$

$$\text{Reynolds number} = \frac{\text{Air speed} \times \text{Rotor outer radius}}{\text{Kinematic viscosity of air}} \tag{2.15}$$

$$\text{Air speed} = \text{Air speed factor} \times \text{Current car speed} \tag{2.16}$$

The convective heat transfer can be controlled by using air speed factors that are different for different parts of the model geometry. The factors given in Figure 2.4 are derived from similar FE simulations [54] to obtain the best agreement with experimental cooling studies on a similar vehicle fitted with a similar brake disc.

2.2.4 RESULTS AND DISCUSSION

Figures 2.5 and 2.6 show temperature contour plots predicted by the FE analysis at the end of the first brake application and at the end of the subsequent cooling period respectively. In order to investigate the temperature and von Mises stress histories, six elements defined (A to F) in Figures 2.5 and 2.6 were selected because these areas are subjected to high temperatures and stresses according to the initial results. From Figure 2.5, the temperature gradients between the rubbing surfaces (points A and B) and point C, and between points B and D are large at the end of the brake application, which may result in high thermal stresses. In addition, the temperature distribution across the outboard surface is more uniform than that across the inboard surface because heat is conducted at a more rapid rate from the latter through the neck and the hub. However, the maximum temperatures on the two rubbing surfaces are very similar at around 380 °C.

Temperatures increase non-uniformly with the braking time according to the position considered as shown in Figure 2.7. This analysis indicates that the brake disc is subjected to maximum temperatures up to around 380 °C at the end of the brake application. Generally, cast iron will be unable to maintain its room-temperature strength at this high temperature condition. Therefore, the stress-strain characteristic of the brake disc cast iron material is investigated at temperatures up to 400 °C as reported in Chapter 3.

Figure 2.8 shows that the temperatures continue to increase at points C and D during the early stages of the cooling period because the thermal energy stored at the rubbing surfaces is still high. However, these temperatures reduce over the later stages of cooling period although they are still slightly high compared to other areas as shown in

Figure 2.6.

2.3 ELASTIC STRESS ANALYSIS

2.3.1 INTRODUCTION

The same brake rotor finite element model as shown in Figure 2.2 for the back-vented brake disc was analysed for thermal stress at each time step of the thermal analysis. The elements used were 20 noded bricks with a quadratic interpolation function The predicted non-uniform temperature distributions from the thermal analysis were used as the input data in this analysis. To evaluate the thermal stresses caused by these temperature distributions, the elastic von Mises stress (σ_e) defined in Equation 2.17 below was considered, since this parameter, which combines the three principal stresses, was assumed to determine yield (onset of plastic deformation) in metals:

$$\sigma_e = \frac{1}{\sqrt{2}}((\sigma_1 - \sigma_2)^2 + (\sigma_2 - \sigma_3)^2 + (\sigma_3 - \sigma_1)^2)^{1/2} \qquad 2.17$$

where σ_1, σ_2 and σ_3 are principal stresses in a Cartesian axis system.

Since the elastic stresses and strains are completely reversible and non-cumulative, the brake disc model was investigated for one cycle of the braking and cooling period only.

2.3.2 METHODOLOGY

The FE methodology for stress analysis is similar to that for temperature analysis. It assumes that the potential energy (Π) of an object, that results from its strain energy (Λ) minus the work done by the external loads (W), should be minimised by differentiating with respect to the nodal displacements {U} as shown in equation 2.18:

$$\frac{\partial \Pi}{\partial \{U\}} = 0 = \frac{\partial (\Lambda - W)}{\partial \{U\}} \qquad (2.18)$$

The strain energy can be calculated from the stresses and strains inside the object. For a linear elastic material model, the stresses are a function of Young's modulus, Poisson's ratio and the strains. In addition, unrestrained or "free" thermal strains can be calculated from the temperature change (ΔT) and the coefficient of linear thermal expansion ($\propto$) as shown in Equation 2.19:

$$\varepsilon = \alpha \cdot \Delta T \tag{2.19}$$

Hence, the material properties required for the elastic FE thermal stress analysis are the Young's modulus, Poisson's ratio and the coefficient of linear thermal expansion. For the present analysis, Young's modulus of 100 GPa, Poisson's ratio of 0.26 and a temperature dependent coefficient of linear thermal expansion as shown in Table 2.2 were assumed.

Temperature (°C)	**Coefficient of linear thermal expansion (K^{-1})**
20	10.42E-6
200	11.58E-6
400	14.58E-6

Table 2.2: Coefficient of linear thermal expansion for grade 150 grey cast iron [8]

2.3.3 BOUNDARY CONDITIONS

Circumferential constraints were applied along both radial sections of the brake disc structural model. In addition, an axial constraint was applied to the hub as shown in Figure 2.9. Only thermal stresses were considered because the mechanical loads due to the pad normal pressure, centrifugal force and inertia force are insignificant in comparison [38]. Therefore, it is the non-uniform distribution of temperature that is likely to have the major influence on the plastic deformation of the brake disc.

2.3.4 RESULTS AND DISCUSSION

Elastic von Mises stress contours at the end of the braking period are shown in Figure 2.10. The points annotated are the same as in the temperature analysis. It can be seen that the brake disc has higher thermal stress on the inboard rubbing surface in comparison to the outboard cheek because the former is connected to the neck, resulting in higher resistance to radial expansion. Due to the bending of the neck as a result of this unbalanced radial constraint, maximum von Mises stresses actually occur at the neck (position D) and at the inner radius of the long vane (position C).

During the cooling period, all induced thermal stresses reduce due to the elastic material model and the minimisation of high temperature gradients. At the end of cooling, thermal stresses are virtually zero as shown in Figure 2.11.

The bending of the neck region at the end of braking is apparent in the displaced shape plot of Figure 2.12 which also shows that the rubbing surfaces of the disc remain relatively straight, indicating a lack of coning. At the end of the cooling period, Figure 2.13 shows that the disc has virtually returned to its original shape, the remaining small radial deformations being due to the slightly non-uniform temperatures, Figure 2.6.

Figures 2.14 and 2.15 show the stress time histories for the selected points during the heating and cooling periods respectively. The element centroid stress that is interpolated from the integration points is considered instead of the nodal stress because it is generally considered to be a more accurate measure of the stress within an element. It can be seen from Figure 2.14 that the effect of high temperature gradients through the brake disc thickness in the early part of the braking cycle causes high thermal stresses at

the cheeks (A and B). These then reduce towards the end of brake application due to the lower temperature gradients. Conversely, the thermal stresses at the neck regions (points C and D) increase throughout braking as the temperature of the rubbing surfaces continue to increase.

According to the characteristics of cast iron, the proportional limit (elastic limit) is high under compressive load and low under tension. Therefore, the mean elastic stress (σ_m) defined in Equation 2.20 is used to investigate whether compression or tension exists at the critical locations:

$$\sigma_m = \frac{\sigma_1 + \sigma_2 + \sigma_3}{3} \tag{2.20}$$

A contour plot of mean stress at the end of the brake application shown in Figure 2.16 reveals that compression occurs at the rubbing surfaces and tension at point C and D. The von Mises stresses at these latter locations (C-D) are definitely beyond the elastic proportional limit for the cast iron material at this temperature. For this reason, it is necessary to include the plastic region with pressure dependence in the material model for more accurately investigating strains and deformations. Derivation of a suitable cast iron material model for the FE method is investigated in Chapter 4.

2.4 FRONT-VENTED BRAKE DISC ANALYSIS

2.4.1 INTRODUCTION

Since the back-vented disc is a non-typical automotive brake disc, a FE model of the front-vented disc more commonly used in the current market was also created in order to investigate the effect of brake disc geometry on the thermal performance. This was achieved by simply axially translating the hub and top-hat sections and re-attaching the neck of the latter to the outboard cheek of the disc as shown in Figure 2.17.

In the front-vented disc analyses, the cyclic thermal load including the boundary conditions, i.e. energy input and output, were assumed to be same as for the back-vented design. Furthermore, the same constraints and material properties were used for the elastic stress analysis. Therefore, only the effect of brake disc geometry was investigated.

2.4.2 RESULTS AND DISCUSSION

2.4.2.1 THERMAL ANALYSIS

Temperature contours at the end of braking application are presented in Figure 2.18. The results reveal that the temperatures have similar trends to those of the back-vented disc except for the area where the neck is connected to the rotor. As expected, the maximum temperature of around 380 °C now occurs at the inboard rotor instead of at the outboard rotor for the back-vented disc. The temperature time histories at the chosen points (A, B, C and D) during the brake application are shown in Figure 2.19. During cooling, the effect of the thermal energy stored in the rotor causes the same trends as for the back-vented disc.

2.4.2.2 ELASTIC STRESS ANALYSIS

It can be clearly seen from Figure 2.20 that the outboard thermal stress is higher than the inboard thermal stress for the front-vented disc as a result of the different neck connection. The effect of neck bending which also occurs in the back-vented disc similarly causes the maximum von Mises stresses at points C and D. The displaced shape plot at the end of brake application in Figure 2.21 reveals that the rubbing surfaces have experienced more coning in comparison to the back-vented disc. In the early part of brake application, Figure 2.22 shows that the thermal stresses at the selected points (A, B and D) have the same trends as those for the back-vented disc

except at point C where the thermal stress reduces at the end of braking. In contrast, for the back-vented disc, the effects of temperature gradients and radial constraints cause the thermal stress at point C to increase throughout braking, Figure 2.14. Moreover, point C is subjected to a compressive mean stress for the front-vented disc as shown in Figure 2.23 compared with tension for the back-vented disc, Figure 2.16. In addition, the mean stress at point D has a negative value, indicating tension at the end of brake application. As a result, the induced thermal stress at point D for the front-vented disc tends to be well beyond the proportional limit in tension for the cast iron material.

2.5 SUMMARY

2.5.1 TEMPERATURE ANALYSIS

During the brake application, the outboard cheek of the back-vented disc model attains a slightly higher temperature and has a more uniform temperature distribution in the radial direction in comparison to the inboard cheek because of the effect of conductive heat transfer through the neck. The maximum temperature at the outer rubbing surface is approximately 379 °C which is sufficiently high to significantly reduce the yield strength of the material and so cause high plastic thermal strains. Furthermore, the temperature gradient is high at the neck due to the effect of heat conduction to the cooler hub. Since there is no thermal input during the cooling period, the thermal energy stored in the brake disc rotor is transferred to the surroundings by convection and conduction, resulting in an equalised overall brake disc temperature of around 80 °C as required by the test conditions

The effect of different brake disc geometry in the front- and back-vented discs is the another factor that controls the maximum temperature of the rubbing surfaces because of the effect of heat conduction through the neck. However, in general, the temperature

response of these two brake disc designs is not significantly different.

2.5.2 THERMAL STRESS ANALYSIS

For the back-vented disc model, the effect of the temperature gradients causes somewhat higher elastic thermal stresses at the inboard cheek of the rotor (154 MPa) compared to the outboard cheek (99.5 MPa). However, maximum von Mises elastic stresses occur at the neck (273 MPa) and near the inner fillet radius of the long vane (442 MPa) due to the constraints applied to the free expansion of the rotor rubbing surfaces. If these stresses are beyond the proportional limit, plastic strains would occur in the brake disc. For the cast iron material, the magnitude of plastic strains is dependent on whether the mean stress is tensile or compressive. Therefore, it is necessary to derive a more realistic inelastic material model with different yield surfaces in tension and compression for application within the brake disc analysis.

For the corresponding front-vented disc, the induced thermal stress at the outboard cheek is higher than that at the inboard cheek. Furthermore, the inner fillet radius of the long vane for the front-vented disc is subjected to high compressive stress whereas the neck experiences tension.

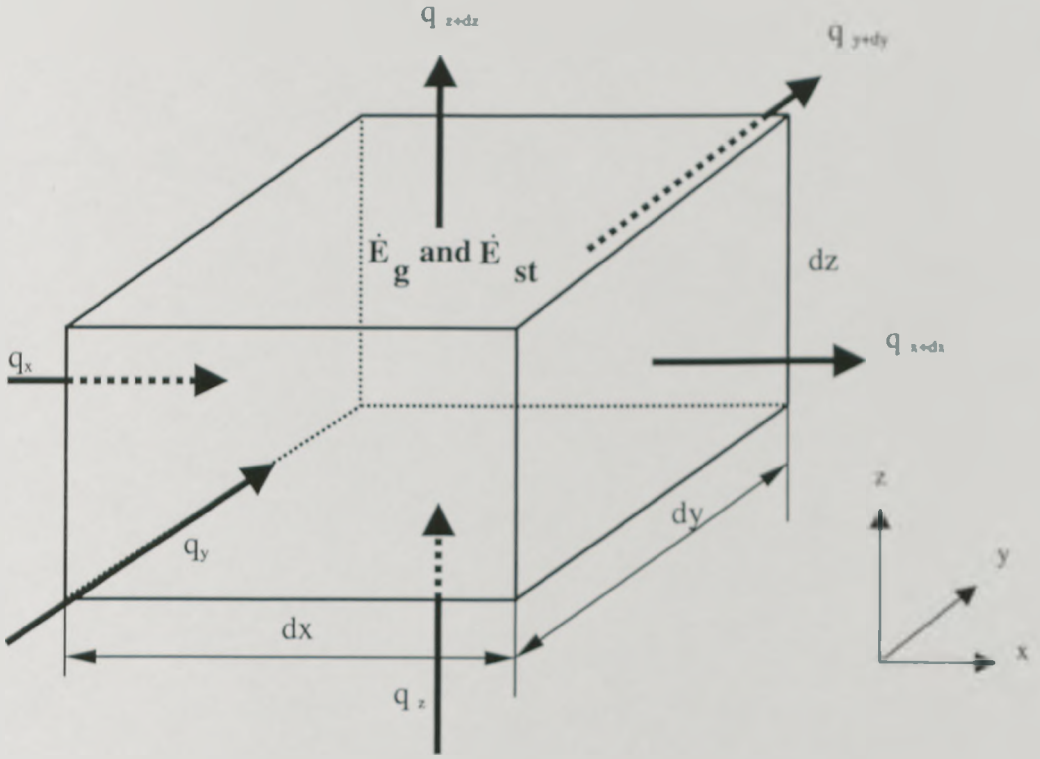

Figure 2.1: Differential control volume, dx dy dz, for conduction analysis in Cartesian co-ordinates

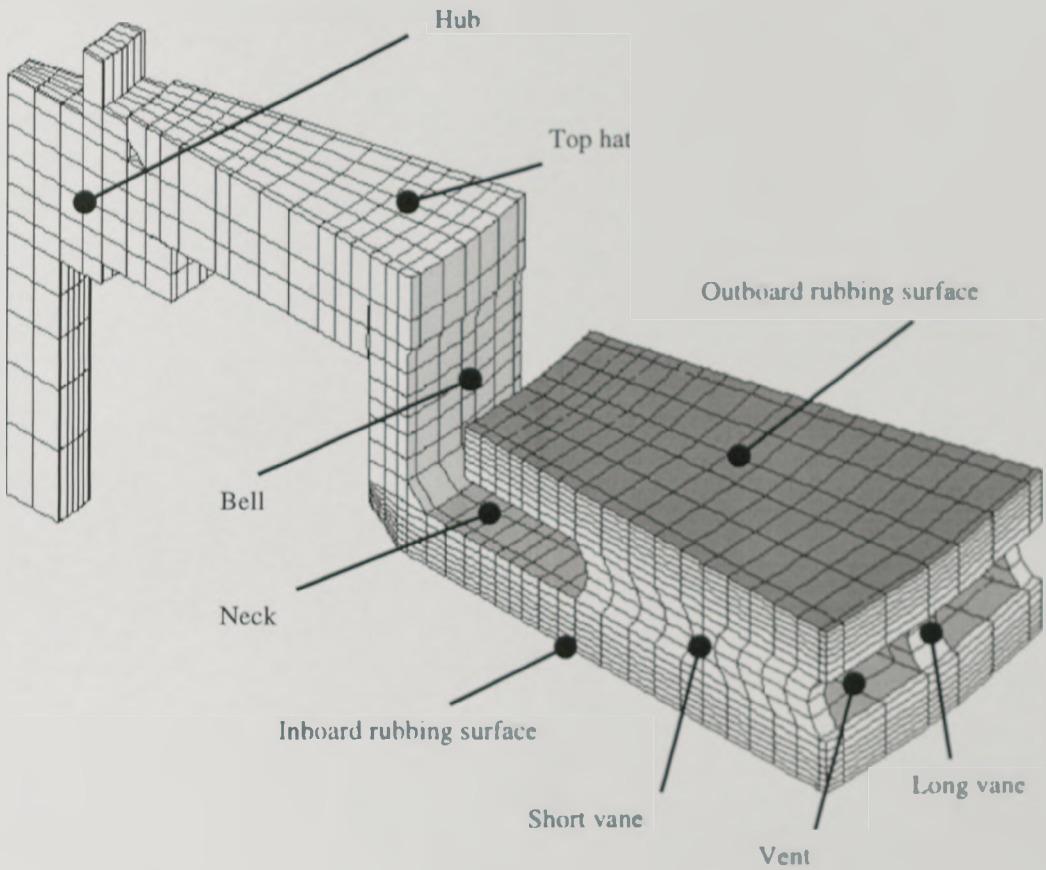

Figure 2.2: Back-vented brake disc model

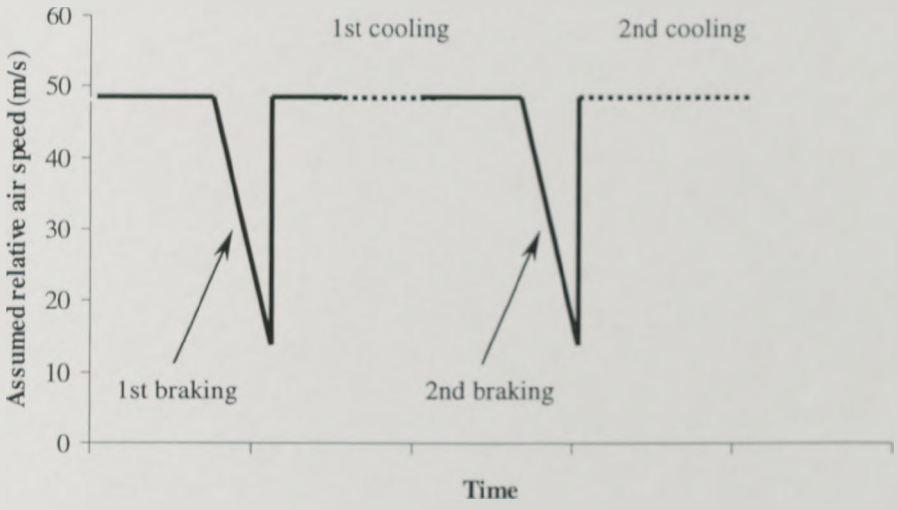

Figure 2.3: Vehicle air speed pattern during braking and cooling for the autobahn driving conditions

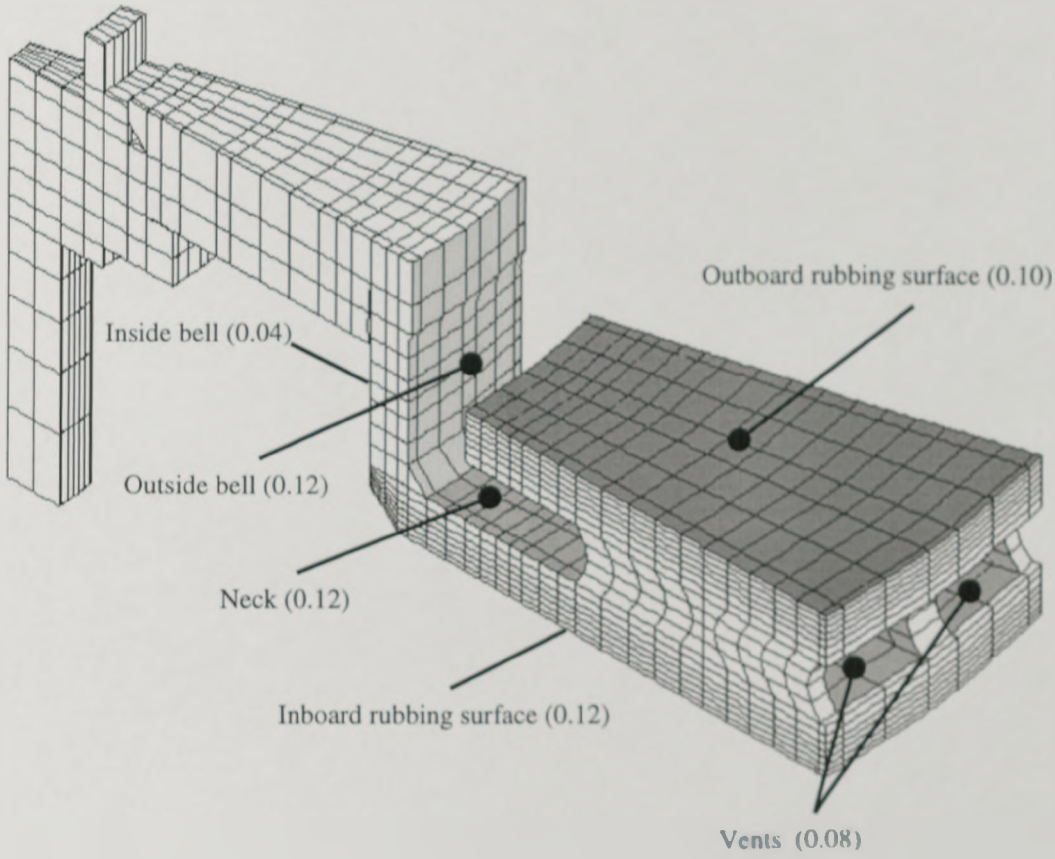

Figure 2.4: The air speed factors for heat convection [54]

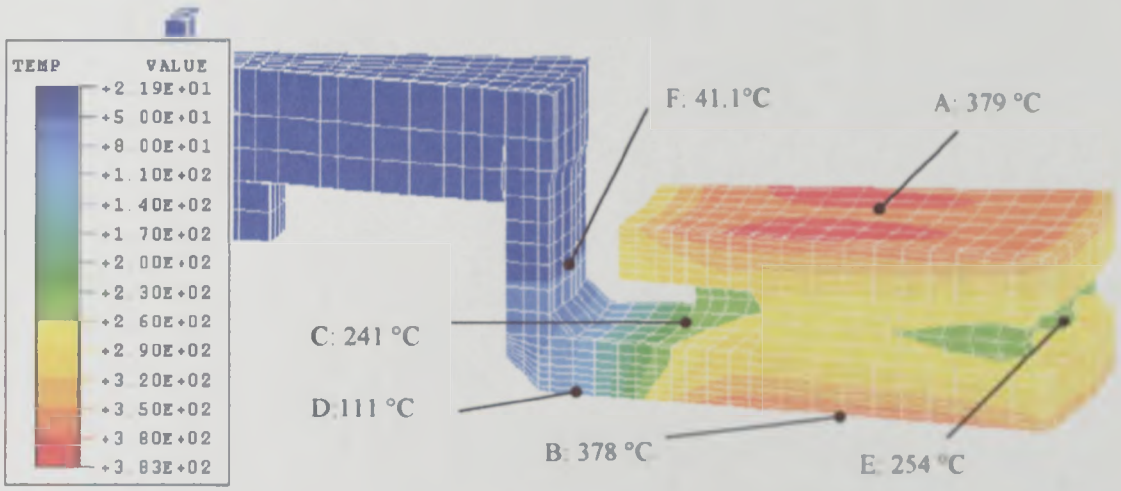

Figure 2.5: Temperature contours at the end of brake application for the back-vented disc

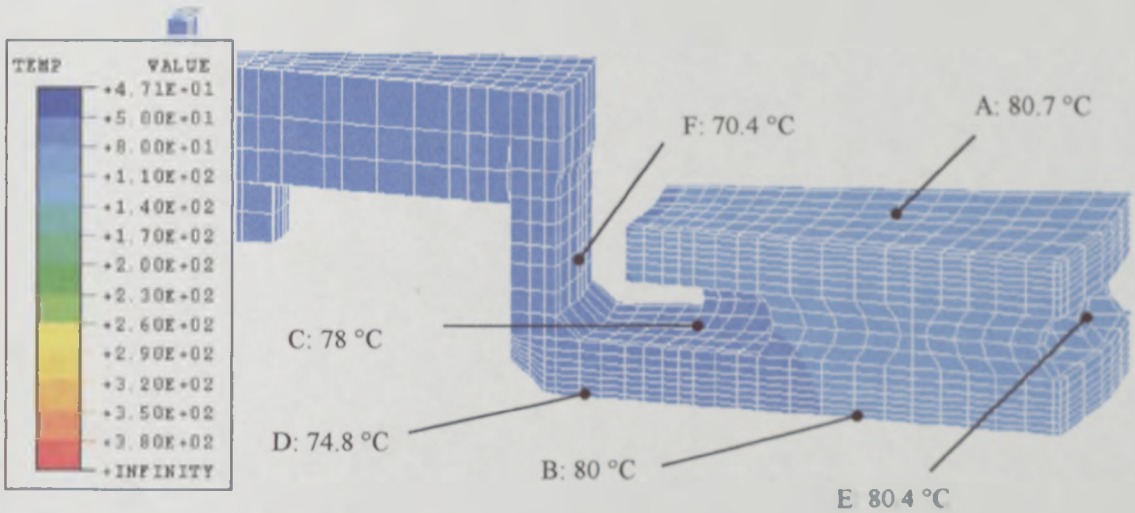

Figure 2.6: Temperature contours at the end of cooling period for the back-vented disc

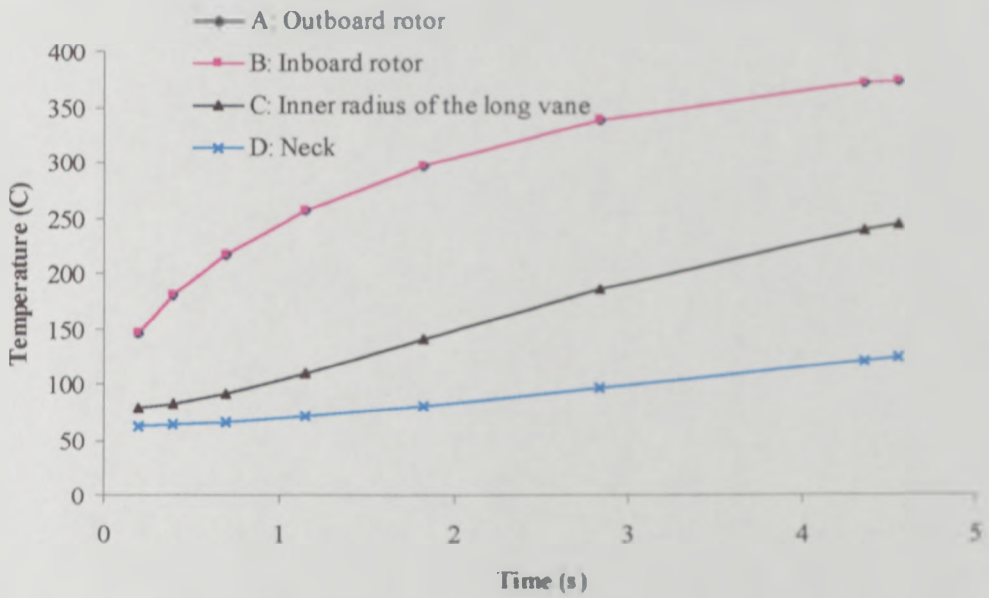

Figure 2.7: Element centroid temperature histories during first brake application for the back-vented disc

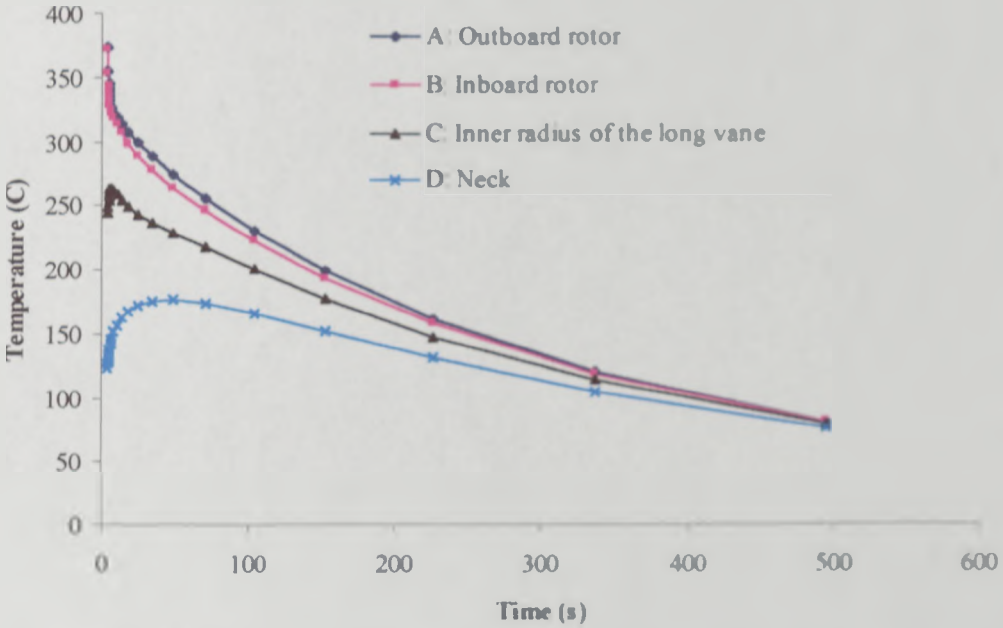

Figure 2.8: Element centroid temperature histories during first cooling period for the back-vented disc

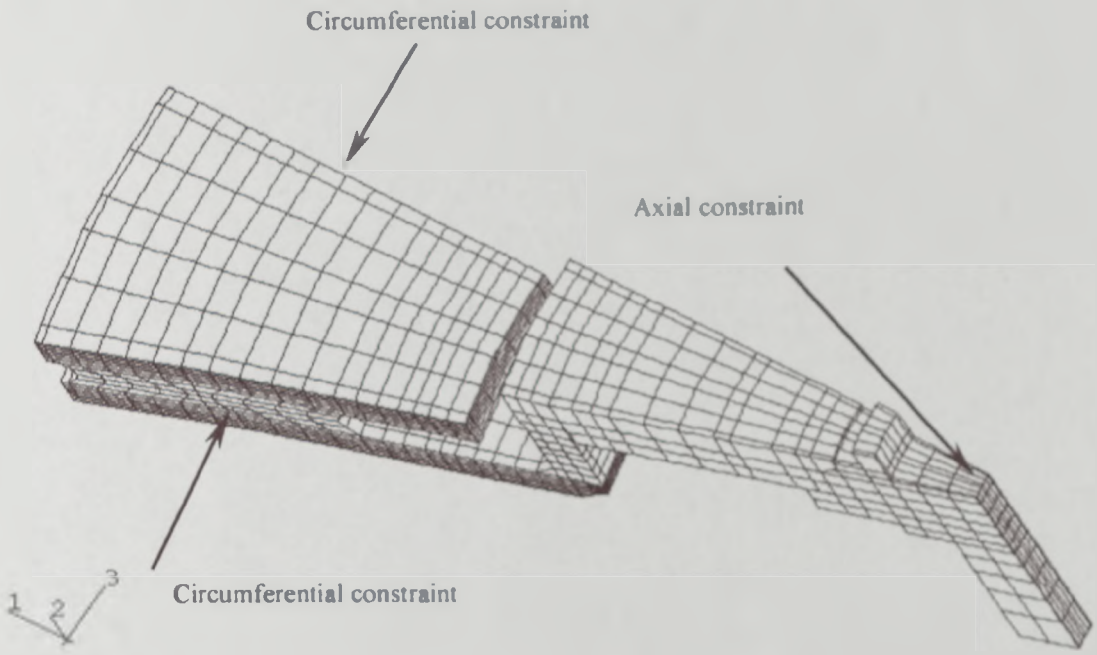

Figure 2.9: Constraints for stress analysis

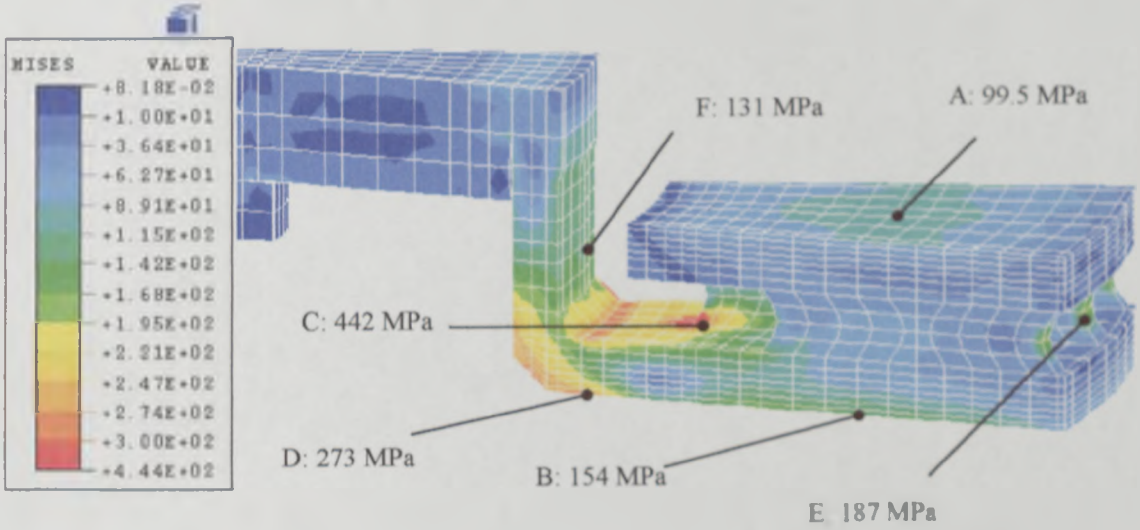

Figure 2.10: Von Mises stress contours at the end of first brake application for the back-vented disc

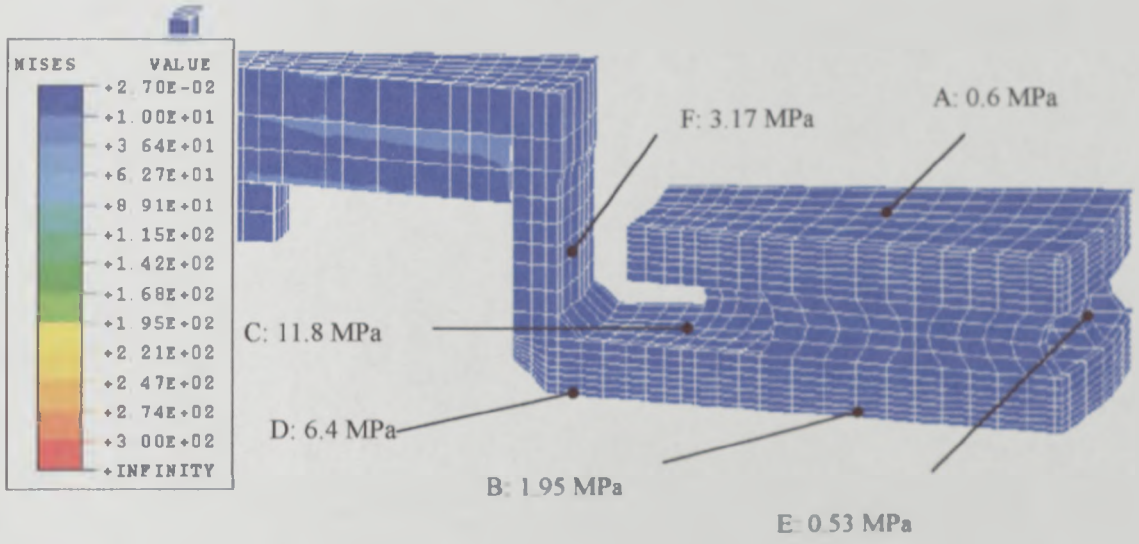

Figure 2.11: Von Mises stress contours at the end of first cooling period for the back-vented disc

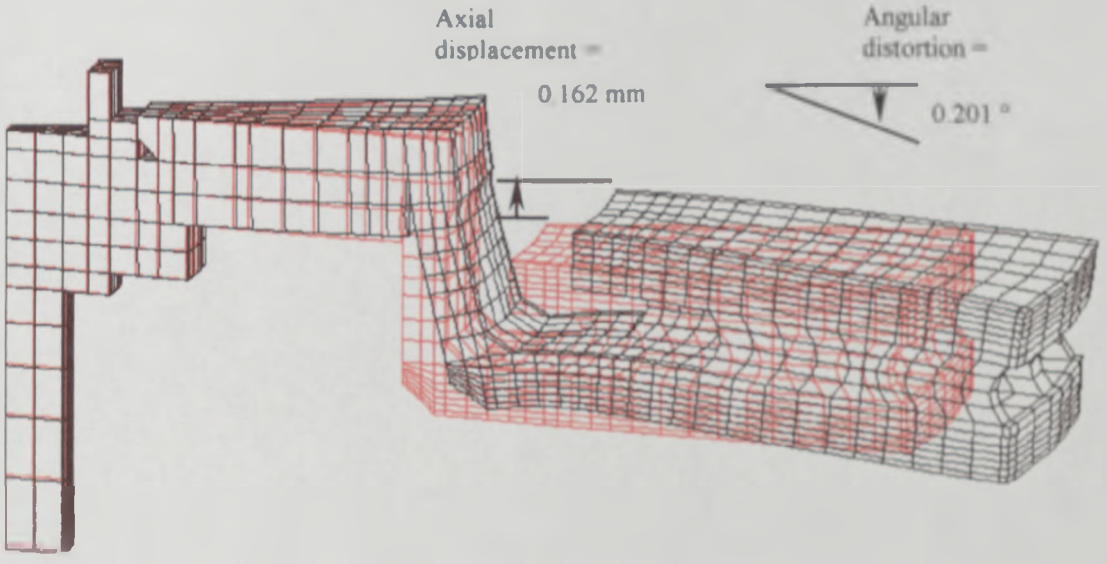

Figure 2.12: Displaced shape at the end of first brake application for the back-vented disc (Red indicates original mesh; Black indicates displaced mesh)

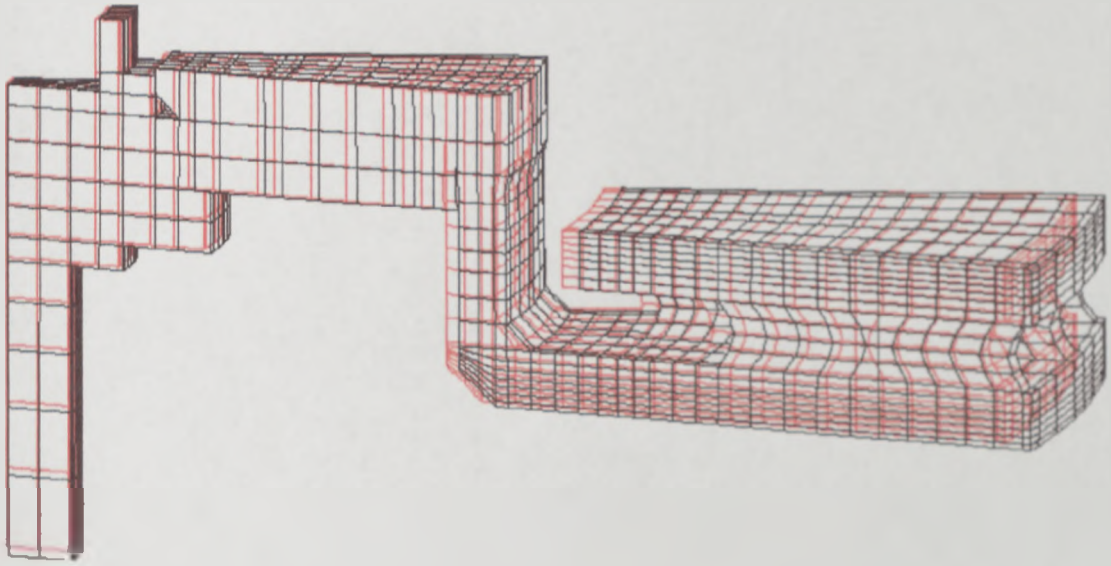

Figure 2.13: Displaced shape at the end of first cooling period for the back-vented disc (Red indicates original mesh; Black indicates displaced mesh)

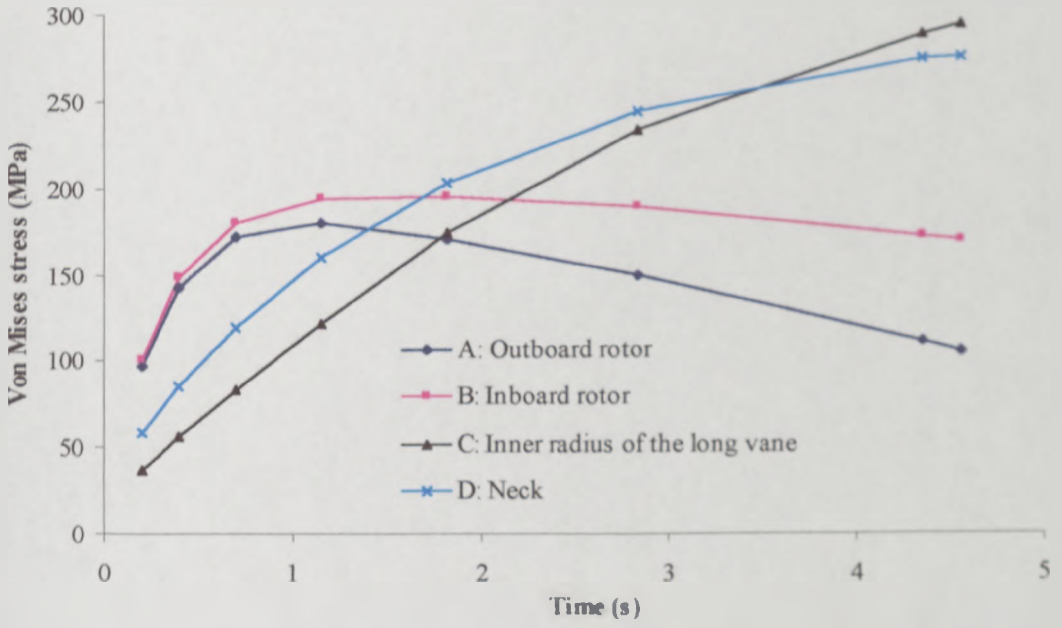

Figure 2.14: Element centroid von Mises stress histories during first brake application for the back-vented disc

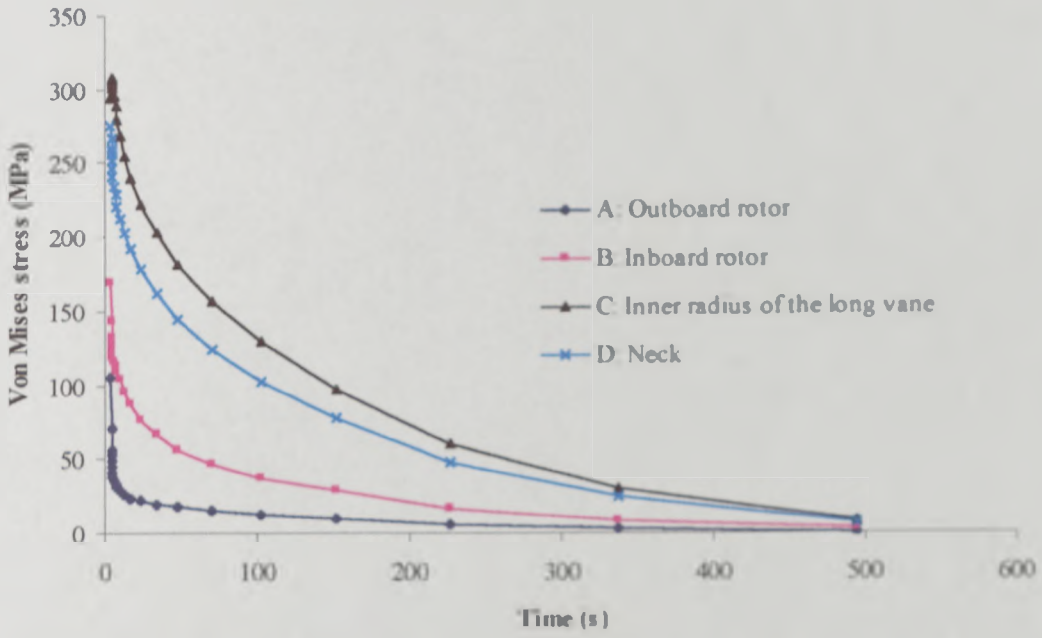

Figure 2.15: Element centroid von Mises stress histories during first cooling period for the back-vented disc

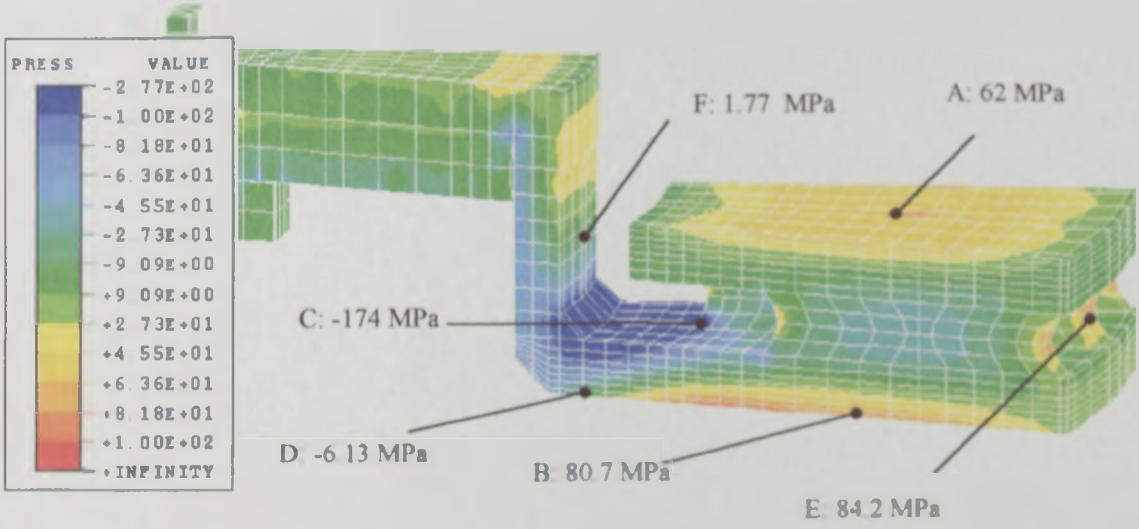

Figure 2.16: Pressure (mean stress) contours at the end of first brake application for the back-vented disc (Negative pressure indicates tensile mean stress)

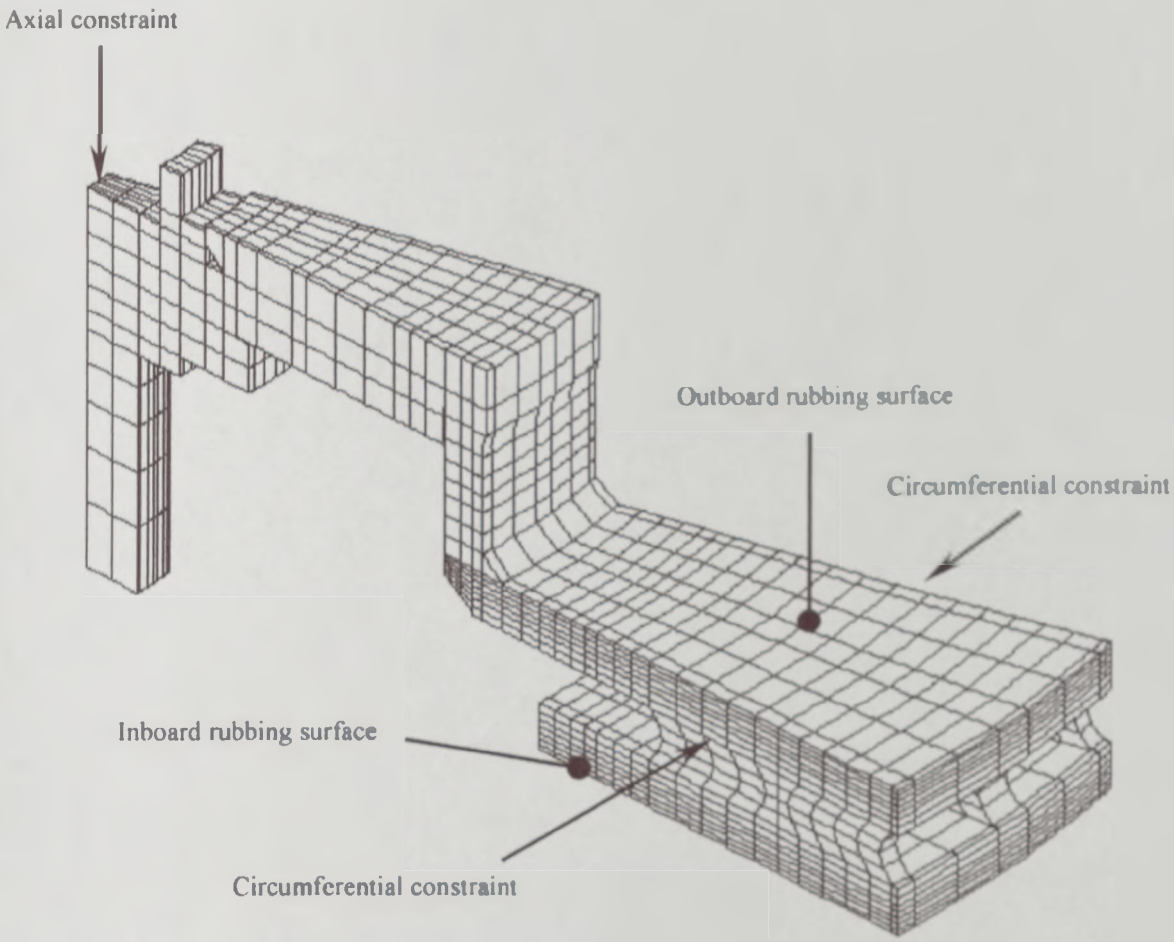

Figure 2.17: Front-vented brake disc model

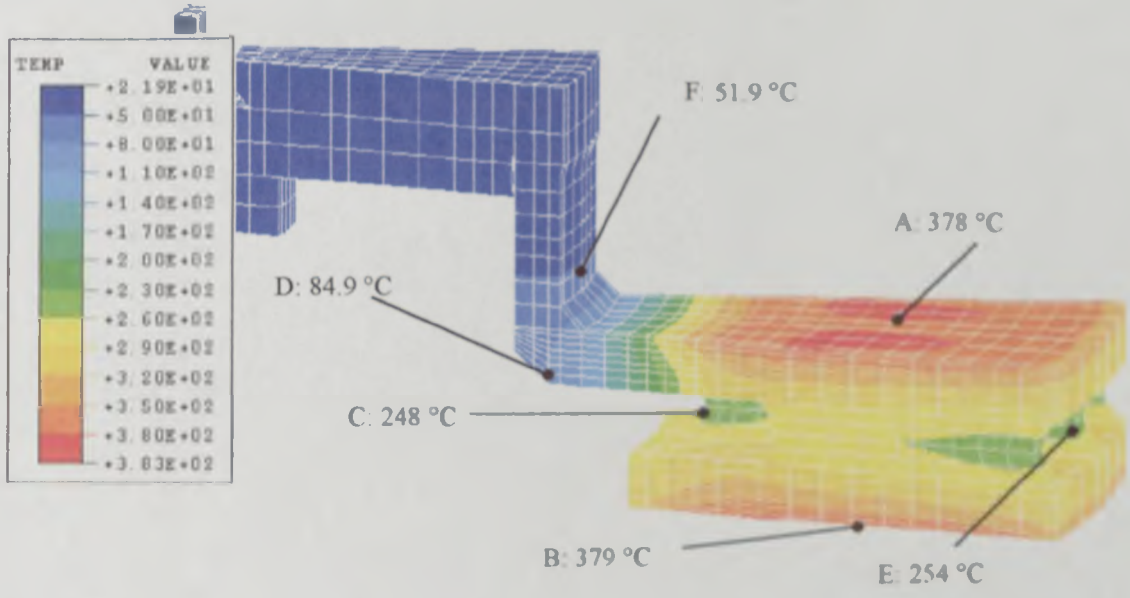

Figure 2.18: Temperature contours at the end of first brake application for the front-vented disc

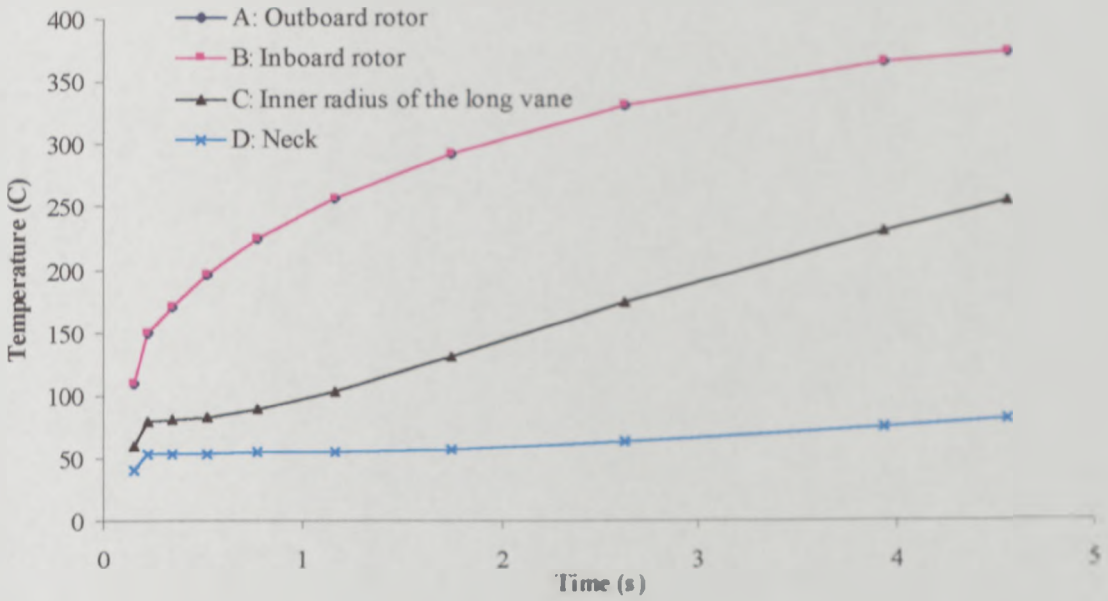

Figure 2.19: Element centroid temperature histories during first brake application for the front-vented disc

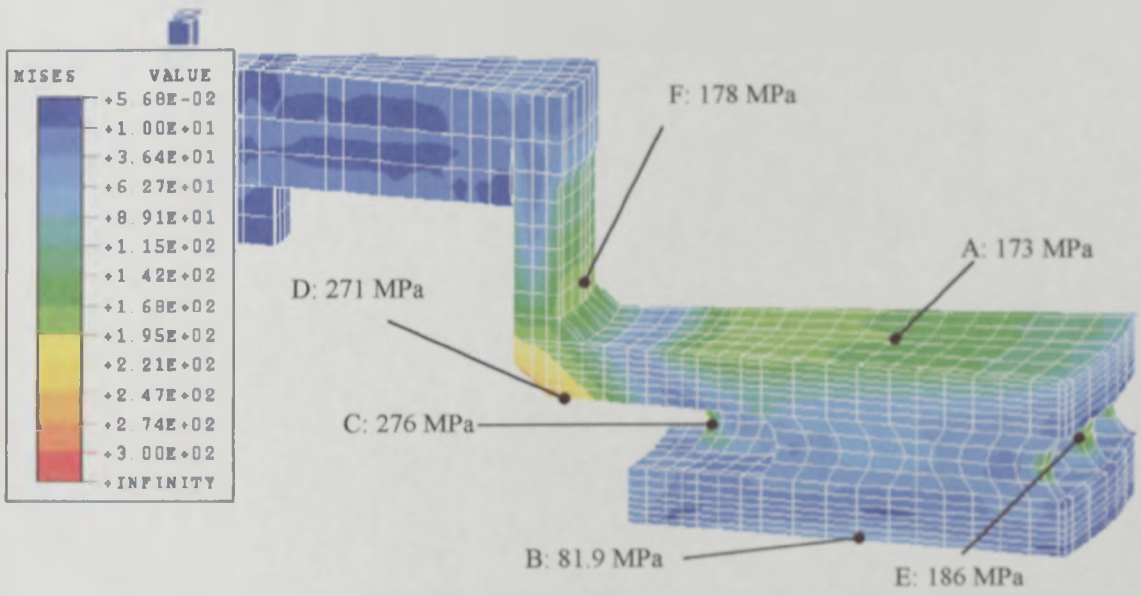

Figure 2.20: Von Mises stress contours at the end of first brake application for the front-vented disc

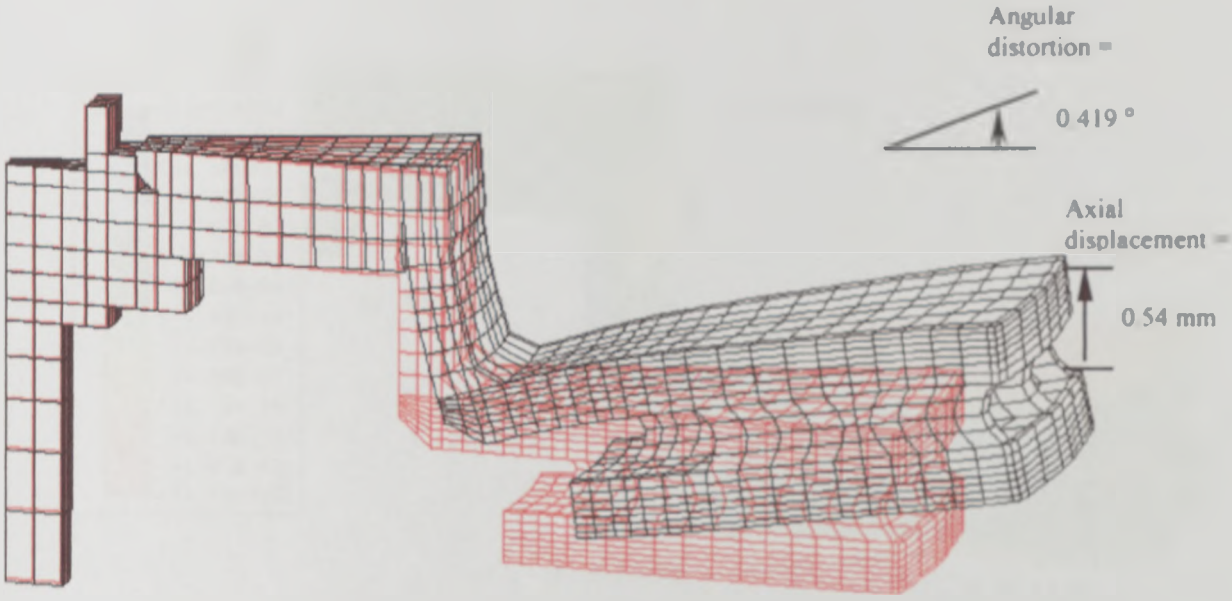

Figure 2.21: Displaced shape at the end of brake application for the front-vented disc (Red indicates original mesh; Black indicates displaced mesh)

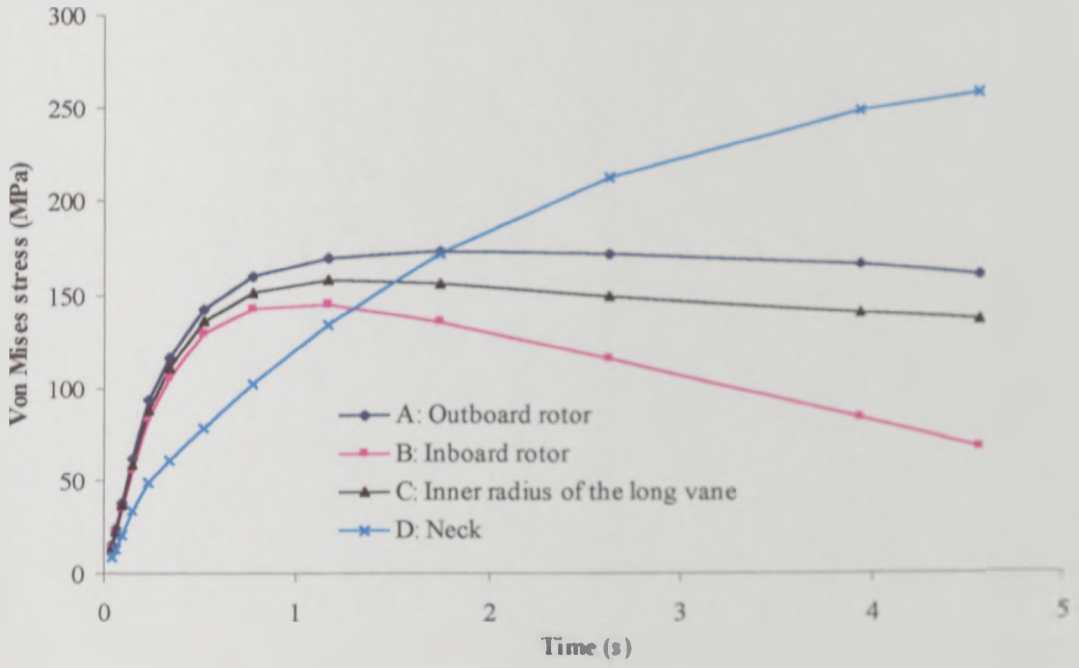

Figure 2.22: Element centroid von Mises stress histories during first brake application for the front-vented disc

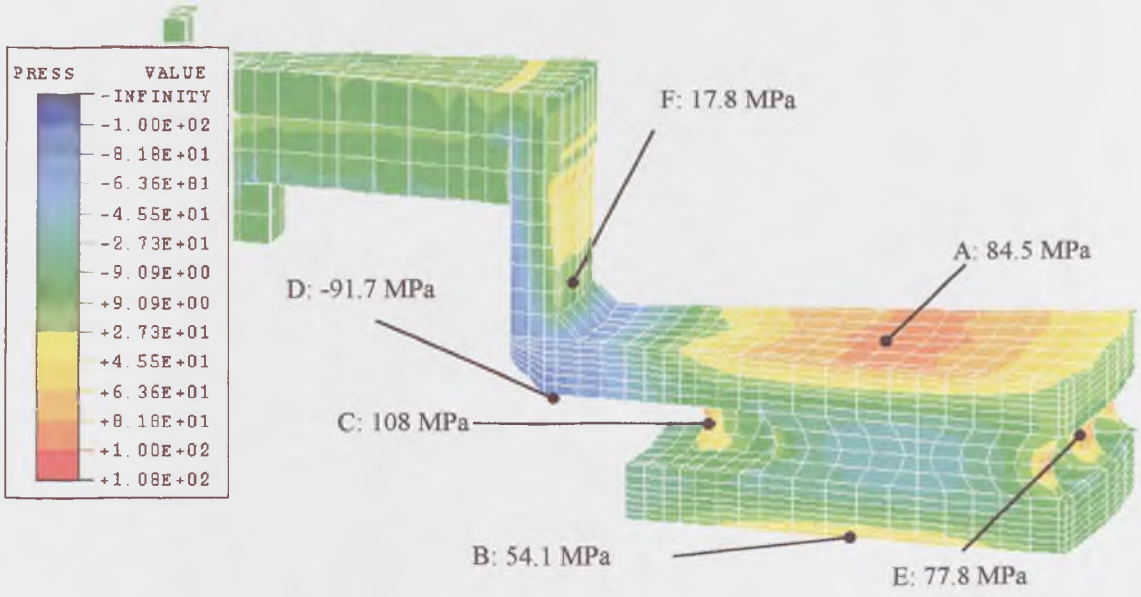

Figure 2.23: Pressure (mean stress) contours at the end of first brake application for the front-vented disc (Negative pressure indicates tensile mean stress)

CHAPTER 3

MATERIAL PROPERTY TESTS AND RESULTS

3.1 INTRODUCTION

Cast iron is a material that has been widely used for a long time in engineering products because it is relatively inexpensive and easily formed into complex shapes. Normally, the grey cast iron used in a typical brake disc consists of two main substances: Graphite flakes and a pearlitic matrix metal. This has a significant effect on the stress-strain response of the material compared with other more homogenous metals and alloys because of the opening and closing of gaps between the graphite flakes and the metal matrix as discussed in Chapter 1. The objective of the experiments described in this Chapter is to find the stress-strain response as a function of the load type, i.e. tension or compression, and temperature for a typical brake disc cast iron. This investigation includes the response under uniaxial and cyclic load using the testing procedures defined in the relevant British Standard [55] and Landgraf [13] respectively. The former standard covers the loading conditions, the specimen dimensions and the definitions of yield strength, proof strength, etc. The latter was used to determine the cyclic stress-strain curve as described in Chapter 1.

In practice, the dimensions of specimens cut from the brake disc cannot comply with the British Standard requirement due to the limited size of the disc. Therefore, specific specimens were designed and analysed using linear FE techniques in order to maintain a uniform stress distribution within the gauge length and to investigate the stress response with several sizes of hole used to grip the specimen in tension and compression without slippage or backlash.

An induction heating furnace was used to heat the specimens to temperatures between 300-400 °C in addition to the room temperature tests. The relationship between the crosshead stroke of the test machine and the specimen strain must be known for the monotonic stress-strain testing because a strain gauge cannot be used to measure strain directly at the elevated temperatures.

In addition to the monotonic loading tests, the multi-step approach was applied to find the cyclic stress-strain curve (CSSC) of the cast iron material. In these tests, the same relation between the stroke and the specimen strain from the previous uniaxial load tests was used to control the strain amplitude under cyclic loading. The resulting hysteresis loops and CSSC's at various temperatures are presented in the final section of this Chapter.

3.2 SPECIMEN DESIGN AND ANALYSIS

3.2.1 SPECIMEN DESIGN

Specimens were machined from the BMW specification 600 36.0 back-vented brake disc supplied by Rover cars as indicated in Figure 3.1. The nominal composition of the grade 150 cast iron is shown in Table 3.1. The final specimen dimensions are indicated in Figure 3.2. Although the specimen cannot follow the British Standard specification, the results from the FE investigation described below demonstrate that the design is satisfactory. The aim of this specimen design is to keep the gauge length as long as possible to ensure a uniform stress distribution over the central area. Furthermore, the cross-section of the specimen is square, giving larger cross-sectional area than for the corresponding circular cross-section. The square cross-section specimen can therefore support a higher load in compression without buckling. In addition, it provides a flat surface that can be used to mount a strain gauge.

Due to the relatively short gripped ends, it was decided to load the specimen through holes drilled in the specimen in order to prevent any slippage. In the experiments, the specimens were subjected to both tension and compression loads. The wedge action specimen grips were designed to prevent any backlash as the load changes from tension to compression as described below. Therefore, the same specimen design could be used for testing under both uniaxial and cyclic loads.

Composition	% weight
Carbon	3.70-3.90
Silicon	1.80-2.20
Magnesium	0.50-0.80
Phosphorous	0.08 (Max.)
Sulphur	0.12 (Max.)
Chromium	0.20 (Max.)
Copper	0.25 (Max.)
Molybdenum	0.10 (Max.)
Nickel	0.20 (Max.)

Table 3.1: Composition of the Rover disc cast iron material [48]

3.2.2 ANALYSIS OF SPECIMENS

For the chosen specimen geometry, the shoulders at the end of the gauge length and the loading holes have the potential to cause failure due to the high stress concentrations created when under load. The easiest way to analyse the specimen design is the finite element method. The objective is to investigate the effect of the specimen geometry, especially the size of the holes, before making specimens for the experiments. The diameters of the hole were assigned values of 4, 5, and 6 mm. The details of this investigation are presented below.

The ABAQUS software was used to perform this investigation. By taking advantage of the test piece symmetry, one quarter of the specimen was modelled with the different hole diameters of 4, 5 and 6 mm as shown in Figure 3.3. The vertical centre line of the model was constrained in the horizontal direction. A simple rigid pin model was created of the same size as the specimen hole in order to represent the contact between the pin and the hole under tension. The cast iron specimen was assumed to be elastic with Young's modulus of 100 GPa and Poisson's ratio of 0.26. The pin was subjected to a 10 kN tensile load giving a nominal tensile stress of 278 MPa in the gauge length and the resulting stress distributions is investigated for the different hole sizes.

3.2.2.1 RESULTS

Figure 3.4 shows that the specimen with the 4 mm hole diameter has the lowest von Mises stress at the end of gauge length compared with the 5 and 6 mm diameter holes, the stress concentration factors relative to the nominal gauge length stresses being 1.20, 1.28 and 1.34 respectively. This is because the specimen with the smallest diameter hole has more material that can transmit the tension load to the gauge length. It can also be seen that the maximum von Mises stress around the hole is not greatly affected by the hole size (the 5 mm diameter hole actually gives the lowest stress concentration factor). Furthermore, the specimen can stand the high von Mises stress around the hole because it is predominantly in compression. Therefore, it can be concluded that the specimen with the 4 mm diameter hole should be used for the experiments.

3.3 TEST EQUIPMENT

3.3.1 DARTEC TEST MACHINE

Specimens were tested in a servo-hydraulic Dartec test machine as shown in Figures 3.5 and 3.6. The stroke-controlled or load-controlled range can be set to any given value

that is limited only by the machine capacity. During operation the current load and crosshead displacement can be displayed and recorded as a function of time. The output signal from the load cell is in the form of a voltage that is dependent on the setting of the Dartec machine. Setting these values depends on the maximum load expected and the resolution of the output data required. Therefore, before testing specimens, the ultimate tensile strength of the material should be firstly estimated in order to obtain the most appropriate setting of the load cell.

3.3.2 INDUCTION HEATING UNIT

For testing at elevated temperatures, it is vital to find equipment to heat the specimen and maintain it at a constant uniform temperature. With the Dartec machine, tests at elevated temperature can be carried out inside an oven. However, the maximum temperature achievable with this oven is only 200 °C. In addition, the length of the specimen and grips is too short to load them inside the oven. For this reason, a Quasar solid state induction generator and a heating coil together with a Raytek control unit was chosen. This induction generator has a maximum output power of 5kW with frequency between 80 and 200 kHz which is sufficient to rapidly heat the specimen with a heating coil up to the required temperature. The control unit consists of a main control box and an infra-red detector. The function of the main control box is to receive a signal from the infra-red detector in order to control and maintain the specimen temperature at a certain value by reducing or increasing the output power from the induction generator. The infra-red detector directs a laser beam on the specimen and converts the infra-red energy measured from the reflection into an electronic signal of the current specimen temperature, Figures 3.7 and 3.8. The signal from the control unit is used to control the magnetic flux generated by the induction heater. Consequently, the system can heat an object with a small volume like the gauge length of the disc brake specimen to an

accurately measured and controlled temperature. However, due to the limitations of the induction heater temperature control unit, maintaining a constant temperature below about 250 °C proved impossible. Therefore, specimens were tested at temperatures of 300, 350 and 400 °C only as well as at ambient temperature.

Another great advantage of the induction heater over the oven is the heating time. The induction heater takes only a few minutes to heat a specimen to a temperature of 400 °C. However, the profile of specimen temperature along the gauge length of the specimen might not be uniform. This problem was overcome by designing the shape of the induction coil to give as uniform a temperature as possible, Appendix 1. The results from measuring the temperature at different positions along the gauge length using a hand-held digital thermocouple thermometer fitted with a surface temperature probe proved that the temperature is only slightly non-uniform even for the maximum temperature of 400 °C as shown in Figure 3.9. This good uniformity of temperature is achieved because the specimen ends are insulated from the grips and the Dartec itself by the design of the gripping arrangement as described in the following section.

3.3.3 GRIP DESIGN

The lower and upper grips were made of high carbon steel (EN 30B) in order to stand high loads during the tests without plastic deformation. The wedges inside the channels together with the pins were used to apply a compression pre-load against the top edge of the specimen as indicated in Figure 3.10. The wedges were fastened with small bolts so as to obtain good contact and eliminate any gaps between the wedges, the specimen and the pins as shown in Figure 3.11. The grips can therefore transmit the loads from the crosshead of the test machine to the specimen without backlash while changing the load direction. The pins were made of ground silver steel and they have high accuracy on

diameter for ensuring good contact with the specimen. Mild steel was used for the wedge because its strength is sufficient for testing at high load.

For testing at elevated temperatures, short bushes made of glass ceramic [56] were used to thermally insulate the specimen from the grips, Figure 3.12. By increasing the diameter of the hole in the specimen from 4 mm to 6 mm, these short bushes with inner diameter of 4 mm could be interference fitted inside the specimen using a heat shrink technique. The procedure starts with heating the specimen with a 6 mm diameter hole in the oven up to 150 °C. At this temperature, the short bushes can be easily inserted due to thermal expansion of specimen. Upon cooling the short bushes are interference fitted inside the specimen hole. Since the bushes are then in fact integral with the specimen, the effective hole size is again 4 mm as optimised by the FE analysis.

To complete the insulation for the elevated temperature tests, the wedge height was reduced by 3 mm in order to insert glass ceramic wedge insulators as indicated in Figure 3.12. The insulator thickness is 3 mm with the same width and length as the base of wedge. Furthermore, the same insulator material was used for the 2 mm thick washers located at the end of the threaded sleeves. The purpose of this design is to prevent the thermal energy transferring from the specimen to the grips thus maintaining the specimen temperature as uniform as possible.

3.3.4 STRAIN GAUGES

The function of a strain gauge is to measure the strain on an object that is subjected to a load. Generally, it is made of a metal that changes its electrical resistance according to its deformation. In practice, the gauge is fixed to the object surface. If the object is subjected to a load, the strain gauge will extend or contract according to the deformation

of the surface, resulting in a change of strain gauge resistance that can be transformed and amplified to give a voltage signal proportional to the deformation. In the uniaxial room temperature tests, Cu-Ni foil strain gauges with a gauge factor of 2.13 and electrical resistance of 120 Ohm were used for investigating the strain response of the specimen. The maximum limiting strain for this strain gauge is of the order of 2%. The strain gauge was fixed halfway along the gauge length of the specimen and aligned in the direction of loading, Figure 3.13. The response of the strain gauge was monitored by means of a strain gauge meter, Figure 3.14, which with the correct setting of the gauge factor gives a maximum output of two volts equivalent to 20000 microstrain.

3.3.5 DATA ACQUISITION UNIT

The PC based 'Labtech' data acquisition unit consists of an integrated hardware and software system that transforms analogue input voltage signals into the digital data that can be recognised by the software in the computer. Therefore, the strain signal from the strain gauge meter and the load signal from the load cell can be recorded at the same time as the crosshead displacement from the Dartec machine. This allows the load and displacement response of the specimen to be investigated as well as the relation between the crosshead displacement and the strain. The calibration of the signal input with the load cell that has been regularly calibrated from the company is illustrated in Appendix 2.

3.4 STRAIN-STROKE CALIBRATION

3.4.1 TEST METHOD

Since strain gauges could not be used on specimens heated to elevated temperatures using the induction heater, it was necessary to establish a relationship between the crosshead displacement of the Dartec and the strain in the specimen. It could then be

assumed that this relationship holds for elevated temperature as well as for the room temperatures tests. This assumption is reasonable because the factors that affect the crosshead displacement - specimen strain relation such as the compliance of the Dartec and the grips should not be affected by the local heating of the specimen itself.

In practice, the computer-based Dartec machine can perform uniaxial load tests by controlling the load or stroke increment. Both modes will affect the strain rate in the specimen in a different way. Therefore, this section concentrates on the investigation of the strain-stroke relation for both load and stroke control. These initial tests were carried out on specimens which had strain gauges attached to their gauge length. Subsequent tests on many more specimens used the crosshead displacement rather than a strain gauge to determine specimen strain.

In the first condition, the load rate of the machine was set at 300 Ns^{-1} and a compression load was applied up to a certain value without fracturing the specimen. During loading, the strain signal and the load signal were recorded by the data acquisition unit. At the same time, the displacement of the Dartec crosshead was also recorded. When the load reached its maximum value, the applied load was reduced to zero. The next step was the investigation of the strain-stroke relation under tension. Before starting, all the signals (the strain, the applied load, and the displacement) were reset to zero. Then the tension load was applied at a rate of 300 Ns^{-1} until the specimen broke.

For the stroke control, the crosshead speed of the Dartec machine was set at 0.05 mms^{-1} and the above procedure repeated i.e. the compression load was firstly applied followed by the tension load up to failure.

3.4.2 RESULTS

As shown in Figure 3.15, the relation between the specimen strain and crosshead displacement for both stroke and load control are almost the same. This means that the strain-stroke relation is independent of load conditions i.e. stroke or load control. In addition, all curves are non-linear with the strain increasing at a higher rate at high stroke increments. This is because the total stroke of the crosshead is the sum of the displacements in the machine, the pins, the wedges, the grips and the specimen itself and the relative magnitude of these will vary with load, as indicated in Figure 3.16.

Figure 3.15 also reveals that the relation between the strain and stroke in compression is different from that in tension. The main reason is that in tension the load was applied directly through the pin, resulting in slight deformation of the pin. In compression, there is less pin deformation because the compressive force was directly applied to the top of specimen, causing lower crosshead displacement in compression than in tension for the same specimen strain.

Figures 3.17-3.20 show plots of the strain gauge output vs. time for the four test conditions. It can be seen that the rate of strain increases during the test for all test conditions, even under displacement control, due to the non-linear compliance effects mentioned above. Figures 3.17-3.20 also illustrate that the mean strain rates for the stroke control tests are higher than those for load control in both tension and compression. In fact, the stroke rate of 0.05 mms^{-1} is the minimum available on the Dartec machine and it is desirable to test at the lowest strain rate possible. According to the relevant British Standard [55], the strain rate for determining the lower yield strength of a specimen shall be between 0.00025 and 0.0025 s^{-1}. If this rate cannot be regulated directly, it must be fixed by regulating the stress rate to between 2 and

10 $MPas^{-1}$ just before yield begins. Since the mean strain rate is lower under load control, the load controlled rate of 300 Ns^{-1} which gives a nominal stress rate of 8.33 $MPas^{-1}$ was used to investigate the stress-strain curves of the cast iron material in the monotonic tests described below.

3.5 MONOTONIC TESTING

3.5.1 METHOD

Since the load history of a specimen may have significant influence on its stress-strain response, a specimen should only be tested once for each condition and then should not be used again in order to obtain further material data. Therefore, separate specimens were used for tests under tension and compression at each temperature (25, 300, 350 and 400 °C).

Load control at 300 Ns^{-1} loading rate was used for the monotonic testing because the mean strain rates were lower than those for the stroke control condition. From the results of the strain-stroke calibration described above, the relation between the stroke of the crosshead Dartec machine and the strain in the specimen was used to obtain the current strain from the measured crosshead displacement. The load was divided by the cross-sectional area of the specimen to give the nominal stress. The monotonic stress-strain curve (MSSC) could then be generated from these results for both tensile and compressive loading at different temperatures. Note that the true stress and strain used to plot these curves were calculated from the nominal stress and strain using the usual relationships for constant volume deformation defined in Equation 3.1:

$$\tilde{\sigma} = \sigma(1+\varepsilon)$$
$$\tilde{\varepsilon} = \ln(1+\varepsilon) \tag{3.1}$$

where

$\tilde{\sigma}$ = True stress

$\tilde{\varepsilon}$ = True strain

σ = Nominal stress

ε = Nominal strain

3.5.2 RESULTS

The stress-strain curves at the four different temperatures are shown in Figure 3.21. These graphs reveal that the cast iron response is dependent on temperature with higher temperatures producing higher strains for a given level of stress as expected. Furthermore, the stress-strain curves in compression are higher than those in tension at all temperatures. This results from the fact that the cast iron is composed of two components: graphite flakes and pearlite matrix. In tension, the graphite flakes cause voids to open in the matrix, resulting in a higher strain for a given level of stress compared with compression where the graphite flakes absorb and transmit the compressive load to the surrounding pearlite matrix.

In both tension and compression, the most significant differences are between temperatures of 300 and 400 °C whereas the differences between the 20 °C and 300 °C curves are less significant given the much greater range of temperature. This might be due to the effect of micro-structural changes over this higher range of temperature. All curves show an increasingly non-linear relationship between stress and strain as the loads are increased due to the onset of plastic deformation.

3.6 CYCLIC TESTING

3.6.1 METHOD

Normally the cyclic strain test is used to investigate the response of a material to cyclic loads. One output of these tests is a cyclic stress-strain curve (CSSC) which describes the stress-strain relation of the cycled material during the early stage of fatigue including such phenomena as cyclic softening and cyclic hardening.

As mentioned in Chapter 1, the two techniques used to determine the CSSC are the incremental test and the multiple step test. In each test, only the strain in the specimen should be controlled in the incremental or step pattern respectively. It is quite difficult to conduct the incremental test on an ordinary machine because the strain in the specimen should be under feedback control. However, if the machine has a closed loop control system using the strain signal from the specimen, the incremental test can be used to obtain the CSSC. Alternatively, a simple test like the multiple step test can be used to find the CSSC on an ordinary machine. In order to apply this test, the strain amplitude is increased only after the hysteresis is saturated i.e. after a steady-state stress-strain cycle is obtained.

In order to obtain the cyclic response of the present brake disc cast iron material, the multiple step test was used. The relation between the specimen strain and crosshead stroke from the strain-stroke calibration was used to maintain a constant strain amplitude in both tension and compression as defined in Table 3.2. In these tests, the cyclic strain amplitude started with a low value and then was increased to a higher value after successive intervals of 50 cycles as shown in Figure 3.22. The specimen was cycled at a frequency of 0.1 Hz using a sawtooth waveform as indicated in the Figure. In addition to testing at room temperature, this mode of testing was also used to find the

cyclic response at elevated temperatures of 300 and 400 °C using the induction heating system described in section 3.3.2. Therefore, three specimens in total were required for these tests.

Cycles	Cyclic strain amplitude (peak-to-peak)	Stroke (mm) in tension	Stroke (mm) in compression
First 50 cycles	0.001536	0.15800	0.1000
Second 50 cycles	0.004516	0.32550	0.2314
Third 50 cycles	0.007500	0.44520	0.3309
Fourth 50 cycles	0.010480	0.54356	0.4143

Table 3.2: Relation between the cyclic strain amplitude and the crosshead stroke

3.6.2 RESULTS

All specimens broke in tension at the first cycle of the third strain amplitude except for the specimen that was tested at 400 °C which broke at the 11^{th} cycle of the second strain amplitude. Therefore, there were no specimens subjected to the fourth cyclic strain amplitude conditions.

From the cyclic stress-time histories shown in Figure 3.23, the peak tensile stress decreases significantly with increasing cyclic strain amplitude whereas the absolute magnitude of the compressive stresses increases. This indicates a degree of cyclic softening in tension and cyclic hardening in compression. The magnitude of these effects is also temperature-dependent as can be seen from comparison of Figure 3.23 (a) and (b). A similar study on the cyclic behaviour of cast iron at room temperature attributed these characteristics to the greater opening of voids around graphite flakes

under cyclic tension and the cyclic strain hardening of the pearlite matrix in compression [16].

In order to find the hysteresis loops for each strain amplitude, the cyclic stress-strain curves were generated as shown in Figure 3.24 for temperatures of 20, 300 and 400 °C. They reveal that the upper (loading in tension) curves are non-linear and the lower (loading in compression) curves are almost linear throughout all cyclic strain amplitudes and temperature conditions. This is mainly the result of the higher plastic deformation accompanied by voids opening around graphite flakes in tension compared to much higher strain hardening in compression.

The peak stress and strain in tension and compression at the end of each strain cycle can be used to form the CSSC's. These curves were compared to the MSSC's in Figure 3.25 for temperatures of 20, 300 and 400 °C. The results show that the MSSC's are above the CSSC's in tension due to cyclic softening whereas, in compression, the CSSC's give generally higher stresses for a given level of plastic strain due to cyclic hardening. However, it should be taken into account that the effect of cyclic load history for these experiments might be another factor to cause these differences in behaviour because a single specimen was tested with four different cyclic amplitudes. The effect of damage accumulation due to previous loading history is illustrated by the fact that the maximum tensile strain for fracture under cyclic loading is lower than under monotonic loading at all temperatures.

3.7 SUMMARY

From the FE analysis of the specimen geometry, it is concluded that the square specimen with a 4 mm diameter hole can be used for the tensile testing because the stress concentration at the shoulder is minimum. In addition, the stress concentration at the hole is not significantly dependent on the diameter of the hole.

The specimen grips fulfilled all the requirements to minimise the backlash for cyclic loading. Furthermore, they were used successfully with the induction coil for testing at elevated temperatures. However, a more direct method of measuring the specimen strain would be desirable e.g. Ettemeyer Speckle Interferometry (ESPI) [57] in order to eliminate the effect of the pin and wedge displacements.

The experimental MSSC's at various temperatures demonstrate that the stress-strain response of the brake disc cast iron is temperature dependent both in tension and compression. Furthermore, the temperature sensitivity increases significantly above 300 °C in both tension and compression. Therefore, errors induced by using the room temperature response will be much greater above 300 °C.

The effects of cyclic loading cause significant differences in the stress-strain response compared with monotonic loading. The cyclic load causes the material to harden in compression and to soften in tension especially at high temperatures. Furthermore, cyclic loading causes fracture at lower strains than under monotonic loading at the same temperature. However, the generation of accurate fatigue life data as a function of stress level and temperature was considered outside the scope of the present work.

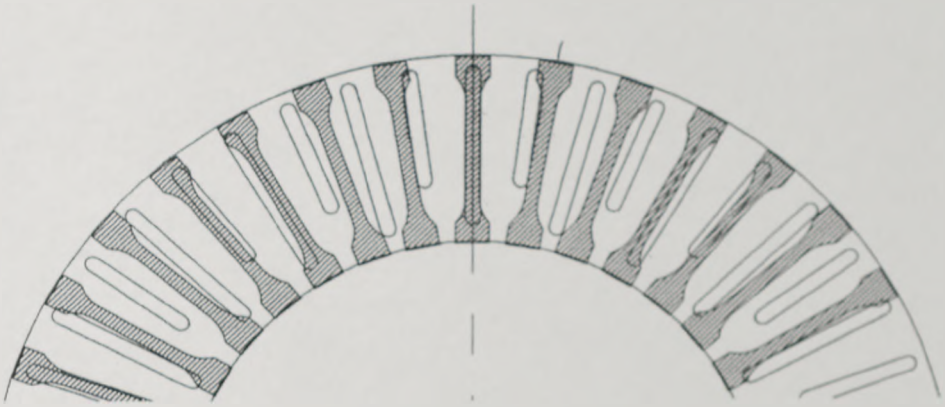

Figure 3.1: Layout of specimens on the rubbing surface

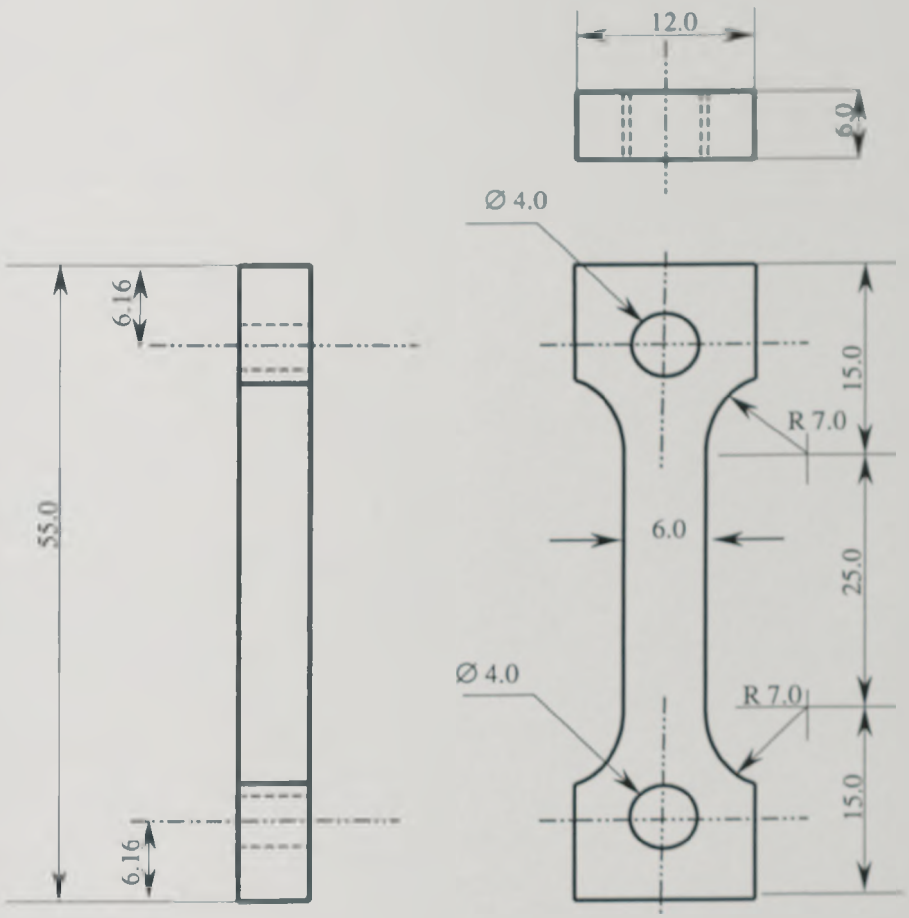

Figure 3.2: Specimen dimension (unit in mm)

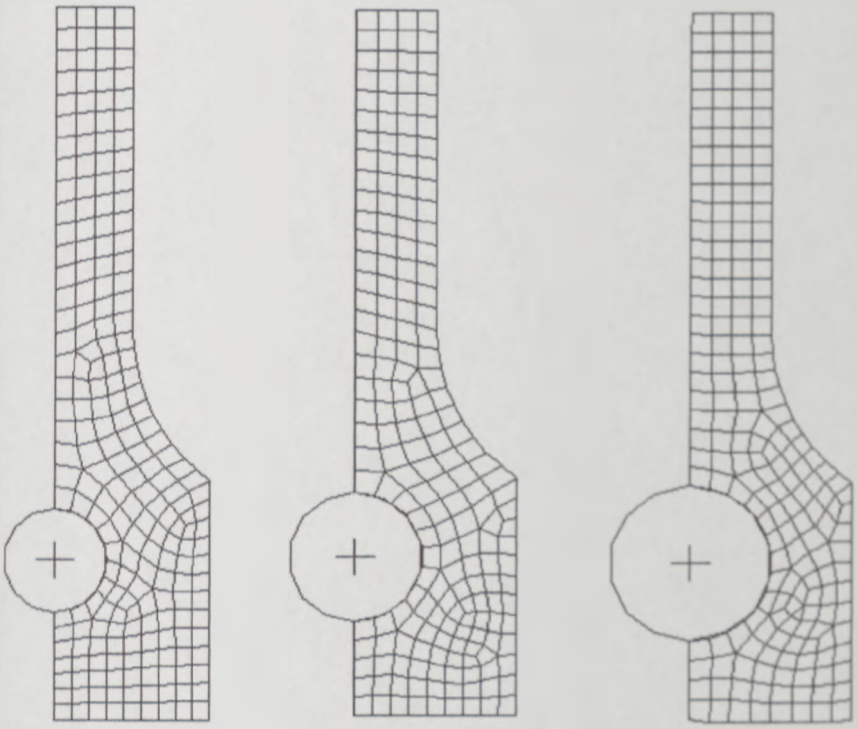

Figure 3.3: Specimen models for 4, 5 and 6 mm diameter holes respectively

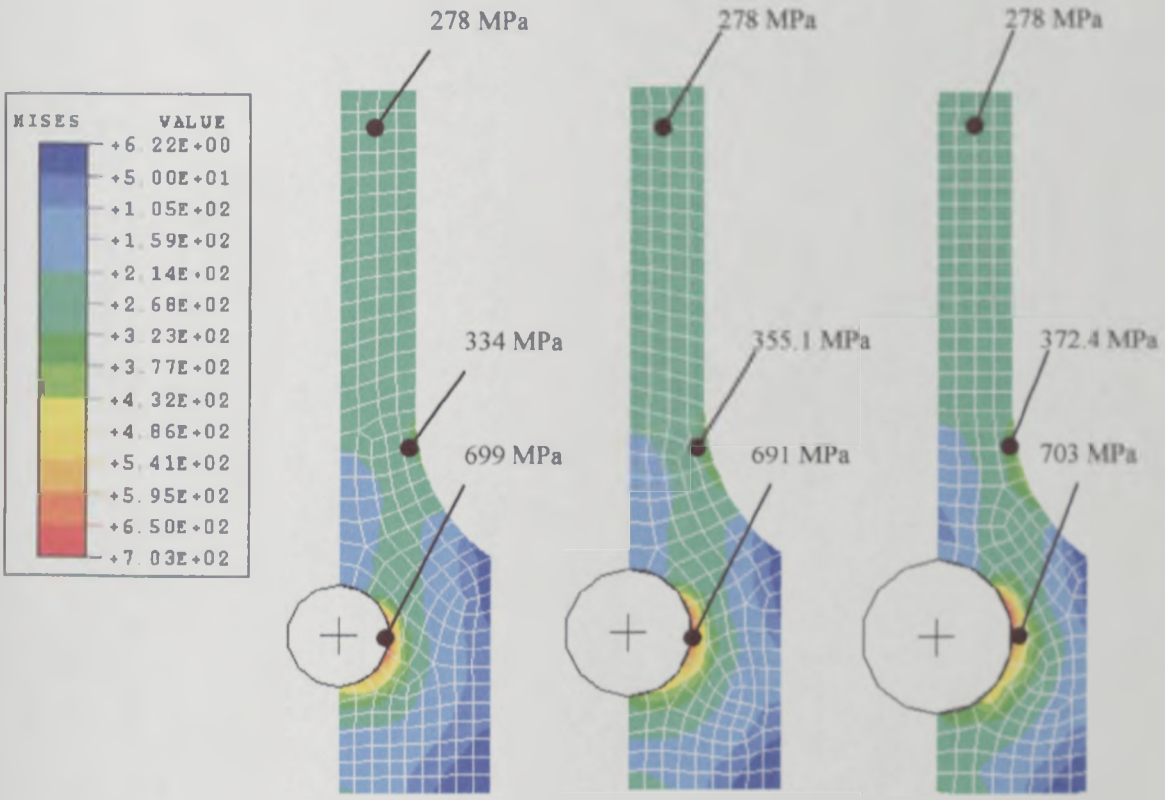

Figure 3.4: Von Mises stresses for specimens with 4, 5 and 6 mm holes respectively

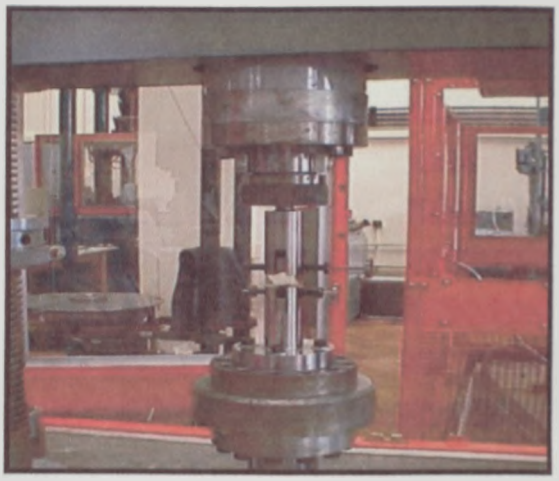

Figure 3.5: Specimen and grips in Dartec machine

Figure 3.6: Console unit of Dartec

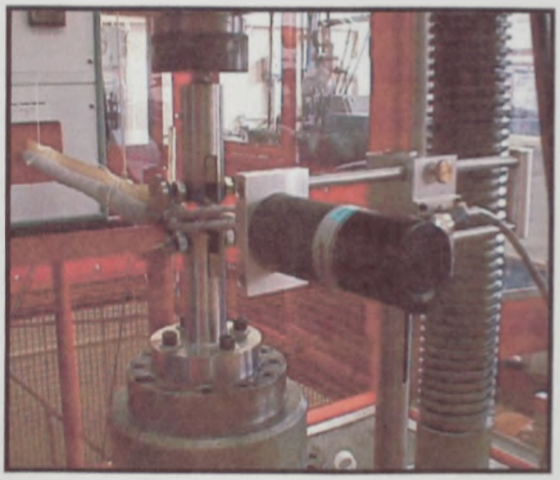

Figure 3.7: Infrared detector and induction heating furnace

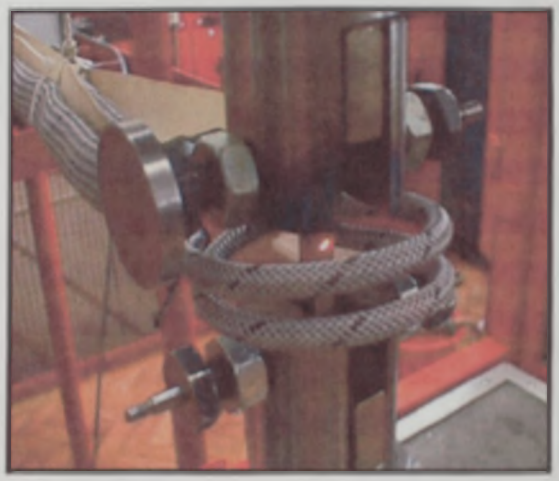

Figure 3.8: Induction coil for high temperature testing

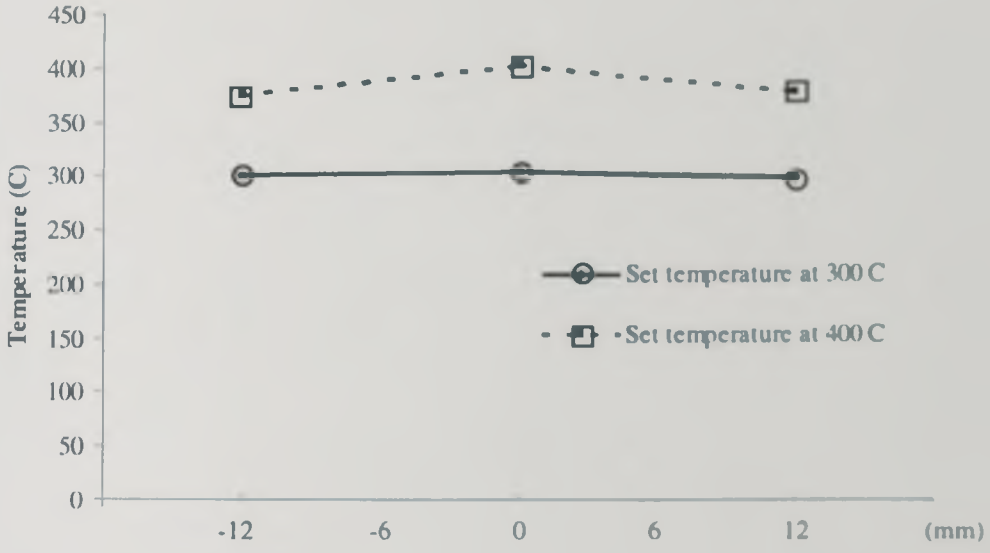

Figure 3.9: Measured temperature profile along the gauge length of specimen

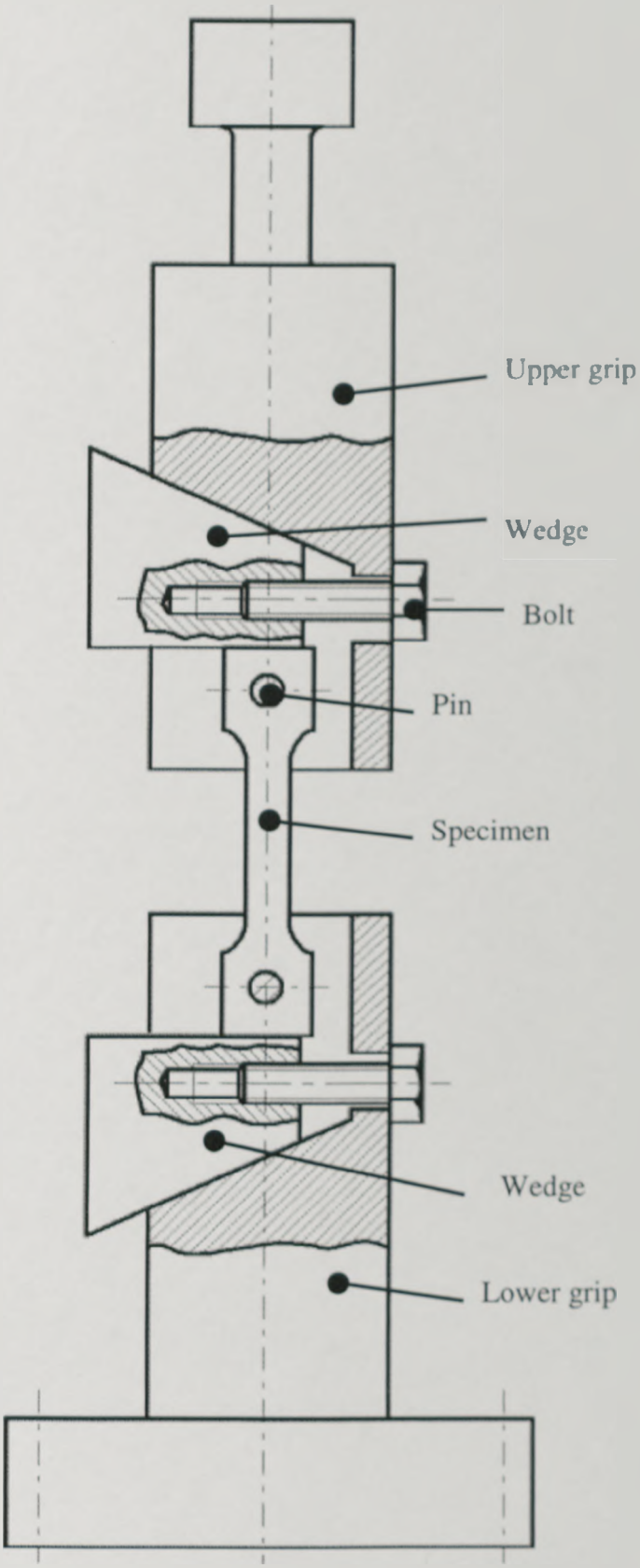

Figure 3.10: Side view of grip assembly

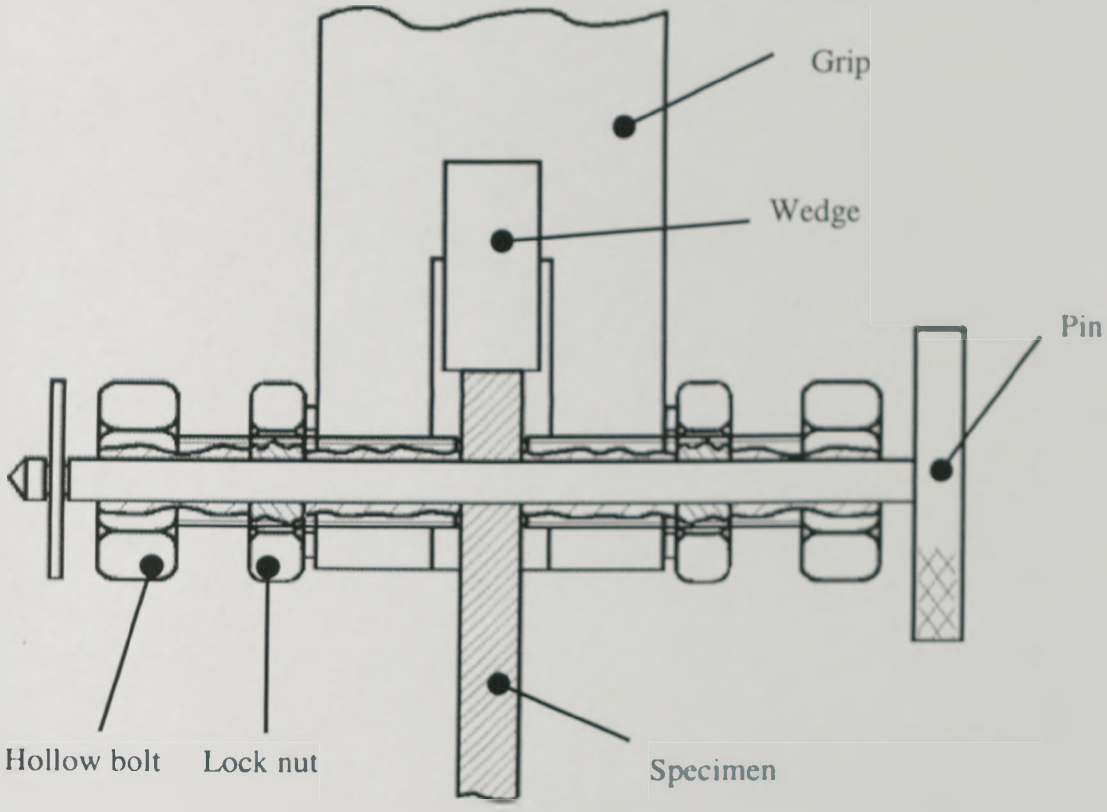

Figure 3.11: Front view of grip assembly

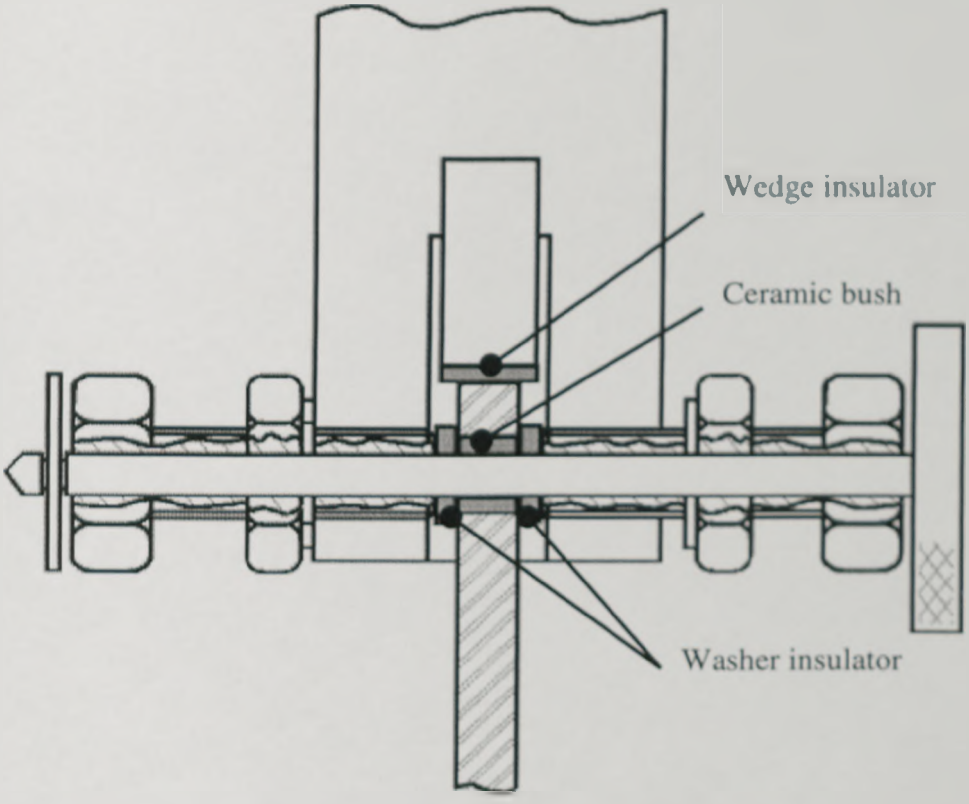

Figure 3.12: Front view of grip assembly for elevated temperature tests

Figure 3.13: Specimen with the strain gauge

Figure 3.14: Strain gauge meter

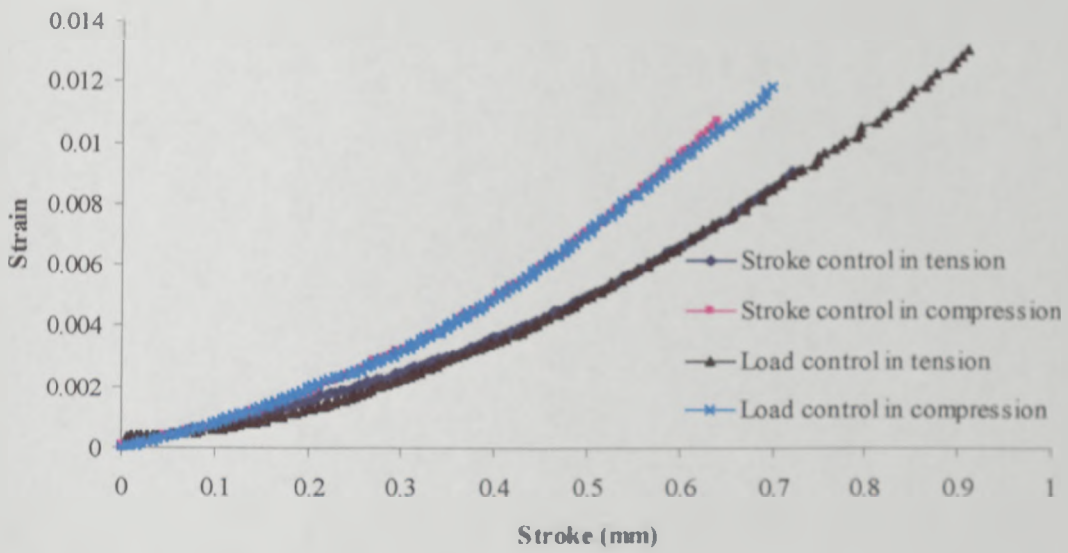

Figure 3.15: Relation between the specimen strain and the crosshead for both load and stroke control

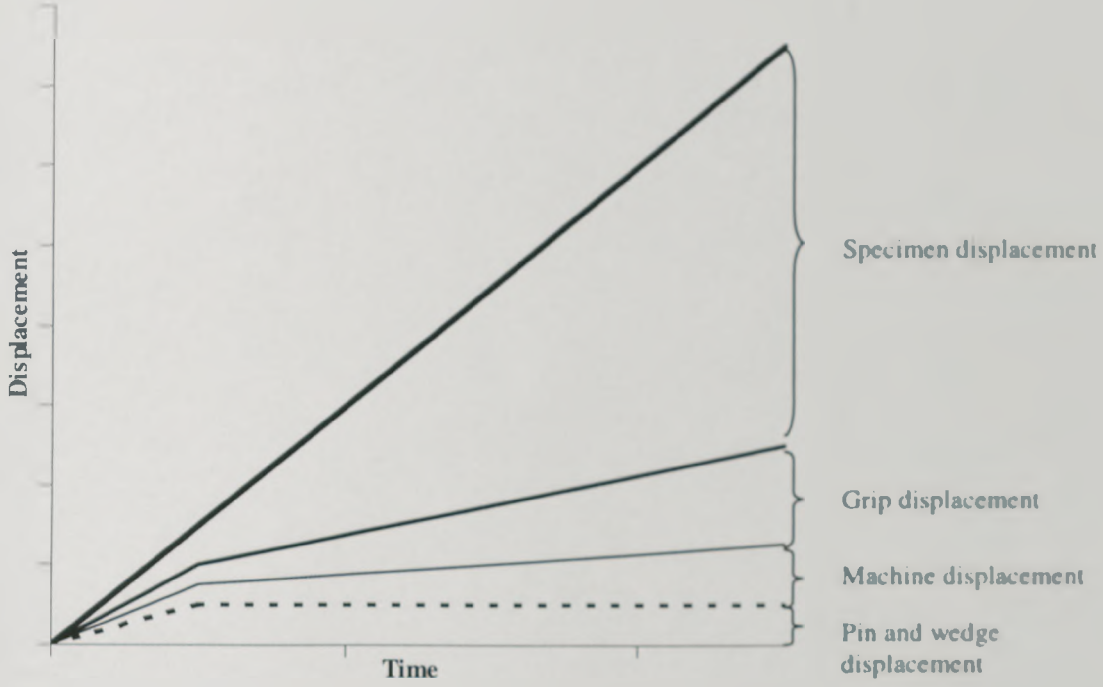

Figure 3.16: Schematic of displacements during monotonic tests

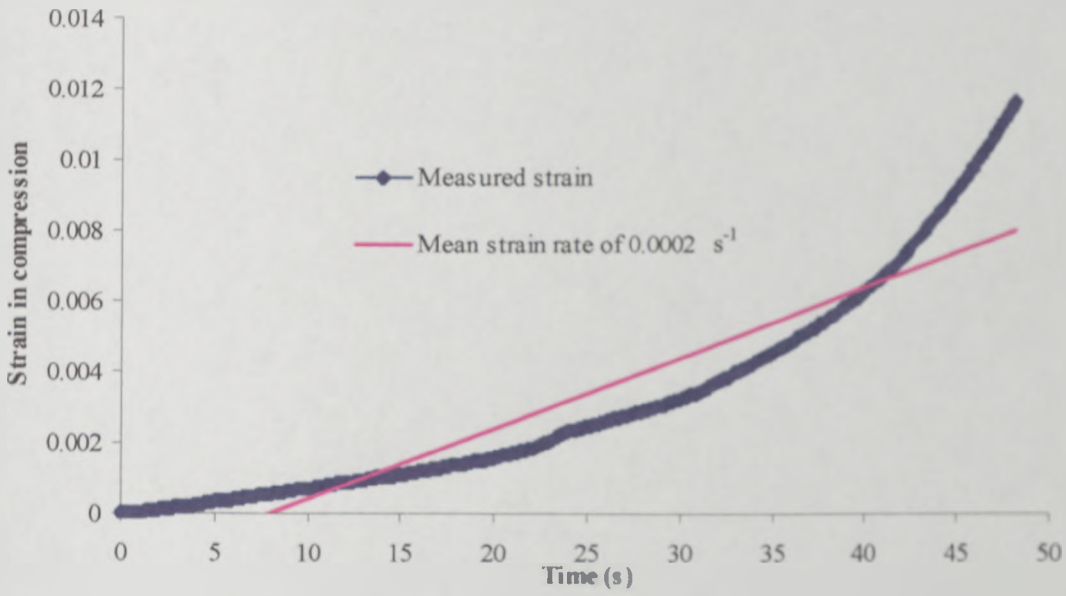

Figure 3.17: Strain time history for load control at 300 Ns^{-1} in compression

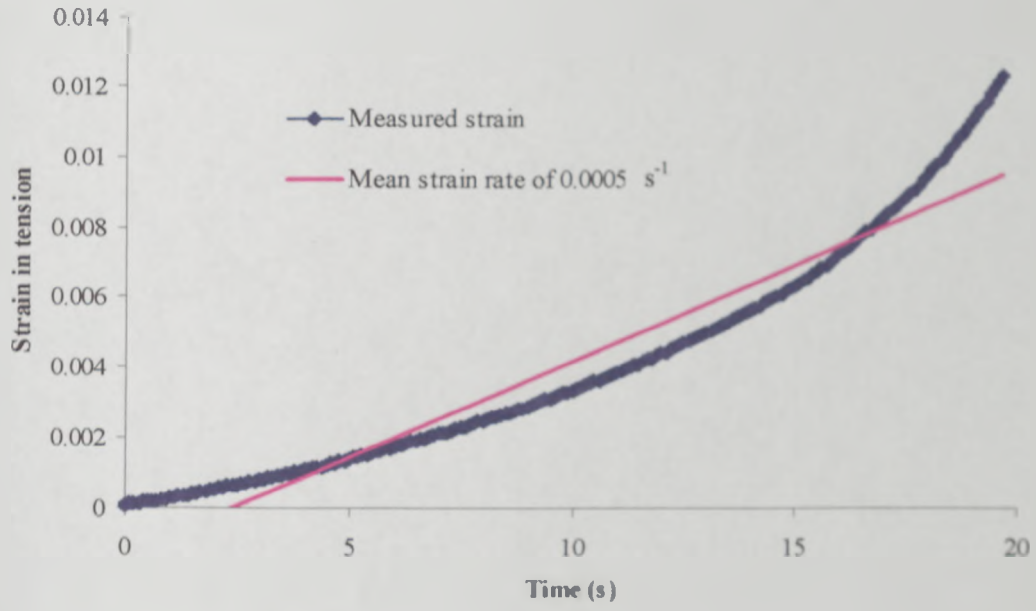

Figure 3.18: Strain time history for load control at 300 Ns^{-1} in tension

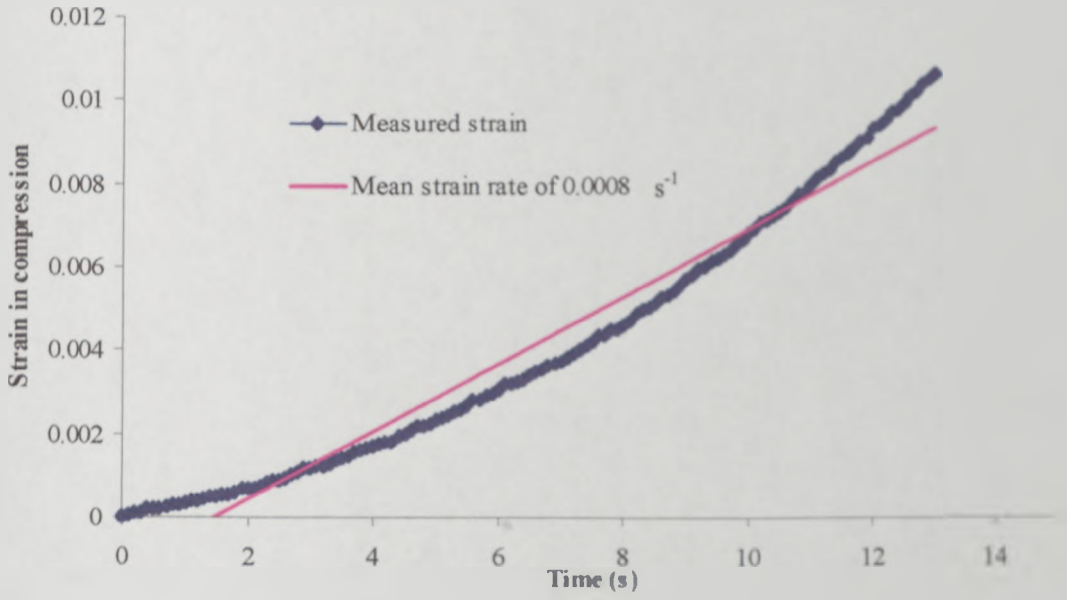

Figure 3.19: Strain time history for stroke control at 0.05 mms^{-1} in compression

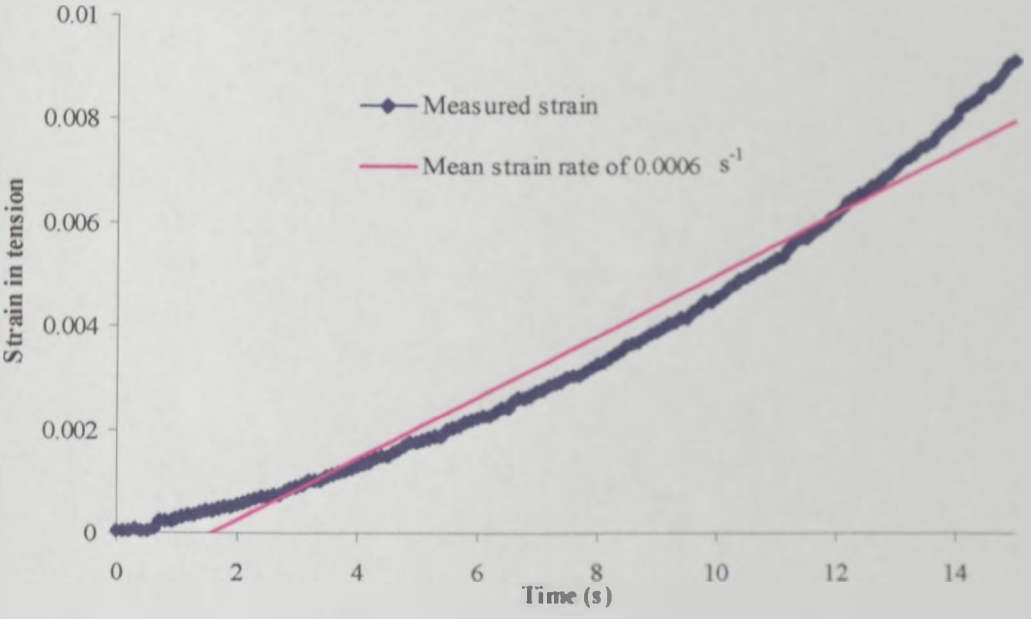

Figure 3.20: Strain time history for stroke control at 0.05 mms^{-1} in tension

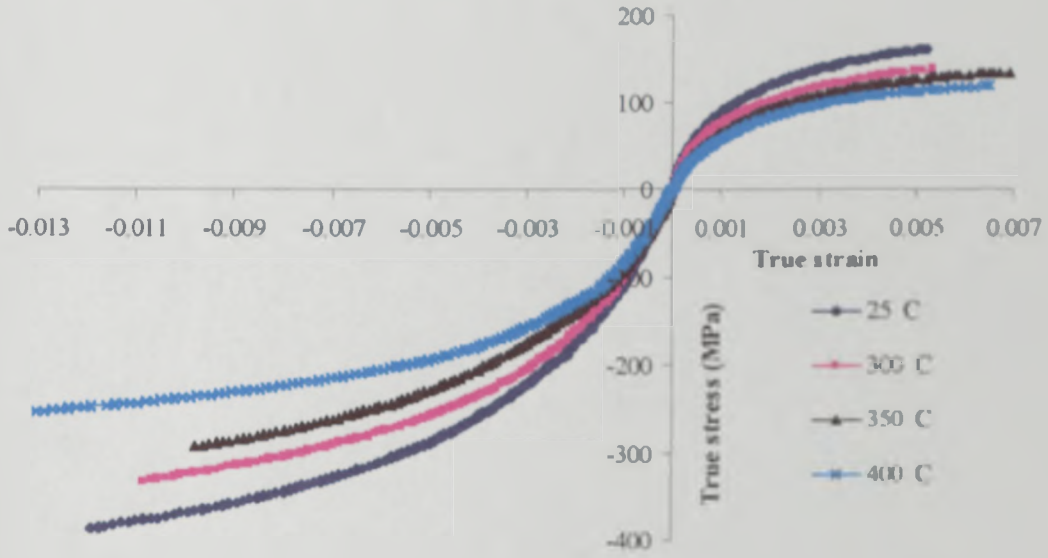

Figure 3.21: True stress-true strain curves for the Rover cast iron disc material

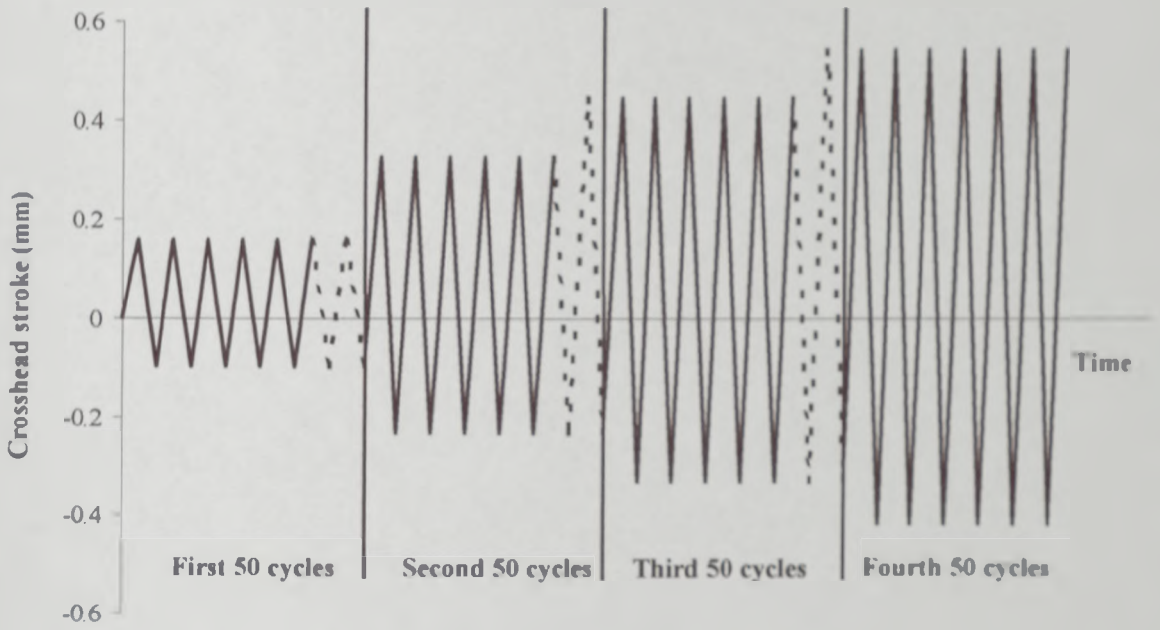

Figure 3.22: Cyclic crosshead stroke time histories

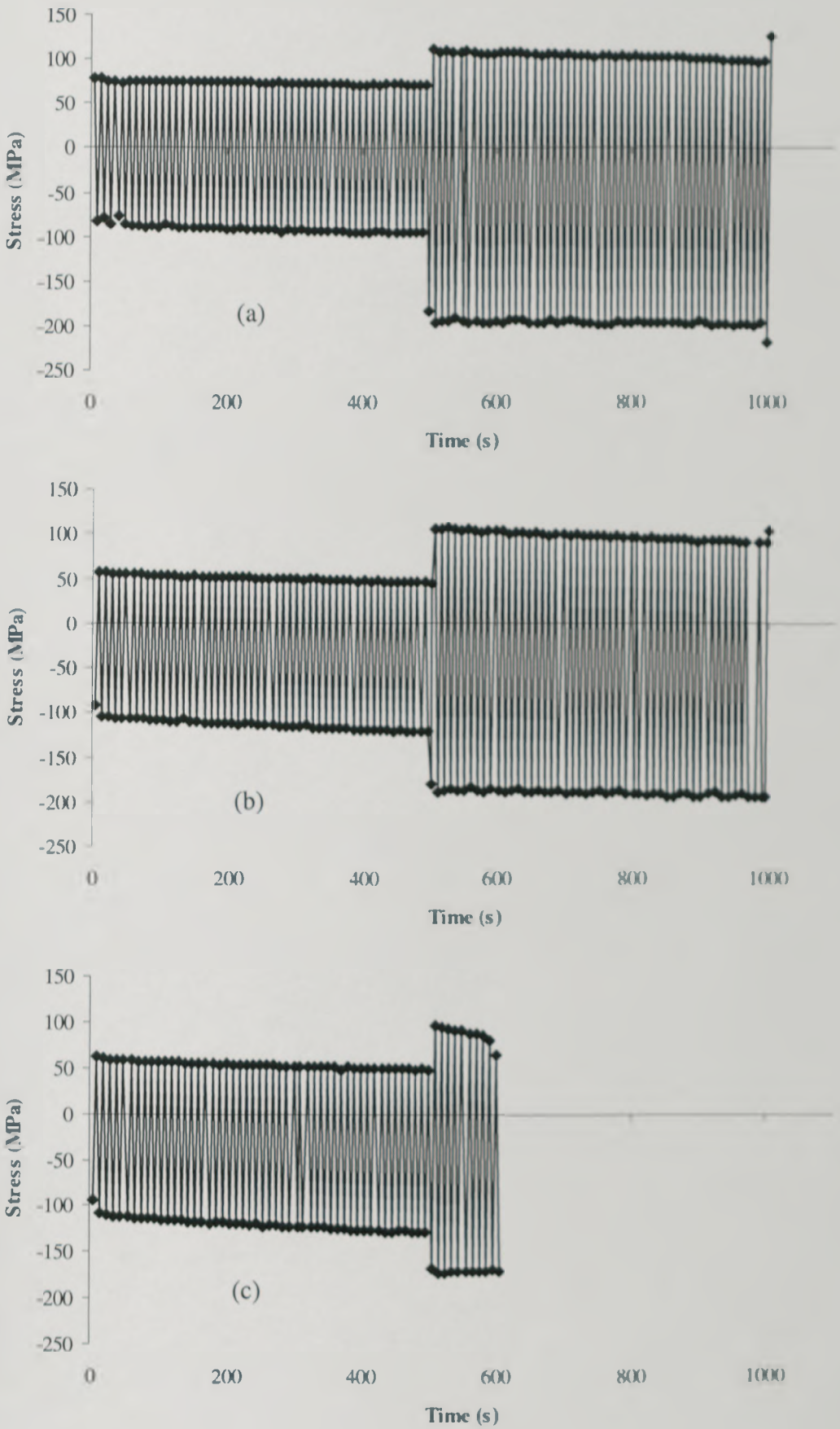

Figure 3.23: Stress time history at (a) room temperature, (b) 300°C, (c) 400°C

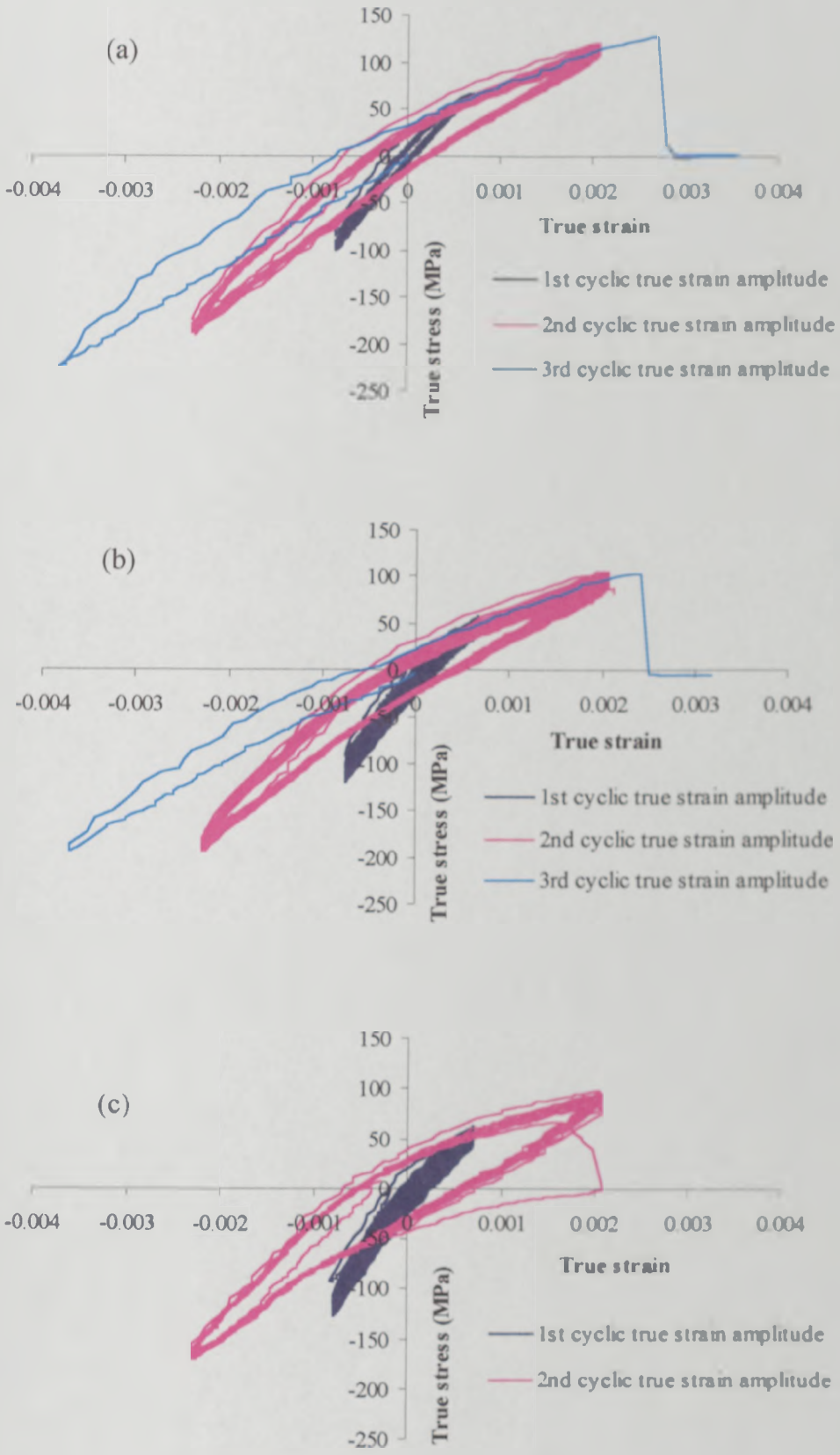

Figure 3.24: Cyclic stress-strain curves at (a) room temperature, (b) 300°C, (c) 400°C

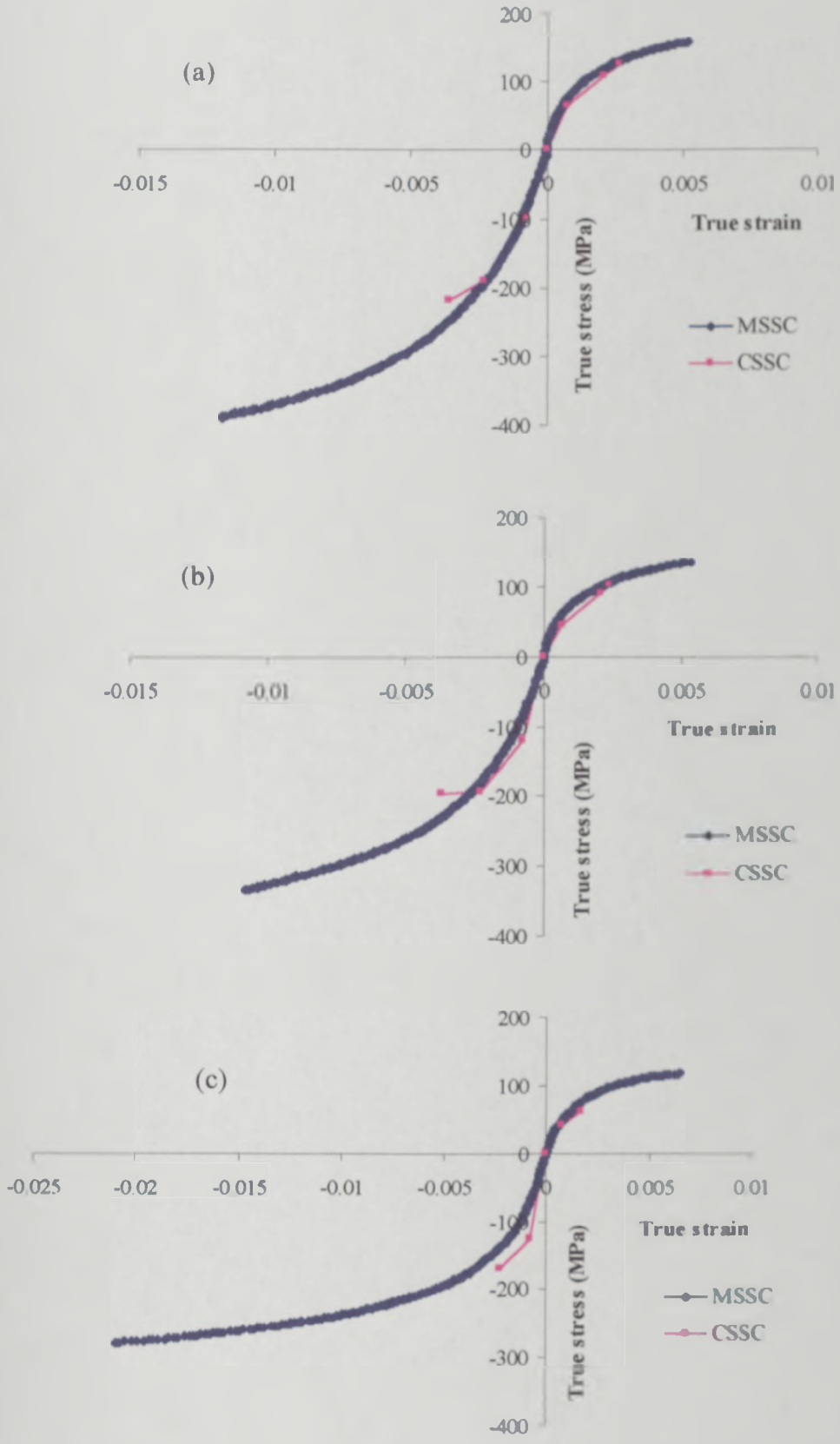

Figure 3.25: Comparison between CSSC and MSSC at (a) room temperature, (b) 300 °C, (c) 400 °C

CHAPTER 4

MATERIAL MODELLING OF CAST IRON

4.1 INTRODUCTION

The FE technique consists of several stages that include the generation of a mesh together with the application of appropriate material models and boundary conditions. The simulation accuracy is improved through successive refinement of the underpinning assumptions. To apply such a technique for investigating the thermal behaviour of cast iron brake discs, a material model must be chosen with great care. This is because of the response characteristics of cast iron to uniaxial loads that result in different yield stresses in tension and compression. General material models for the FE technique assume that the material has the same yield behaviour in both tension and compression. This Chapter focuses on the development of a more realistic material model for cast iron that can be used in conjunction with existing FE techniques but firstly investigates the material model currently available for cast iron in ABAQUS version 5.7 [41]. Specific models for a particular material can also be created in a user-developed subroutine option. This Chapter investigates such a user-developed material model for standard von Mises plasticity with isotropic hardening to give confidence in the development of the Fortran coding required. It proceeds to describe a more complex user-developed subroutine material model especially developed for cast iron by the author. The response of these material models to external loads is investigated using the simple FE model described below.

4.1.1 FINITE ELEMENT MODEL

The FE model used to investigate the characteristics of the different material models represented the square cross-section gauge length of the specimen that was designed for

the material property tests reported in Chapter 3. The main reason for choosing this model was that the material properties measured with this specimen, notably the Young's modulus and monotonic stress-strain curves in tension and compression at various temperatures, were themselves used to create the material models. The results of applying the models could therefore be compared directly with the experimental results.

The gauge length model consists of 900 twenty noded solid elements each with a quadratic interpolation function as shown in Figure 4.1. Zero displacement constraints were applied to the model in the first and third directions along the gauge length and the nodes at the bottom of the gauge length were constrained in the second direction as shown in the Figure. For all investigations in this Chapter, the top of the gauge length was subjected to external load in the second direction. However, all nodes of the gauge length model were assumed to have a constant temperature so as to eliminate the effect of temperature changes.

4.2 ABAQUS STANDARD CAST IRON MODEL

4.2.1 METHODOLOGY

Before developing the theory behind this material model, some definitions of stress states are firstly introduced. The stress state at any location may be characterised by a stress tensor $[\sigma]$. Its components in the Cartesian co-ordinate system (x, y, z) can be represented in matrix form as shown in Equation 4.1:

$$[\sigma] = \begin{bmatrix} \sigma_{xx} & \sigma_{xy} & \sigma_{xz} \\ \sigma_{yx} & \sigma_{yy} & \sigma_{yz} \\ \sigma_{zx} & \sigma_{zy} & \sigma_{zz} \end{bmatrix} \tag{4.1}$$

Due to the symmetry of the stress tensor, only six stress components $\{\sigma\}$ are independent as shown in Equation 4.2:

$$\{\sigma\}=\{\sigma_{xx},\sigma_{yy},\sigma_{zz},\sigma_{xy},\sigma_{yz},\sigma_{zx}\} \tag{4.2}$$

However, in plasticity theory [58-59], it is customary to decompose the stress tensor into two parts; the deviatoric stress tensor [S] and the hydrostatic stress tensor [P]:

$$[\sigma] = [S]-[P] \tag{4.3}$$

where [S] and [P] are given by:

$$[S]=\begin{bmatrix} S_{xx} & S_{xy} & S_{xz} \\ S_{yx} & S_{yy} & S_{yz} \\ S_{zx} & S_{zy} & S_{zz} \end{bmatrix} \tag{4.4}$$

$$[P]=\begin{bmatrix} -\frac{1}{3}(\sigma_{xx}+\sigma_{yy}+\sigma_{zz}) & 0 & 0 \\ 0 & -\frac{1}{3}(\sigma_{xx}+\sigma_{yy}+\sigma_{zz}) & 0 \\ 0 & 0 & -\frac{1}{3}(\sigma_{xx}+\sigma_{yy}+\sigma_{zz}) \end{bmatrix} \tag{4.5}$$

From the matrix [S], the principal deviatoric stresses $\{S_1, S_2, S_3\}$ can be found from Equation 4.6 which can be expanded to polynomial form as shown in Equation 4.7:

$$\det\begin{bmatrix} (S_{xx}-S) & S_{xy} & S_{zz} \\ S_{yx} & (S_{yy}-S) & S_{yz} \\ S_{zx} & S_{zy} & (S_{zz}-S) \end{bmatrix}=0 \tag{4.6}$$

$$S^3 - J_1'S^2 + J_2'S - J_3' = 0 \tag{4.7}$$

where

$$J_1' = S_{xx} + S_{yy} + S_{zz} = S_1 + S_2 + S_3$$

$$J_2' = \frac{1}{2}(S_{xx}S_{xx} + S_{xy}S_{xy} + S_{xz}S_{xz} + S_{yx}S_{yx} + S_{yy}S_{yy} + S_{yz}S_{yz} + S_{zx}S_{zx} + S_{zy}S_{zy} + S_{zz}S_{zz})$$

$$= \frac{1}{2}(S_1^2 + S_2^2 + S_3^2)$$

$$J_3' = \det\begin{bmatrix} S_{xx} & S_{xy} & S_{xz} \\ S_{yx} & S_{yy} & S_{yz} \\ S_{zx} & S_{zy} & S_{zz} \end{bmatrix} = S_1 S_2 S_3 \qquad (4.8)$$

J_1', J_2' and J_3' are the first, second and third invariants of the deviatoric stress tensor respectively.

The yield surface for the ABAQUS cast iron material model and its plastic flow characteristics are now introduced. The model used a composite yield surface to describe the different behaviour in tension and compression. The maximum principal stress (Rankine criterion) was used to govern yielding in tension while the von Mises stress (octahedral shear stress yield criterion) was used for yielding in compression. Figure 4.2 illustrates the yield surface in principal stress space. Within the interior of this yield surface, the stress state is in the elastic region.

The theory behind this yield surface comes from the relationship that exists between the hydrostatic pressure stress (P), von Mises stress (σ_e), yield stresses in tension and compression (σ_t and σ_c), and the location of stress state (θ) that combine to define the tensile (F_t) and compressive (F_c) yield functions:

$$F_t = \frac{2}{3}\cos(\theta)\sigma_e - P - \sigma_t = 0$$
$$F_c = \sigma_e - \sigma_c = 0 \qquad (4.9)$$

Figure 4.3 shows tensile and compressive yield functions, F_t and F_c, respectively in the form of the von Mises stress (σ_e) plotted against the hydrostatic pressure stress (P). In Equation 4.9, θ is used to locate the stress state in the tension yield surface. Figure 4.4 indicates the location of the stress state related to θ in the plane that is perpendicular to the hydrostatic pressure axis (P). It can be seen clearly that the boundary of the tensile yield surface (F_t) varies according to θ, whilst the von Mises surface is independent of θ within the hydrostatic pressure plane. To calculate θ in Equation 4.9, the third invariant of the deviatoric stress tensor (J_3) and the von Mises equivalent stress (σ_e) are used as shown in Equation 4.10:

$$\cos(3\theta) = \left(\frac{J_3}{\sigma_e}\right)^3$$
$$\sigma_e = \sqrt{\frac{3}{2}(S_1^2 + S_2^2 + S_3^2)} \tag{4.10}$$

If a material is loaded to a stress state on the yield surface and an additional loading increment causes the prediction of a stress state outside this original yield surface, plastic strain occurs and the yield surface moves. In principle, it is impossible to have a stress state that lies outside the yield surface. Therefore, during the application of external load, the yield surface can potentially move or change shape such that the current stress state always lies on the yield surface. The basic theory used to determine the amount of plastic strain is obtained from Drucker's and Von Mises' postulates [60]. The former assumed that the body will remain in equilibrium and positive work will be done during the application of the load increment. The latter postulated that the plastic strain increment, $d\{\varepsilon^{pl}\}$, is derivable from a plastic potential function, $G\{\sigma\}$, that is a scalar function of the stress state as shown in Equation 4.11:

$$d\{\varepsilon^{pl}\} = \Delta\lambda \frac{\partial G}{\partial\{\sigma\}} \tag{4.11}$$

The plastic strain multiplier, $\Delta\lambda$, is a positive scalar quantity. If the plastic potential function is the same as the yield function, $G\{\sigma\} = F\{\sigma\}$, the plastic strain increment is associated with the yield surface. Therefore, Drucker's formulation is called an associated flow rule. Otherwise, the non-associated flow rule can be used, $G\{\sigma\} \neq F\{\sigma\}$.

For the plastic characteristic of the cast iron yield surface, the tensile and compressive potential functions (G_t and G_c) which are hydrostatic pressure dependent, are introduced as shown in Figure 4.5. It can be clearly seen that the graph consists of two parts: G_t and G_c which represent one section of the ellipse and the straight line respectively as defined by Equation 4.12:

$$\frac{(P - G_t)^2}{b^2} + \sigma_e^{\,2} = 9G_t^2 \text{ when } P < \frac{\sigma_c}{3}$$
$$\sigma_e = 3G_c \text{ when } P \geq \frac{\sigma_c}{3} \qquad (4.12)$$

The shape of the ellipse associated with the tensile potential function is controlled by the parameter b and is forced to pass the points $(-\gamma\sigma_t/3, \gamma\sigma_t)$ and $(\sigma_c/3, \sigma_c)$ where $\gamma = 2\sigma_c(1+\nu_{pl})/(3\sigma_t)$ controls the volumetric plastic strain increment. The quantities σ_c, σ_t and ν_{pl} are the compressive yield stress, the tensile yield stress and the plastic Poisson's ratio respectively. The plastic Poisson's ratio is obtained from the absolute value of the ratio of the transverse to the longitudinal plastic strain under uniaxial tension. Thus, the parameter b^2 for G_t is equal to $(\sigma_c + \gamma\sigma_t)/9(\sigma_c - \gamma\sigma_t)$.

Since there are two plastic potential functions with the ABAQUS standard cast iron material model, the plastic strain increments in tension and compression are unique. To obtain these definitions, the volumetric ($\dot{\varepsilon}^{pl}_{vol}$) and deviatoric [$\dot{e}^{pl}$] components of plastic strain rate [$\dot{\varepsilon}^{pl}$] are introduced as shown in Equation 4.13:

$$[\dot{\varepsilon}^{pl}]=\begin{bmatrix}\dot{\varepsilon}^{pl}_{vol} & 0 & 0\\ 0 & \dot{\varepsilon}^{pl}_{vol} & 0\\ 0 & 0 & \dot{\varepsilon}^{pl}_{vol}\end{bmatrix}+\begin{bmatrix}(\dot{\varepsilon}^{pl}_{xx}-\dot{\varepsilon}^{pl}_{vol}) & \dot{\varepsilon}^{pl}_{xy} & \dot{\varepsilon}^{pl}_{xz}\\ \dot{\varepsilon}^{pl}_{yx} & (\dot{\varepsilon}^{pl}_{yy}-\dot{\varepsilon}^{pl}_{vol}) & \dot{\varepsilon}^{pl}_{yz}\\ \dot{\varepsilon}^{pl}_{zx} & \dot{\varepsilon}^{pl}_{zy} & (\dot{\varepsilon}^{pl}_{zz}-\dot{\varepsilon}^{pl}_{vol})\end{bmatrix} \tag{4.13}$$

where $$\dot{\varepsilon}^{pl}_{vol}=\frac{1}{3}(\dot{\varepsilon}^{pl}_{xx}+\dot{\varepsilon}^{pl}_{yy}+\dot{\varepsilon}^{pl}_{zz})$$

and

$$[\dot{e}^{pl}]=\begin{bmatrix}\dot{e}^{pl}_{xx} & \dot{e}^{pl}_{xy} & \dot{e}^{pl}_{xz}\\ \dot{e}^{pl}_{yx} & \dot{e}^{pl}_{yy} & \dot{e}^{pl}_{yz}\\ \dot{e}^{pl}_{zx} & \dot{e}^{pl}_{zy} & \dot{e}^{pl}_{zz}\end{bmatrix}=\begin{bmatrix}(\dot{\varepsilon}^{pl}_{xx}-\dot{\varepsilon}^{pl}_{vol}) & \dot{\varepsilon}^{pl}_{xy} & \dot{\varepsilon}^{pl}_{xz}\\ \dot{\varepsilon}^{pl}_{yx} & (\dot{\varepsilon}^{pl}_{yy}-\dot{\varepsilon}^{pl}_{vol}) & \dot{\varepsilon}^{pl}_{yz}\\ \dot{\varepsilon}^{pl}_{zx} & \dot{\varepsilon}^{pl}_{zy} & (\dot{\varepsilon}^{pl}_{zz}-\dot{\varepsilon}^{pl}_{vol})\end{bmatrix}$$

The equivalent value of deviatoric plastic strain rate is then obtained from Equation 4.14:

$$\dot{\bar{e}}^{pl}=\sqrt{\frac{2}{3}[\dot{e}^{pl}]:[\dot{e}^{pl}]} \tag{4.14}$$

Now the rates of the equivalent plastic strains in tension and compression ($\dot{\bar{\varepsilon}}^{pl}_{t}$ and $\dot{\bar{\varepsilon}}^{pl}_{c}$) become:

$$\begin{aligned}\dot{\bar{\varepsilon}}^{pl}_{c}&=\dot{\bar{e}}^{pl}\\ \dot{\bar{\varepsilon}}^{pl}_{t}&=\frac{1}{\sigma_{t}}(\dot{\varepsilon}^{pl}_{vol}+\sigma_{c}\,\dot{\bar{e}}^{pl})\end{aligned} \tag{4.15}$$

Equation 4.15 means that the rate of deviatoric plastic strain ($\dot{\bar{e}}^{pl}$) controls the rate of the equivalent plastic strains in tension and compression ($\dot{\bar{\varepsilon}}^{pl}_{t}$ and $\dot{\bar{\varepsilon}}^{pl}_{c}$). Only one case exists in which these latter are independent, and this occurs when the volumetric plastic strain rate ($\dot{\varepsilon}^{pl}_{vol}$) causes only tensile equivalent plastic strain rate ($\dot{\bar{\varepsilon}}^{pl}_{t}$). To illustrate these relations, Figure 4.6 shows that under compressive loading conditions the rates of deviatoric ($\dot{\bar{e}}^{pl}$) and volumetric plastic strains ($\dot{\varepsilon}^{pl}_{vol}$) occur, resulting in the increase of

yield surfaces in tension and compression due to the rate of equivalent plastic strains in tension and compression ($\dot{\bar{\varepsilon}}_t^{pl}$ and $\dot{\bar{\varepsilon}}_c^{pl}$), Equation 4.15. At the opposite end of the loading spectrum, when subject to pure hydrostatic tension, the deviatoric plastic strain rate is zero, $\dot{\bar{e}}^{pl} = 0$. Thus, $\dot{\bar{\varepsilon}}_t^{pl}$ is a function of $\dot{\varepsilon}_{vol}^{pl}$ and $\dot{\bar{\varepsilon}}_c^{pl} = 0$. As a result, the compressive yield stress (σ_c) does not evolve, but the tensile yield stress (σ_t) does evolve and is updated according to ε_{vol}^{pl} as shown in Figure 4.7.

4.2.2 INVESTIGATION OF ABAQUS STANDARD CAST IRON MATERIAL MODEL

The behaviour of the above ABAQUS standard cast iron material was explored using the FE model of the gauge length sample taken from the back-vented brake disc as defined in sections 4.1.1. In this model (and all the anisotropic yield models that follow), the material was assumed to follow the measured MSSC's in tension and compression at each temperature with the initial yield point defined as the first deviation of linearity in these stress-strain curves. The plastic Poisson's ratio needed to determine the cast iron characteristics in tension was assumed to take the value of 0.039 [11]. The full details of material properties used are summarised in Appendix 3. To investigate the effects of cyclic loading, the top of the gauge length model was subjected to axial loads between 90 and 250 MPa in tension and compression respectively for two cycles at a constant temperature of 300 °C as shown in Figure 4.8.

The equivalent plastic strains in tension and compression predicted by ABAQUS at the top of the gauge length model were compared in Figure 4.9 to the tensile and compressive plastic strains from the experimental data at 300 °C defined in Figure 3.21. To obtain the experimental plastic strains, the total strain at the induced stress excluding the elastic strain was calculated in the first cycle. In the first tensile period, the predicted

tensile equivalent plastic strain increases according to the MSSC because the induced stress is beyond the tensile yield surface. At the same time, the compressive equivalent plastic strain increases due to the increase of the deviatoric plastic strain. This means that the cast iron yield surface is enlarged in both the tensile and compressive regions.

After the tensile load reaches the maximum value, the gauge length model was subjected to a compressive load up to 250 MPa in the first compression period. During this period, the compressive equivalent plastic strain remains constant until the induced stress increases beyond the current yield surface. In a similar way to the event in the first tension period, the tensile equivalent plastic strain increases before the end of the compressive load period due to the effect of the deviatoric plastic strain.

Due to the enlarged yield surface at the end of the first compression period, the tensile and compressive plastic strains are constant throughout the second cyclic load. In this cycle, the material behaves elastically since stresses remain within the yield surface ("elastic shakedown").

From this investigation, it can be concluded that the equivalent plastic strains in both tension and compression are used to indicate the plastic strain state of the FE model. In tension, the equivalent plastic strain is a function of the deviatoric and volumetric plastic strains. Conversely, the compressive equivalent plastic strain is controlled by the deviatoric plastic strain only. Therefore, if the FE model is subjected to cyclic uniaxial loads, both equivalent plastic strains increase and are higher than the expected value particularly for tensile loading. This contrasts with the experimental observation in which cast iron suffered cyclic softening in tension as a result of the progressive damage in the material from the opening of voids. This effect is not well represented by the

standard ABAQUS cast iron material model which predicts a higher rate of strain hardening in tension than in compression due to the contribution of the volumetric strain as shown in Equation 4.15.

4.3 STANDARD PLASTICITY MATERIAL MODEL

4.3.1 STANDARD ISOTROPIC STRAIN HARDENING MATERIAL MODEL

This material model is very commonly used for metal plasticity calculations because it uses only the single von Mises yield criterion, and the Drucker's and von Mises's postulates with associated flow rule for plastic behaviour. For isotropic hardening, if a material is subjected to load beyond the elastic region, the yield surface is expanded whilst its centre remains stationary on the σ_1-σ_2 plane as shown in Figure 4.10. In ABAQUS, the plastic strain increment, $d\{\varepsilon^{pl}\}$, can be calculated from Drucker's and von Mises's associated flow rule as follows:

$$d\{\varepsilon^{pl}\} = d\bar{\varepsilon}^{pl} \frac{3}{2} \frac{\{S\}}{\sigma_e} \tag{4.16}$$

where $d\bar{\varepsilon}^{pl}$ is the equivalent plastic strain increment, $\{S\}$ is the principal deviatoric stress matrix$\{S_1, S_2, S_3\}$ and σ_e is the von Mises stress. This plastic characteristic requires that the von Mises equivalent stress is equal to the yield stress defined by a uniaxial plastic strain-stress relation of the form:

$$\sigma_e = \sigma_o = f(\bar{\varepsilon}^{pl}, \text{temperature}) \tag{4.17}$$

The expression above shows that the yield stress (σ_o) is a function of the equivalent plastic strain, ($\bar{\varepsilon}^{pl}$), and temperature, which are determined from the element values at the current load, using a linear interpolation from the data input between plastic strain and temperature as shown in Appendix 3.

4.3.2 USER-DEVELOPED SUBROUTINE ISOTROPIC STRAIN HARDENING MATERIAL MODEL

The ABAQUS standard program has interfaces that allow new material models, including the ABAQUS cast iron model, to be added using the Fortran programming language. To implement a material model, the Fortran based subroutine requires users to assign the stress and strain states, the Jacobian matrix of the constitutive model and so on. The following section describes a procedure used by the present author to create a general isotropic strain hardening material model which used the von Mises yield criterion with temperature dependence. Plastic strain generated at element data was used to determine the temperature dependent yield stress at current load condition using a linear interpolation from the data input between stress and plastic strain at various temperature conditions shown in Appendix 3. The Fortran coding for this user-developed material model is given in Appendix 4. By comparing the results of applying this model with the standard ABAQUS isotropic hardening material model, confidence in the accuracy and robustness of the user-developed subroutine was generated.

Figure 4.11 shows the flowchart for the material model with temperature dependence when the stress state is in the elastic region. Comparison between the current yield stress in tension or compression and the von Mises stress from element data is the key to determine whether the stress state is beyond the elastic region. Figure 4.12 shows the flowchart when the von Mises stress from element data is greater than the current yield stress. Returning the stresses to the yield surface is achieved using the backward Euler method [61].

To demonstrate this method, Figure 4.13 shows the first prediction due to the strain increment $\{\Delta\varepsilon\}$, resulting in the increase of the stress state from A to B, i.e.

$$\{\sigma_B\} = [D]\{\Delta\varepsilon\} + \{\sigma_A\} \tag{4.18}$$

where [D] is the elastic stiffness matrix defined in Figure 4.11.

Since the stress state $\{\sigma_B\}$ at B is located outside the yield surface, the yield function (F) is more than zero and the correction of the stress state from B to C is essential as shown in Figure 4.14. At this stage, the plastic strain increment $\{\Delta\varepsilon^{pl}\}$can be calculated as follows:

$$\{\Delta\varepsilon^{pl}\} = \Delta\lambda\left(\frac{\partial F}{\partial\{\sigma\}}\right) \tag{4.19}$$

where $\Delta\lambda$ is the plastic strain multiplier. The yield function (F) is a function of the current yield surface (σ_o) and von Mises stress (σ_e) defined as

$$F = \sigma_e - \sigma_o(\bar{\varepsilon}^{pl}) \tag{4.20}$$

As a result of reducing the stress state using the backward Euler procedure, the stress state at C, $\{\sigma_C\}$, becomes:

$$\{\sigma_C\} = \{\sigma_B\} - [D]\{\Delta\varepsilon^{pl}\} \tag{4.21}$$

Applying Equation 4.19 yields :

$$\{\sigma_C\} = \{\sigma_B\} - \Delta\lambda_B[D]\frac{\partial F}{\partial\{\sigma\}} \tag{4.22}$$

or

$$\{\Delta\sigma_C\} = \{\sigma_C\} - \{\sigma_B\} = -\Delta\lambda_B[D]\frac{\partial F}{\partial\{\sigma\}} \tag{4.23}$$

From the von Mises yield criterion [61], the plastic strain multiplier ($\Delta\lambda$) is equal to the equivalent plastic strain $\Delta\bar{\varepsilon}^{pl}$calculated from $\sqrt{\frac{2}{3}\{\Delta\varepsilon^{pl}\}:\{\Delta\varepsilon^{pl}\}}$.

According to Equation 4.22, the plastic strain multiplier,$\Delta\lambda_B$, at B can be determined by firstly using the Taylor expansion as shown in Equation 4.24:

$$\Delta F = F_C - F_B = \frac{\partial F}{\partial \{\sigma\}}^T \{\Delta\sigma\} + \frac{\partial F}{\partial \sigma_o}\frac{\partial \sigma_o}{\partial \bar{\varepsilon}^{pl}}\Delta\bar{\varepsilon}^{pl} = 0 \tag{4.24}$$

or

$$F_C = F_B + \frac{\partial F}{\partial \{\sigma\}}^T \{\Delta\sigma_C\} + \frac{\partial F}{\partial \sigma_o}\frac{\partial \sigma_o}{\partial \bar{\varepsilon}^{pl}}\Delta\bar{\varepsilon}^{pl} \tag{4.25}$$

With $\frac{\partial F}{\partial \sigma_o} = -1$ from Equation 4.20, $\Delta\lambda = \Delta\bar{\varepsilon}^{pl}$, $F_C = 0$ and $\{\Delta\sigma_C\}$ from Equation 4.23, the manipulation of Equation 4.25 yields the value of the plastic strain multiplier ($\Delta\lambda_B$) at B:

$$\Delta\lambda_B = \frac{F_B}{\frac{\partial F}{\partial \{\sigma\}}^T [D] \frac{\partial F}{\partial \{\sigma\}} + \frac{\partial \sigma_o}{\partial \{\bar{\varepsilon}^{pl}\}}} \tag{4.26}$$

From the flowchart in Figure 4.12, the new yield surface function at C is again checked. If F_C is greater than zero, the second correction is applied to reduce the stress state to the next yield surface as shown in the feedback loop of Figure 4.12 and in the σ_1-σ_2 plane of Figure 4.15. The stress state at D, $\{\sigma_D\}$, and the plastic strain multiplier at point C, $\Delta\lambda_C$, are obtained using a similar derivation as shown in Equations 4.27 and 4.28:

$$\{\sigma_D\} = \{\sigma_C\} - \Delta\lambda_C [D] \frac{\partial F}{\partial \{\sigma\}}, \text{ at C} \tag{4.27}$$

$$\Delta\lambda_C = \frac{F_C}{\frac{\partial F}{\partial \{\sigma\}}^T [D] \frac{\partial F}{\partial \{\sigma\}} + \frac{\partial \sigma_o}{\partial \{\bar{\varepsilon}^{pl}\}}} \tag{4.28}$$

The back loop procedure should be repeated until the current yield surface function is reduced to zero. After the yield criterion is satisfied, the Jacobian matrix $[D_t]$ is updated as specified in the flow chart of Figure 4.12.

To derive this new Jacobian matrix, the stress state increment $\{\Delta\sigma\}$ and the generalised plastic strain multiplier ($\Delta\lambda$) are introduced. Equation 4.29 shows that the stress state increment $\{\Delta\sigma\}$ can be derived from the stiffness matrix [D], the total strain increment $\{\Delta\varepsilon\}$ and the plastic strain increment $\{\Delta\varepsilon^{pl}\}$:

$$\{\Delta\sigma\} = [D][\{\Delta\varepsilon\} - \{\Delta\varepsilon^{pl}\}] \tag{4.29}$$

Replacing $\{\Delta\varepsilon^{pl}\}$ from Equation 4.19 gives:

$$\{\Delta\sigma\} = [D][\{\Delta\varepsilon\} - \Delta\lambda\frac{\partial F}{\partial\{\sigma\}}] \tag{4.30}$$

The generalised plastic strain multiplier ($\Delta\lambda$) can be calculated from the yield surface increment (ΔF) in Equation 4.24 by substituting $\Delta\bar{\varepsilon}^{pl} = \Delta\lambda$ as shown in Equation 4.31:

$$\Delta F = \frac{\partial F}{\partial\{\sigma\}}^{T}\{\Delta\sigma\} + \frac{\partial F}{\partial\sigma_o}\frac{\partial\sigma_o}{\partial\bar{\varepsilon}^{pl}}\Delta\lambda = 0 \tag{4.31}$$

Replacing $\frac{\partial F}{\partial\sigma_o} = -1$ and substituting Equation 4.30 into Equation 4.31 give:

$$\frac{\partial F}{\partial\{\sigma\}}^{T}\left([D][\{\Delta\varepsilon\} - \Delta\lambda\frac{\partial F}{\partial\{\sigma\}}]\right) - \frac{\partial\sigma_o}{\partial\bar{\varepsilon}^{pl}}\Delta\lambda = 0 \tag{4.32}$$

Thus,

$$\Delta\lambda = \frac{\frac{\partial F}{\partial\{\sigma\}}^{T}[D]\{\Delta\varepsilon\}}{\frac{\partial F}{\partial\{\sigma\}}^{T}[D]\frac{\partial F}{\partial\{\sigma\}} + \frac{\partial\sigma_o}{\partial\{\bar{\varepsilon}^{pl}\}}} \tag{4.33}$$

Applying ($\Delta\lambda$) from Equation 4.33 into Equation 4.30 gives:

$$\{\Delta\sigma\} = [D]\left[\{\Delta\varepsilon\} - \left(\frac{\frac{\partial F}{\partial\{\sigma\}}^{T}[D]\{\Delta\varepsilon\}}{\frac{\partial F}{\partial\{\sigma\}}^{T}[D]\frac{\partial F}{\partial\{\sigma\}} + \frac{\partial\sigma_o}{\partial\{\bar{\varepsilon}^{pl}\}}}\right)\frac{\partial F}{\partial\{\sigma\}}\right] \tag{4.34}$$

Manipulating Equation 4.34 gives:

$$\{\Delta\sigma\} = [D]\left[[I] - \left(\frac{\frac{\partial F}{\partial\{\sigma\}}\frac{\partial F}{\partial\{\sigma\}}^{T}[D]}{\frac{\partial F}{\partial\{\sigma\}}^{T}[D]\frac{\partial F}{\partial\{\sigma\}} + \frac{\partial\sigma_o}{\partial\{\bar{\varepsilon}^{pl}\}}}\right)\right]\{\Delta\varepsilon\} \tag{4.35}$$

Therefore, the new Jacobian matrix $[D_t]$ is:

$$[D_t] = [D]\left[[I] - \left(\frac{\frac{\partial F}{\partial\{\sigma\}}\frac{\partial F}{\partial\{\sigma\}}^{T}[D]}{\frac{\partial F}{\partial\{\sigma\}}^{T}[D]\frac{\partial F}{\partial\{\sigma\}} + \frac{\partial\sigma_o}{\partial\{\bar{\varepsilon}^{pl}\}}}\right)\right] \tag{4.36}$$

4.3.3 INVESTIGATION OF ISOTROPIC HARDENING MATERIAL MODELS

The purpose of this section is to investigate and validate the isotropic hardening material model developed by the author using the above theory. To this end, comparison between the standard and user-developed subroutine isotropic material models was carried out using the FE model defined in Section 4.1.1. Both material models used the monotonic stress-strain curve in tension from the cast iron material tests, Chapter 3. The full details of material properties used are summarised in Appendix 3. The top of the gauge length was subjected to a tensile load up to 90 MPa at a constant temperature of 300 °C.

Figure 4.16 shows the response of these material models compared to the monotonic stress-strain input data. It can be seen that both material models after yielding follow exactly the experimental monotonic curve. Thus the user-developed isotropic hardening material model has been validated against the standard ABAQUS material model.

4.4 USER-DEVELOPED SUBROUTINE MATERIAL MODEL FOR CAST IRON

4.4.1 METHODOLOGY

According to the current investigation of the ABAQUS standard cast iron material model reported in section 4.2.2 of this thesis, the main deficiency of this model is that the boundary of the yield surface is enlarged in both tension and compression simultaneously for uniaxial loads. Therefore, the objective of this section is to develop a material model for cast iron with temperature dependence in which tensile plastic strain was assumed to be independent of the compressive plastic strain. In other words, the relation between the stress and plastic strain should comply with the monotonic stress-strain curves in tension and compression independently. Also there seems to be little justification for using a Rankine yield criterion to control tensile yield in the ABAQUS cast iron material model. The user-developed routine therefore used a von Mises criterion in both tension and compression.

Using a similar approach to that used to develop the preceding isotropic hardening model with temperature dependence, it is possible to implement a material model for cast iron using the hydrostatic pressure stress to separate the tensile and compressive regions as shown in Figure 4.17. The yield stress with temperature dependence is determined from element values using a linear interpolation from the stress and plastic strain data as shown in Appendix 3. The flow charts in Figures 4.18-4.20 show the procedure used to create a material model that complies with the required assumptions for cast iron. However, the solution from this material model in some cases did not converge. For example, as shown in Figure 4.21, the stress state at position A is increased to position B that has a positive hydrostatic pressure due to the strain increment. At this stage, the reduction of the stress state using the backward Euler

procedure is required until the stress state is corrected to position D (the second compressive yield surface). If the FE model is subjected to another load, the stress state is increased to position E that has a negative hydrostatic pressure. The second correction is needed to reduce the stress state at position E. However, the solution cannot converge because the calculation requires many iterations to reduce the stress state at position E to the new tensile yield surface at position F (the first tensile yield surface). This problem is thought to be due to the abrupt transition between the tensile and compressive regions as indicated in Figure 4.17. Therefore, a transition zone that connects the compressive and the tensile yield surfaces must be developed as described below.

4.4.2 INVESTIGATION OF MATERIAL MODELS FOR CAST IRON

To obtain the most effective material model for cast iron, various transition zones of hydrostatic pressure in the tensile region, i.e. 10, 30 and 100 MPa, were considered as shown in Figure 4.22. Material properties used in these models are summarised in Appendix 3. The specimen gauge length model with these different transition zones was subjected to a uniaxial tensile load of 86.25 MPa at 20 °C, which should produce a plastic strain of 2.6502E-4 according to the room temperature monotonic stress-strain curve. The results, shown in Table 4.1, reveal that the equivalent plastic strain for 10 MPa hydrostatic pressure transition zone is exactly equal to the required value. However, the yield surface for 10 MPa hydrostatic pressure transition zone changes rapidly between tension and compression in comparison to that for 30 and 100 MPa which may cause convergence problems. In addition, the equivalent plastic strains predicted for the models with 10 and 30 MPa transition zones are not significantly different. Therefore, it can be concluded that the user-developed material model for cast iron should have a hydrostatic pressure of 30 MPa for the transition zone between

tension and compression as a compromise between accuracy and numerical robustness. The Fortran coding for this final user-developed model for cast iron is given in Appendix 5.

To investigate further the user-developed subroutine, a schematic load pattern was applied to the specimen gauge length model shown in Figure 4.8 during which the temperature of 300 °C remains constant. In this investigation, the equivalent plastic strain histories in tension and compression at the top of the gauge length model predicted by the user-developed subroutine cast iron material model were compared to those from the monotonic plastic strain-stress curve at the same temperature. The results from Figure 4.23 reveal that the user-developed subroutine predicted tensile plastic strains are initially lower than the monotonic plastic strain at the same stress state due to the 30 MPa transition zone. However, the predicted compressive plastic strain is independent of the tensile plastic strain which fulfils the required assumption. During the onset of the first compression load, no compressive plastic strain occurs until the stress state rises beyond the compressive yield surface. The model then predicts the same value as given by the monotonic plastic stress-strain curve in compression that was calculated from the total strain at the induced stress excluding the elastic strain. No further tensile plastic strain occurs during this period and there is therefore no increase in tension yield stress (no cyclic strain hardening). This then is in contrast to the results from the standard ABAQUS cast iron model for the same cyclic load shown in Figure 4.9. Thus, by making yielding in tension independent of that in compression (and vice versa), numerical results are much closer to the measured MSSC's for cast iron which are themselves close to the equivalent CSSC's (see Figure 3.25).

Transition zone hydrostatic pressure (MPa)	Equivalent plastic strain in tension
10	2.65E-4
30	2.52E-4
100	0.0

Table 4.1: Comparison of equivalent plastic strain for various hydrostatic pressure transition zones

4.5 SUMMARY

4.5.1 STANDARD ABAQUS CAST IRON MATERIAL MODEL

Rankine and von Mises yield surfaces together with associated potential functions were used to create the standard ABAQUS cast iron material model that has different yield stresses in tension and compression. Moreover, tensile equivalent plastic strain is related to compressive equivalent plastic strain due to the effect of the deviatoric plastic strain, resulting in the simultaneous enlargement of the yield surface in tension and compression. Therefore, when a specimen is subjected to uniaxial cyclic loads, strain hardening occurs in both tension and compression even though experimental evidence suggests that cyclic strain softening occurs in tension [16].

4.5.2 USER-DEVELOPED SUBROUTINE MATERIAL MODEL

The assumption of independent plastic strain increments in tension and compression was suggested to improve the features of the standard ABAQUS cast iron material model. Moreover a von Mises yield criterion, that was implemented in both tension and compression with temperature dependence, is different from Josefson's yield criterion that used a modified von Mises yield criterion with temperature independence [44]. The

Rankine criterion used by the standard ABAQUS material model in tension was assumed to be based on the known fracture characteristics of cast iron rather than on the yield behaviour of a voided ductile solid under tension. The results of simple case study investigations reveal that the user-developed cast iron model with a transition zone between tension and compression over a hydrostatic pressure of 30 MPa can be used to accurately simulate the basic response of cast iron under cyclic loads in both tension and compression.

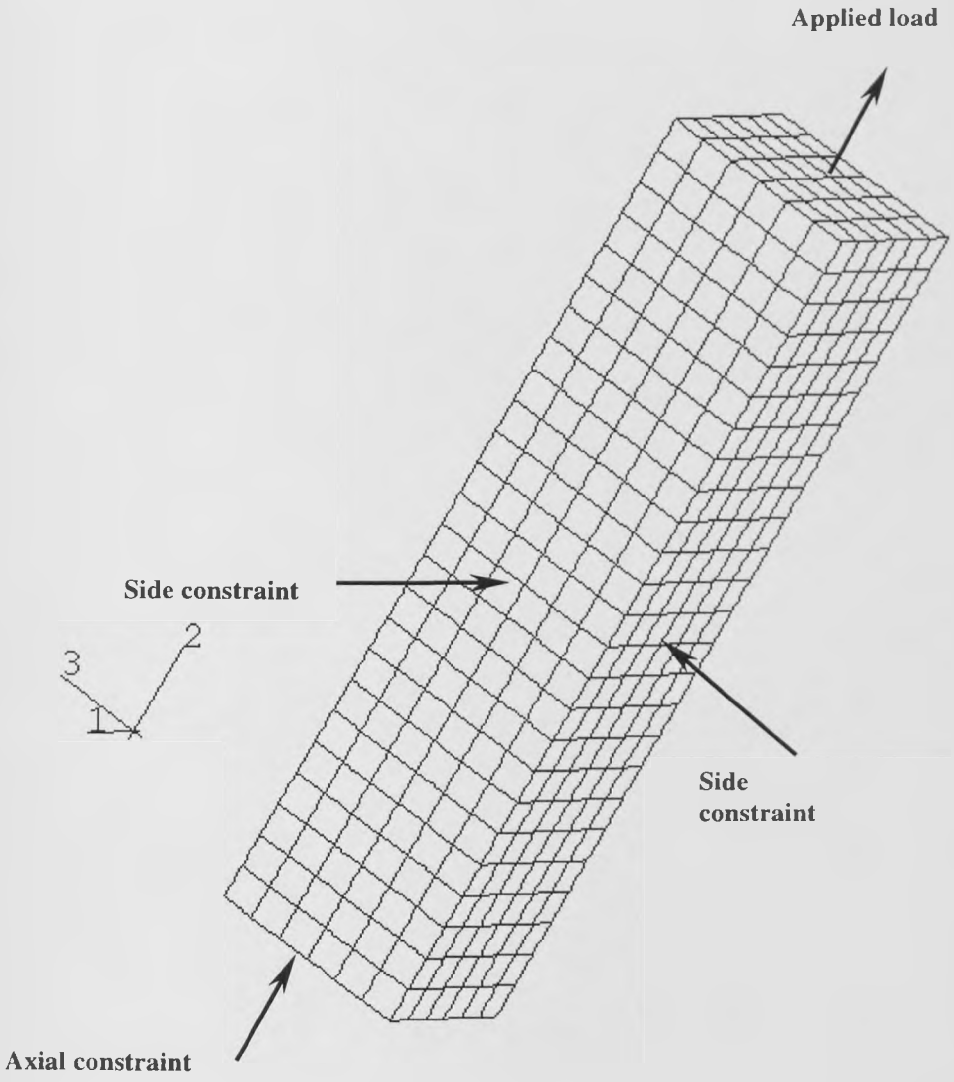

Figure 4.1: Gauge length model

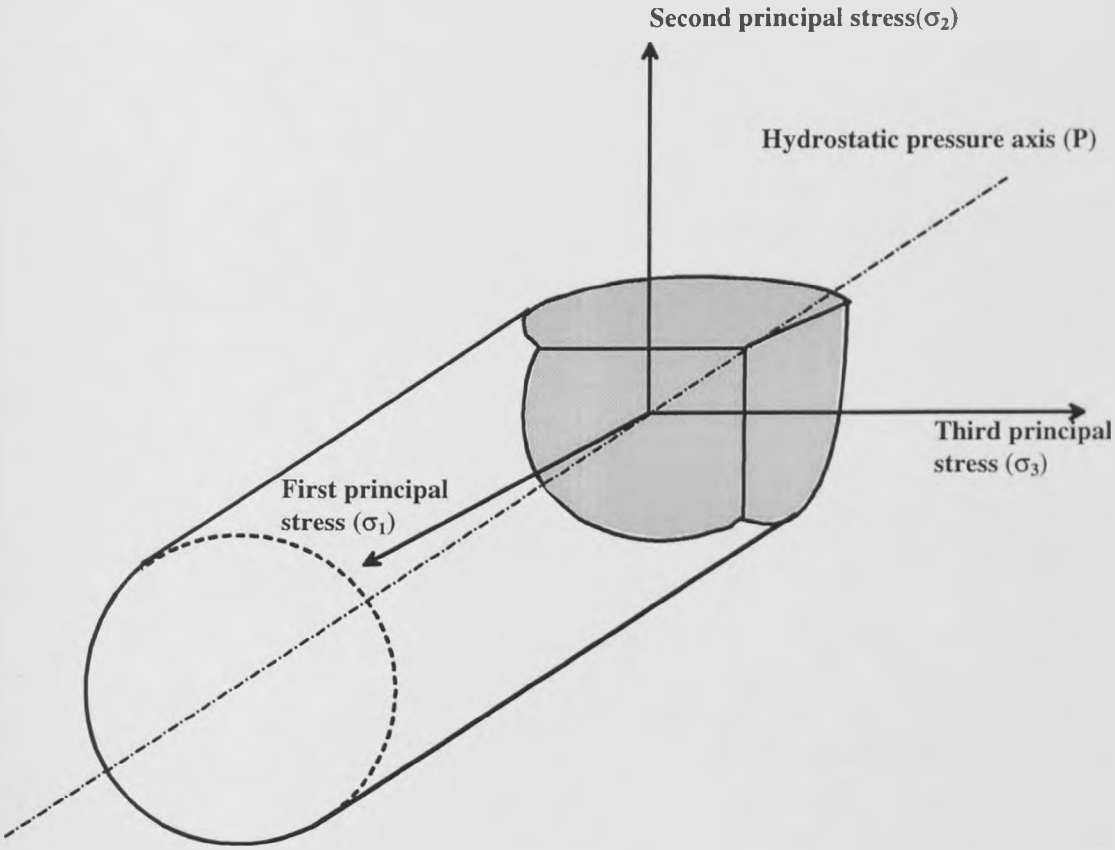

Figure 4.2: Schematic of the ABAQUS standard cast iron yield surface in principal stress space [41]

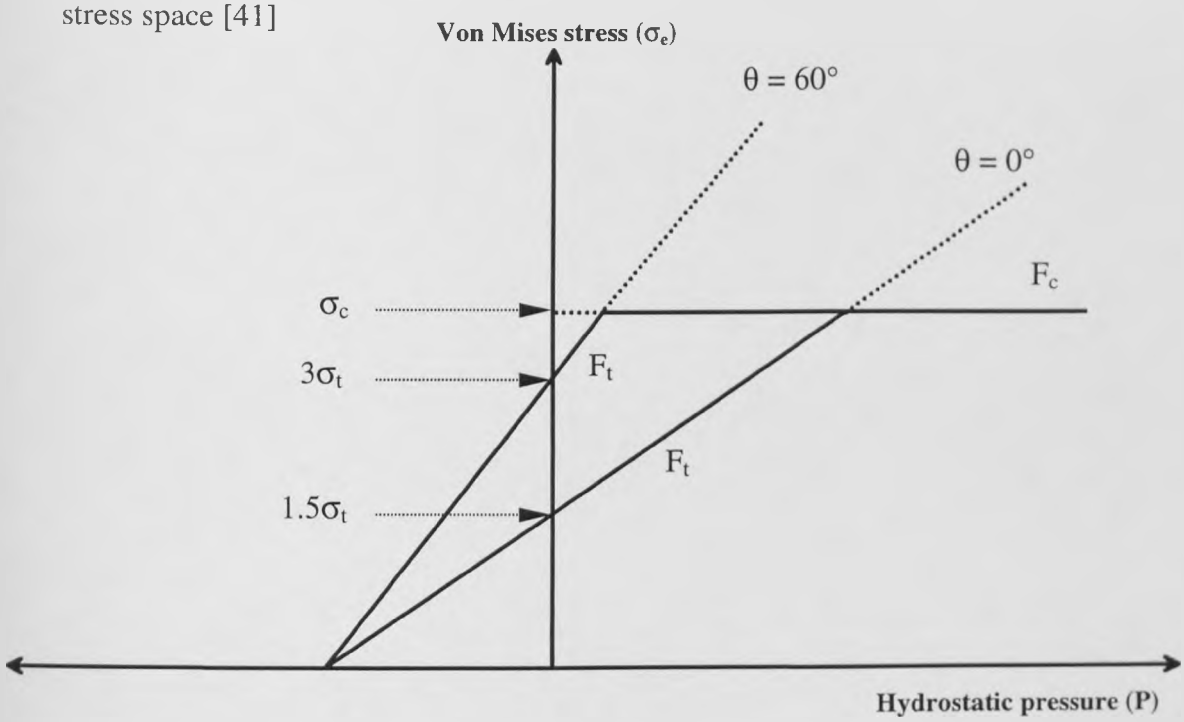

Figure 4.3: Schematic of the yield function in the plane of von Mises stress (σ_e) against the hydrostatic pressure (P)

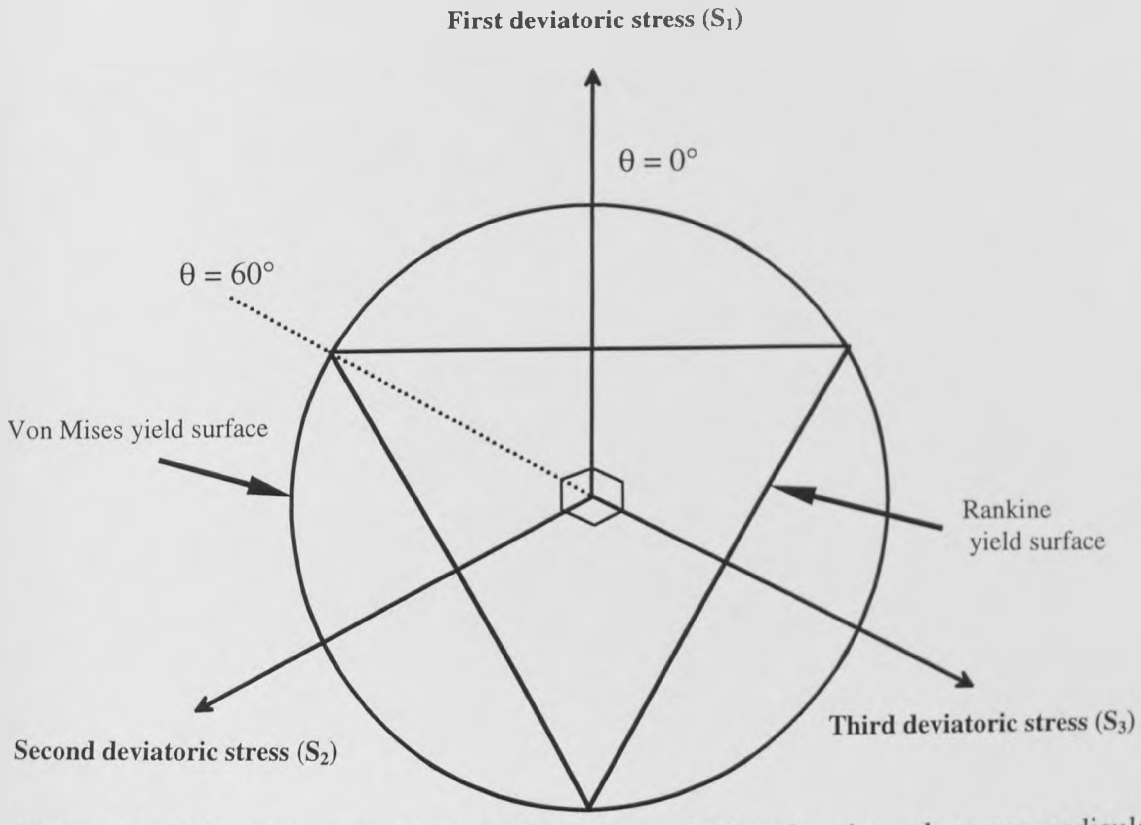

Figure 4.4: Schematic of the ABAQUS cast iron yield surface in a plane perpendicular to the hydrostatic stress axis

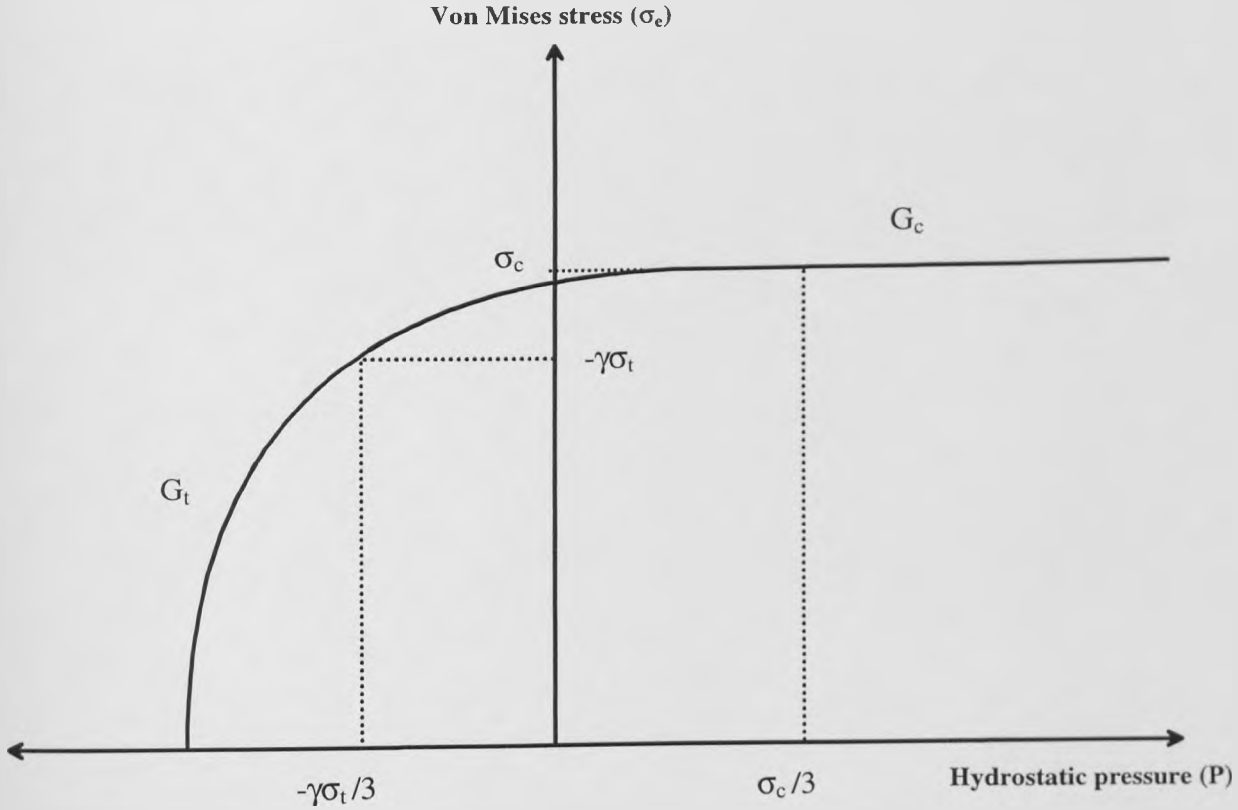

Figure 4.5: Schematic of the flow potentials in the plane of von Mises stress (σ_e) against hydrostatic pressure (P)

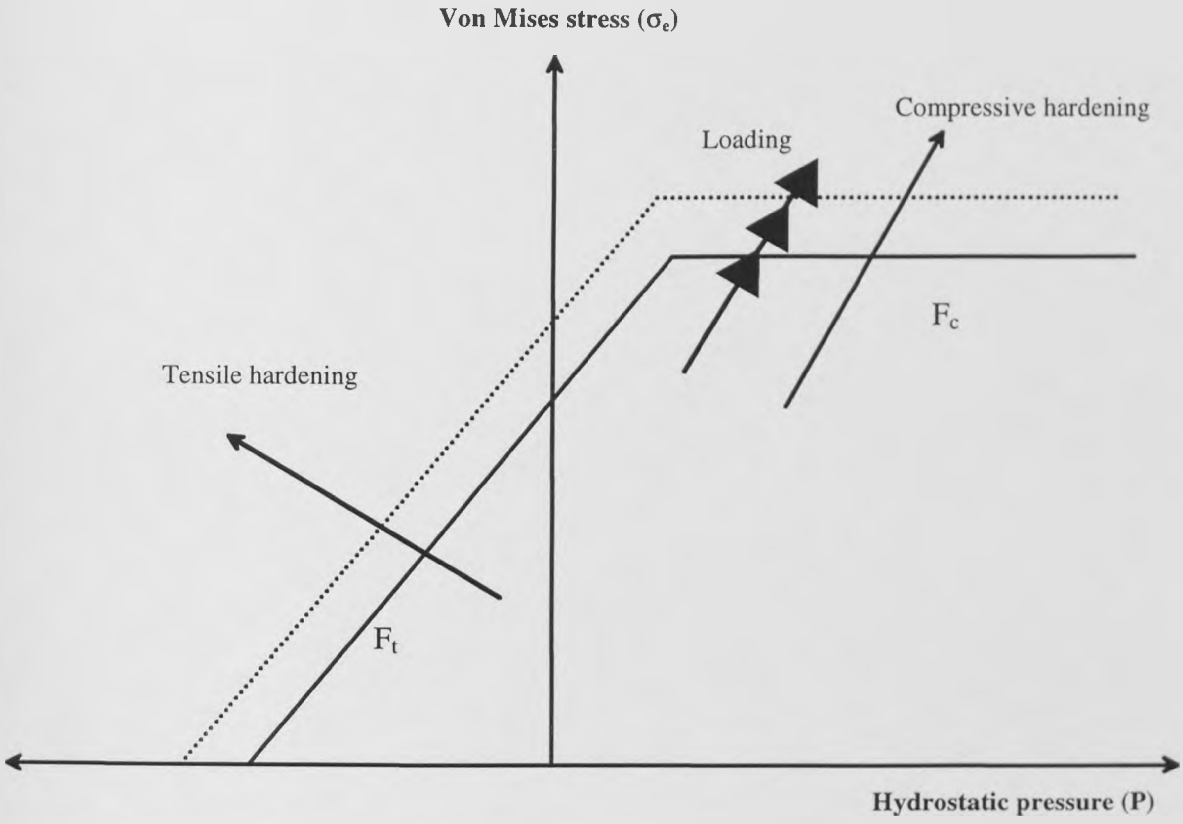

Figure 4.6: Yield surface enlargement due to the rate of deviatoric plastic strain ($\dot{\bar{e}}^{pl}$)

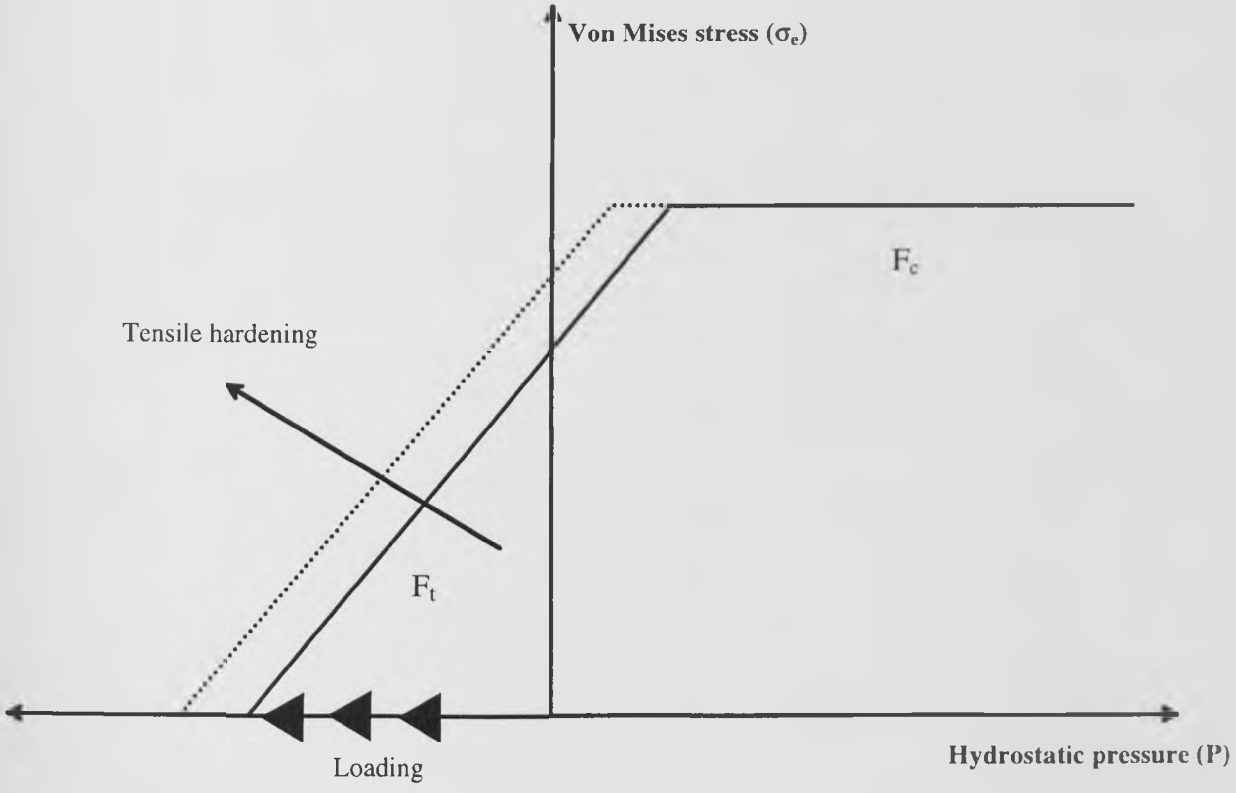

Figure 4.7: Yield surface enlargement due to the rate of volumetric plastic strain ($\dot{\varepsilon}^{pl}_{vol}$)

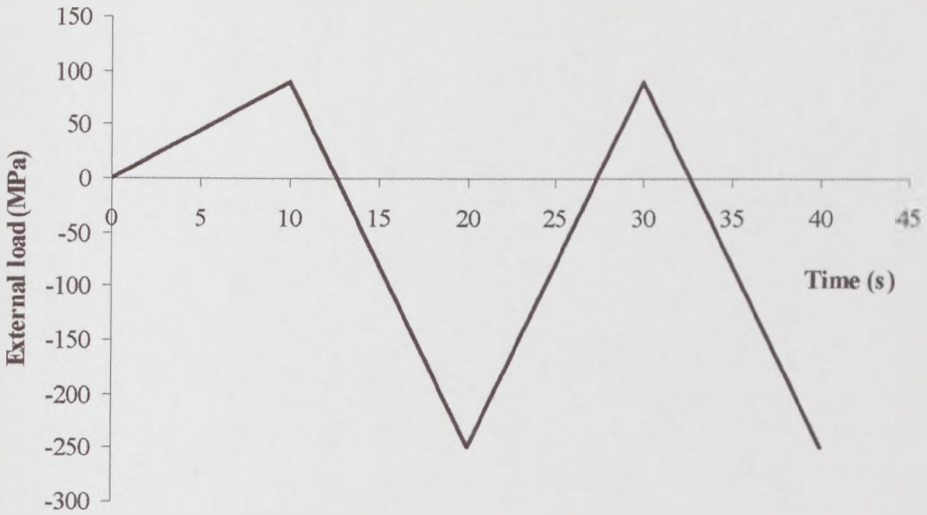

Figure 4.8: Cyclic external load used in FE model of specimen gauge length

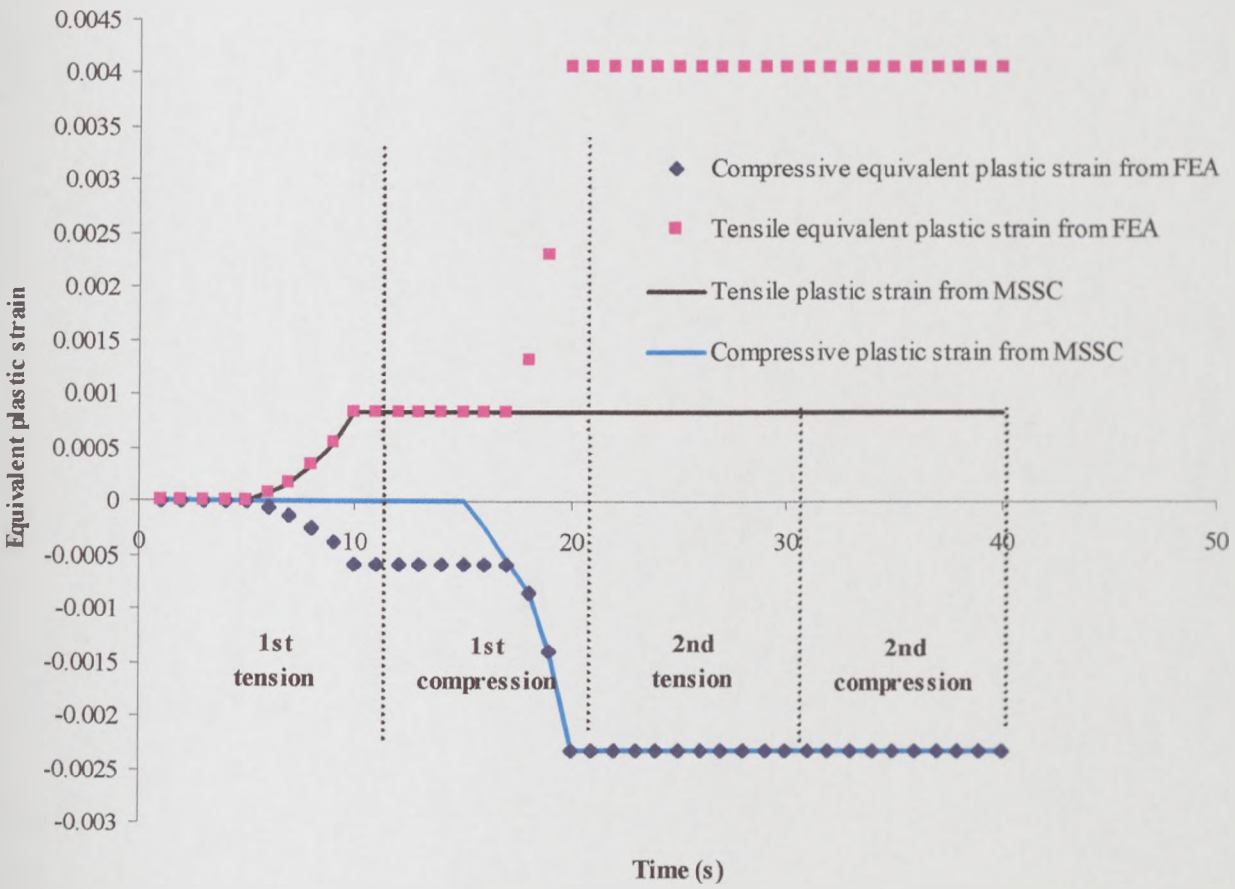

Figure 4.9: Tensile and compressive plastic strain response for ABAQUS standard cast iron material model

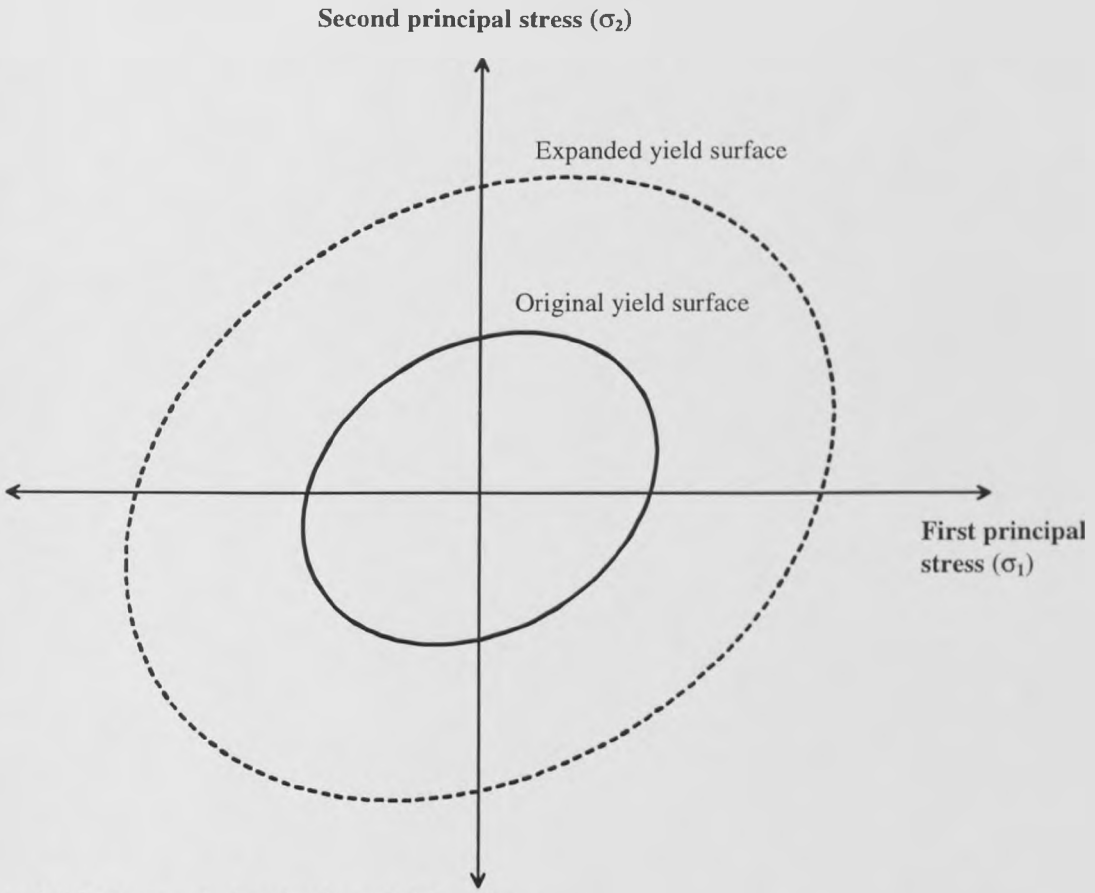

Figure 4.10: Isotropic hardening yield surface

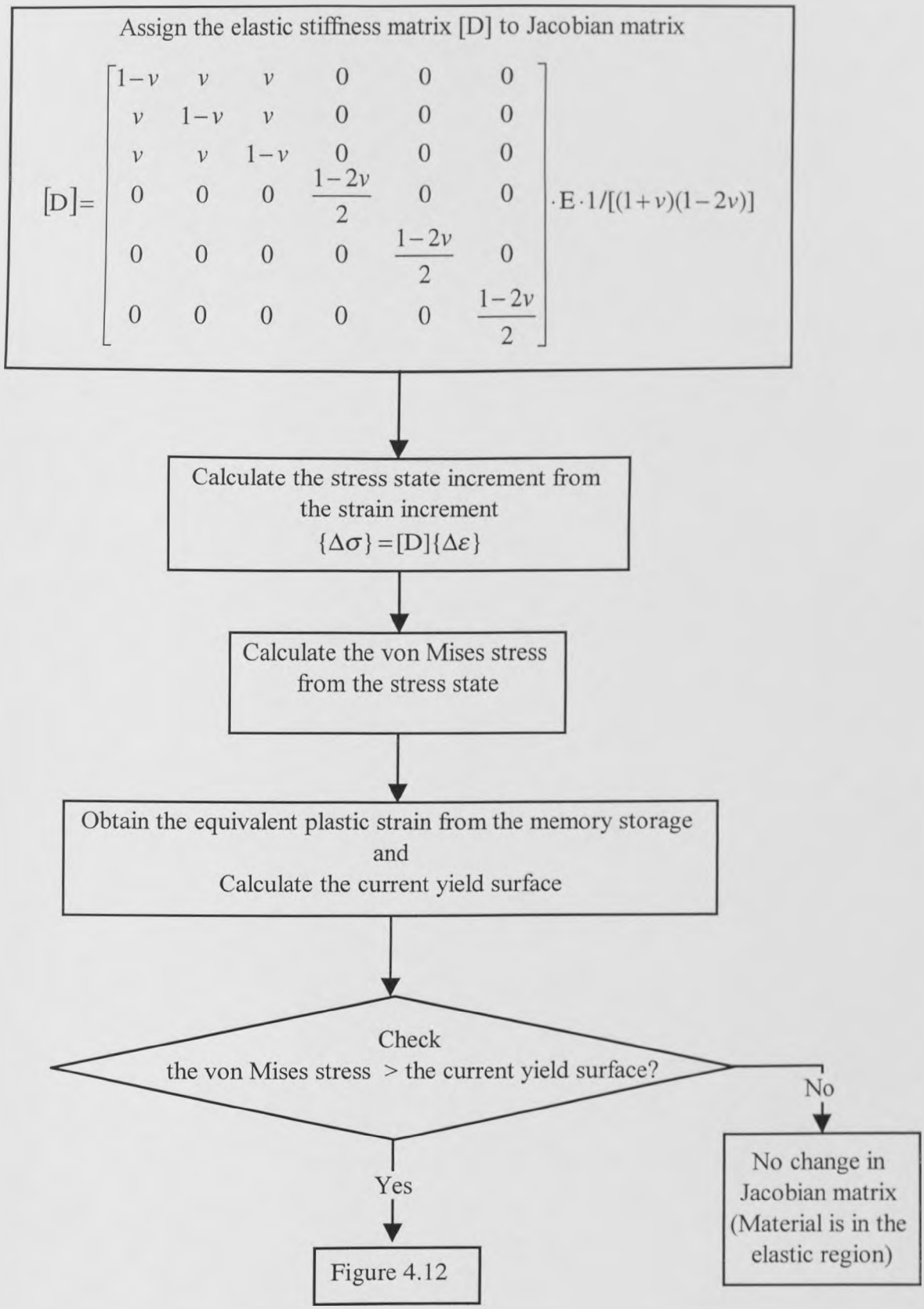

Figure 4.11: Flow chart for isotropic hardening material model in the elastic region

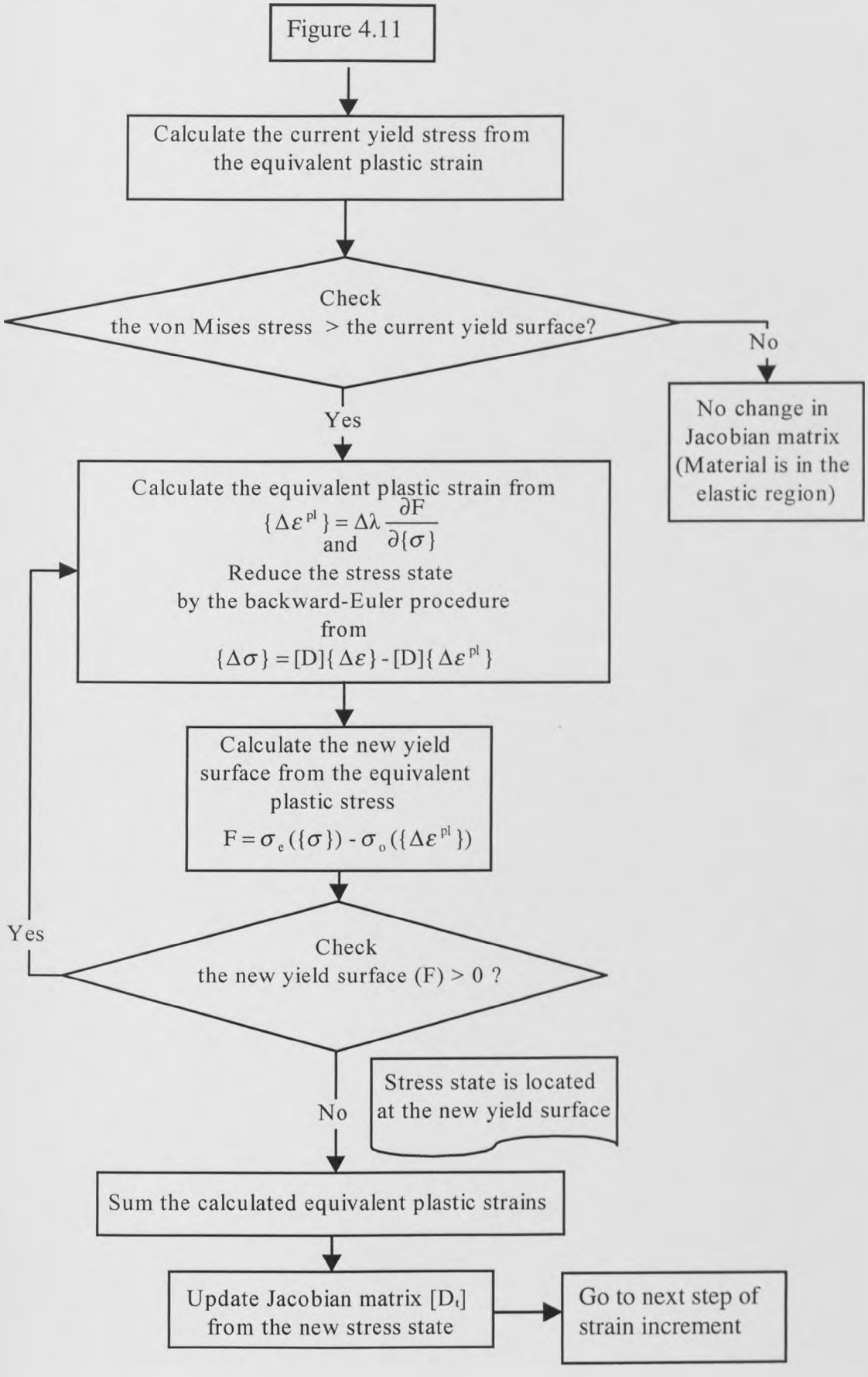

Figure 4.12: Flow chart for isotropic hardening material model in the plastic region

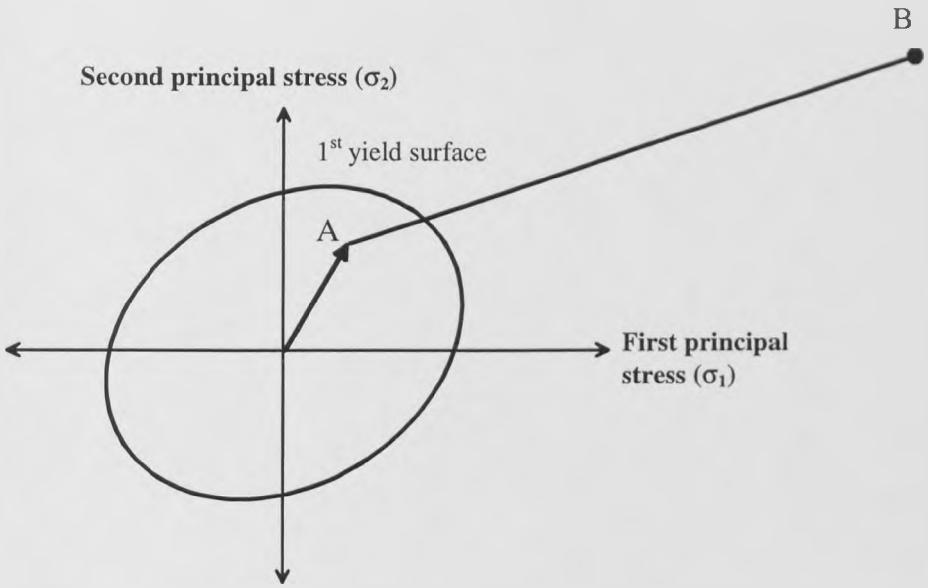

Figure 4.13: Prediction of the stress state from initial elastic analysis

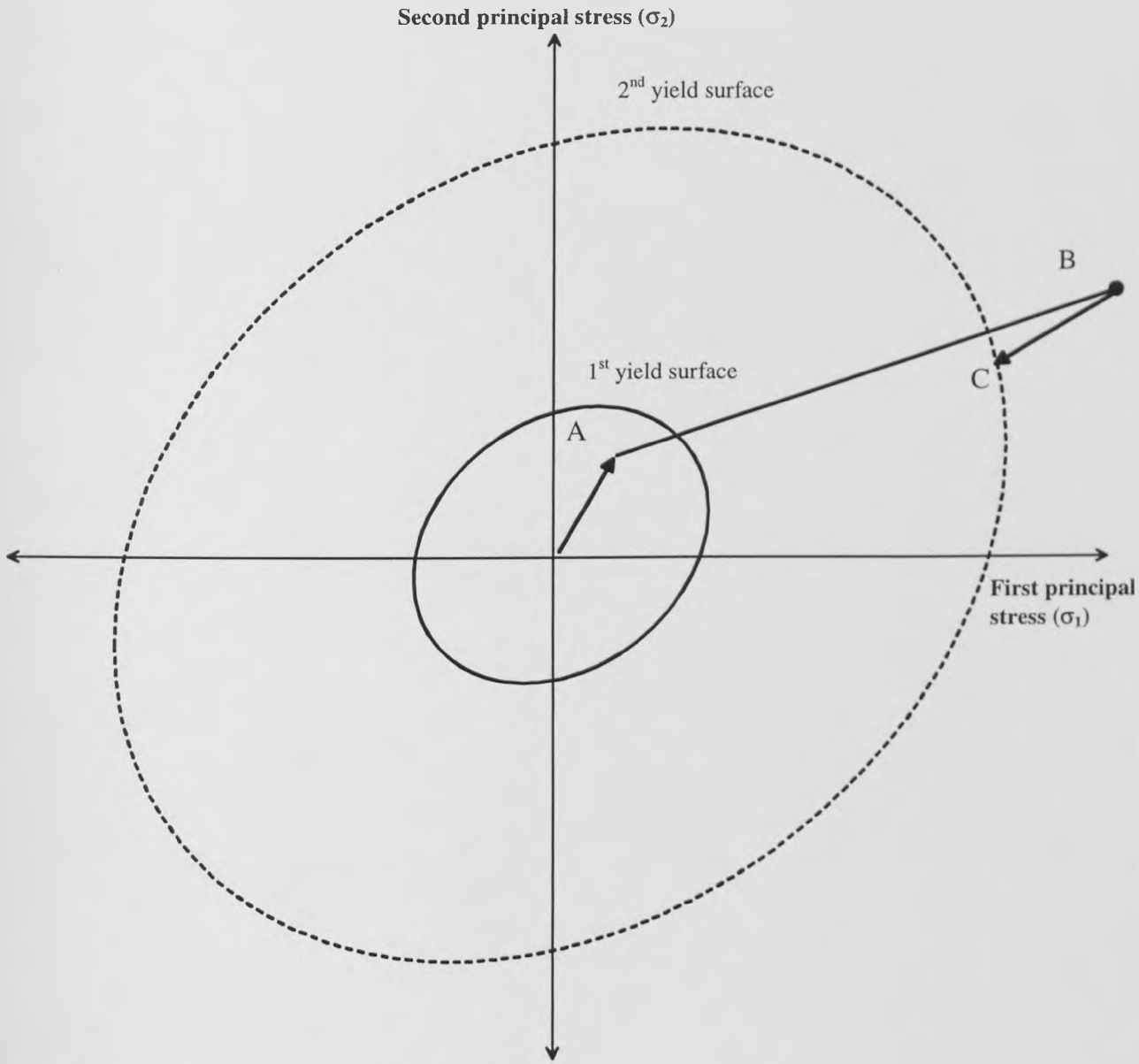

Figure 4.14: First correction of the stress state

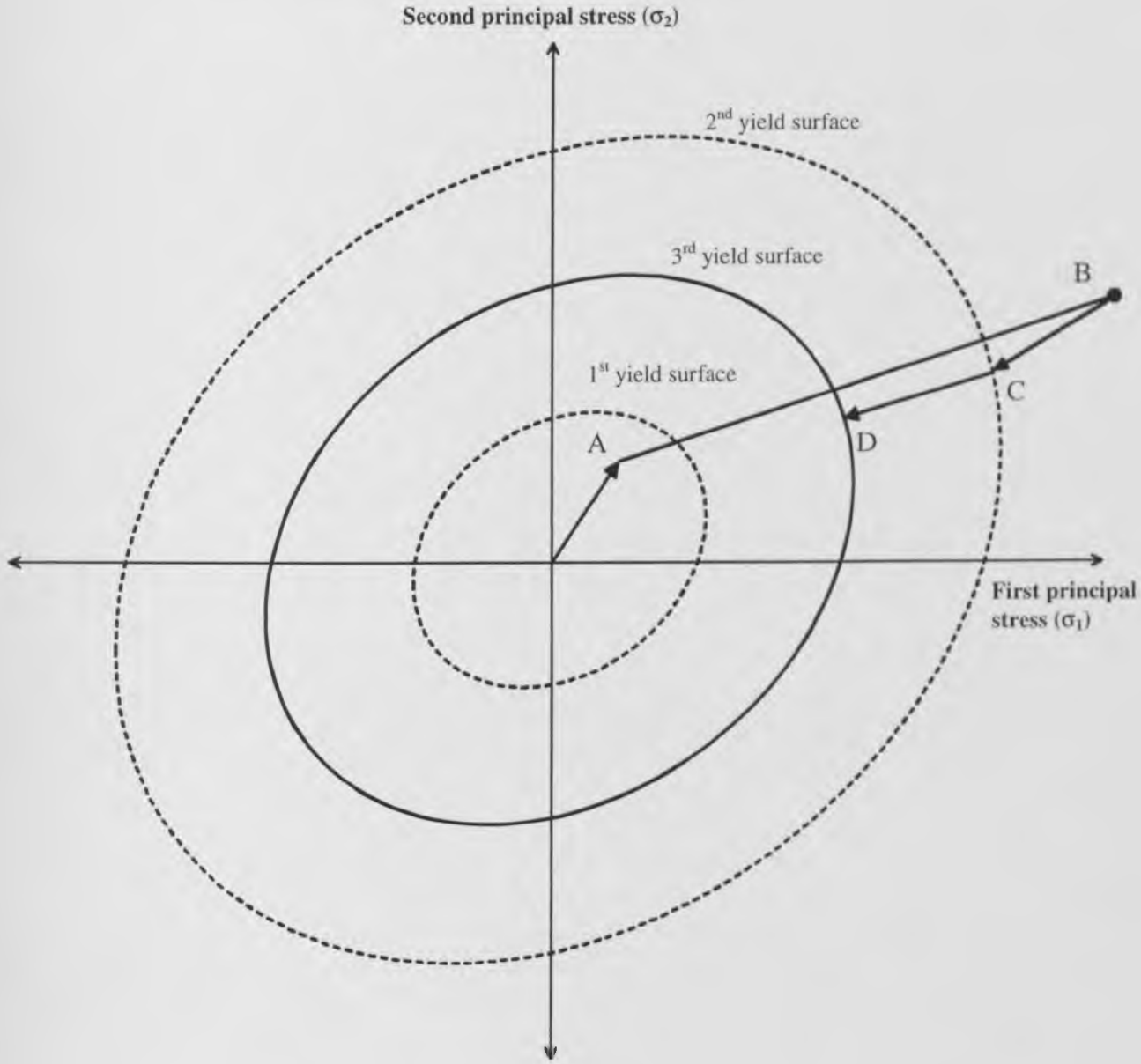

Figure 4.15: Second correction of the stress state

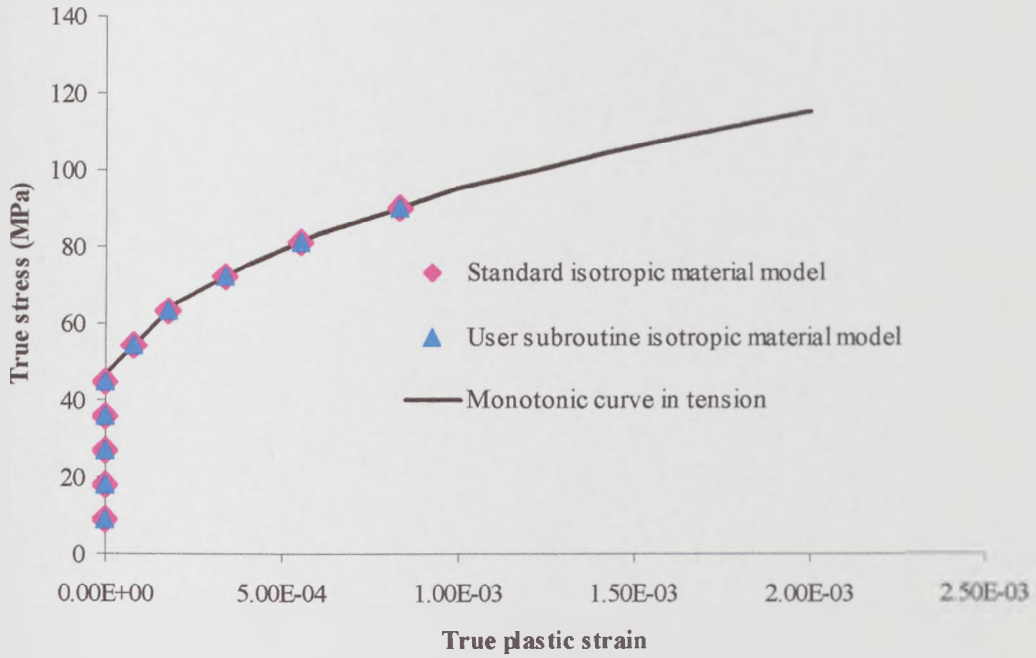

Figure 4.16: Plastic strain and stress response from gauge length models

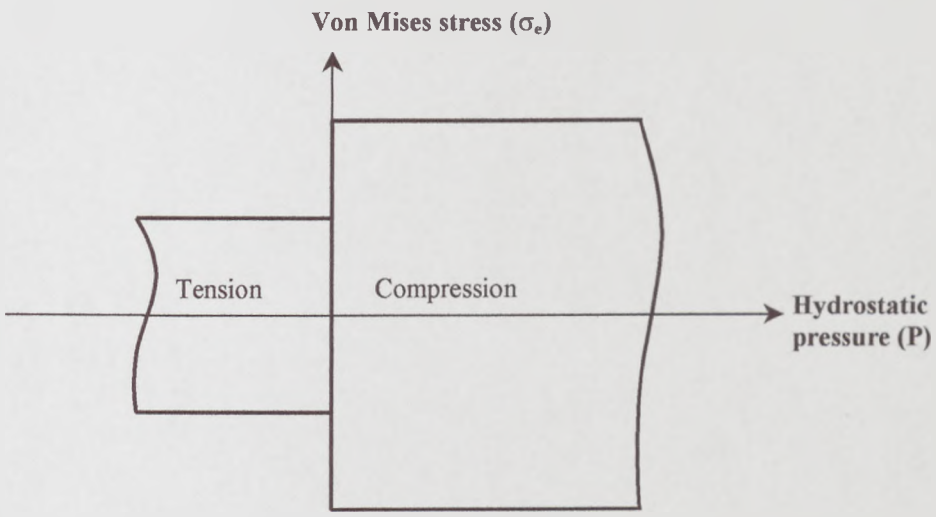

Figure 4.17: User-developed subroutine material model for cast iron without transition zone

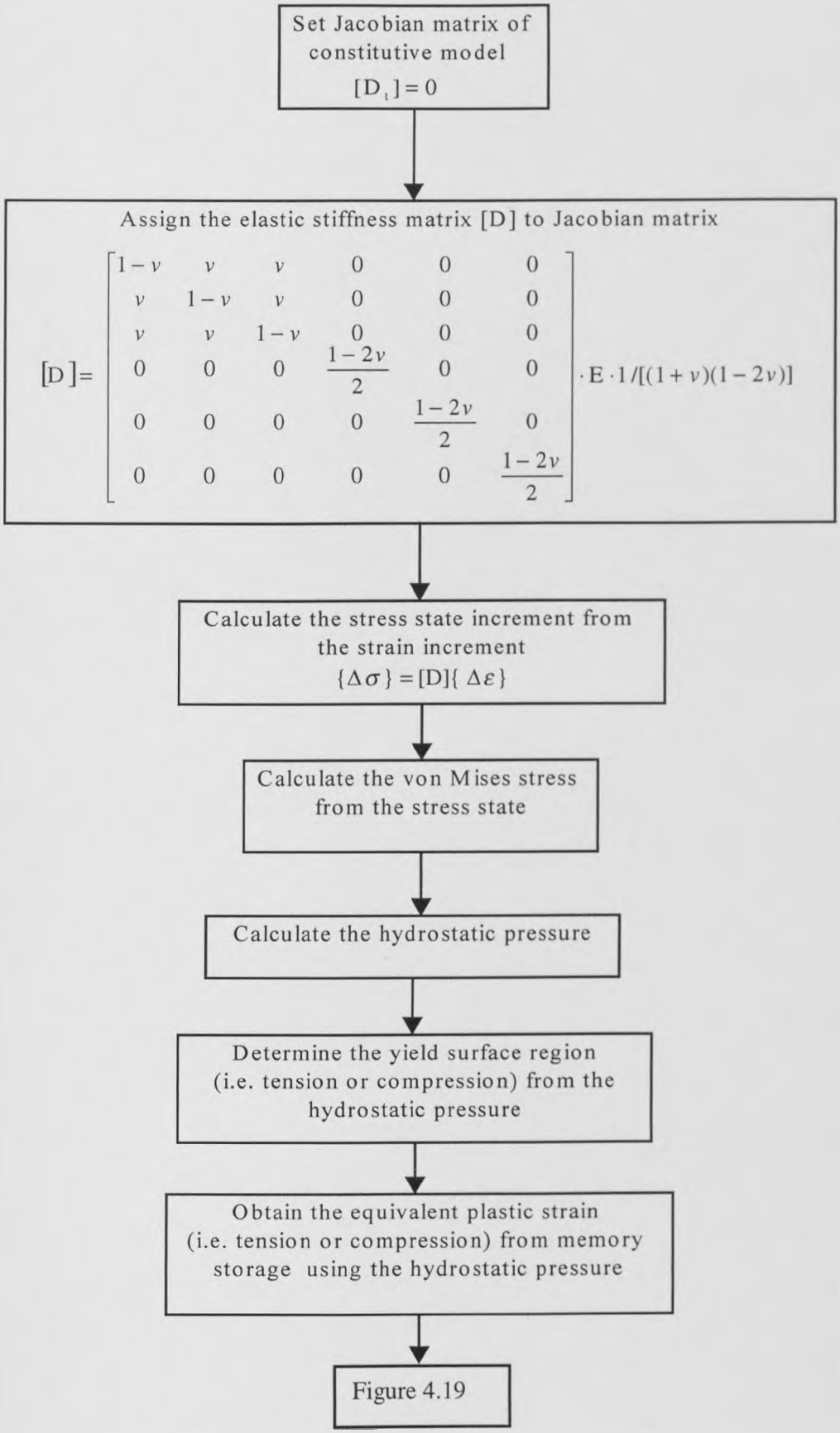

Figure 4.18: Flow chart (A) for cast iron user-developed subroutine isotropic material model

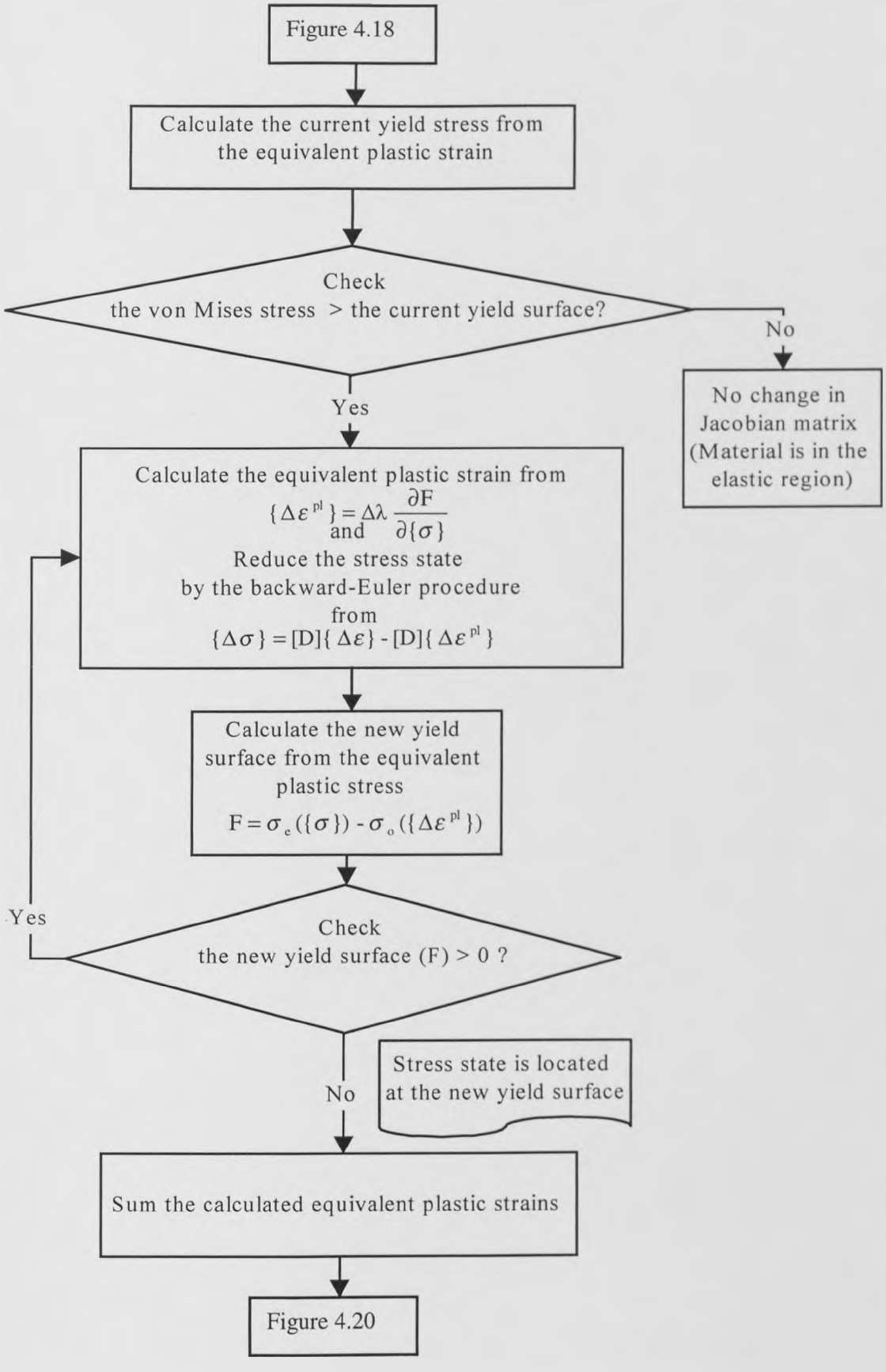

Figure 4.19: Flow chart (B) for cast iron user-developed subroutine isotropic material model

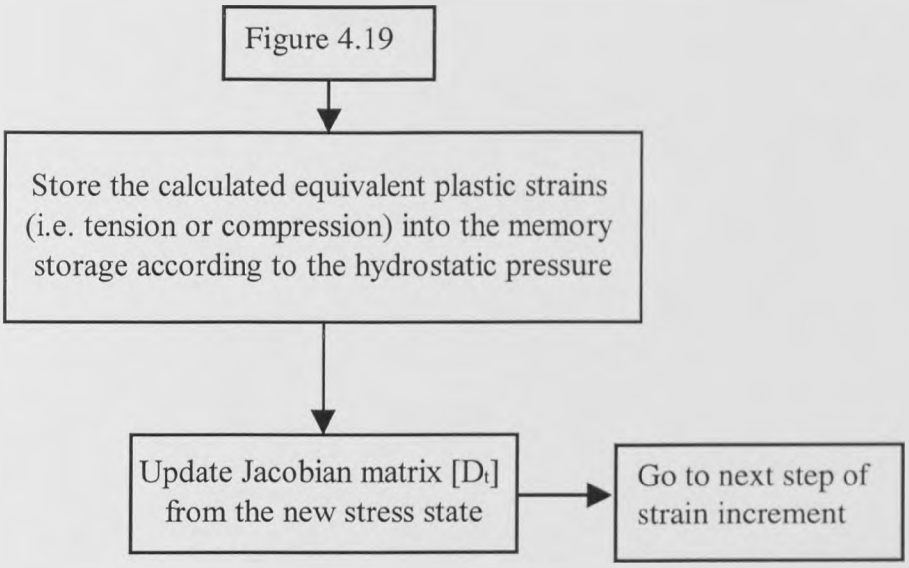

Figure 4.20: Flow chart (C) for cast iron user-developed subroutine isotropic material model

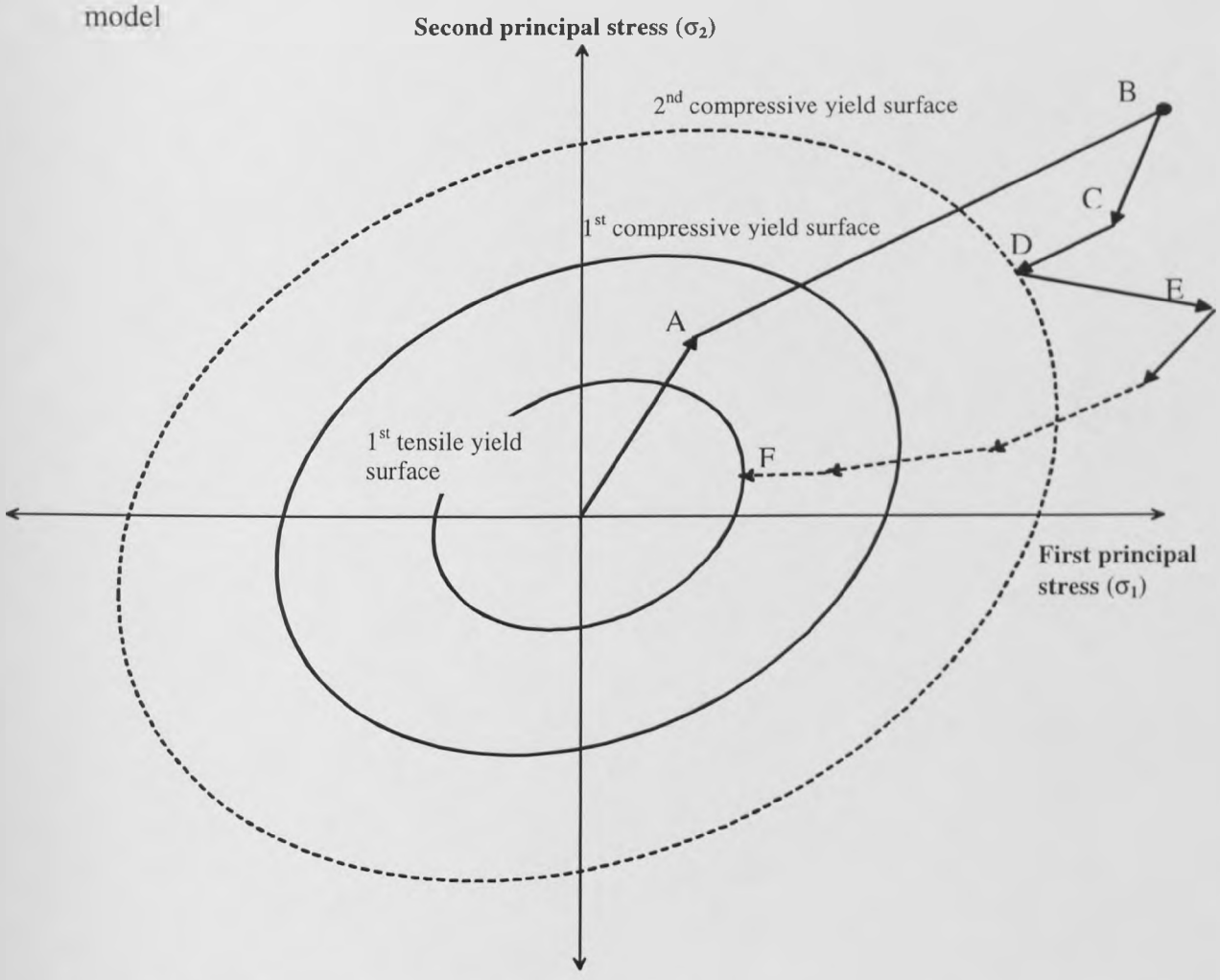

Figure 4.21: Stress states without transition zone

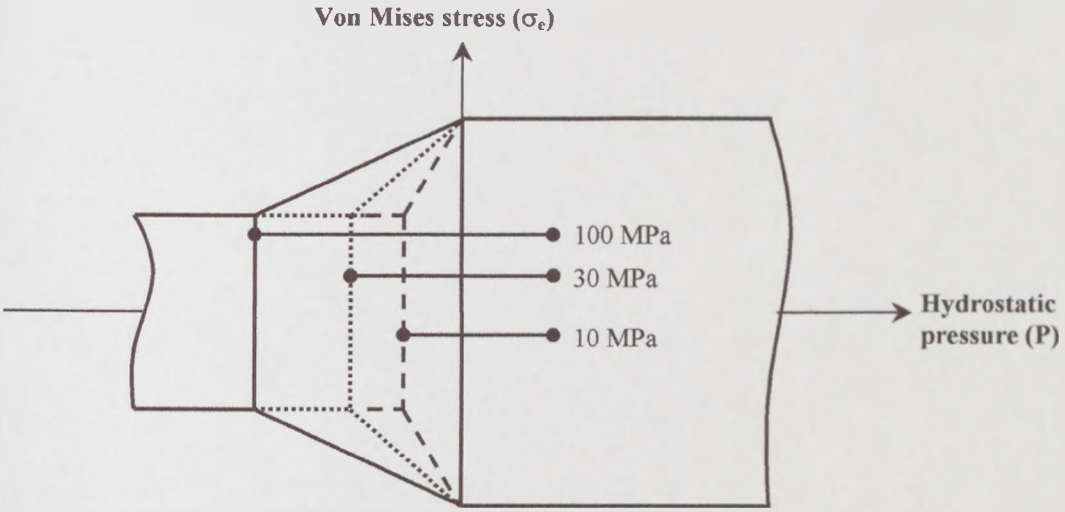

Figure 4.22: Yield surface with transition zones over 10, 30 and 100 MPa tensile hydrostatic pressure

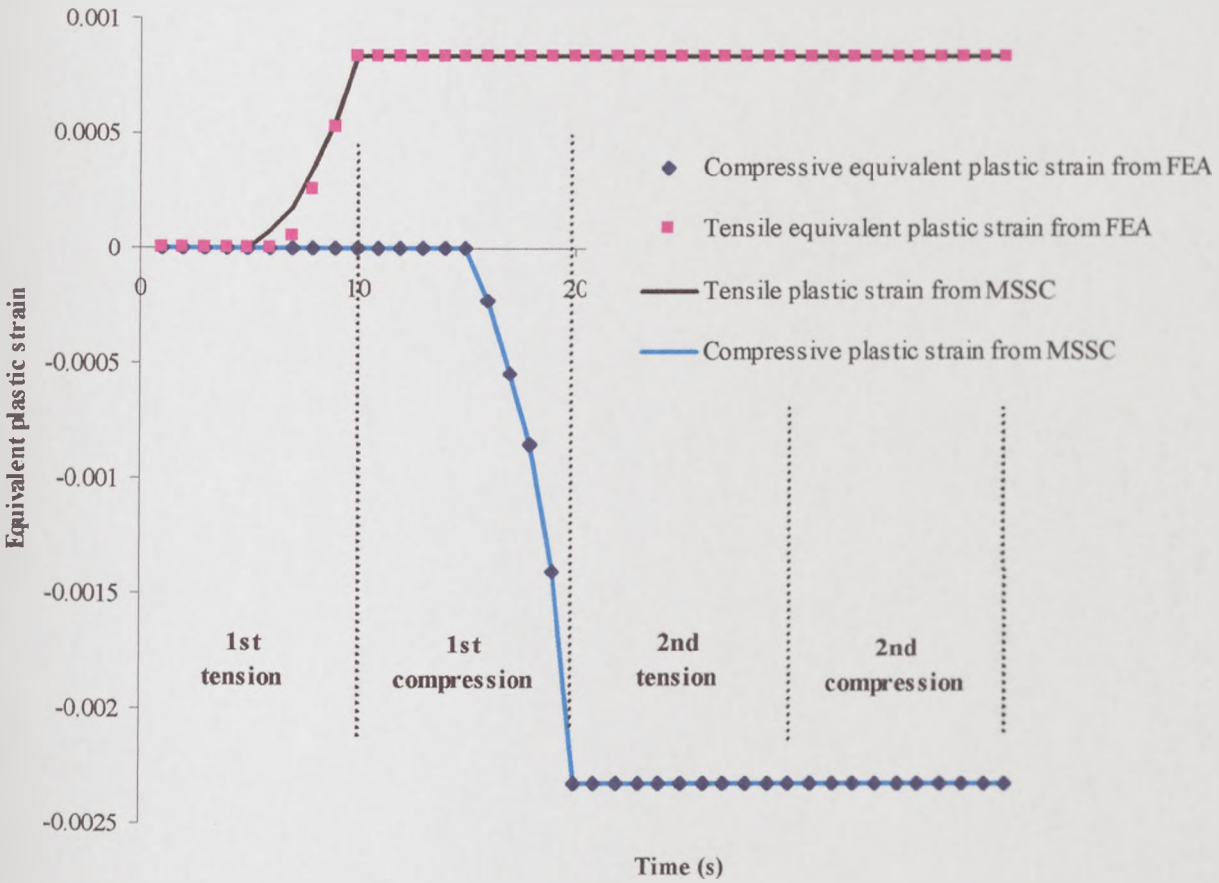

Figure 4.23: Tensile and compressive plastic strain response for user-developed subroutine cast iron material model

CHAPTER 5

NON-LINEAR FINITE ELEMENT ANALYSIS OF BRAKE DISC

5.1 INTRODUCTION

Since the single thermal cycle analysis of severe braking and cooling under autobahn driving conditions reported in Chapter 2 induced thermal stresses in the Rover brake disc beyond the material yield stress, it became essential to introduce inelastic stress analysis to accurately predict stresses and accumulated plastic strains. Inelastic stress and plastic strain accumulation with temperature dependence can be simulated in both the standard ABAQUS cast iron and user-developed subroutine material models described in Chapter 4. The objective of the present Chapter is to investigate the application of each of these material models to the Rover back-vented disc design. Similarly, the front-vented disc is also investigated with the user-developed subroutine model to enable comparison of the effects of brake disc geometry on plastic strain accumulation.

In order to achieve these objectives, the same brake rotor finite element models for both back-and front-vented discs, as introduced in Chapter 2, were used for the inelastic stress analysis. Firstly the predicted non-uniform temperature distributions were used as input data to the structural analyses in order to estimate the inelastic stresses during a single thermal cycle i.e. braking and cooling. Since the temperature distribution at the end of the cooling period was similar to the pre-braking condition, the non-uniform temperature data from the first thermal cycle was assumed to also apply during subsequent identical cycles within the eight stop autobahn driving cycle. However, unlike the elastic analysis, the inelastic analysis must be carried out at each time step of

the thermal analysis in order to correctly estimate the accumulation of plastic strain. Similarly the residual stresses and accumulated plastic strains at the end of each cooling period were carried forward to the next brake application of the eight stop cycle.

5.2 APPLICATION OF THE ABAQUS STANDARD CAST IRON MATERIAL MODEL TO THE BACK-VENTED DISC

5.2.1 METHOD

In this section, the standard ABAQUS cast iron material model was used for investigating the inelastic thermal stresses during a severe brake application and subsequent cooling of the Rover back-vented disc. For the present analysis, the material model requires the true stress-strain data points at different temperatures for each mode of loading i.e. tension or compression. The code then linearly interpolates between these data points to give the yield stress at any strain or temperature. The material data in the form of monotonic true stress-strain curves for the brake disc cast iron was presented in Chapter 3. These curves were inputted as data points to ABAQUS as indicated in Appendix 3. ABAQUS interprets them according to the assumed yield criteria in the standard cast iron material model which is a Rankine maximum stress criterion in tension and the standard von Mises criterion in compression.

5.2.2 RESULTS AND DISCUSSION

Contours of von Mises stress and equivalent plastic strain in tension and compression at the end of the first brake application and at the end of the cooling period are shown in Figures 5.1 and 5.2 respectively. In ABAQUS, contour plots of these variables are nodal variables which are themselves extrapolated from the 27 element integration point values employed within each of the 3D quadratic brick elements. However the element centroid values, derived from the integration point values, represent the most accurate

calculated values and are therefore added to the Figures in parentheses at the key locations in the contour plots. It can be seen that in comparison with the elastic stresses at the end of the brake application shown in Figure 2.10, von Mises stresses at the selected positions are similar but lower in magnitude due to the effect of the elevated temperature plasticity. In addition, a residual stress distribution still remains in Figure 5.2 even though the temperature has now fallen to a uniform 80 °C at the end of cooling period.

From the plastic strain contours at the end of brake application and of the cooling period, all selected positions have apparently experienced plastic strain accumulation in both tension and compression particularly at the cheeks of the rubbing surfaces. It is clear that this is an artefact in the implementation of the ABAQUS cast iron material model since these regions are subject to compression only throughout the brake application and therefore should not be subject to tensile plastic strain accumulation. The main reason for this artefact is the assumption that increase of compressive plastic strain on the rubbing surfaces simultaneously causes expansion of the yield surfaces in both tension and compression. This expansion is a function of the deviatoric plastic strain only which requires the strain to increase in tension and compression simultaneously as discussed in Chapter 4.

5.3 APPLICATION OF CAST IRON USER-DEVELOPED SUBROUTINE MODEL TO THE BACK-VENTED DISC

In the previous section, it has been demonstrated that the ABAQUS standard cast iron material model may not accurately predict plastic strain accumulation in regions where there may be reversals in the direction of straining i.e. compression to tension and vice

versa, and certainly does not allow for the cyclic softening in tension seen experimentally. With this shortcoming in mind, the user subroutine material model for cast iron has been proposed and developed in Chapter 4 based on the assumption that the tensile plastic strain should be independent of the compressive stress and vice versa. It was decided to apply the proposed material model to the back-vented disc in order to validate the model coding and demonstrate the shortcoming of the ABAQUS standard cast iron material model. The data points from the measured monotonic true stress-strain curves in compression and tension with temperature dependence were specified in the user-developed subroutine as detailed in Appendix 5.

5.3.1 RESULTS AND DISCUSSION FOR BACK-VENTED DISC MODEL

5.3.1.1 FIRST BRAKE APPLICATION

Figure 5.3 shows von Mises stress and plastic strain contour plots at the end of the first brake application. Contours of von Mises stress are similar but not identical to those from the standard cast iron material model, Figure 5.1. In comparison with the elastic stress analysis, the neck connection still causes high thermal stress at the inboard rubbing surface, thus resulting in higher plastic strain accumulation in comparison with the outboard rubbing surface. However, the von Mises stress at the inner radius of the long vane (position C) is not the maximum as found in the elastic stress analysis because plastic deformation occurs in tension at a lower stress than for those regions experiencing compression.

From the plastic strain contour plots, it can be seen clearly that the user-developed subroutine for cast iron, Figure 5.3 (b) and (c), provides more physically realistic results than the ABAQUS standard cast iron material model, Figure 5.1 (b) and (c), because the rubbing surfaces are found to have only compressive plastic strain accumulation.

Moreover, they reveal that further compressive plastic strain accumulation can be found at the neck (position D), the bell (position F) and the outer radius of the long vane (position E) due to the effect of bending as a result of the unbalanced radial constraints. However, the same effect causes tensile plastic strain to accumulate at position C which is in tension throughout the brake application. Even though plastic deformation occurs within the brake disc at the end of first brake application, the trend of the displaced brake disc geometry, Figure 5.4, is similar to that predicted in the elastic stress analysis, Figure 2.12. The moderate angular distortion indicates that the back-vented design of disc is able to reduce the coning effect in spite of the severity of the brake application.

It can also be seen from the contour plots that the centroidal results are more accurate than the nodal values. For instance, a nodal value of tensile plastic strain exists at position D even though position D has zero element centroid tensile plastic strain. One possible reason is that the selected element at position D might be close to other elements that are subjected to tensile loads and the nodal value at position D is calculated by extrapolation from the integration points of all elements surrounding the node.

The von Mises stress histories at the same positions A to D as used in the elastic analysis are shown in Figure 5.5. It can be clearly seen that the high thermal gradients through the brake disc thickness cause high thermal stresses at the cheeks (positions A and B) in the early part of the first brake application. As a result, the compressive plastic strains at these locations rapidly increase up to one second into the brake application, Figure 5.6, because at this braking time the material yield strength is reduced due to the high temperature. However, after one second, the high thermal stresses at positions A and B gradually reduce towards the end of the brake application because of the lower

temperature gradients. Thus, the compressive plastic strains at positions A and B remain approximately constant. It is also clearly seen that the thermal stresses and plastic straining at the inboard rubbing surface (position B) are higher than that at the outboard rubbing surface (position A) throughout the braking time due to the asymmetrical constraint offered by the neck to which the inboard cheek is attached in this back-vented design.

Before investigating thermal stress histories at positions C and D, the element centroid mean stress histories from the selected positions should be examined to determine whether a state of compression or tension exists because these positions are subjected to both local thermal gradients and gross bending due to the unbalanced radial constraints. Thus, Figure 5.7 reveals that compression exists on the rubbing surfaces (positions A and B) as expected. The neck region (position D) also experiences compression due to the temperature gradients between positions B and D as predicted by the elastic stress analysis in Chapter 2 and shown in Figure 2.5. However, the thermal stress history at position D is different from that on the rubbing surfaces (positions A and B) in that the von Mises stress continues to increase throughout the brake application, Figure 5.5, since the bending effect due to the unbalanced radial constraints remains after the temperature gradients at the cheeks (positions A and B) reduce in the early brake application. As a result of the increasing thermal stress at position D and the reducing compressive yield strength due to the high temperature, the compressive plastic strain gradually increases throughout the brake application, Figure 5.6.

In contrast to the rubbing surfaces (positions A and B) and the neck area (position D), the inner radius of the long vane (position C) is subjected to tension throughout the brake application, Figure 5.7. Since the mean stress at position C is within the transition

region of 30 MPa, the yield stress is higher than the purely tensile yield stress but lower than the compressive yield strength due to the linear interpolation between these yield surfaces. As a result of the tensile plastic strain hardening and the simultaneous contraction of the yield surface due to the increasing temperature, the element centroid von Mises stress at position C is virtually constant after one second of braking time, Figure 5.5. However, the plastic strain continues to increase and, after about two seconds into the brake application, becomes the highest plastic strain anywhere in the brake disc. The fact that this strain is tensile may have implications for the early onset of thermal cracking in this region.

5.3.1.2 FIRST COOLING PERIOD

As shown in Figure 5.8, contour plots of von Mises stress and equivalent plastic strains at the end of the first cooling period reveal that the effect of high thermal load on the brake disc model causes residual stresses and permanent plastic deformations even though the surface temperatures are reduced to the preloaded uniform condition of 80°C. Furthermore, the inner radius of the long vane (position C) has the highest residual thermal stress both in terms of nodal and element centroidal values. This position is also the only one to experience both tensile and compressive plastic strain accumulation during the brake application and cooling period respectively because of the unbalanced radial constraint between the outboard and inboard cheeks. All other positions indicate only compressive strains in terms of the more accurate centroidal values.

At the end of cooling period, Figure 5.9 reveals that the brake disc cannot return to its original shape and undergoes a small degree of permanent brake disc coning. Figure 5.10 shows that the element centroid von Mises stress histories at the selected

positions are completely different from those predicted by the elastic analysis, Figure 2.15, due to the influence of plastic deformation and the changing mean stress conditions. The latter can be seen clearly from the element centroid mean stress histories shown in Figure 5.11. During the first cooling period, the mean stresses at the rubbing surfaces (positions A and B) change from compression to tension whereas the inner radius of the long vane (position C) becomes subject to compression since the cheeks are no longer able to contract to their stress-free state. Therefore, the element centroid von Mises stresses at these positions (A, B and C) are first reduced and then increase again before the end of the cooling period. At position D, the mean stress near the neck indicates compression throughout both the braking and cooling period.

Although the thermal loads at the rubbing surfaces, positions A and B, change from compression to tension, the tensile yield strength of the cast iron material is increased according to the lower temperature and there are no increments of tensile plastic strain accumulation at positions A and B. Similarly, no further compressive plastic strain accumulates at position D during cooling because the thermal stress is lower than the current compressive yield strength which is increased due to the lower temperature. However, the temperatures at the rubbing surfaces still cause bending, resulting in an increase of the tensile plastic strain at the inner radius of the long vane (position C) in the early cooling period as shown in Figure 5.12. After about 100s into the cooling period, the change of direction of the mean stress at this location causes compressive plastic strain to accumulate at position C even though the current yield strength of the material is increased due to the lower temperature. Thus this is one location which experiences stress reversal and plastic strain accumulation in both tension and compression during a single thermal cycle.

5.3.1.3 EFFECT OF FURTHER THERMAL CYCLES

Since both tensile and compressive plastic strains accumulated at the inner radius of long vane by the end of the first cooling period, it is worth investigating trends associated with the autobahn driving cycle which requires eight identical thermal cycles to be completed. As a result of applying further thermal cycles, it was found that the compressive plastic strain at position C saturates (i.e. remains constant) after two subsequent thermal cycles. Conversely, the tensile plastic strain increases for every new brake application as shown in Figure 5.13. Similarly, the compressive plastic strain at the neck (position D) gradually increases during each brake application.

At the rubbing surfaces, the outboard cheek (position A) has no further accumulation of plastic strain throughout the eight thermal cycles, Figure 5.14. However, the plastic strain at the inboard cheek (position B) is constant only up to the fifth thermal cycle. This is likely to be due to the effect of compressive plastic strain accumulation at the neck area (position D) that results in the onset of further plastic strain at position B after five thermal cycles.

To understand the relation between the total strain accumulated and the associated thermal stresses, the total strain (elastic and plastic strain components) is plotted against von Mises stress for the eight thermal cycles at positions A-B and C-D as shown in Figures 5.15 and 5.16 respectively. There is no additional thermal stress and total strain after the first cycle at the outboard cheek (position A). However, due to the increment of plastic strain at the inboard cheek (position B), a corresponding increment of thermal stress can be seen. Also, the inboard cheek has the highest thermal stress during the first thermal cycle. From Figure 5.16, the situation at location D appears relatively straightforward as there is no reversal of direction of plastic strain: after the first cycle,

there are small additional increments of strain in compression with every subsequent cycle with no evidence of full saturation. At location C, there is a reversal of mean stress as typified in Figure 5.11 with every cycle although plastic strain accumulates in tension only for every cycle after the first, Figure 5.13. Again there is no evidence of full saturation after eight cycles and it is noted that the total accumulated plastic strain predicted is greater than the true strains at failure from the cyclic tests which were about 0.0025 in tension. This is an indication that thermal cracking may be a problem at this location although as previously noted no attempt has been made in the present work to accurately derive fatigue data.

5.4 APPLICATION OF CAST IRON USER-DEVELOPED SUBROUTINE MODEL TO THE FRONT-VENTED DISC

In a similar fashion to the inelastic analysis of the back-vented disc, the front-vented disc model as described in Chapter 2 was investigated using the cast iron user-developed subroutine. The predicted non-uniform temperature distributions were again used as input data together with the same constraints as for elastic stress analysis. To simulate the eight stop autobahn driving condition, temperature distributions from the first thermal cycle were assumed to apply in all the subsequent cycles.

5.4.1 RESULTS AND DISCUSSION FOR FRONT-VENTED DISC MODEL

5.4.1.1 FIRST BRAKE APPLICATION

At the end of the first brake application, the contour plots of von Mises stress, compressive and tensile plastic strains shown in Figure 5.17 reveal that the effect of the neck connection causes the front-vented brake disc to have a different thermal response compared with the back-vented design, Figure 5.3. As expected, the induced thermal stress at the outboard rubbing surface (A) is higher than that at the inboard rubbing

surface (B), leading to higher plastic strains on the former. The maximum centroidal values of compressive plastic strain occur at position C and of tensile plastic strain at position D at the end of the first brake application due to the effect of the neck connection. In contrast, positions C and D for the back-vented disc are subjected to tensile and compressive plastic strains respectively, Figure 5.3. Comparison of the displaced shapes of the front-and back-vented designs at the end of the first brake application, Figures 5.4 and 5.18, reveal that the front-vented disc displays a greater degree of coning. However, at the selected positions, the maximum element centroid plastic strains in compression and tension for the front-vented disc are less than those for the back-vented disc design.

The element centroid von Mises stress histories shown in Figure 5.19 clearly indicate that the neck connection causes higher stresses on the outboard rubbing surface (position A) than on the inboard surface (position B) from the beginning of the brake application. As for the back-vented disc, high temperature gradients on the rubbing surfaces (positions A and B) in the early part of the brake application cause high thermal stresses that gradually reduce towards the end of brake application due to lower temperature gradients. Furthermore, the bending effect due to the unbalanced radial constraint causes compressive and tensile thermal stresses at position C and D respectively as indicated by the mean stress histories in Figure 5.20. The thermal stress at the inner radius of the long vane (position C) increases rapidly during the early brake application but eventually reduces by the end of the brake application due to the lower temperature gradients. The tensile thermal stress at the neck (position D) gradually increases throughout the early brake application and is then approximately constant since the bending effect due to the much hotter cheeks is still present. This is reflected in the continuing increase of tensile plastic strain at position D throughout the brake

application whereas the compression strains at positions A, B and C remain constant over the latter part of the braking cycle, Figure 5.21.

5.4.1.2 FIRST COOLING PERIOD

Figure 5.22 shows that residual thermal stress and plastic strains at the end of the cooling period are lower than those for the back-vented disc, Figure 5.8. Comparison between Figures 5.22 and 5.17 reveals that there is no further accumulation of compressive plastic strain at locations A, B and C. In contrast, Figure 5.23 reveals that while tensile plastic strains at position D remain constant, compressive plastic straining starts to occur before the end of cooling period. Thus, plastic strain reversal is found at the neck (position D) for the front-vented disc instead of at position C for the back-vented disc. This is presumably due to greater gross deformation of the front-vented design which requires reverse plastic yielding at the neck to accommodate the contraction of the rubbing surface during cooling. Furthermore, the disc brake geometry cannot return to its original shape due to the effect of plastic deformation at the neck (position D), Figure 5.24.

5.4.1.3 EFFECT OF FURTHER THERMAL CYCLES

After the first cooling period, it is found that only the neck (position D) has any increase of plastic strain, Figure 5.25. However, the compressive plastic strain accumulation becomes stable after three thermal cycles in the sequence. This is further shown in Figure 5.26, which plots von Mises stresses against total strains in tension and compression at position D. In comparison with the corresponding results for the back-vented disc, Figure 5.16, the compressive plastic strain at position D is lower. However, there is a tensile strain at this position which continues to accumulate after eight cycles. This is an indication that the neck region of the front-vented design may be vulnerable

to thermally-induced cracking.

In similar fashion to the back-vented disc, there is no additional compressive plastic strain at the inboard cheek (position B) as shown in Figure 5.27. However, due to the neck connection and its associated plastic strain accumulation at position D, the outboard cheek (position A) experiences additional compressive plastic strain after four thermal cycles. Figure 5.28 shows the thermal stresses plotted against the total strains in each cycle as a result of these effects on the outboard and inboard cheeks (positions A and B). It can be seen that, as with the back-vented disc, the highest thermal stress at the outboard cheek (position A) is found in the first thermal cycle.

5.5 SUMMARY

From the initial inelastic stress analyses, it can be concluded that the ABAQUS standard cast iron material model is not ideally suited for investigating the thermal response of brake discs as indicated by the simultaneous increase of compressive and tensile plastic strains at certain critical locations. However, the user-developed subroutine material model developed from the rotor material tests satisfies the basic demand that plastic strain in tension and compression should accumulate separately and independently. As a result of applying the user-developed subroutine material model to the back- and front-vented discs, it has been demonstrated that the effect of the neck connection causes not only different thermal stress responses but also different displaced shapes during braking.

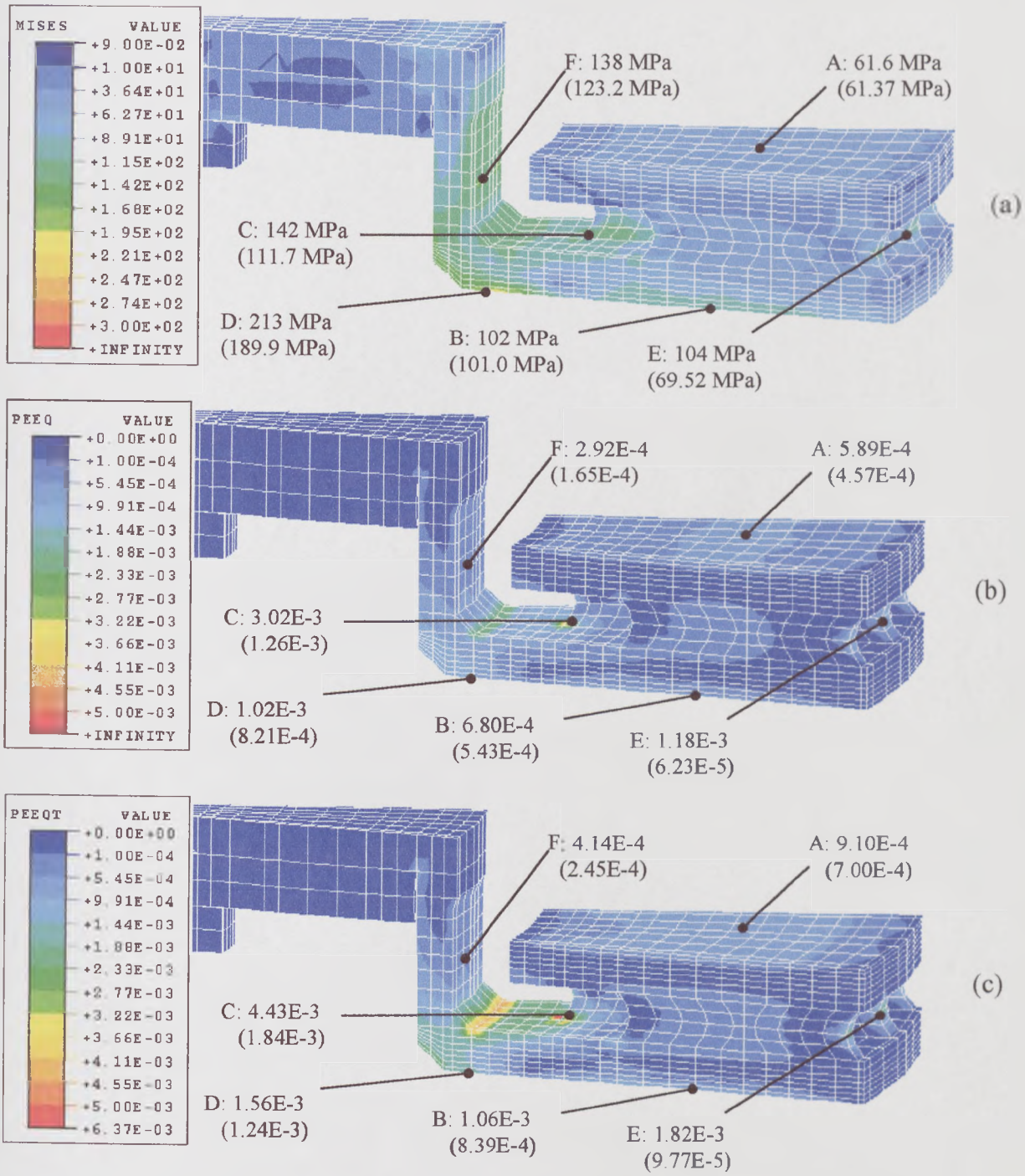

Figure 5.1: Results of inelastic finite element analysis at the end of first brake application for the back-vented disc with standard ABAQUS cast iron material model: (a) von Mises stress, (b) compressive equivalent plastic strain, (c) tensile equivalent plastic strain (Numbers in parentheses indicate the element centroid values of variables)

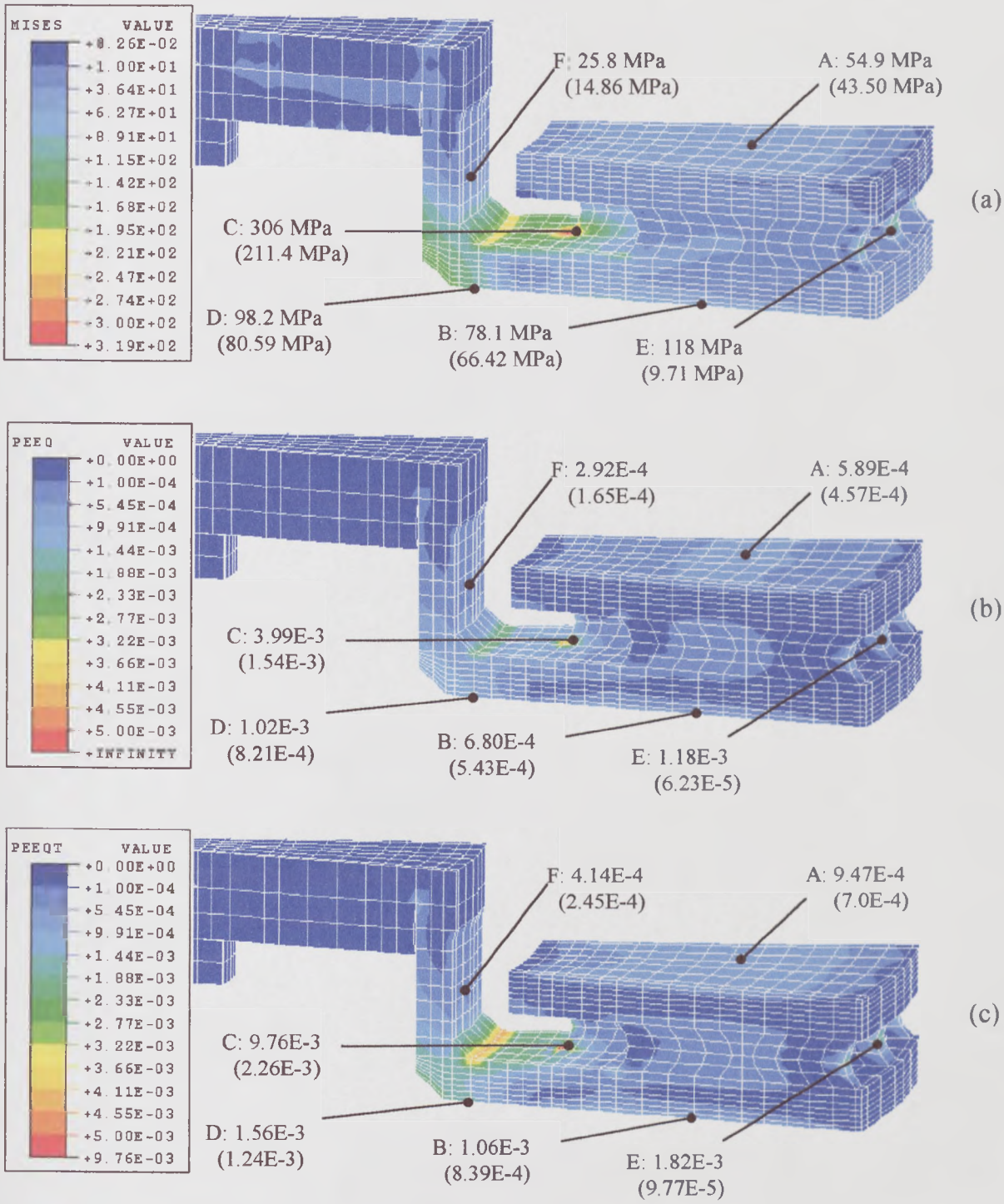

Figure 5.2: Results of inelastic finite element analysis at the end of first cooling period for the back-vented disc with standard ABAQUS cast iron material model: (a) von Mises stress, (b) compressive equivalent plastic strain, (c) tensile equivalent plastic strain (Numbers in parentheses indicate the element centroid values of variables)

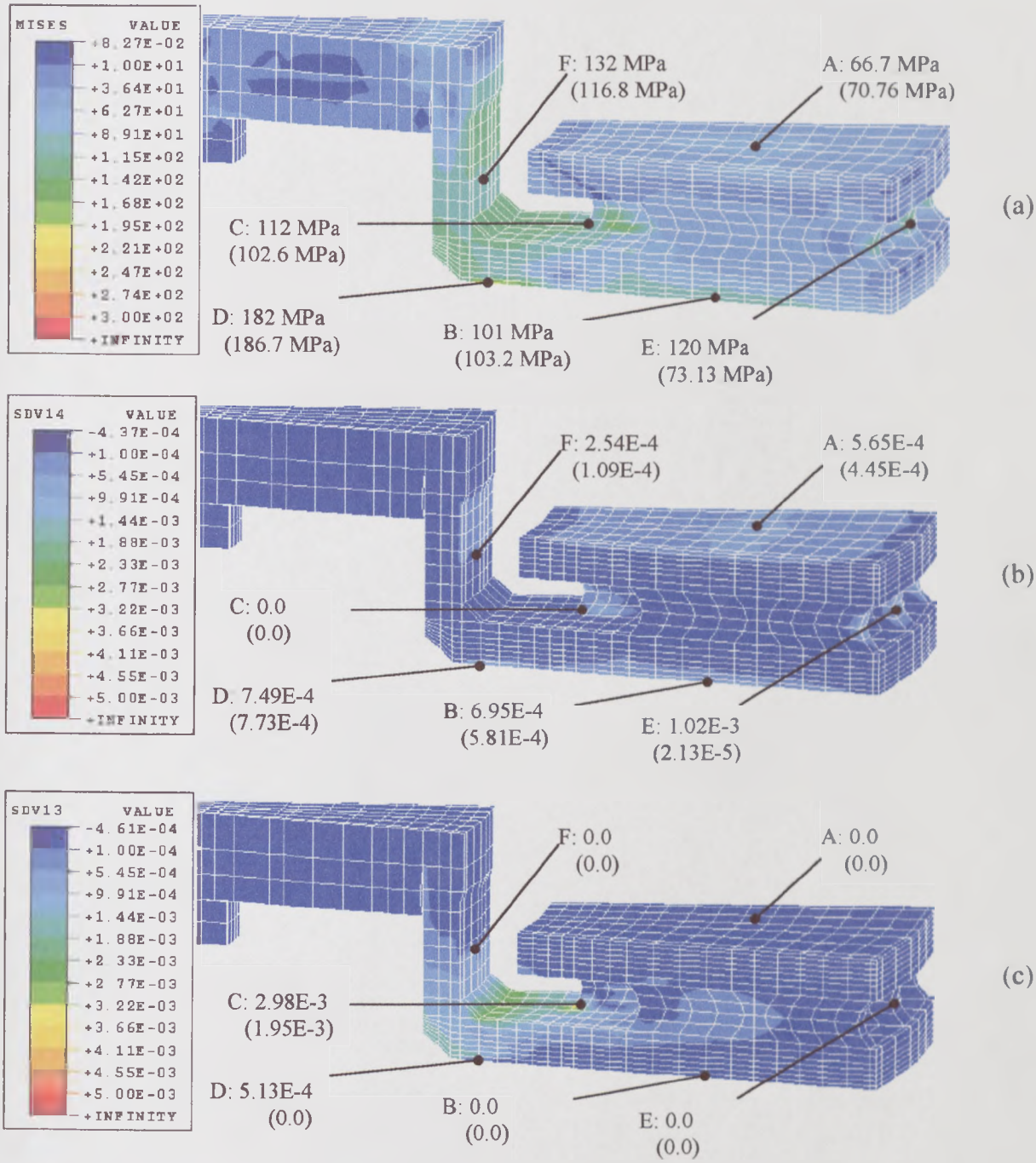

Figure 5.3: Results of inelastic finite element analysis at the end of first brake application for the back-vented disc with the cast iron user-developed subroutine: (a) von Mises stress, (b) compressive equivalent plastic strain, (c) tensile equivalent plastic strain (Numbers in parentheses indicate the element centroid values of variables)

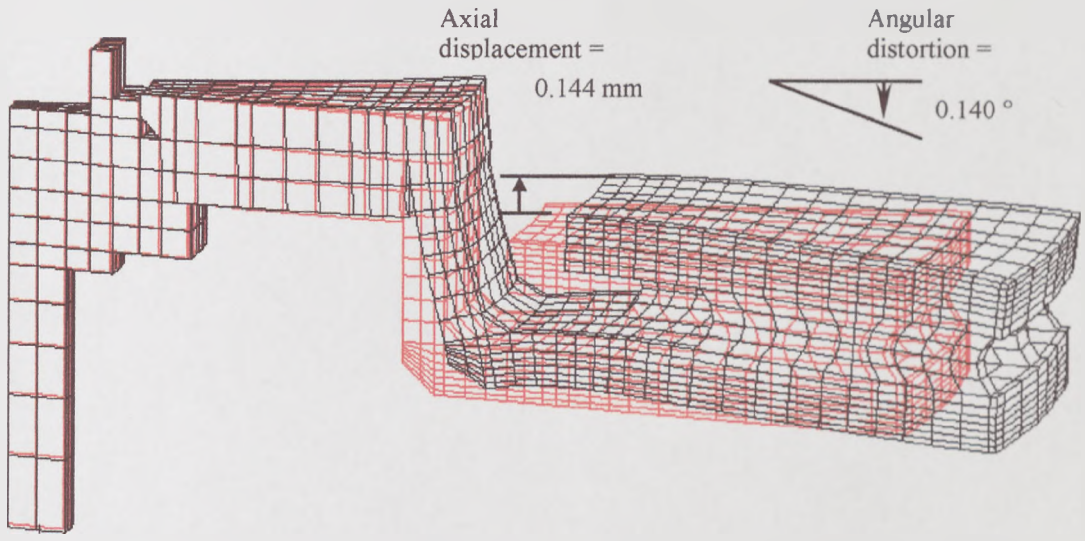

Figure 5.4: Displaced shape at the end of first brake application for the back-vented disc with the cast iron user-developed subroutine (Red indicates original mesh; Black indicates displaced mesh)

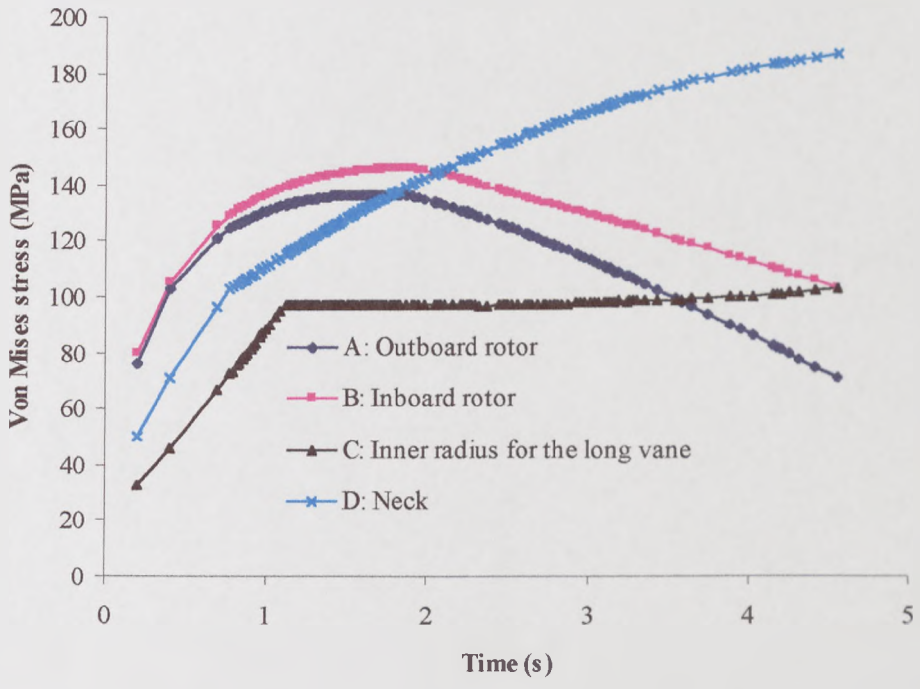

Figure 5.5: Element centroid von Mises stress histories during first brake application for the back-vented disc with the cast iron user-developed subroutine

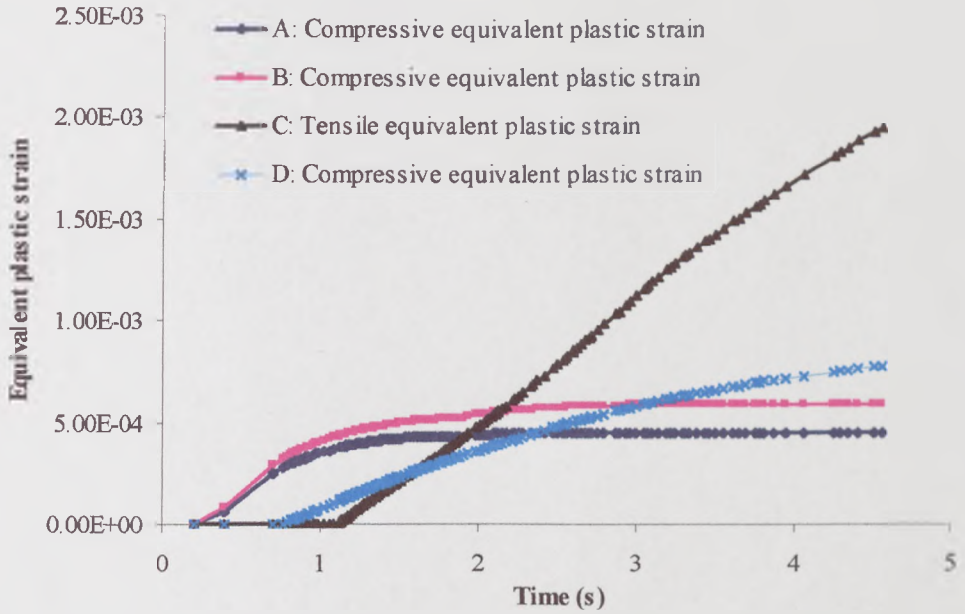

Figure 5.6: Element centroid equivalent plastic strain histories during first brake application for the back-vented disc with the cast iron user-developed subroutine

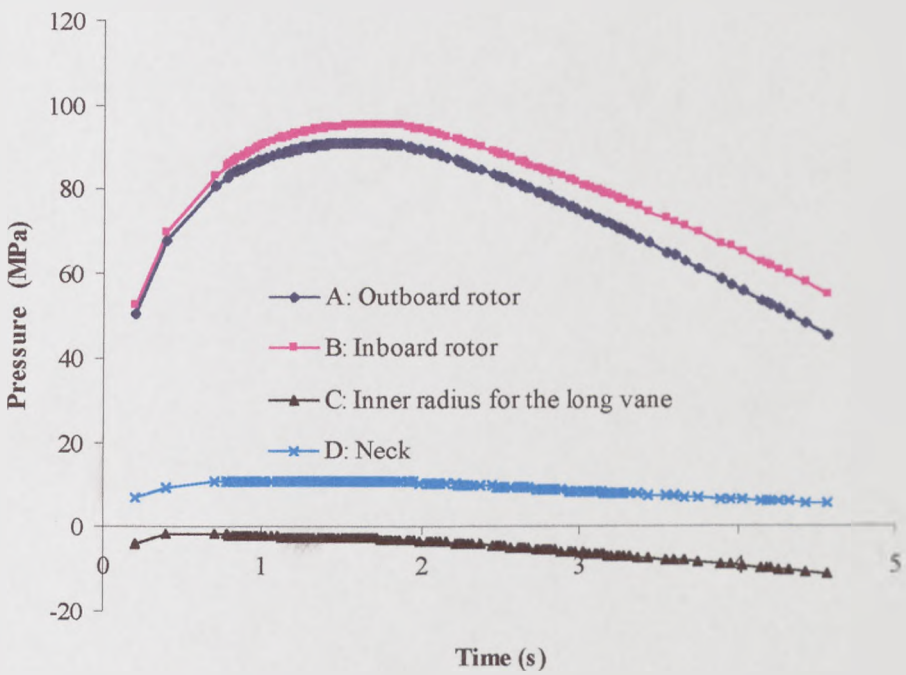

Figure 5.7: Element centroid pressure histories during first brake application for the back-vented disc with the cast iron user-developed subroutine (Negative pressure indicates tensile mean stress)

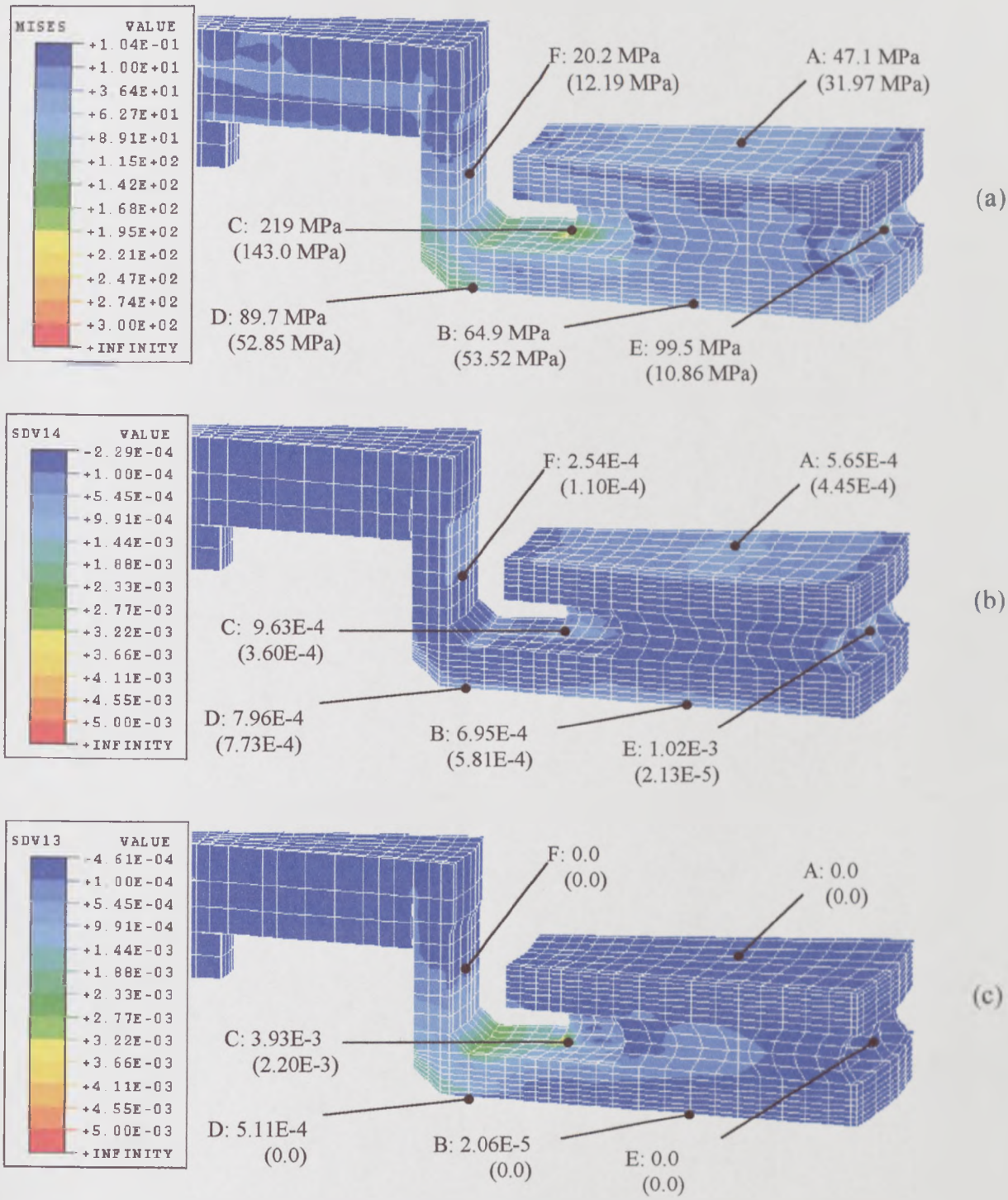

Figure 5.8: Results of inelastic finite element analysis at the end of first cooling period for the back-vented disc with the cast iron user-developed subroutine: (a) von Mises stress, (b) compressive equivalent plastic strain, (c) tensile equivalent plastic strain (Numbers in parentheses indicate the element centroid values of variables)

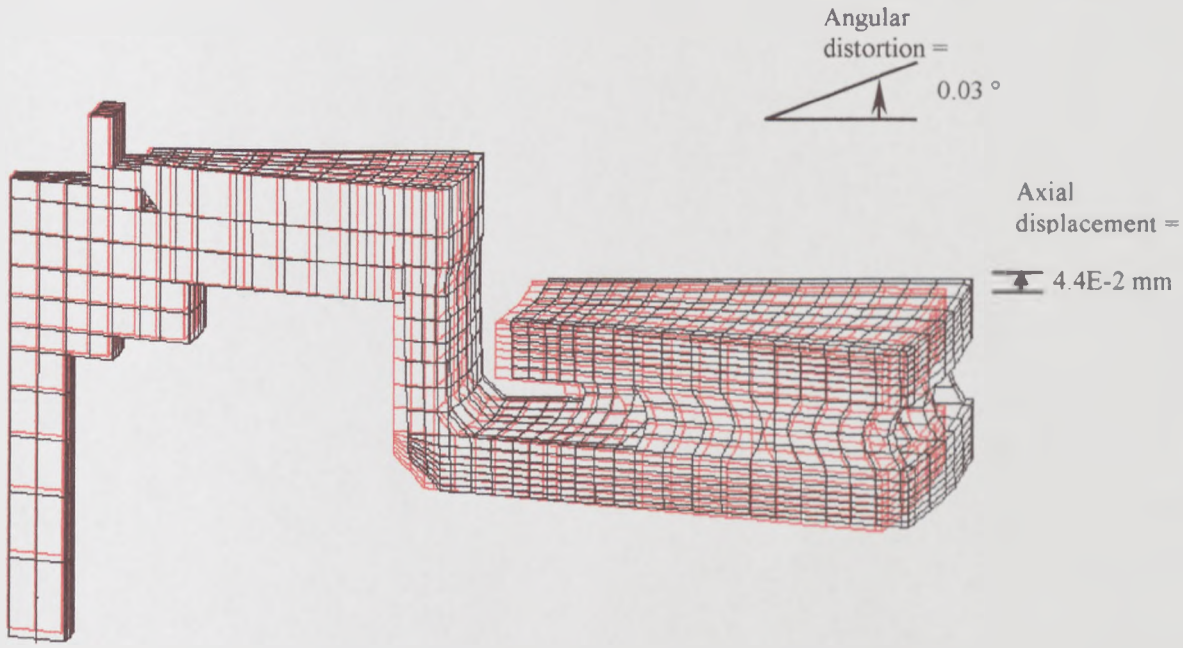

Figure 5.9: Displaced shape at the end of first cooling period for the back-vented disc with the cast iron user-developed subroutine (Red indicates original mesh; Black indicates displaced mesh)

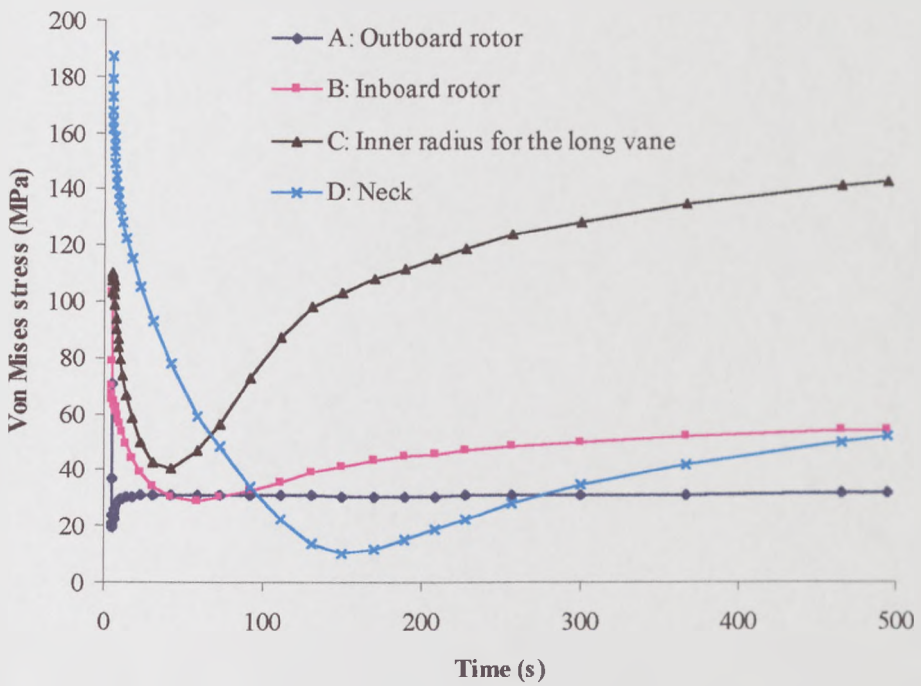

Figure 5.10: Element centroid von Mises stress histories during first cooling period for the back-vented disc with the cast iron user-developed subroutine

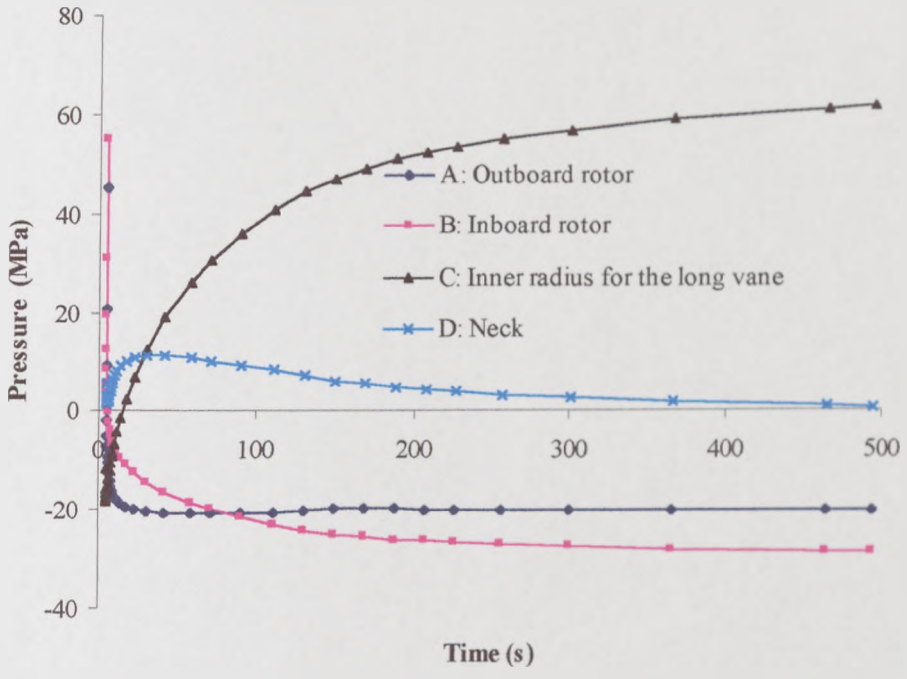

Figure 5.11: Element centroid pressure histories during first cooling period for the back-vented disc with the cast iron user-developed subroutine (Negative pressure indicates tensile mean stress)

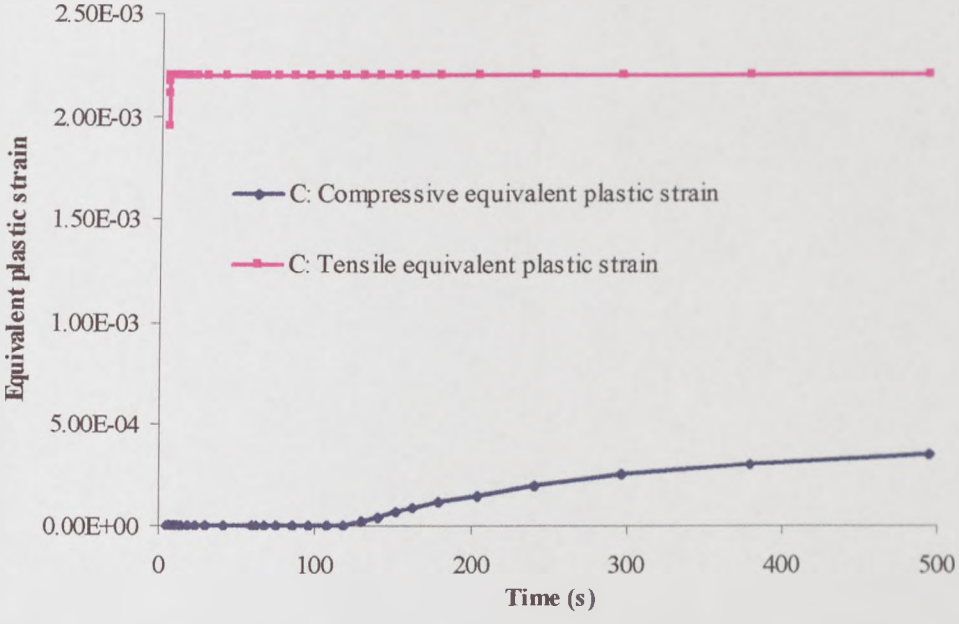

Figure 5.12: Element centroid equivalent plastic strain history (position C) during first cooling period for the back-vented disc with the cast iron user-developed subroutine

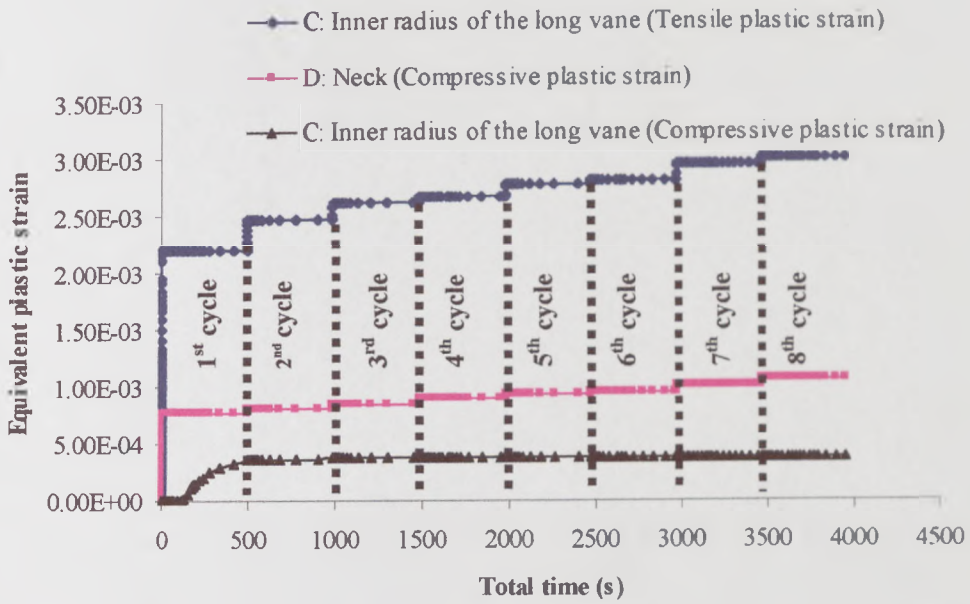

Figure 5.13: Element centroid plastic strain histories for the back-vented disc with the cast iron user-developed subroutine over eight thermal cycles

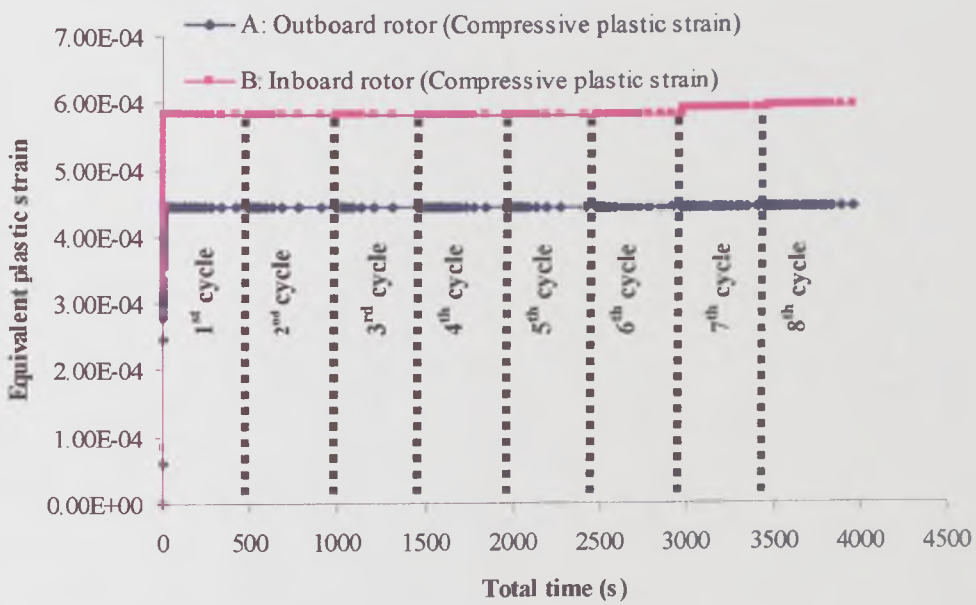

Figure 5.14: Element centroid plastic strain histories for the back-vented disc with the cast iron user-developed subroutine over eight thermal cycles

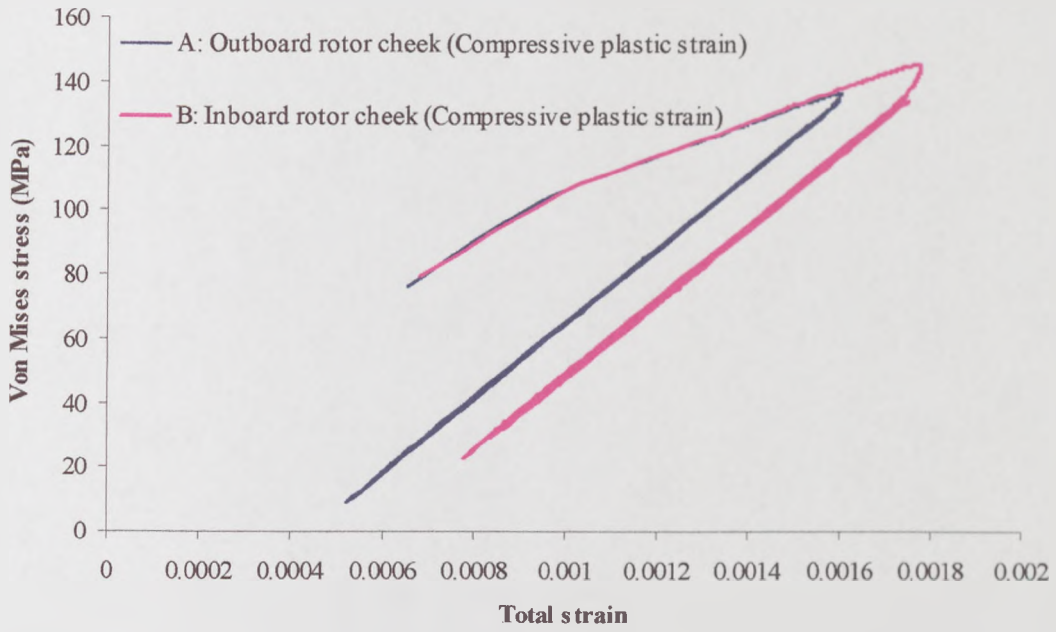

Figure 5.15: Element centroid von Mises stress versus total strain for the back-vented disc with the cast iron user-developed subroutine over eight thermal cycles

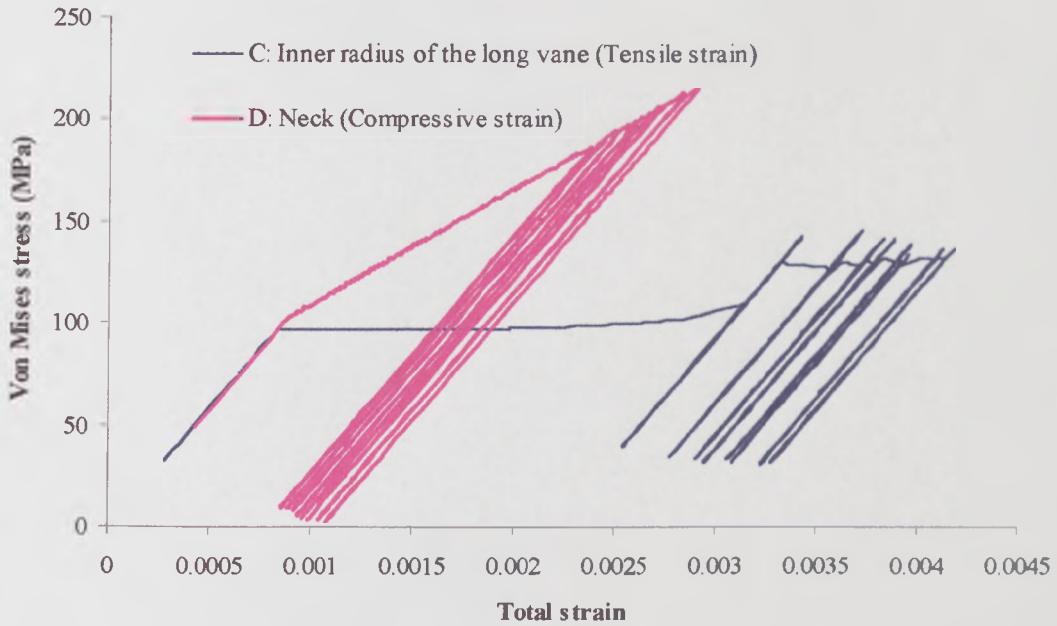

Figure 5.16: Element centroid von Mises stress versus total strain for the back-vented disc with the cast iron user-developed subroutine over eight thermal cycles

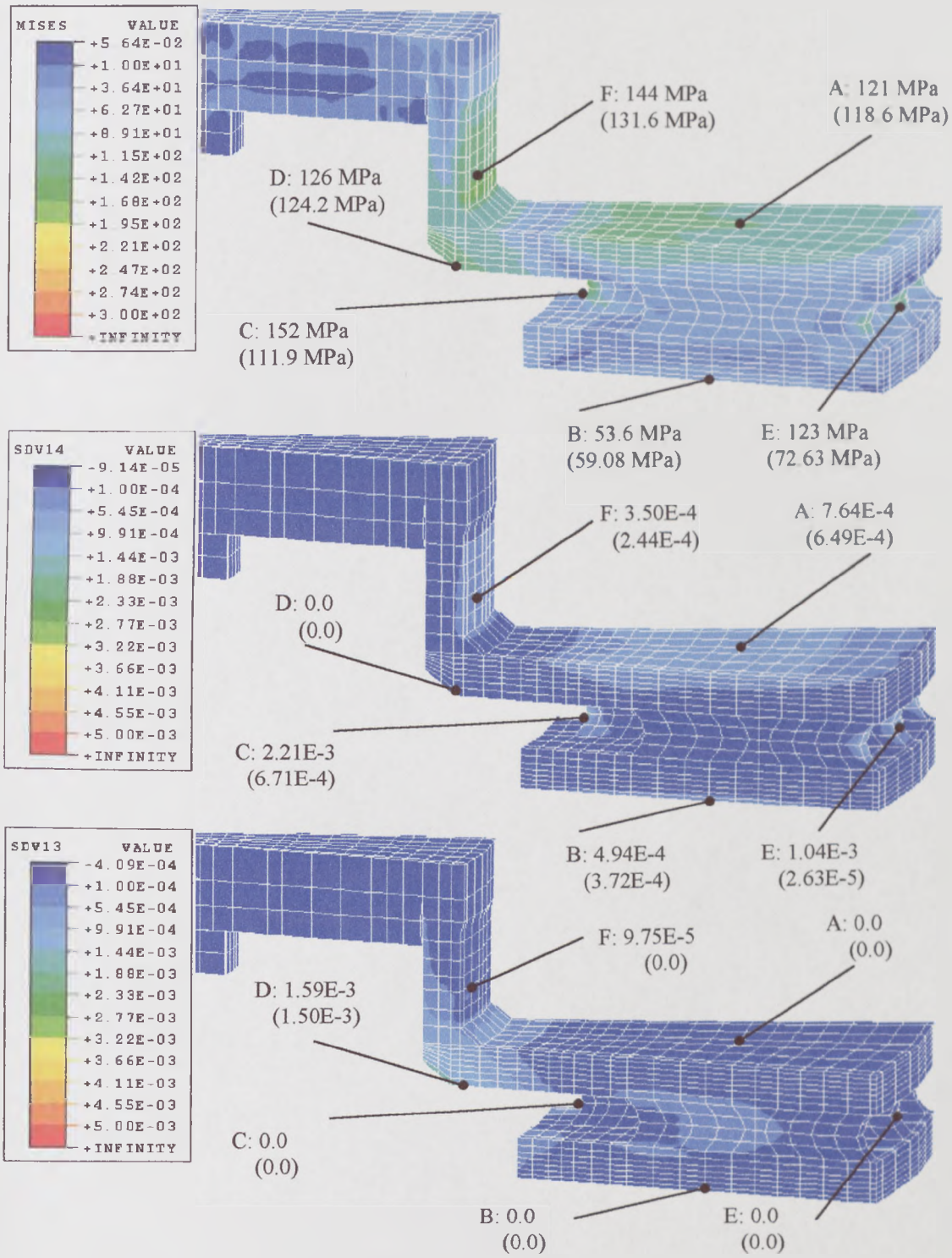

Figure 5.17: Results of inelastic finite element analysis at the end of first brake application for the front-vented disc with the cast iron user-developed subroutine: (a) von Mises stress, (b) compressive equivalent plastic strain, (c) tensile equivalent plastic strain (Numbers in parentheses indicate the element centroid values of variables)

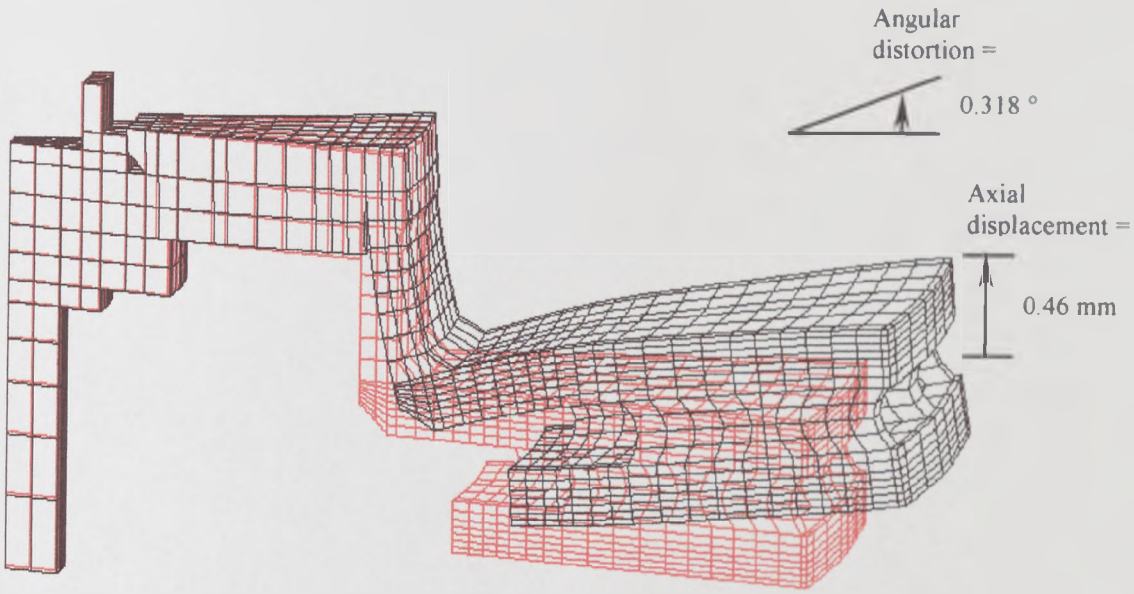

Figure 5.18: Displaced shape at the end of first brake application for the front-vented disc with the cast iron user-developed subroutine (Red indicates original mesh; Black indicates displaced mesh)

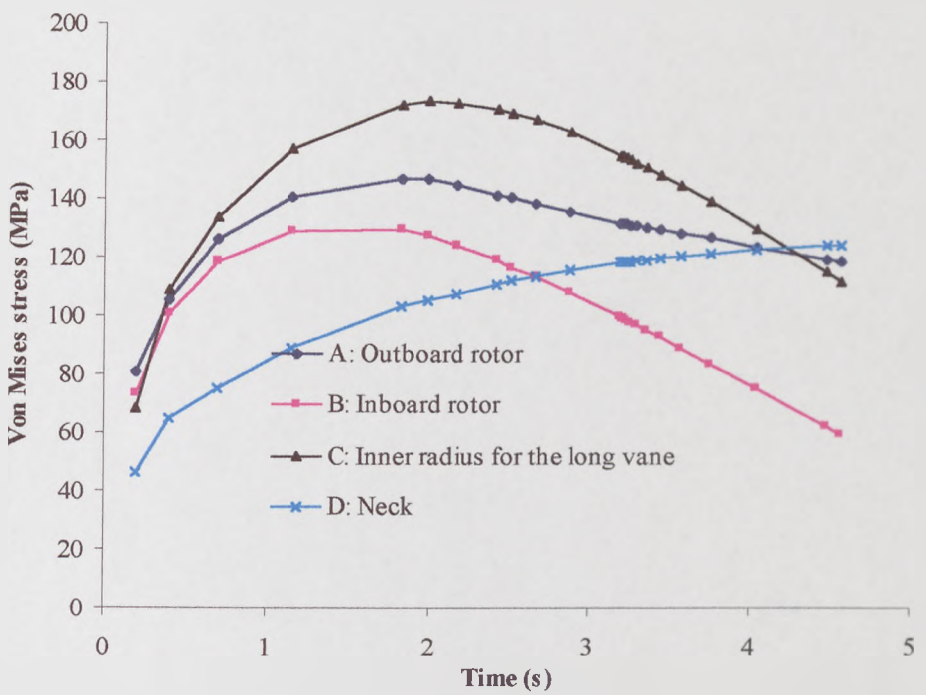

Figure 5.19: Element centroid von Mises stress histories during first brake application for the front-vented disc with the cast iron user-developed subroutine

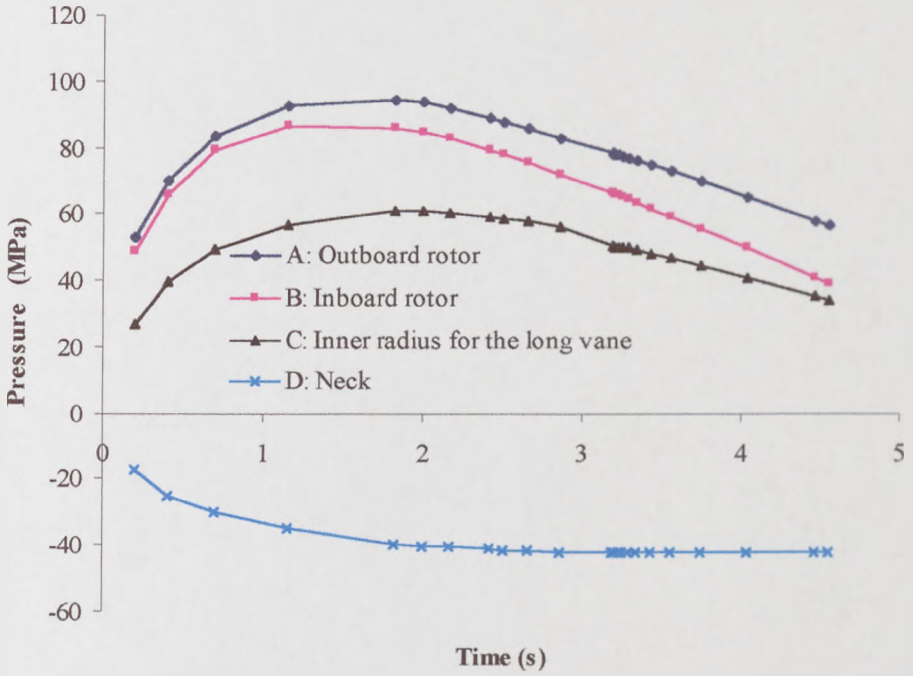

Figure 5.20: Element centroid pressure histories during first brake application for the front-vented disc with the cast iron user-developed subroutine (Negative pressure indicates tensile mean stress)

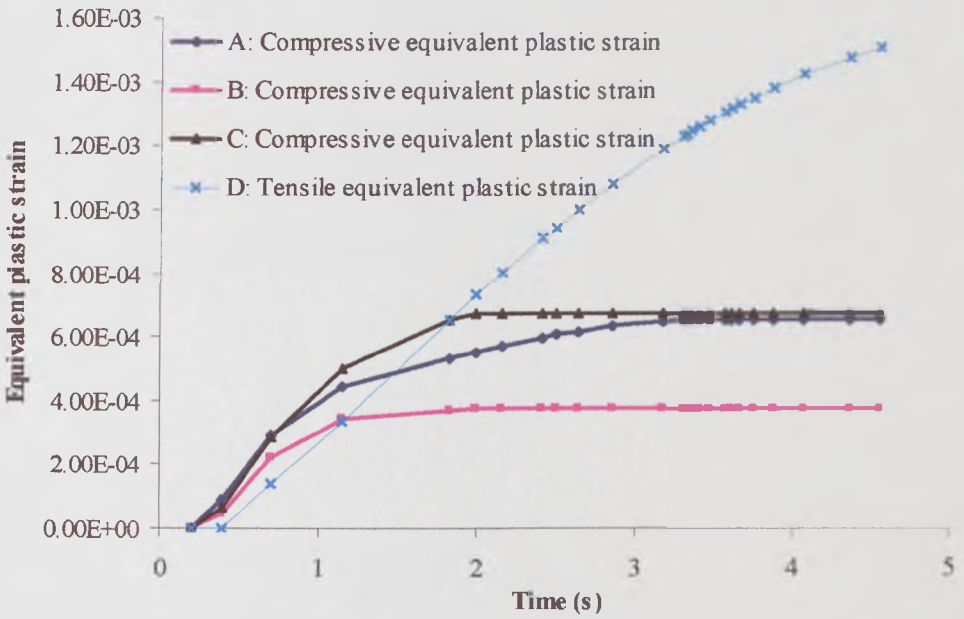

Figure 5.21: Element centroid equivalent plastic strain histories during first brake application for the front-vented disc with the cast iron user-developed subroutine

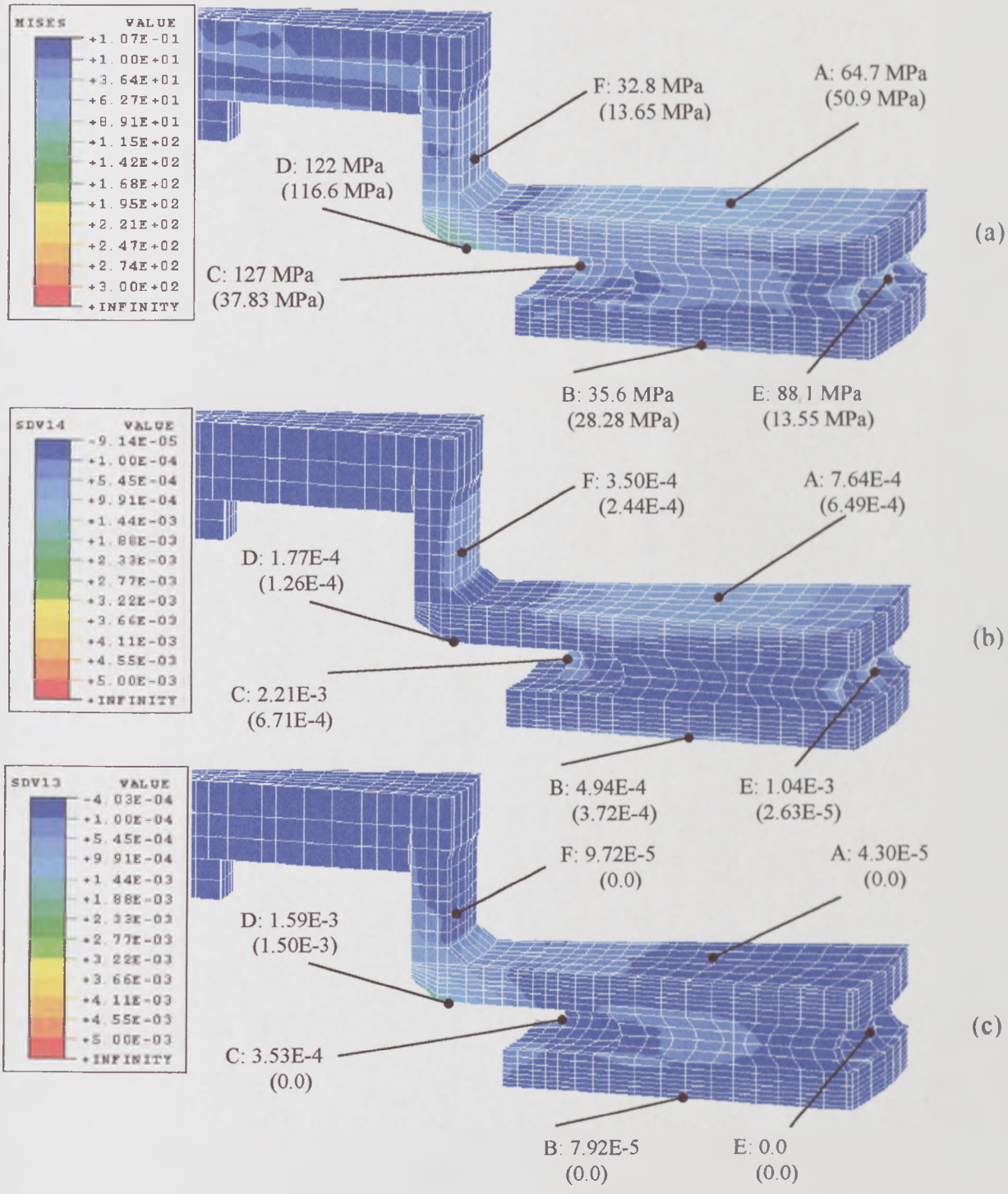

Figure 5.22: Results of inelastic finite element analysis at the end of first cooling period for the front-vented disc with the cast iron user-developed subroutine: (a) von Mises stress, (b) compressive equivalent plastic strain, (c) tensile equivalent plastic strain (Numbers in parentheses indicate the element centroid values of variables)

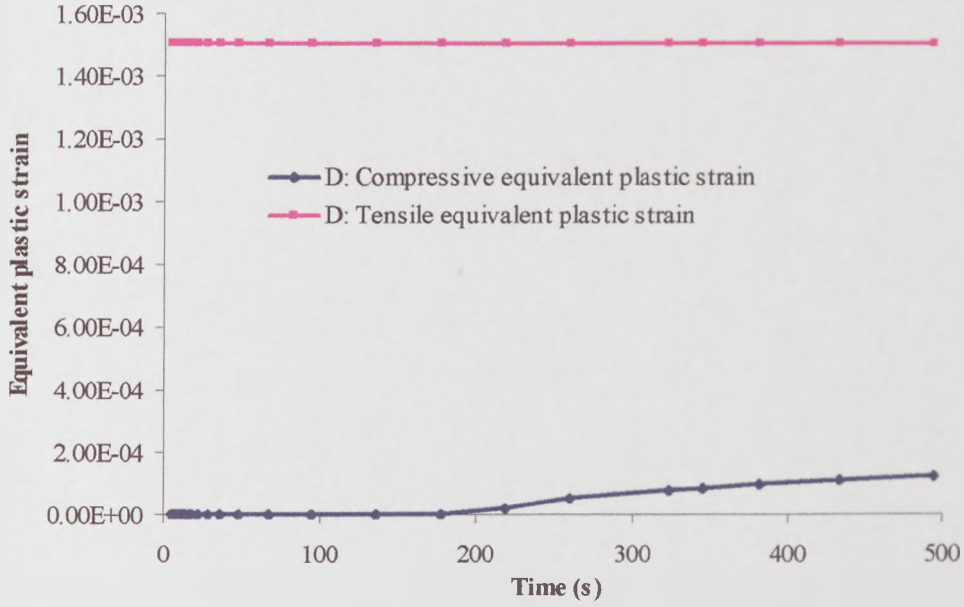

Figure 5.23: Element centroid equivalent plastic strain histories (position D) during first cooling period for the front-vented disc with the cast iron user-developed subroutine

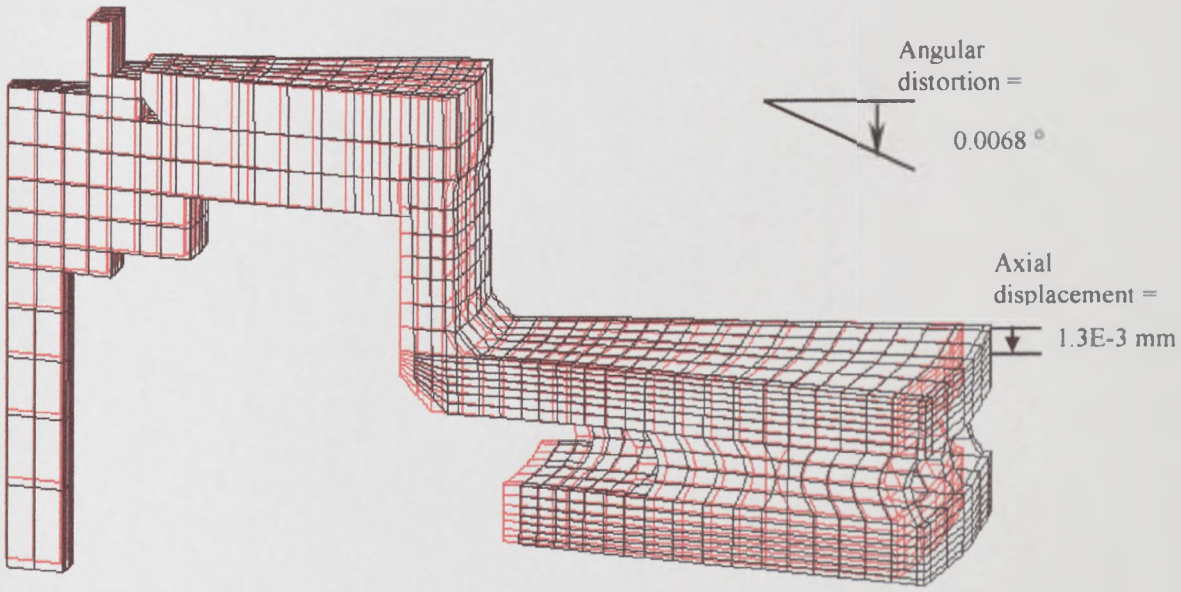

Figure 5.24: Displaced shape at the end of first cooling period for the front-vented disc with the cast iron user-developed subroutine (Red indicates original mesh; Black indicates displaced mesh)

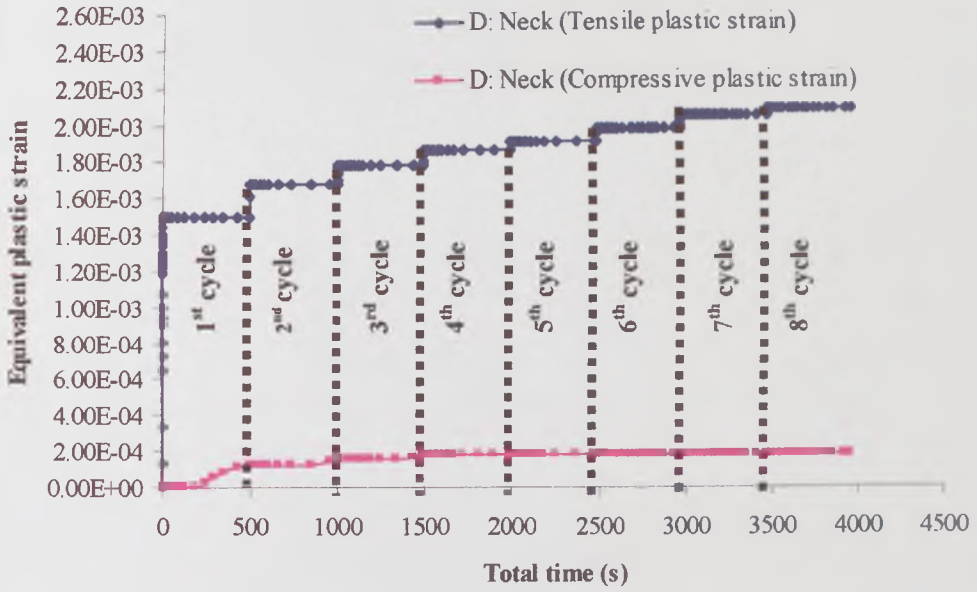

Figure 5.25: Element centroid plastic strain histories for the front-vented disc with the cast iron user-developed subroutine over eight thermal cycles

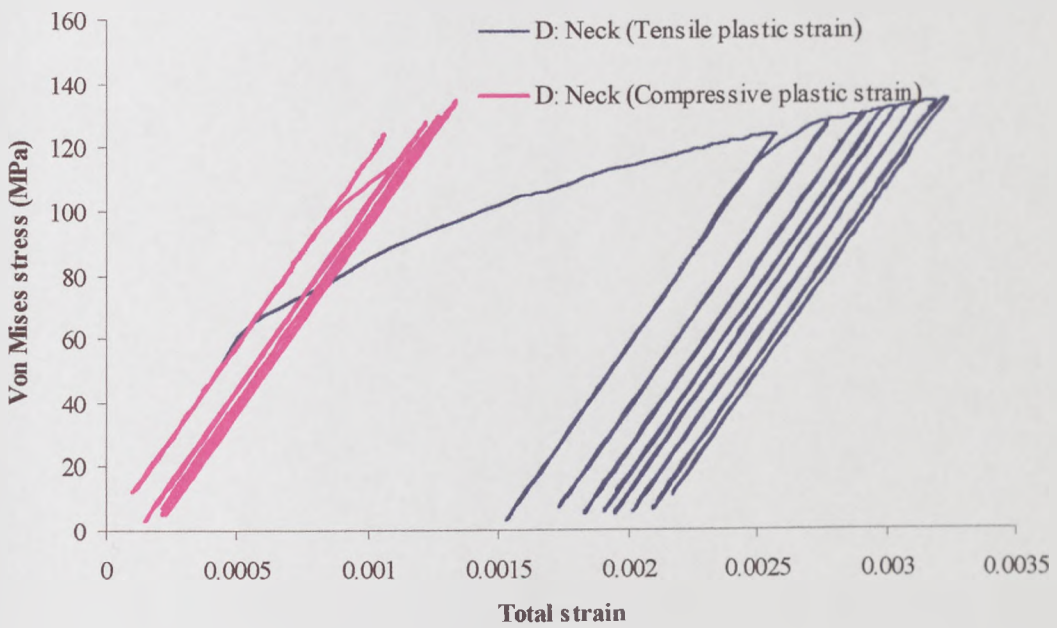

Figure 5.26: Element centroid von Mises stress versus total strain for the front-vented disc with the cast iron user-developed subroutine over eight thermal cycles

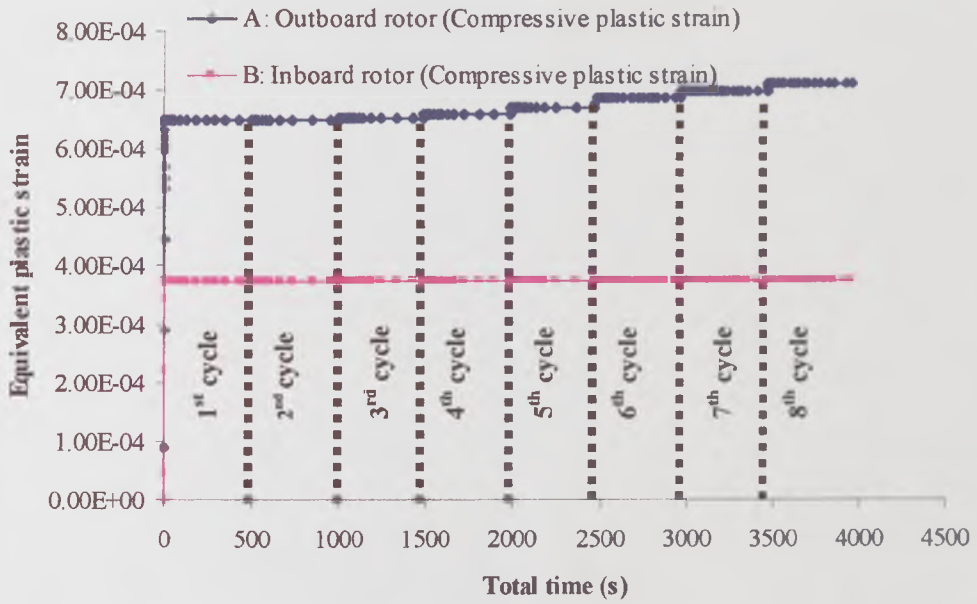

Figure 5.27: Element centroid plastic strain histories for the front-vented disc with the cast iron user-developed subroutine over eight thermal cycles

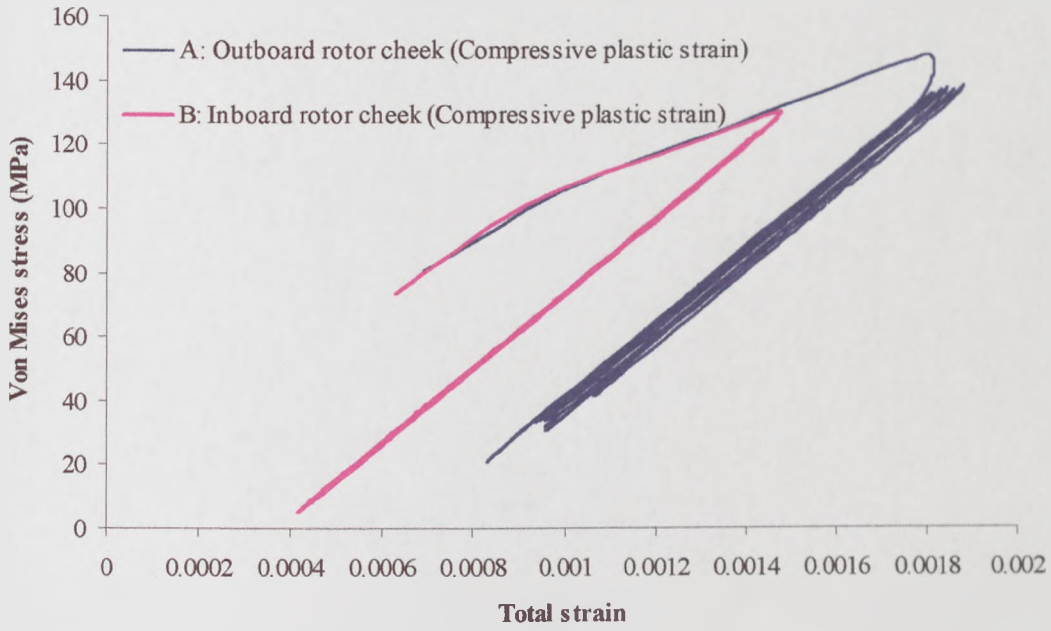

Figure 5.28: Element centroid von Mises stress versus total strain for the front-vented disc with the cast iron user-developed subroutine over eight thermal cycles

CHAPTER 6

DISCUSSION

6.1 TEMPERATURE AND ELASTIC STRESS ANALYSIS

The maximum temperature during the brake application was found on the outboard rubbing surface of the back-vented disc and on the inboard surface of the front-vented disc as was expected because of the different paths for heat conduction to the neck. Furthermore, the results were typical of the response of brake discs during sudden and severe brake applications [21,29]. Therefore, the temperature analysis is sufficiently accurate for the thermal stress analysis considered in this thesis. However, in practice, validation of predicted temperatures against experimental results should ultimately be carried out in order to optimize the heat loss coefficients and give heightened confidence in the results.

The accuracy of the solutions from the elastic thermal analysis depends on whether the calculated stress is within the limit of linear elasticity for the material. For the thermal conditions investigated in Chapter 2, the maximum elastic stresses were higher than this limit which was determined by the material property tests in Chapter 3. However, the elastic stress analysis, which is commonly used in investigating the thermal stress response of brake discs [34,35,38], provided adequately accurate predictions of the gross thermal distortion of the disc. For example, it clearly showed the greater degree of coning expected from a front-vented disc compared with the corresponding back-vented design. However, there was some loss of accuracy of prediction of the maximum deflections compared with the more sophisticated inelastic stress analysis.

6.2 MECHANICAL PROPERTY TESTS

The results of the monotonic loading tests clearly indicated the onset of non-linearity in the stress-strain response of cast iron at relatively low strains. This is particularly true in tension where the effect is attributed to debonding of the graphite flakes and the subsequent plastic deformation of the pearlite matrix. Even in compression, there was significant curvature in the stress-strain curve but the stress at which this initiated was much higher than in tension. The effect of elevated temperature was to significantly increase the strain at a given level of stress, particularly as the temperature was raised from 300 to 400°C. All of these effects should ideally be taken into account in deriving an accurate temperature-dependent non-linear model for the material.

The specially-designed wedge-action grips worked well and allowed stress reversals to be applied to the cast iron specimens without significant backlash effects. The cyclic stress-strain curves generated show that cast iron suffered cyclic softening in the tension part of the cycle and cyclic hardening in compression as reported by Gilbert [16]. However, the present work extended these results to the high temperature range that is experienced by brake discs in service. The incorporation of accurate models of non-linear cyclic hardening into a general-purpose computer code such as ABAQUS is non-trivial and was not attempted as part of this project. In fact, comparison between the CSSC and the corresponding MSSC indicated that the difference was not large. Therefore, a material model based on the latter is a reasonable approximation for studies of repeated thermal cycles in brake discs. No attempt was made to model the low cyclic fatigue properties of the cast iron in the present work and the magnitude of the cyclic plastic strain accumulated was taken as a measure of the damage that may potentially lead to fracture.

6.3 MATERIAL MODELLING

The results from investigating the performance of the ABAQUS standard cast iron material model in Chapter 4 revealed that the model produced simultaneous strain hardening of both the tensile and compressive yield stresses. This was due to the relationship between the equivalent plastic strains in tension and compression which are embodied within the model. Thus under uniaxial load, simultaneous enlargement of the yield surface in tension and compression occurred because of the deviatoric plastic strain that was used to define the equivalent plastic strain in both tension and compression. This contrasts with the assumption that the mechanism of non-linear strain accumulation in tension (i.e. debonding between graphite flakes and matrix metal) is different from that in compression (i.e. normal strain hardening). For this reason, the two mechanisms should not be coupled. In comparison with the experimental results in Chapter 3, the calculated results from the ABAQUS material model wrongly predicted that compressive stress reversals under cyclic loading caused significant strain hardening in tension as well as compression whereas the experimental results indicated cyclic strain softening in tension.

Furthermore, the ABAQUS material model used the Rankine principal stress criterion in tension and the von Mises stress criterion in compression to indicate yield of cast iron. This assumption was based on the typical fracture surface that was found for cast iron under biaxial tension by Grassi and Cornet [40] and Coffin and Schenectady [11]. This is another misleading aspect of the ABAQUS cast iron model since the yield characteristics of cast iron in the tensile region are likely to be close to those of a porous material and can therefore be based on the von Mises stress criterion [11]. This is because debonding of graphite flakes causes voids to develop in the pearlite matrix. According to Tvergaard and Needleman [42,43], the yield surface of a porous material

is a function of the von Mises stress and the hydrostatic pressure. Therefore, it is concluded that the ABAQUS material model for cast iron is unsuitable to use in investigating plastic strain and its subsequent accumulation under cyclic loading within brake discs.

In contrast, the results from the user-developed subroutine material model were more accurate since the tensile plastic strain is independent of the compressive plastic strain and vice versa. This means that the yield surface in tension is expanded only if the stress state is loaded beyond the tensile elastic limit and is not affected by yielding in compression. This will minimise, and in many cases eliminate, the cyclic strain hardening in tension which was not seen experimentally. In addition, the von Mises stress yield surface was used in both tension and compression to simulate the porous material characteristics in tension and the normal metal plasticity in compression. For numerical reasons, a transition zone equivalent to 30 MPa tensile hydrostatic pressure has been introduced between the tensile and compressive yield surfaces within which a linear variation of yield stress was assumed. As a result, the equivalent tensile plastic strain within the mean stress transition zone between tension and compression yield surfaces was initially slightly lower than suggested by the experimental MSSC but this was not a significant effect.

6.4 INELASTIC STRESS ANALYSIS

From application of the user-developed subroutine to the back-vented disc, compressive plastic strain only occurred at the rubbing surfaces which were subjected to compression (i.e. there was no corresponding tensile strain predicted as with the standard ABAQUS model) and vice versa for the areas subject to tensile plastic strain. During the brake application, the outboard rubbing surface (position A) had lower plastic strain

accumulation than the inboard rubbing surface (position B). Position B experienced additional compressive plastic strain increments after five thermal cycles because the high plastic strain accumulation at the neck (position D) also continued to increase during subsequent thermal cycles. The inner radius of the long vane (position C) was subjected to high tensile plastic strain during the brake application followed by compressive plastic strain before the end of the cooling period. Moreover, the tensile plastic strain at position C increased in all subsequent thermal cycles up to and including the eighth thermal cycle considered. However, the compressive plastic strain accumulation at this location became stable after only two thermal cycles.

Since the front-vented disc allowed a greater degree of radial thermal expansion than the back-vented disc, the maximum element centroidal stresses as predicted by the user-developed subroutine at the selected positions were lower. In contrast to the back-vented disc response, the compressive plastic strains at the outboard rubbing surface were higher than at the inboard rubbing surface. Furthermore, the neck was the only area subject to tensile plastic straining which continued to accumulate albeit at lower rate for subsequent thermal cycles. As a result of this accumulation, the compressive plastic strain at the outboard cheek (position A) began to increase after four applications of thermal load.

Even though the front-vented disc experienced less plastic strain accumulation than the back-vented disc, the degree of coning was higher. A practical result of this is that the front-vented disc will experience high local thermal heat flux at the inner and outer rubbing radii of the inboard and outboard rotor surfaces respectively, resulting in higher plastic strain accumulation than predicted by the simple model which assumed a uniform pressure distribution.

The results of the cyclic load tests on the cast iron specimens revealed that the brake disc specimens fractured in tension at a strain of less than 0.0025. Hence, the back-vented disc may experience cracking at the inner radius of the long vane after two applications of thermal load because of the high tensile plastic strain accumulation (0.0026) predicted at this location. For the front-vented disc, the neck area may be subjected to cracking after the eighth thermal cycle because the tensile plastic strain accumulation also became greater than 0.0025. However this prediction of cracking was based on the plastic strain accumulation rather than fatigue analysis. For more accuracy, the fatigue life data of the material should be measured at various strain amplitudes and temperatures, which was beyond the scope of the present work. Note that no significant tensile strains were predicted at the rubbing surfaces for either disc design in contrast with the experimental observations that radial cracking or crazing of rubbing surfaces can occur. This may be because the thermal conditions considered were not severe enough for this particular disc design or because of shortcomings that still exist in the material model such as the inability to predict cyclic strain softening in tension i.e. a contraction of the tensile yield surface as voids grow and damage accumulates in the material.

CHAPTER 7

CONCLUSIONS AND FUTURE WORK

7.1 CONCLUSIONS

The main conclusions drawn from the programme of work reported in this thesis are as follows:

- The FE technique can be used to investigate the temperature response of brake discs during the brake application and subsequent cooling period. However, the validity of the results is dependent on how faithfully the physical boundary conditions and material properties are represented in the analysis.

- Elastic stress analysis was unable to accurately predict the thermal stress response of brake discs because the high temperature gradients during severe brake applications resulted in high thermal stresses beyond the yield strength of the material. However, elastic analysis can be used to investigate the deformations of brake discs under thermal loading. These vary according to the brake disc geometry: a back-vented design provided a much lower degree of disc coning than the corresponding front-vented design but at the expense of higher thermal stresses.

- The monotonic stress-strain curves of the cast iron material from the Rover brake disc became non-linear at low strains indicating plasticity and voiding within the material. Furthermore, they were different in tension and compression and quite sensitive to temperature, particularly as the temperature was raised above 300°C. The effect of cyclic loading on the brake disc cast iron specimens has also been investigated at a variety of temperature conditions. The cast iron material also

displayed cyclic hardening in compression and cyclic softening in tension. Fracture occurred at lower strains in comparison with these under monotonic loading at the same temperature.

- The standard cast iron material model in the widely-used commercial FE package ABAQUS can be used to investigate the stress response of materials that have different stress-strain behaviour in tension and compression. However, this material model used a Rankine yield criterion for yield in tension and a standard von Mises criterion in compression together with non-associated plastic flow rules. Moreover, the equivalent plastic strain in tension is directly related to the associated plastic strain in compression and vice versa. This is despite the fact that the mechanisms for inelastic straining in tension and compression are different due to the effect of the opening and closing of gaps between the graphite flakes and metal matrix. Therefore, this material model is unsuitable for estimating the plastic strain accumulation under cyclic loading in the disc brake thermal stress analysis.

- Based on the assumption of independent plastic strain mechanisms in tension and compression, a user-developed subroutine material model has been developed to represent the cast iron properties with different yield strengths in tension and compression which were also a function of temperature. Furthermore, both tensile and compressive yield surfaces used the von Mises stress criterion with the associated flow rule in order to simplify the material model. In order to provide a smooth transition between tensile and compressive yield regimes, a linear transition zone of 30 MPa hydrostatic pressure has been determined as being near optimum in terms of providing numerical robustness with minimal loss of accuracy of strain prediction.

- The application of the user-developed subroutine material model to the back- and front-vented disc models is more realistic in terms of tensile and compressive plastic strain accumulations. The results indicated that a high compressive plastic strain occurred at the inboard rubbing surface during the brake application for the back-vented disc and at the outboard rubbing surface for the front-vented disc. Moreover, cyclic plastic strain reversals between tension and compression were found at the inner radius of the long vane for the back-vented disc and at the neck area for the front-vented disc. Based on the maximum plastic strain accumulation, the back-vented disc would experience cracking at the inner radius of the long vane with fewer thermal cycle than the front-vented disc for which cracking would occur at the neck area.

- It is thought that the user-developed cast iron material model will find application in the analysis of thermal stress and plastic strain accumulation associated with a wide variety of cast iron components such as, for example, engine blocks and cylinder heads. Furthermore, its use need not be restricted to automotive components.

7.2 FUTURE WORK

There is significant scope for further work and this is summarised below:

- A full 3D analysis of the brake disc including the pads should be considered in order to investigate the effects of rotating heat source and the non-uniform heat flux over the rubbing surfaces due to non-uniform pressure distributions.

- It has not been possible to determine the monotonic and cyclic stress-strain curves on the cast iron material between 25-300°C because of the limitation of the induction heating system. It is important that this is obtained because of the high temperature gradients found during the brake application. Also, the yield surface of cast iron when subject to biaxial loads should be investigated in order to study its anisotropic yield behaviour in tension and compression.

- The fatigue behaviour of the brake disc cast iron material should be investigated over a range of cyclic strain amplitudes in order to predict the fatigue life. Furthermore, the effect of different strain amplitudes in tension and compression should be considered since the damage mechanisms are different.

- Modifying the user-developed subroutine material model for cast iron should be considered in order to simulate the effect of void growth on the yield surface in tension by, for example, the adoption of a Gurson-type yield criterion and associated void growth law [42,43]. In addition, the cyclic softening in tension and hardening in compression should be taken in account.

- A programme of experimental work needs to be undertaken using a full size dynamometer since it can subject the brake to the same sequence of high energy stops that has been modelled in the numerical simulation. This will provide the necessary data needed to validate the model and provide an indication of the location of possible fracture sites.

REFERENCES

[1] **Metzler, H.**, *'The Brake Rotor -Friction Partner of Brake Linings'*, SAE Technical Paper Series: 900847, 1990

[2] **Angus, H. T., Lamb A. D. and Scholes J. P.,** *'Conditions Leading to Failure in Cast Iron Brakes',* BICRA Journal, Vol. 14, No. 4, pp 371-385, 1966

[3] **Limpert, R.**, *'An Investigation of Thermal Conditions Leading to Surface Rupture of Cast Iron Rotors'*, SAE Technical Paper Series: 720447,1972

[4] **Rainbolt, J. D.**, *'Effect of Disk Material Selection on Disk Brake Rotor Configuration'*, SAE Technical Paper Series: 750733,1975

[5] **Ferdani, P. and Holme, J. D.,** *'Some Factors Influencing Rotor and Friction Material Design for Commercial Vehicle Disc Brakes',* Autotech 95, IMechE Paper No C498/12/188, 1995

[6] **Jimbo, Y., Mibe, T., Akiyama, K., Matsui, H., Yoshida, M. and Ozawa, A.**, *'Development of High Thermal Conductivity Cast Iron for Brake Disk Rotors'*, SAE Technical Paper Series: 900002,1990

[7] **Ellis, K.**, *'The Effect of Cast Iron Disc Brake Metallurgy on Friction and Wear Characteristics'*, Automotive Braking: Recent Developments and Future Trends, Barton, D. C. and Haigh, M. J., Eds, PEP, UK, 1998

[8] **Gilbert, G. N. J.**, *'Engineering Data On Gray Cast Irons-- SI Unit'*, British Cast Iron Research Association, BCIRA 1977

[9] **British Standards Institution**, Classification of Gray Cast Iron, BS 1452: 1977, 1977

[10] **Hecht, R. L., Dinwiddie, R. B., Porter, W. D. and Wang, H.**, *'Thermal Transport Properties of Grey Cast Iron'*, SAE Technical Paper Series: 962126,1996

[11] **Coffin, Jr. L. F. and Schenectady, N. Y.,** *'The Flow and Fracture of a Brittle Material'*, Journal of Applied Mechanics, Vol. 17, (Trans. ASME, Vol. 72), pp 233-248, Sept. 1950

[12] **Van Leeuwen, H. O.,** *'Heating Methods in Materials Testing at Elevated temperatures'*, Nationaal Lucht-en Ruimtevaartlaboratorium, The Netherlands, TM-M 2087, April 1961

[13] **Landgraf, R. W., Morrow, J. and Endo, T.,***'Determination of the Cyclic Stress-Strain Curve'*, Journal of Materials, JMLSA, Vol.4 No. 1, pp 176-188, March 1969

[14] **Koibuchi, K. and Kotani, S.**, *'The Role of Cyclic Stress-Strain Behaviour On Fatigue Damage Under Varying Load'*, Cyclic Stress-strain behaviour-Analysis, Experimentation, and Failure Prediction, ASTM STP 519, American Society for Testing and Materials, pp 229-245, 1973

[15] **Coffin Jr., L. F.,** *'Low-Cycle Fatigue'*, American Society for Metals: Metals Engineering Quarterly, Vol. 3, 1963

[16] **Gilbert, G. N. J.**, *'The Cyclic Stress/Strain Properties and Fatigue Properties of a Flake Graphite Cast Iron Tested under Strain-Controlled-a Detailed Study'*, British Cast Iron Research Association, BCIRA 1985

[17] **Slot, T., Stentz, R. H. and Berling, J. T.,** *'Controlled-Strain Testing Procedures'*, Manual on Low Cyclic Fatigue Testing, ASTM STP 465, American Society for Testing and Materials, pp 100-128, 1969

[18] **Carden, A. E.,** *'Fatigue at Elevated Temperatures: A Review of Test Methods,'* Fatigue at Elevated Temperature ASTM STP 520, American society for Testing and Materials, pp 195-223, 1973

[19] **Dike, G.**, *'Temperature Distribution in Disc Brakes'*, Transactions of Machine Element Division, Lund Technical University, Lund, Sweden, 1976

[20] **Blot, B.**, *'Computation of a thermally stressed brake disc'*, SAE Technical Paper Series: 890086,1989

[21] **Sheridan, D. C., Kutchey, J. A. and Samie, F.**, *'Approaches to the Thermal Modeling of Disc Brakes'*, SAE Technical Paper Series: 880256, 1988

[22] **Yano, M. and Murata, M.**, *'Heat flow on Disc brakes'*, SAE Technical Paper Series: 931084, 1993

[23] **Samie, F. and Sheridan, D. C.**, *'Contact analysis for a passenger car disc brake'*, SAE Technical Paper Series: 900005, 1990

[24] **Lee, Y. S., Brooks, P. C., Barton, D. C. and Crolla, D. A.**, *'A Study of Disc Brake Squeal Propensity Using a Parametric Finite Element Model'*, Vehicle Noise and Vibration, IMechE Conference Transactions No C521/009/98,1998

[25] **Richmond, J. W., Kao, T. K., and Moore M. W.**, *'The Development of Computational Analysis Techniques for Disc Brake Pad Design'*, Advances in Automotive Braking Technology: Design Analysis and Material, Weetwood Hall, Leeds, UK, 1996

[26] **Rinsdorf, A.**, *'Evaluation of the energy input in pad and disc during a brake application'*, SAE Technical Paper Series: 942086, 1994

[27] **Tirovic, M. and Day, A. J.**, *'Disc brake interface pressure distributions'*, Proc. Instn Mech Engrs Vol. 205, pp 137-146, 1991

[28] **Limpert, R.**, *'The Thermal Performance of Automotive Disc Brakes'*, SAE Technical Paper Series: 750873, 1975

[29] **Noyes, R. N. and Vickers P. T.**, *'Prediction of Surface Temperatures in Passenger Car Disc Brakes'*, SAE Technical Paper Series: 690457,1969

[30] **Schwartz, H. W., Hartter, L. L., Rhee, S. K., and Byers, J. E.**, *'Evaluation of Gray Iron Brake Discs for Trucks by Thermal Modelling'*, SAE Technical Paper Series: 751013,1975

[31] **Dennis, R. W., Newstead, C., Ede, A. J.**, *'The Heat Transfer From a Rotating Disc in an air crossflow'*, Proc. 4th, Int. Heat Transfer Conf. Paris, 1970

[32] **Cobb, E. C. and Saunders, O. A.,** *'Heat Transfer from a Rotating Disk'*, Proc. Royal Society (Series A), Vol. 236, pp 343-351, 1956

[33] **Daudi, A. R., Dickerson, W. E. and Narain, M.**, *'Hayes' Increased Airflow Rotor Design'*, Automotive Braking: Recent Developments and Future Trends, Barton, D. C. and Haigh, M. J., Eds, PEP, UK, 1998

[34] **Fukano, A. and Matsui, H.**, *'Development of Disc-Brake Design Method Using Computer Simulation of Heat Phenomena'*, SAE Technical Paper Series 860634, 1986

[35] **Timtner, K. H.**, *'Calculation of Disc Brakes Components Using the Finite Element Method with Emphasis on Weight Deduction'*, SAE Technical Paper Series: 790396, 1979

[36] **Bailey, T. P., Buckingham, J. T. and D'cruz, A. H.**, *'Optimisation of Brake Disc Design using Thermal Imaging and Finite Element Techniques'*, Autotech, 1991

[37] **D'Cruz, A. H.,** *'Surface Crack Initiation in Ventilated Disc Brakes under Transient Thermal Loading'*, Paper C382/05, IMechE, 1989

[38] **Medonos, S.**, *'Study of Structural Behaviour of Ventilated Brake Disc'*, SAE Technical Paper Series: 831316, 1983

[39] **Downling, N. E.**, *'Mechanical Behaviour of Materials: Engineering Methods for Deformation, Fracture, and Fatigue'*, Prentice-Hall Interantional Editions, pp 252, 1993

[40] **Grassi, R., C. and Cornet, I.,** *'Fracture of Gray Cast Iron Tubes under Biaxial Stresses'*, Jnl. of Applied Mechanics, Vol. 16 (Trans. ASME, Vol. 71), pp 178-182, June 1949

[41] **ABAQUS**, Version 5.7, Hibbitt, Karlsson and Sorensen, Inc., 1997

[42] **Tvergaard, V.,** *'Ductile Fracture by Cavity Nucleation between Larger Voids'*, Journal of the Mechanics and Physics of Solids,Vol. 30, No. 4, pp 265-286, 1982

[43] **Tvergaard, V., and Needleman, A.** *'Analysis of the Cup-cone Fracture in a Round Tensile Bar'*, Acta Metallurgic, Vol. 32, No. 1, pp 157-169, 1984

[44] **Josefson, B. L., Stigh, U. and Hjelm, H. E.,** *'A Nonlinear Kinematic Hardening Model for Elastoplastic Deformations in Grey Cast Iron'*, Journal of Engineering Materials and Technology, Vol. 117/145, April, 1995

[45] **Hillier, V.A.W.,** *'Fundamentals of Motor Vehicle Technology'*, 4th Edition, Stanley Thornes (Publishers) Ltd, pp 386, 1991

[46] **Automotive Handbook**, SAE Society of Automotive Engineerings, 3rd Edition, Robert Bosch GmbH, ISBN 1-56091-372-X, 1993

[47] **Manson, S. S.,***'Thermal Stress and Low-cyclic Fatigue'*, McGraw-Hill, New York, pp 126-129,1966

[48] **Private communication from RD1 Brake and Controls Department**, Rover Company, UK

[49] **Zienkiewicz, O. C.,***'The Finite Element Method in Engineering Science'*, McGraw-Hill, London, pp 33-35,1971

[50] **Koetniyom, S.,** Transfer Report for PhD, Mechanical Engineering, University of Leeds,1997

[51] **Baker, A. K.,** *'Vehicle Braking'*, Pentech Press London: Plymouth, pp 284-286, 1986

[52] **Society of Automotive Engineerings (SAE),** Automotive Handbook, 3rd Edition, 1993

[53] **Kao, T., Richmond, J. W. and Moore, M. W.,** *'The Application of Predictive Techniques to Study Thermo-elastic Instability of Brakes'*, SAE technical Paper Series SAE 942087, 1994

[54] **Grieve, D. G., Barton, D. C., Crolla, D. A. and Buckingham, J. T.,** *'Design of a Lightweight Automotive Brake Disc using Finite Element and Taguchi Techniques'*, Proc. Instn. Mech. Engrs, 212, Part D, 1998

[55] **British Standards Institution**, BS EN 10 002-1:1990, *'Tensile Testing of Metallic Materials: Part1. Method of test at ambient temperature'*, 1990

[56] **RS Components**, Macor Mechanical Ceramic Material, 232-5418, Po Box 99, Corby, Northants, NN17 9RS, 1997

[57] **Wegner, R. and Ettemeyer**, A., *'Fast Stress and Strain Analysis with MicroStar'*, Dr. Ettemeyer Application Report, No. 05-98, Dr Ettemeyer GmbH and Co. Heinz-Ruhmann-Str. 207, D-89231 Neu-Ulm, Germany

[58] **Khan. A. S. and Huang Sujian**, *'Continuum Theory of Plasticity'*, John Wiley and Sons, pp 82-87, 1995

[59] **Blazynski, T. Z.**, *'Applied Elasto-plasticity of Solids'*, Macmillan Press, London, pp 30-38, 1983

[60] **Stouffer, D. C. and Dame, L. T.,** *'Inelastic Deformation of Metals: Models, Mechanical Properties, and Metallurgy'*, John Wiley and Sons, pp 207-213, 1996

[61] **Crisfield, M. A.,** *'Non-linear Finite Element Analysis of Solids and Structures'*, Volume 1, John Wiley and Sons, pp 152-178, 1995

APPENDICES

APPENDIX 1: TEST EQUIPMENT

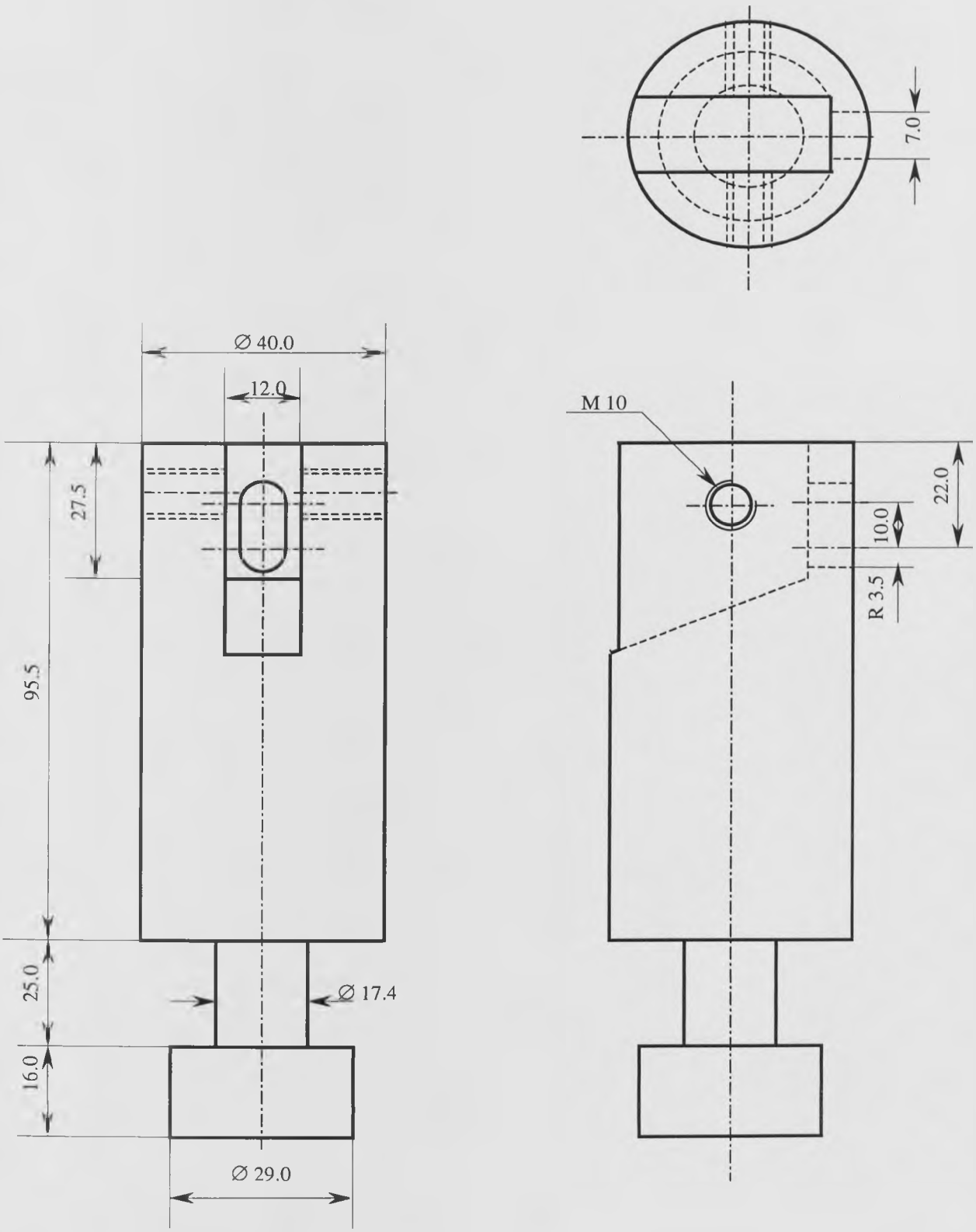

Figure 1A: Upper grip dimension (unit in mm)

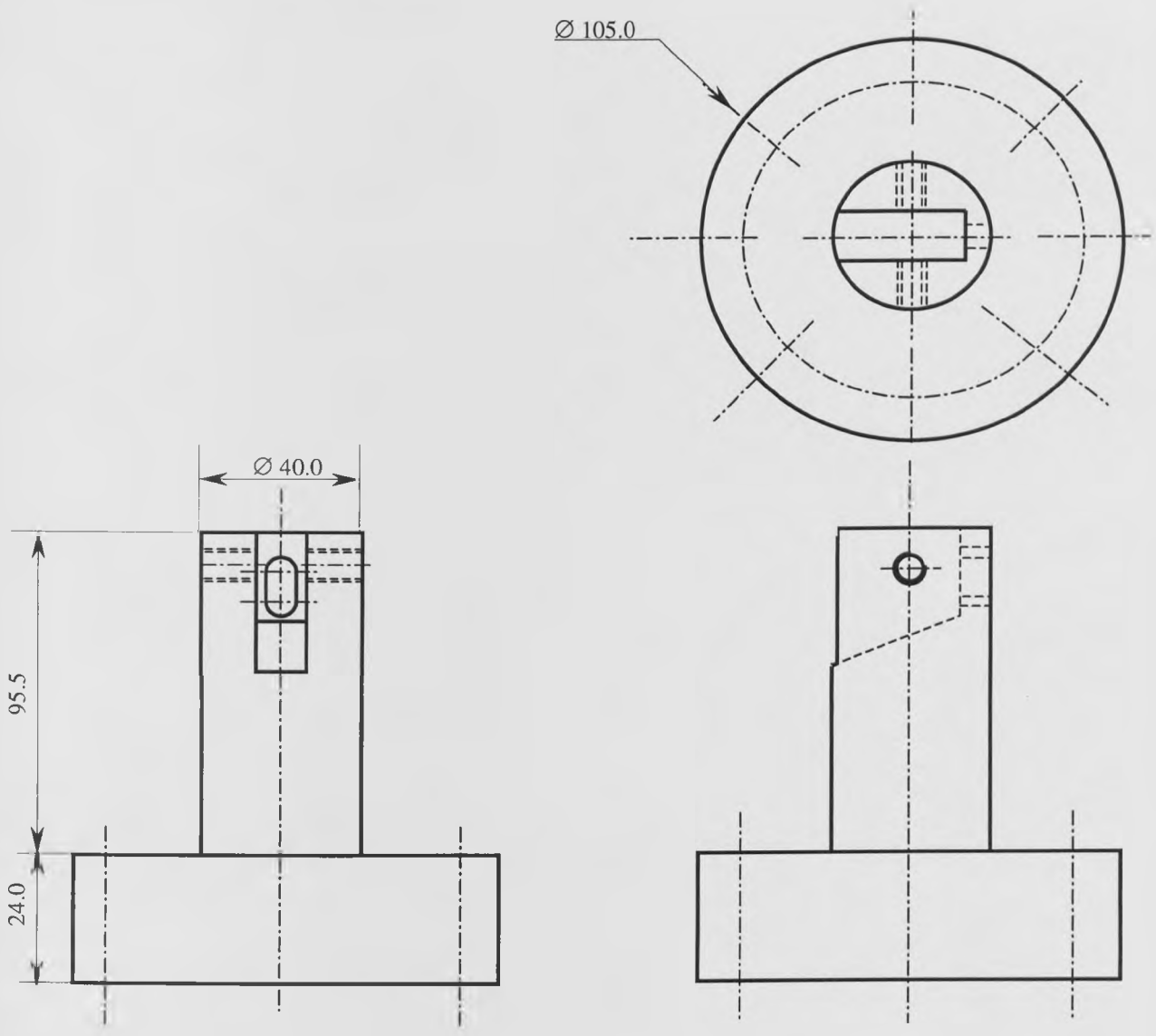

Figure 1B: Lower grip dimension (unit in mm; dimension at the head is the same as the lower grip dimension)

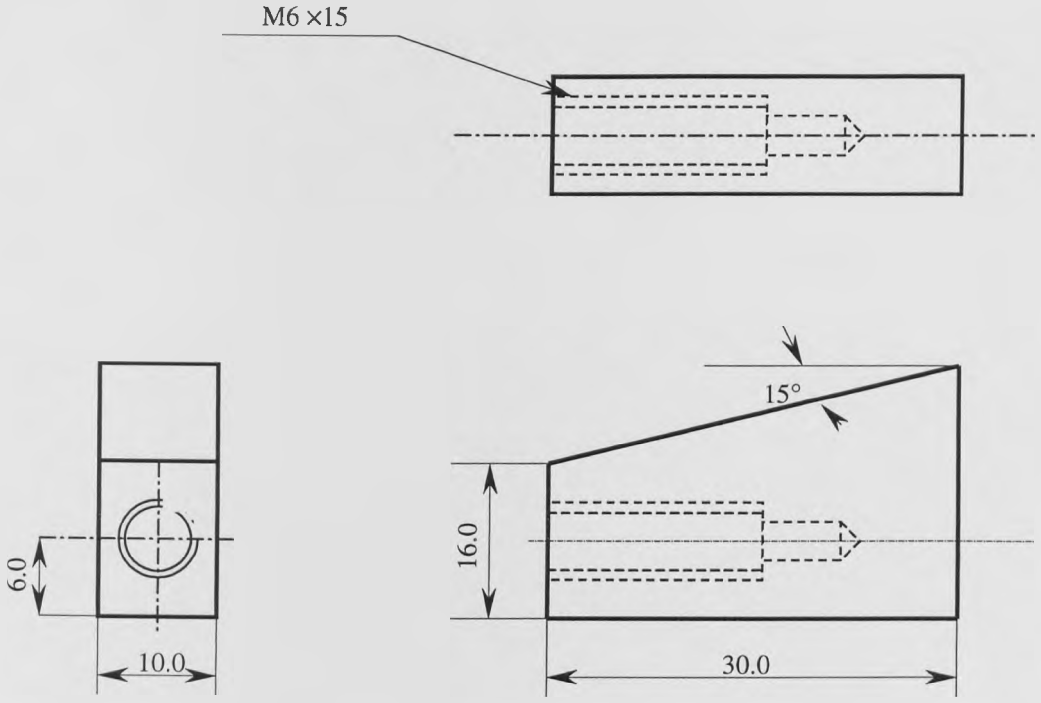

Figure 1C: Wedge dimension (unit in mm)

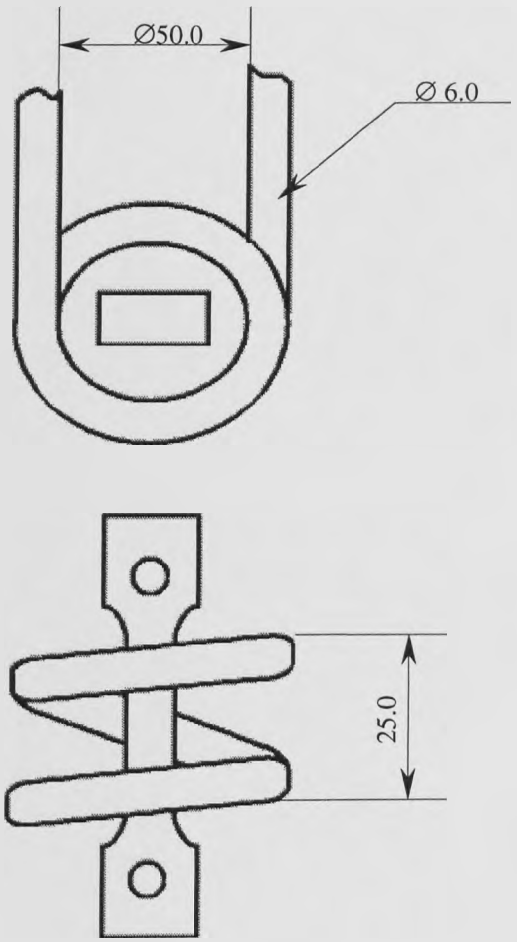

Figure 1D: Induction coil dimension (unit in mm)

APPENDIX 2: CALIBRATION OF DATA ACQUISITION WITH LOAD CELL FROM DARTEC MACHINE

It is essential to calibrate the voltage signal from the PC based 'Labtech' data acquisition by applying a tensile test on a specimen. The Labtech input signal data obtained from the load cell of Dartec machine were linearly interpolated in order to determine the external load value. Comparison between the Labtech load with the self-recording load history data of Dartec machine that has been regularly calibrated by the Dartec company is shown in Figure 2A. It reveals that the data acquisition is efficiently accurate to be used for recording voltage signals from either a load cell or a strain gauge.

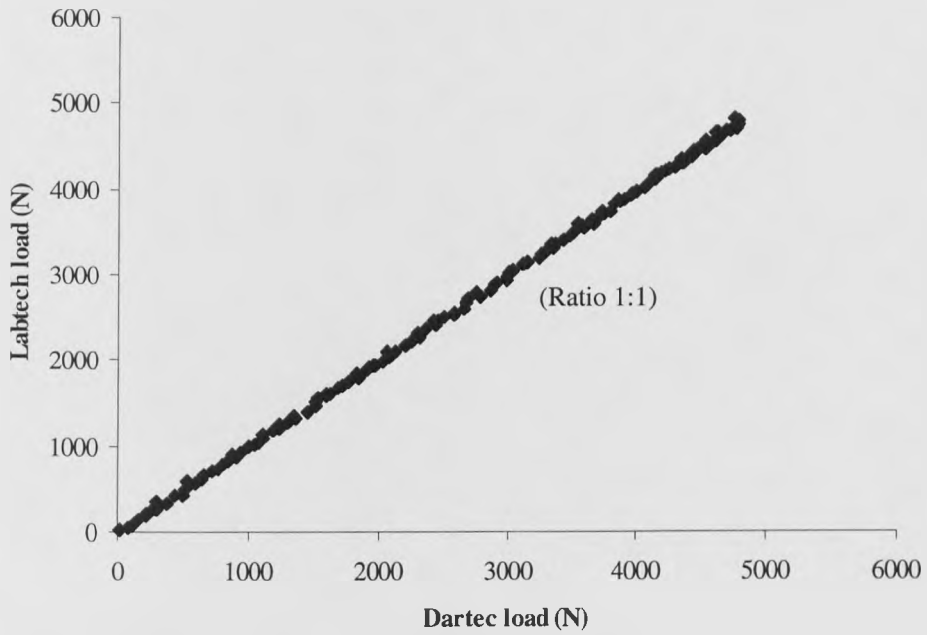

Figure 2A: Data comparison between Dartec machine and Labtech acquisition

APPENDIX 3: CAST IRON MATERIAL PROPERTIES

Temperature (°C)	Conductivity (W/mm/°C)	Specific heat (J/kg/°C)	Coefficient of linear thermal expansion (K^{-1})	Poisson's ratio	Density (kg m^{-3})
20	0.0533	103	10.42E-6	0.26	7050
100	0.0525	247	N/A	0.26	7050
200	0.0515	427	11.58E-6	0.26	7050
300	0.0505	607	N/A	0.26	7050
400	0.0495	697	14.58E-6	0.26	7050

Table 3A: Grade 150 cast iron material properties for temperature and stress analysis [8]

Plastic Poisson's ratio [11]: 0.039

Young's modulus: 116.5 GPa

True tensile plastic strain	True tensile stress (MPa) at 25°C	True tensile stress (MPa) at 300°C	True tensile stress (MPa) at 350°C	True tensile stress (MPa) at 400°C
0.0000	65.00	47.00	19.00	13.00
0.0002	82.02	65.01	45.01	38.01
0.0004	95.04	75.03	58.82	50.02
0.0006	104.06	83.05	68.04	59.04
0.0008	110.09	89.07	76.06	67.05
0.0010	117.12	95.10	83.08	74.07
0.0012	122.15	99.72	88.61	78.09
0.0014	126.68	104.15	93.13	82.92
0.0016	130.71	107.97	97.16	86.14
0.0018	134.74	111.80	99.68	89.76
0.0020	138.28	115.23	103.71	92.48
0.0022	140.81	118.26	106.23	96.21
0.0024	143.84	120.29	108.76	97.73
0.0026	146.38	122.82	111.29	100.26
0.0028	148.41	124.35	113.82	101.78
0.0030	151.45	125.88	115.85	104.31
0.0032	153.49	128.11	117.88	105.34
0.0034	155.03	129.94	118.90	107.16
0.0036	156.56	131.47	120.93	108.89

Table 3B: True stress-plastic strain input data in tension for stress analysis

True compressive plastic strain	True compressive stress at 25°C	True compressive stress 300 °C	True compressive stress 350 °C	True compressive stress 400 °C
0.0000	105.00	89.00	77.00	68.00
0.0010	220.22	198.20	160.17	141.17
0.0020	270.54	242.48	202.42	173.40
0.0030	301.90	265.80	233.73	193.66
0.0040	326.30	284.13	252.04	207.94
0.0050	343.71	299.49	269.39	218.23
0.0060	357.13	309.85	281.74	226.52
0.0070	370.58	321.23	291.09	234.83
0.0080	380.02	329.62	300.46	242.14
0.0090	392.50	336.00	307.84	246.45
0.0100	400.97	345.42	316.23	252.78
0.0109	409.46	351.83	322.62	257.10
0.0119	415.93	359.26	330.03	261.43
0.0129	424.45	365.69	336.45	265.77
0.0139	430.95	371.12	341.86	268.09

Table 3C: True stress-plastic strain input data in compression for stress analysis

APPENDIX 4: USER-DEVELOPED STANDARD MATERIAL MODEL WITH ISOTROPIC HARDENING

```
*DEPVAR
14
*USER SUBROUTINE
      SUBROUTINE UMAT(STRESS,STATEV,DDSDDE,SSE,SPD,SCD,
     1 RPL,DDSDDT,DRPLDE,DRPLDT,STRAN,DSTRAN,
     2 TIME,DTIME,TEMP,DTEMP,PREDEF,DPRED,MATERL,NDI,NSHR,NTENS,
     3 NSTATV,PROPS,NPROPS,COORDS,DROT,PNEWDT,CELENT,
     4 DFGRD0,DFGRD1,NOEL,NPT,KSLAY,KSPT,KSTEP,KINC)
C
      INCLUDE 'ABA_PARAM.INC'
C
      CHARACTER*8 MATERL
      DIMENSION STRESS(NTENS),STATEV(NSTATV),
     1 DDSDDE(NTENS,NTENS),DDSDDT(NTENS),DRPLDE(NTENS),
     2 STRAN(NTENS),DSTRAN(NTENS),TIME(2),PREDEF(1),DPRED(1),
     3 PROPS(NPROPS),COORDS(3),DROT(3,3),
     4 DFGRD0(3,3),DFGRD1(3,3)

      REAL VALUE,X,EQPLAS1,SHYDRO,SYIELD,HARD,DEQPL,SYIEL0,Y
C
      DIMENSION EELAS(6),EPLAS(6),FLOW(6)
      DIMENSION ETHERM(6),DTHERM(6),DELDSE(6,6)
      PARAMETER (ONE=1.0D0,TWO=2.0D0,THREE=3.0D0,SIX=6.0D0)
      DATA NEWTON,TOLER/10,1.D-6/
C
C -------------------------------------------------------------
C     UMAT FOR ISOTROPIC ELASTICITY AND ISOTROPIC PLASTICITY
C
C     CAN NOT BE USED FOR PLANE STRESS
C -------------------------------------------------------------
C     PROPS(1) - E
C     PROPS(2) - NU
C
C     CALLS UHARD FOR CURVE OF SYIELD VS. PEEQ
C -------------------------------------------------------------
C
      IF (NDI.NE.3) THEN
        WRITE(6,1)
 1      FORMAT(//,30X,'***ERROR - THIS UMAT MAY ONLY BE USED FOR ',
     1         'ELEMENTS WITH THREE DIRECT STRESS COMPONENTS')
      ENDIF
C
C     ELASTIC PROPERTIES
C
C
C ASSIGN YOUNG'S MODULUS AND POISSON'S RATIO
      EMOD0=116500.0
      ENU=0.26
C DETERMINE ELASTIC STIFFNESS MATRIX
    IF(ENU.GT.0.4999.AND.ENU.LT.0.5001) ENU=0.499
      EBULK30=EMOD0/(ONE-TWO*ENU)
      EG20=EMOD0/(ONE+ENU)
      EG0=EG20/TWO
      EG30=THREE*EG0
      ELAM0=(EBULK30-EG20)/THREE

C FOR TEMPERATURE INCREMENT
      EMOD=116500.0
      EBULK3=EMOD/(ONE-TWO*ENU)
      EG2=EMOD/(ONE+ENU)
      EG=EG2/TWO
      EG3=THREE*EG
      ELAM=(EBULK3-EG2)/THREE
C  ELASTIC STIFFNESS AT THE END OF INCREMENT AND STIFFNESS CHANGE
C
      DO 20 K1=1,NTENS
        DO 10 K2=1,NTENS
          DDSDDE(K2,K1)=0.0
          DELDSE(K2,K1)=0.0
 10     CONTINUE
 20   CONTINUE
```

```
C
      DO 40 K1=1,NDI
       DO 30 K2=1,NDI
         DDSDDE(K2,K1)=ELAM
         DELDSE(K2,K1)=ELAM-ELAM0
 30    CONTINUE
       DDSDDE(K1,K1)=EG2+ELAM
       DELDSE(K1,K1)=EG2+ELAM-EG20-ELAM0
 40   CONTINUE
      DO 50 K1=NDI+1,NTENS
       DDSDDE(K1,K1)=EG
       DELDSE(K1,K1)=EG-EG0
 50   CONTINUE
C
     VALUE = TEMP+DTEMP
C ASSIGN THE EXPANSION COEFFIICIENT
      IF (VALUE .LT. 200.0) THEN
       EXPAN_C=0.00001
      ELSE
       EXPAN_C=0.0000125
      END IF
C    CALCULATE THERMAL EXPANSION
      DO K1 =1, NDI
       ETHERM(K1)=EXPAN_C*TEMP
       DTHERM(K1)=EXPAN_C*DTEMP
      END DO
C    CALCULATE STRESS FROM ELASTIC STRAINS AND THERMAL STRAIN
C
      DO K1=NDI+1,NTENS
        ETHERM(K1) = 0.0
        DTHERM(K1) = 0.0
      END DO
      DO 70 K1=1,NTENS
       DO 60 K2=1,NTENS
         STRESS(K2)=STRESS(K2)+DDSDDE(K2,K1)*(DSTRAN(K1)-DTHERM(K1))
     1                +DELDSE(K2,K1)*( STRAN(K1)-ETHERM(K1))
 60    CONTINUE
       ETHERM(K1)=ETHERM(K1)+DTHERM(K1)
 70   CONTINUE
C
C    RECOVER ELASTIC AND PLASTIC STRAINS
C
      DO 80 K1=1,NTENS
        EELAS(K1)=STATEV(K1)+DSTRAN(K1)-ETHERM(K1)
        EPLAS(K1)=STATEV(K1+NTENS)
 80   CONTINUE
      EQPLAS=STATEV(1+2*NTENS)
      EQPLAS1=STATEV(1+2*NTENS+1)
C
C    IF NO YIELD STRESS IS GIVEN, MATERIAL IS TAKEN TO BE ELASTIC
C
      IF(NPROPS.GT.2.AND.PROPS(3).GT.0.0) THEN
C
C      MISES STRESS
C
       SHYDRO=(STRESS(1)+STRESS(2)+STRESS(3))/THREE
       SMISES=(STRESS(1)-STRESS(2))*(STRESS(1)-STRESS(2)) +
     1        (STRESS(2)-STRESS(3))*(STRESS(2)-STRESS(3)) +
     1        (STRESS(3)-STRESS(1))*(STRESS(3)-STRESS(1))
       DO 90 K1=NDI+1,NTENS
          SMISES=SMISES+SIX*STRESS(K1)*STRESS(K1)
 90    CONTINUE
       SMISES=SQRT(SMISES/TWO)
C
C      HARDENING CURVE, GET YIELD STRESS
C
        X = EQPLAS
        Y = EQPLAS1
     CALL UHARD(SYIEL0,HARD,X,VALUE,SHYDRO,Y)
C      DETERMINE IF ACTIVELY YIELDING
C
       IF (SMISES.GT.(1.0+TOLER)*SYIEL0) THEN
C
C        FLOW DIRECTION
C
        SHYDRO=(STRESS(1)+STRESS(2)+STRESS(3))/THREE
        ONESY=ONE/SMISES
        DO 110 K1=1,NDI
```

```
        FLOW(K1)=ONESY*(STRESS(K1)-SHYDRO)
 110    CONTINUE
        DO 120 K1=NDI+1,NTENS
          FLOW(K1)=STRESS(K1)*ONESY
 120    CONTINUE
C
C     SOLVE FOR EQUIV STRESS AND PLASTIC STRAIN
C
      SYIELD=SYIEL0
      DEQPL=0.0
      DO 130 KEWTON=1,NEWTON
        RHS=SMISES-EG3*DEQPL-SYIELD
        DEQPL=DEQPL+RHS/(EG3+HARD)
        CALL UHARD(SYIELD,HARD,X+DEQPL,VALUE,SHYDRO,Y)
        IF(ABS(RHS).LT.TOLER*SYIEL0) GOTO 140
 130    CONTINUE
      WRITE(6,2) NEWTON
 2     FORMAT(//,30X,'***WARNING - PLASTICITY ALGORITHM DID NOT ',
     1    'CONVERGE AFTER ',I3,' ITERATIONS')
 140    CONTINUE
      EFFHRD=EG3*HARD/(EG3+HARD)
C
C     CALC STRESS AND UPDATE STRAINS
C
      DO 150 K1=1,NDI
        STRESS(K1)=FLOW(K1)*SYIELD+SHYDRO
        EPLAS(K1)=EPLAS(K1)+THREE*FLOW(K1)*DEQPL/TWO
        EELAS(K1)=EELAS(K1)-THREE*FLOW(K1)*DEQPL/TWO
 150    CONTINUE
      DO 160 K1=NDI+1,NTENS
        STRESS(K1)=FLOW(K1)*SYIELD
        EPLAS(K1)=EPLAS(K1)+THREE*FLOW(K1)*DEQPL
        EELAS(K1)=EELAS(K1)-THREE*FLOW(K1)*DEQPL
 160    CONTINUE
      X=X+DEQPL
      SPD=DEQPL*(SYIEL0+SYIELD)/TWO
C
C     UPDATE JACOBIAN
C
      EFFG=EG*SYIELD/SMISES
      EFFG2=TWO*EFFG
      EFFG3=THREE*EFFG2/TWO
      EFFLAM=(EBULK3-EFFG2)/THREE
      DO 220 K1=1,NDI
        DO 210 K2=1,NDI
          DDSDDE(K2,K1)=EFFLAM
 210      CONTINUE
        DDSDDE(K1,K1)=EFFG2+EFFLAM
 220    CONTINUE
      DO 230 K1=NDI+1,NTENS
        DDSDDE(K1,K1)=EFFG
 230    CONTINUE
      DO 250 K1=1,NTENS
        DO 240 K2=1,NTENS
          DDSDDE(K2,K1)=DDSDDE(K2,K1)+FLOW(K2)*FLOW(K1)
     1                  *(EFFHRD-EFFG3)
 240      CONTINUE
 250    CONTINUE
    ENDIF
   ENDIF
C
C STORE STRAINS IN STATE VARIABLE ARRAY
C
   DO 310 K1=1,NTENS
    STATEV(K1)=EELAS(K1)
    STATEV(K1+NTENS)=EPLAS(K1)
310  CONTINUE
   STATEV(1+2*NTENS)=X
C
   RETURN
   END
C
C  SUBROUTINE FOR DETERMING YIELD STRESS AND PLASTIC STRAIN
   SUBROUTINE UHARD(SYIELDD,HARDD,IN_X,TEMP,HYDRO,IN_Y)
C    INCLUDE 'ABA_PARAM.INC'
   REAL  TABLE(2,15),HARDD,DDDEQPL,TABLE1(2,19)
   REAL  TEMP,HYDRO,IN_X,EQPL0,EQPL1,DSYIEL,SYIEL11,SYIEL00
   REAL  SYIELDD
```

```
      REAL YIELDD,YHARDD,YEQPL1,IN_Y,YEQPL0,YDDEQPL
      REAL YYIEL00,YYIEL11,YDSYIEL
      REAL XIELDD,XHARDD,XEQPL1,XEQPL0,XDDEQPL
      REAL XYIEL00,XYIEL11,XDSYIEL
C
      NVALUE = 15
      NVALUE1 = 19
C
C     ASSIGN THE VALUE OF STRESS STRAIN CURVE
C
C      TENSION STRESS STRAIN CURVE
C     TENSION REGION
C
          IF (TEMP .LT. 25.0) THEN
            TABLE1(1,1) =65.0
          ELSEIF ((TEMP .GE. 25.0) .AND. (TEMP .LT. 300.0)) THEN
            TABLE1(1,1) = -0.065455*TEMP + 66.636364
          ELSEIF ((TEMP .GE. 300.0) .AND. (TEMP .LT. 350.0)) THEN
            TABLE1(1,1) = -0.56*TEMP + 215
          ELSEIF ((TEMP .GE. 350.0) .AND. (TEMP .LT. 400.0)) THEN
            TABLE1(1,1) =-0.12*TEMP + 61
          ELSE
            TABLE1(1,1) =13.0
          ENDIF
C
          IF (TEMP .LT. 25.0) THEN
            TABLE1(1,2) =82.0164
          ELSEIF ((TEMP .GE. 25.0) .AND. (TEMP .LT. 300.0)) THEN
            TABLE1(1,2) = -0.061831*TEMP + 83.562164
          ELSEIF ((TEMP .GE. 300.0) .AND. (TEMP .LT. 350.0)) THEN
            TABLE1(1,2) = -0.4000800*TEMP + 185.0370000
          ELSEIF ((TEMP .GE. 350.0) .AND. (TEMP .LT. 400.0)) THEN
            TABLE1(1,2) = -0.1400280*TEMP + 94.0188000
          ELSE
            TABLE1(1,2) = 38.0076
          ENDIF
C
          IF (TEMP .LT. 25.0) THEN
            TABLE1(1,3) =95.038
          ELSEIF ((TEMP .GE. 25.0) .AND. (TEMP .LT. 300.0)) THEN
            TABLE1(1,3) =  -0.0727564*TEMP + 96.8569091
          ELSEIF ((TEMP .GE. 300.0) .AND. (TEMP .LT. 350.0)) THEN
            TABLE1(1,3) = -0.3241296*TEMP + 172.2688800
          ELSEIF ((TEMP .GE. 350.0) .AND. (TEMP .LT. 400.0)) THEN
            TABLE1(1,3) = -0.1760704*TEMP + 120.448160
          ELSE
            TABLE1(1,3) =50.02
          ENDIF
C
          IF (TEMP .LT. 25.0) THEN
            TABLE1(1,4) =104.0624
          ELSEIF ((TEMP .GE. 25.0) .AND. (TEMP .LT. 300.0)) THEN
            TABLE1(1,4) =  -0.0764095*TEMP + 105.9726364
          ELSEIF ((TEMP .GE. 300.0) .AND. (TEMP .LT. 350.0)) THEN
            TABLE1(1,4) = -0.3001800*TEMP + 173.1038000
          ELSEIF ((TEMP .GE. 350.0) .AND. (TEMP .LT. 400.0)) THEN
            TABLE1(1,4) =-0.1801080*TEMP + 131.0786000
          ELSE
            TABLE1(1,4) =59.0354
          ENDIF
C
          IF (TEMP .LT. 25.0) THEN
            TABLE1(1,5) =110.088
          ELSEIF ((TEMP .GE. 25.0) .AND. (TEMP .LT. 300.0)) THEN
            TABLE1(1,5) =  -0.0764247*TEMP + 111.9986182
          ELSEIF ((TEMP .GE. 300.0) .AND. (TEMP .LT. 350.0)) THEN
            TABLE1(1,5) =-0.2602080*TEMP + 167.1336000
          ELSEIF ((TEMP .GE. 350.0) .AND. (TEMP .LT. 400.0)) THEN
            TABLE1(1,5) = -0.1801440*TEMP + 139.1112000
          ELSE
            TABLE1(1,5) =67.0536
          ENDIF
C
          IF (TEMP .LT. 25.0) THEN
            TABLE1(1,6) =117.117
          ELSEIF ((TEMP .GE. 25.0) .AND. (TEMP .LT. 300.0)) THEN
```

```
  TABLE1(1,6) = -0.0800800*TEMP + 119.11900
ELSEIF ((TEMP .GE. 300.0) .AND. (TEMP .LT. 350.0)) THEN
  TABLE1(1,6) = -0.2402400*TEMP + 167.1670000
ELSEIF ((TEMP .GE. 350.0) .AND. (TEMP .LT. 400.0)) THEN
  TABLE1(1,6) =  -0.1801800*TEMP + 146.1460000
ELSE
  TABLE1(1,6) =74.074
ENDIF
C
IF (TEMP .LT. 25.0) THEN
  TABLE1(1,7) =122.1464
ELSEIF ((TEMP .GE. 25.0) .AND. (TEMP .LT. 300.0)) THEN
  TABLE1(1,7) = -0.0815523*TEMP + 124.1852073
ELSEIF ((TEMP .GE. 300.0) .AND. (TEMP .LT. 350.0)) THEN
  TABLE1(1,7) =-0.2222664*TEMP + 166.399440
ELSEIF ((TEMP .GE. 350.0) .AND. (TEMP .LT. 400.0)) THEN
  TABLE1(1,7) =-0.2102520*TEMP + 162.194400
ELSE
  TABLE1(1,7) =78.0936
ENDIF
C
IF (TEMP .LT. 25.0) THEN
  TABLE1(1,8) =126.6771
ELSEIF ((TEMP .GE. 25.0) .AND. (TEMP .LT. 300.0)) THEN
  TABLE1(1,8) =  -0.0819327*TEMP + 128.7254182
ELSEIF ((TEMP .GE. 300.0) .AND. (TEMP .LT. 350.0)) THEN
  TABLE1(1,8) =  -0.2203080*TEMP + 170.238000
ELSEIF ((TEMP .GE. 350.0) .AND. (TEMP .LT. 400.0)) THEN
  TABLE1(1,8) =  -0.2042856*TEMP + 164.630160
ELSE
  TABLE1(1,8) =82.91592
ENDIF
C
IF (TEMP .LT. 25.0) THEN
  TABLE1(1,9) =130.7088
ELSEIF ((TEMP .GE. 25.0) .AND. (TEMP .LT. 300.0)) THEN
  TABLE1(1,9) = -0.0826775*TEMP + 132.7757382
ELSEIF ((TEMP .GE. 300.0) .AND. (TEMP .LT. 350.0)) THEN
  TABLE1(1,9) = -0.2163456*TEMP + 172.876160
ELSEIF ((TEMP .GE. 350.0) .AND. (TEMP .LT. 400.0)) THEN
  TABLE1(1,9) = -0.2203520*TEMP + 174.278400
ELSE
  TABLE1(1,9) =86.1376
ENDIF
C
IF (TEMP .LT. 25.0) THEN
  TABLE1(1,10) =134.7421
ELSEIF ((TEMP .GE. 25.0) .AND. (TEMP .LT. 300.0)) THEN
  TABLE1(1,10) =  -0.083423*TEMP + 136.827665
ELSEIF ((TEMP .GE. 300.0) .AND. (TEMP .LT. 350.0)) THEN
  TABLE1(1,10) = -0.242436*TEMP + 184.53156
ELSEIF ((TEMP .GE. 350.0) .AND. (TEMP .LT. 400.0)) THEN
  TABLE1(1,10) = -0.198356*TEMP + 169.103840
ELSE
  TABLE1(1,10) =89.76128
ENDIF
C
IF (TEMP .LT. 25.0) THEN
  TABLE1(1,11) =138.276
ELSEIF ((TEMP .GE. 25.0) .AND. (TEMP .LT. 300.0)) THEN
  TABLE1(1,11) = -0.083804*TEMP + 140.371091
ELSEIF ((TEMP .GE. 300.0) .AND. (TEMP .LT. 350.0)) THEN
  TABLE1(1,11) = -0.230460*TEMP + 184.368000
ELSEIF ((TEMP .GE. 350.0) .AND. (TEMP .LT. 400.0)) THEN
  TABLE1(1,11) = -0.224448*TEMP + 182.2638
ELSE
  TABLE1(1,11) =92.4846
ENDIF
C
IF (TEMP .LT. 25.0) THEN
  TABLE1(1,12) =140.8091
ELSEIF ((TEMP .GE. 25.0) .AND. (TEMP .LT. 300.0)) THEN
  TABLE1(1,12) =  -0.081998*TEMP + 142.859055
ELSEIF ((TEMP .GE. 300.0) .AND. (TEMP .LT. 350.0)) THEN
  TABLE1(1,12) =-0.240528*TEMP + 190.41800
ELSEIF ((TEMP .GE. 350.0) .AND. (TEMP .LT. 400.0)) THEN
  TABLE1(1,12) = -0.200440*TEMP + 176.387200
ELSE
```

```
      TABLE1(1,12) =96.2112
     ENDIF
C
     IF (TEMP .LT. 25.0) THEN
      TABLE1(1,13) =143.8444
     ELSEIF ((TEMP .GE. 25.0) .AND. (TEMP .LT. 300.0)) THEN
      TABLE1(1,13) = -0.085660*TEMP + 145.985891
     ELSEIF ((TEMP .GE. 300.0) .AND. (TEMP .LT. 350.0)) THEN
      TABLE1(1,13) =-0.230552*TEMP + 189.45360
     ELSEIF ((TEMP .GE. 350.0) .AND. (TEMP .LT. 400.0)) THEN
      TABLE1(1,13) = -0.220528*TEMP + 185.94520
     ELSE
      TABLE1(1,13) =97.734
     ENDIF
C
     IF (TEMP .LT. 25.0) THEN
      TABLE1(1,14) =146.3796
     ELSEIF ((TEMP .GE. 25.0) .AND. (TEMP .LT. 300.0)) THEN
      TABLE1(1,14) = -0.085677*TEMP + 148.521518
     ELSEIF ((TEMP .GE. 300.0) .AND. (TEMP .LT. 350.0)) THEN
      TABLE1(1,14) = -0.230598*TEMP + 191.997900
     ELSEIF ((TEMP .GE. 350.0) .AND. (TEMP .LT. 400.0)) THEN
      TABLE1(1,14) = -0.220572*TEMP + 188.48880
     ELSE
      TABLE1(1,14) =100.26
     ENDIF
C
     IF (TEMP .LT. 25.0) THEN
      TABLE1(1,15) =148.4144
     ELSEIF ((TEMP .GE. 25.0) .AND. (TEMP .LT. 300.0)) THEN
      TABLE1(1,15) = -0.087517*TEMP + 150.602327
     ELSEIF ((TEMP .GE. 300.0) .AND. (TEMP .LT. 350.0)) THEN
      TABLE1(1,15) = -0.210588*TEMP + 187.523600
     ELSEIF ((TEMP .GE. 350.0) .AND. (TEMP .LT. 400.0)) THEN
      TABLE1(1,15) =-0.240672*TEMP + 198.053000
     ELSE
      TABLE1(1,15) =101.7842
     ENDIF
C
     IF (TEMP .LT. 25.0) THEN
      TABLE1(1,16) =151.453
     ELSEIF ((TEMP .GE. 25.0) .AND. (TEMP .LT. 300.0)) THEN
      TABLE1(1,16) = -0.093005*TEMP + 153.778136
     ELSEIF ((TEMP .GE. 300.0) .AND. (TEMP .LT. 350.0)) THEN
      TABLE1(1,16) =-0.200600*TEMP + 186.056500
     ELSEIF ((TEMP .GE. 350.0) .AND. (TEMP .LT. 400.0)) THEN
      TABLE1(1,16) = -0.230690*TEMP + 196.588000
     ELSE
      TABLE1(1,16) =104.312
     ENDIF
C
     IF (TEMP .LT. 25.0) THEN
      TABLE1(1,17) =153.4896
     ELSEIF ((TEMP .GE. 25.0) .AND. (TEMP .LT. 300.0)) THEN
      TABLE1(1,17) = -0.092294*TEMP + 155.796960
     ELSEIF ((TEMP .GE. 300.0) .AND. (TEMP .LT. 350.0)) THEN
      TABLE1(1,17) =-0.204653*TEMP + 189.504480
     ELSEIF ((TEMP .GE. 350.0) .AND. (TEMP .LT. 400.0)) THEN
      TABLE1(1,17) = -0.250800*TEMP + 205.656000
     ELSE
      TABLE1(1,17) =105.336
     ENDIF
C
     IF (TEMP .LT. 25.0) THEN
      TABLE1(1,18) =155.0253
     ELSEIF ((TEMP .GE. 25.0) .AND. (TEMP .LT. 300.0)) THEN
      TABLE1(1,18) = -0.091218*TEMP + 157.305755
     ELSEIF ((TEMP .GE. 300.0) .AND. (TEMP .LT. 350.0)) THEN
      TABLE1(1,18) =-0.220748*TEMP + 196.164700
     ELSEIF ((TEMP .GE. 350.0) .AND. (TEMP .LT. 400.0)) THEN
      TABLE1(1,18) = -0.234796*TEMP + 201.081360
     ELSE
      TABLE1(1,18) =107.16312
     ENDIF
C
     IF (TEMP .LT. 25.0) THEN
      TABLE1(1,19) =156.5616
     ELSEIF ((TEMP .GE. 25.0) .AND. (TEMP .LT. 300.0)) THEN
```

```
          TABLE1(1,19) =  -0.091236*TEMP + 158.842509
        ELSEIF ((TEMP .GE. 300.0) .AND. (TEMP .LT. 350.0)) THEN
          TABLE1(1,19) = -0.210756*TEMP + 194.698400
        ELSEIF ((TEMP .GE. 350.0) .AND. (TEMP .LT. 400.0)) THEN
          TABLE1(1,19) =-0.240864*TEMP + 205.236200
        ELSE
          TABLE1(1,19) =108.8906
        ENDIF
       TABLE1(2,1)=0.0
       TABLE1(2,2)=0.0002
       TABLE1(2,3)=0.0004
       TABLE1(2,4)=0.0006
       TABLE1(2,5)=0.0008
       TABLE1(2,6)=0.0010
       TABLE1(2,7)=0.0012
       TABLE1(2,8)=0.0014
       TABLE1(2,9)=0.0016
       TABLE1(2,10)=0.0018
       TABLE1(2,11)=0.0020
       TABLE1(2,12)=0.0022
       TABLE1(2,13)=0.0024
       TABLE1(2,14)=0.0026
       TABLE1(2,15)=0.0028
       TABLE1(2,16)=0.0030
       TABLE1(2,17)=0.0032
       TABLE1(2,18)=0.0034
       TABLE1(2,19)=0.0036


C   SET YIELD STRESS TO LAST VALUE OF TABLE, HARDENING TO ZERO
    SYIELDD=TABLE1(1,NVALUE1)
    HARDD=0.0
C
C   IF MORE THAN ONE ENTRY, SEARCH TABLE
C
    IF(NVALUE1.GT.1) THEN
     DO 430 K1=1,NVALUE1-1
       EQPL1=TABLE1(2,K1+1)
       IF(IN_X .LT. EQPL1) THEN
        EQPL0=TABLE1(2,K1)
        IF(EQPL1 LE.EQPL0) THEN
          WRITE(6,1)
          CALL XIT
        ENDIF
C
C       CURRENT YIELD STRESS AND HARDENING
C
       DDDEQPL=EQPL1-EQPL0
       SYIEL00=TABLE1(1,K1)
       SYIEL11=TABLE1(1,K1+1)
       DSYIEL=SYIEL11-SYIEL00
       HARDD=DSYIEL/DDDEQPL
       SYIELDD=SYIEL00+(IN_X-EQPL0)*HARDD
       GOTO 440
       ENDIF
 430     CONTINUE
 440     CONTINUE
    ENDIF
RETURN
    END
```

APPENDIX 5: USER-DEVELOPED SUBROUTINE MATERIAL MODEL FOR CAST IRON

```
*DEPVAR
14
*USER SUBROUTINE
      SUBROUTINE UMAT(STRESS,STATEV,DDSDDE,SSE,SPD,SCD,
     1 RPL,DDSDDT,DRPLDE,DRPLDT,STRAN,DSTRAN,
     2 TIME,DTIME,TEMP,DTEMP,PREDEF,DPRED,MATERL,NDI,NSHR,NTENS,
     3 NSTATV,PROPS,NPROPS,COORDS,DROT,PNEWDT,CELENT,
     4 DFGRD0,DFGRD1,NOEL,NPT,KSLAY,KSPT,KSTEP,KINC)
C
      INCLUDE 'ABA_PARAM.INC'
C
      CHARACTER*8 MATERL
      DIMENSION STRESS(NTENS),STATEV(NSTATV),
     1 DDSDDE(NTENS,NTENS),DDSDDT(NTENS),DRPLDE(NTENS),
     2 STRAN(NTENS),DSTRAN(NTENS),TIME(2),PREDEF(1),DPRED(1),
     3 PROPS(NPROPS),COORDS(3),DROT(3,3),
     4 DFGRD0(3,3),DFGRD1(3,3)

      REAL VALUE,X,EQPLAS1,SHYDRO,SYIELD,HARD,DEQPL,SYIEL0,Y
C
      DIMENSION EELAS(6),EPLAS(6),FLOW(6)
      DIMENSION ETHERM(6),DTHERM(6),DELDSE(6,6)
      PARAMETER (ONE=1.0D0,TWO=2.0D0,THREE=3.0D0,SIX=6.0D0)
      DATA NEWTON,TOLER/10,1.D-6/
C
C
      IF (NDI.NE.3) THEN
        WRITE(6,1)
 1      FORMAT(//,30X,'***ERROR - THIS UMAT MAY ONLY BE USED FOR ',
     1         'ELEMENTS WITH THREE DIRECT STRESS COMPONENTS')
      ENDIF
C
C     ELASTIC PROPERTIES
C     ASSIGN YOUNG'S MODULUS AND POSSION'S RATIO
      EMOD0=116500.0
      ENU=0.26
      VALUE = TEMP+DTEMP
IF(ENU.GT.0.4999.AND.ENU.LT.0.5001) ENU=0.499
      EBULK30=EMOD0/(ONE-TWO*ENU)
      EG20=EMOD0/(ONE+ENU)
      EG0=EG20/TWO
      EG30=THREE*EG0
      ELAM0=(EBULK30-EG20)/THREE

C FOR TEMPERATURE INCREMENT
      EMOD=116500.0
EBULK3=EMOD/(ONE-TWO*ENU)
      EG2=EMOD/(ONE+ENU)
      EG=EG2/TWO
      EG3=THREE*EG
      ELAM=(EBULK3-EG2)/THREE
C     ELASTIC STIFFNESS AT THE END OF INCREMENT AND STIFFNESS DUE TO TEMPERATURE
C
      DO 20 K1=1,NTENS
        DO 10 K2=1,NTENS
          DDSDDE(K2,K1)=0.0
          DELDSE(K2,K1)=0.0
 10     CONTINUE
 20   CONTINUE
C
      DO 40 K1=1,NDI
        DO 30 K2=1,NDI
          DDSDDE(K2,K1)=ELAM
          DELDSE(K2,K1)=ELAM-ELAM0
 30     CONTINUE
        DDSDDE(K1,K1)=EG2+ELAM
        DELDSE(K1,K1)=EG2+ELAM-EG20-ELAM0
 40   CONTINUE
      DO 50 K1=NDI+1,NTENS
        DDSDDE(K1,K1)=EG
        DELDSE(K1,K1)=EG-EG0
```

```
 50  CONTINUE
C
C  ASSIGN EXPANSION COEFFICIENT
IF (VALUE .LT. 200.0) THEN
      EXPAN_C=0.00001
     ELSE
      EXPAN_C=0.0000125
     END IF
C    CALCULATE THERMAL EXPANSION
     DO K1 =1, NDI
      ETHERM(K1)=EXPAN_C*TEMP
      DTHERM(K1)=EXPAN_C*DTEMP
     END DO
C    CALCULATE STRESS FROM ELASTIC STRAINS AND THERMAL STRAIN
C
     DO K1=NDI+1,NTENS
       ETHERM(K1) = 0.0
       DTHERM(K1) = 0.0
     END DO
     DO 70 K1=1,NTENS
      DO 60 K2=1,NTENS
        STRESS(K2)=STRESS(K2)+DDSDDE(K2,K1)*(DSTRAN(K1)-DTHERM(K1))
    1                 +DELDSE(K2,K1)*( STRAN(K1)-ETHERM(K1))
 60    CONTINUE
      ETHERM(K1)=ETHERM(K1)+DTHERM(K1)
 70   CONTINUE
C
C    RECOVER ELASTIC AND PLASTIC STRAINS
C
     DO 80 K1=1,NTENS
       EELAS(K1)=STATEV(K1)+DSTRAN(K1)-ETHERM(K1)
       EPLAS(K1)=STATEV(K1+NTENS)
 80   CONTINUE
     EQPLAS=STATEV(1+2*NTENS)
     EQPLAS1=STATEV(1+2*NTENS+1)
C
C    IF NO YIELD STRESS IS GIVEN, MATERIAL IS TAKEN TO BE ELASTIC
C
     IF(NPROPS.GT.2.AND.PROPS(3).GT.0.0) THEN
C
C      MISES STRESS
C
      SHYDRO=(STRESS(1)+STRESS(2)+STRESS(3))/THREE
      SMISES=(STRESS(1)-STRESS(2))*(STRESS(1)-STRESS(2)) +
    1       (STRESS(2)-STRESS(3))*(STRESS(2)-STRESS(3)) +
    1       (STRESS(3)-STRESS(1))*(STRESS(3)-STRESS(1))
      DO 90 K1=NDI+1,NTENS
         SMISES=SMISES+SIX*STRESS(K1)*STRESS(K1)
 90    CONTINUE
      SMISES=SQRT(SMISES/TWO)
C
C      HARDENING CURVE, GET YIELD STRESS
C
IF (SHYDRO .LE. 0.0) THEN
       X = EQPLAS1
       Y = EQPLAS

ELSE
        X = EQPLAS
        Y = EQPLAS1
C    X FROM EQPLAS TENSION
      ENDIF
      CALL UHARD(SYIEL0,HARD,X,VALUE,SHYDRO,Y)
C
C      DETERMINE IF ACTIVELY YIELDING
C
      IF (SMISES.GT.(1.0+TOLER)*SYIEL0) THEN
C
C       FLOW DIRECTION
C
       SHYDRO=(STRESS(1)+STRESS(2)+STRESS(3))/THREE
       ONESY=ONE/SMISES
       DO 110 K1=1,NDI
         FLOW(K1)=ONESY*(STRESS(K1)-SHYDRO)
 110     CONTINUE
       DO 120 K1=NDI+1,NTENS
         FLOW(K1)=STRESS(K1)*ONESY
 120     CONTINUE
```

```
C
C     SOLVE FOR EQUIV STRESS AND PLASTIC STRAIN
C
      SYIELD=SYIEL0
      DEQPL=0.0
      DO 130 KEWTON=1,NEWTON
        RHS=SMISES-EG3*DEQPL-SYIELD
        DEQPL=DEQPL+RHS/(EG3+HARD)
        CALL UHARD(SYIELD,HARD,X+DEQPL,VALUE,SHYDRO,Y)
        IF(ABS(RHS).LT.TOLER*SYIEL0) GOTO 140
 130    CONTINUE
      WRITE(6,2) NEWTON
 2     FORMAT(//,30X,'***WARNING - PLASTICITY ALGORITHM DID NOT ',
     1    'CONVERGE AFTER ',I3,' ITERATIONS')
 140    CONTINUE
      EFFHRD=EG3*HARD/(EG3+HARD)
C
C     CALC STRESS AND UPDATE STRAINS
C
      DO 150 K1=1,NDI
        STRESS(K1)=FLOW(K1)*SYIELD+SHYDRO
        EPLAS(K1)=EPLAS(K1)+THREE*FLOW(K1)*DEQPL/TWO
        EELAS(K1)=EELAS(K1)-THREE*FLOW(K1)*DEQPL/TWO
 150    CONTINUE
      DO 160 K1=NDI+1,NTENS
        STRESS(K1)=FLOW(K1)*SYIELD
        EPLAS(K1)=EPLAS(K1)+THREE*FLOW(K1)*DEQPL
        EELAS(K1)=EELAS(K1)-THREE*FLOW(K1)*DEQPL
 160    CONTINUE
      X=X+DEQPL
      SPD=DEQPL*(SYIEL0+SYIELD)/TWO
C
C     UPDATE JACOBIAN
C
      EFFG=EG*SYIELD/SMISES
      EFFG2=TWO*EFFG
      EFFG3=THREE*EFFG2/TWO
      EFFLAM=(EBULK3-EFFG2)/THREE
      DO 220 K1=1,NDI
        DO 210 K2=1,NDI
          DDSDDE(K2,K1)=EFFLAM
 210      CONTINUE
        DDSDDE(K1,K1)=EFFG2+EFFLAM
 220    CONTINUE
      DO 230 K1=NDI+1,NTENS
        DDSDDE(K1,K1)=EFFG
 230    CONTINUE
      DO 250 K1=1,NTENS
        DO 240 K2=1,NTENS
          DDSDDE(K2,K1)=DDSDDE(K2,K1)+FLOW(K2)*FLOW(K1)
     1                  *(EFFHRD-EFFG3)
 240      CONTINUE
 250    CONTINUE
     ENDIF
    ENDIF
C
C STORE STRAINS IN STATE VARIABLE ARRAY
C
    DO 310 K1=1,NTENS
     STATEV(K1)=EELAS(K1)
     STATEV(K1+NTENS)=EPLAS(K1)
 310  CONTINUE
    IF (SHYDRO .LE. 0.0) THEN
     STATEV(1+2*NTENS+1)=X
C ASSIGN X TO STATE14
    ELSE
     STATEV(1+2*NTENS)=X

    ENDIF
C
    RETURN
    END
C
C  SUBROUTINE FOR DETERMINING YIELD STRESS AND PLASTIC STRAIN  FROM STRESS STRAIN CURVES
    SUBROUTINE UHARD(SYIELDD,HARDD,IN_X,TEMP,HYDRO,IN_Y)
C     INCLUDE 'ABA_PARAM.INC'
    REAL  TABLE(2,15),HARDD,DDDEQPL,TABLE1(2,19)
    REAL  TEMP,HYDRO,IN_X,EQPL0,EQPL1,DSYIEL,SYIEL11,SYIEL00
```

```
      REAL  SYIELDD
      REAL YIELDD,YHARDD,YEQPL1,IN_Y,YEQPL0,YDDEQPL
      REAL YYIEL00,YYIEL11,YDSYIEL
      REAL XIELDD,XHARDD,XEQPL1,XEQPL0,XDDEQPL
      REAL XYIEL00,XYIEL11,XDSYIEL
C
      NVALUE = 15
      NVALUE1 = 19
C
C     ASSIGN THE VALUE OF STRESS STRAIN CURVE
C
C     COMPRESSION REGION
C
C
            IF (TEMP .LT. 25.0) THEN
              TABLE(1,1) =105.0
            ELSEIF ((TEMP .GE. 25.0) .AND. (TEMP .LT. 300.0)) THEN
              TABLE(1,1) = -0.058182*TEMP + 106.454545
            ELSEIF ((TEMP .GE. 300.0) .AND. (TEMP .LT. 350.0)) THEN
              TABLE(1,1) =-0.240000*TEMP + 161.000000
            ELSEIF ((TEMP .GE. 350.0) .AND. (TEMP .LT. 400.0)) THEN
              TABLE(1,1) =-0.180000*TEMP + 140.000000
            ELSE
              TABLE(1,1) =68.0
            ENDIF
C
            IF (TEMP .LT. 25.0) THEN
              TABLE(1,2) =220.22
            ELSEIF ((TEMP .GE. 25.0) .AND. (TEMP .LT. 300.0)) THEN
              TABLE(1,2) = -0.080080*TEMP + 222.22200
            ELSEIF ((TEMP .GE. 300.0) .AND. (TEMP .LT. 350.0)) THEN
              TABLE(1,2) =-0.760560*TEMP + 426.366000
            ELSEIF ((TEMP .GE. 350.0) .AND. (TEMP .LT. 400.0)) THEN
              TABLE(1,2) = -0.380020*TEMP + 293.177000
            ELSE
              TABLE(1,2) =141.169
            ENDIF
C
            IF (TEMP .LT. 25.0) THEN
              TABLE(1,3) =270.54
            ELSEIF ((TEMP .GE. 25.0) .AND. (TEMP .LT. 300.0)) THEN
              TABLE(1,3) = -0.102022*TEMP + 273.090545
            ELSEIF ((TEMP .GE. 300.0) .AND. (TEMP .LT. 350.0)) THEN
              TABLE(1,3) = -0.801200*TEMP + 482.84400
            ELSEIF ((TEMP .GE. 350.0) .AND. (TEMP .LT. 400.0)) THEN
              TABLE(1,3) =-0.580440*TEMP + 405.578000
            ELSE
              TABLE(1,3) =173.402
            ENDIF
C
            IF (TEMP .LT. 25.0) THEN
              TABLE(1,4) =301.903
            ELSEIF ((TEMP .GE. 25.0) .AND. (TEMP .LT. 300.0)) THEN
              TABLE(1,4) = -0.131302*TEMP + 305.185545
            ELSEIF ((TEMP .GE. 300.0) .AND. (TEMP .LT. 350.0)) THEN
              TABLE(1,4) =-0.641320*TEMP + 458.191000
            ELSEIF ((TEMP .GE. 350.0) .AND. (TEMP .LT. 400.0)) THEN
              TABLE(1,4) =-0.801320*TEMP + 514.191000
            ELSE
              TABLE(1,4) =193.663
            ENDIF
C
            IF (TEMP .LT. 25.0) THEN
              TABLE(1,5) =326.3
            ELSEIF ((TEMP .GE. 25.0) .AND. (TEMP .LT. 300.0)) THEN
              TABLE(1,5) = -0.153338*TEMP + 330.133455
            ELSEIF ((TEMP .GE. 300.0) .AND. (TEMP .LT. 350.0)) THEN
              TABLE(1,5) = -0.641760*TEMP + 476.660000
            ELSEIF ((TEMP .GE. 350.0) .AND. (TEMP .LT. 400.0)) THEN
              TABLE(1,5) = -0.882080*TEMP + 560.772000
            ELSE
              TABLE(1,5) =207.94
            ENDIF
C
            IF (TEMP .LT. 25.0) THEN
              TABLE(1,6) =343.71
            ELSEIF ((TEMP .GE. 25.0) .AND. (TEMP .LT. 300.0)) THEN
```

```
      TABLE(1,6) =  -0.160800*TEMP + 347.730000
     ELSEIF ((TEMP .GE. 300.0) .AND. (TEMP .LT. 350.0)) THEN
      TABLE(1,6) = -0.602000*TEMP + 480.090000
     ELSEIF ((TEMP .GE. 350.0) .AND. (TEMP .LT. 400.0)) THEN
      TABLE(1,6) = -1.023300*TEMP + 627.545000
     ELSE
      TABLE(1,6) =218.225
     ENDIF
C
     IF (TEMP .LT. 25.0) THEN
      TABLE(1,7) =357.13
     ELSEIF ((TEMP .GE. 25.0) .AND. (TEMP .LT. 300.0)) THEN
      TABLE(1,7) = -0.171935*TEMP + 361.428364
     ELSEIF ((TEMP .GE. 300.0) .AND. (TEMP .LT. 350.0)) THEN
      TABLE(1,7) =-0.562160*TEMP + 478.496000
     ELSEIF ((TEMP .GE. 350.0) .AND. (TEMP .LT. 400.0)) THEN
      TABLE(1,7) = -1.104440*TEMP + 668.294000
     ELSE
      TABLE(1,7) =226.518
     ENDIF
C
     IF (TEMP .LT. 25.0) THEN
      TABLE(1,8) =370.576
     ELSEIF ((TEMP .GE. 25.0) .AND. (TEMP .LT. 300.0)) THEN
      TABLE(1,8) =  -0.179429*TEMP + 375.061727
     ELSEIF ((TEMP  GE. 300.0) .AND. (TEMP .LT. 350.0)) THEN
      TABLE(1,8) = -0.602800*TEMP + 502.073000
     ELSEIF ((TEMP .GE. 350.0) .AND. (TEMP .LT. 400.0)) THEN
      TABLE(1,8) = -1.125320*TEMP + 684.95500
     ELSE
      TABLE(1,8) =234.827
     ENDIF
C
     IF (TEMP .LT. 25.0) THEN
      TABLE(1,9) =380.016
     ELSEIF ((TEMP .GE. 25.0) .AND. (TEMP .LT. 300.0)) THEN
      TABLE(1,9) =  -0.183273*TEMP + 384.597818
     ELSEIF ((TEMP .GE. 300.0) .AND. (TEMP .LT. 350.0)) THEN
      TABLE(1,9) = -0.583040*TEMP + 504.528000
     ELSEIF ((TEMP .GE. 350.0) .AND. (TEMP .LT. 400.0)) THEN
      TABLE(1,9) =-1.166400*TEMP + 708.704000
     ELSE
      TABLE(1,9) =242.144
     ENDIF
C
     IF (TEMP .LT. 25.0) THEN
      TABLE(1,10) =392.501
     ELSEIF ((TEMP .GE. 25.0) .AND. (TEMP .LT. 300.0)) THEN
      TABLE(1,10) = -0.205469*TEMP + 397.637727
     ELSEIF ((TEMP .GE. 300.0) .AND. (TEMP .LT. 350.0)) THEN
      TABLE(1,10) =-0.563240*TEMP + 504.969000
     ELSEIF ((TEMP .GE. 350.0) .AND. (TEMP .LT. 400.0)) THEN
      TABLE(1,10) =-1.227740*TEMP + 737.544000
     ELSE
      TABLE(1,10) =246.448
     ENDIF
C
     IF (TEMP .LT. 25.0) THEN
      TABLE(1,11) =400.97
     ELSEIF ((TEMP .GE. 25.0) .AND. (TEMP .LT. 300.0)) THEN
      TABLE(1,11) =  -0.202000*TEMP + 406.020000
     ELSEIF ((TEMP .GE. 300.0) .AND. (TEMP .LT. 350.0)) THEN
      TABLE(1,11) =-0.583800*TEMP + 520.560000
     ELSEIF ((TEMP .GE. 350.0) .AND. (TEMP .LT. 400.0)) THEN
      TABLE(1,11) =-1.269000*TEMP + 760.38000
     ELSE
      TABLE(1,11) =252.78
     ENDIF
C
     IF (TEMP .LT. 25.0) THEN
      TABLE(1,12) =409.455
     ELSEIF ((TEMP .GE. 25.0) .AND. (TEMP .LT. 300.0)) THEN
      TABLE(1,12) =  -0.209553*TEMP + 414.693818
     ELSEIF ((TEMP .GE. 300.0) .AND. (TEMP .LT. 350.0)) THEN
      TABLE(1,12) =-0.584180*TEMP + 527.082000
     ELSEIF ((TEMP .GE. 350.0) .AND. (TEMP .LT. 400.0)) THEN
      TABLE(1,12) =-1.310340*TEMP + 781.23800
     ELSE
```

```
        TABLE(1,12) =257.102
       ENDIF
C
       IF (TEMP .LT. 25.0) THEN
        TABLE(1,13) =415.932
       ELSEIF ((TEMP .GE. 25.0) .AND. (TEMP .LT. 300.0)) THEN
        TABLE(1,13) =  -0.206080*TEMP + 421.084000
       ELSEIF ((TEMP .GE. 300.0) .AND. (TEMP .LT. 350.0)) THEN
        TABLE(1,13) = -0.584560*TEMP + 534.62800
       ELSEIF ((TEMP .GE. 350.0) .AND. (TEMP .LT. 400.0)) THEN
        TABLE(1,13) = -1.372000*TEMP + 810.232000
       ELSE
        TABLE(1,13) =261.432
       ENDIF
C
       IF (TEMP .LT. 25.0) THEN
        TABLE(1,14) =424.447
       ELSEIF ((TEMP .GE. 25.0) .AND. (TEMP .LT. 300.0)) THEN
        TABLE(1,14) = -0.213651*TEMP + 429.788273
       ELSEIF ((TEMP  GE. 300.0) .AND. (TEMP .LT. 350.0)) THEN
        TABLE(1,14) =-0.584940*TEMP + 541.175000
       ELSEIF ((TEMP .GE. 350.0) .AND. (TEMP .LT. 400.0)) THEN
        TABLE(1,14) = -1.413520*TEMP + 831.178000
       ELSE
        TABLE(1,14) =265.77
       ENDIF
C
       IF (TEMP .LT. 25.0) THEN
        TABLE(1,15) =430.95
       ELSEIF ((TEMP .GE. 25.0) .AND. (TEMP .LT. 300.0)) THEN
        TABLE(1,15) = -0.217549*TEMP + 436.388727
       ELSEIF ((TEMP .GE. 300.0) .AND. (TEMP .LT. 350.0)) THEN
        TABLE(1,15) = -0.585320*TEMP + 546.72000
       ELSEIF ((TEMP .GE. 350.0) .AND. (TEMP .LT. 400.0)) THEN
        TABLE(1,15) = -1.475400*TEMP + 858.248000
       ELSE
        TABLE(1,15) =268.088
       ENDIF

      TABLE(2,1)=0.0
      TABLE(2,2)=0.001
      TABLE(2,3)=0.002
      TABLE(2,4)=0.003
      TABLE(2,5)=0.004
      TABLE(2,6)=0.005
      TABLE(2,7)=0.006
      TABLE(2,8)=0.007
      TABLE(2,9)=0.008
      TABLE(2,10)=0.009
      TABLE(2,11)=0.010
      TABLE(2,12)=0.011
      TABLE(2,13)=0.012
      TABLE(2,14)=0.013
      TABLE(2,15)=0.014

C     TENSION STRESS STRAIN CURVE
C     TENSION REGION
C

       IF (TEMP .LT. 25.0) THEN
        TABLE1(1,1) =65.0
       ELSEIF ((TEMP .GE. 25.0) .AND. (TEMP .LT. 300.0)) THEN
        TABLE1(1,1) = -0.065455*TEMP + 66.636364
       ELSEIF ((TEMP .GE. 300.0) .AND. (TEMP .LT. 350.0)) THEN
        TABLE1(1,1) = -0.56*TEMP + 215
       ELSEIF ((TEMP .GE. 350.0) .AND. (TEMP .LT. 400.0)) THEN
        TABLE1(1,1) =-0.12*TEMP + 61
       ELSE
        TABLE1(1,1) =13.0
       ENDIF
C
       IF (TEMP .LT. 25.0) THEN
        TABLE1(1,2) =82.0164
       ELSEIF ((TEMP .GE. 25.0) .AND. (TEMP .LT. 300.0)) THEN
        TABLE1(1,2) = -0.061831*TEMP + 83.562164
       ELSEIF ((TEMP .GE. 300.0) .AND. (TEMP .LT. 350.0)) THEN
        TABLE1(1,2) = -0.4000800*TEMP + 185.0370000
       ELSEIF ((TEMP .GE. 350.0) .AND. (TEMP .LT. 400.0)) THEN
```

```
      TABLE1(1,2) = -0.1400280*TEMP + 94.0188000
     ELSE
      TABLE1(1,2) = 38.0076
     ENDIF
C
     IF (TEMP .LT. 25.0) THEN
      TABLE1(1,3) =95.038
     ELSEIF ((TEMP .GE. 25.0) .AND. (TEMP .LT. 300.0)) THEN
      TABLE1(1,3) =  -0.0727564*TEMP + 96.8569091
     ELSEIF ((TEMP .GE. 300.0) .AND. (TEMP .LT. 350.0)) THEN
      TABLE1(1,3) = -0.3241296*TEMP + 172.2688800
     ELSEIF ((TEMP .GE. 350.0) .AND. (TEMP .LT. 400.0)) THEN
      TABLE1(1,3) = -0.1760704*TEMP + 120.448160
     ELSE
      TABLE1(1,3) =50.02
     ENDIF
C
     IF (TEMP .LT. 25.0) THEN
      TABLE1(1,4) =104.0624
     ELSEIF ((TEMP .GE. 25.0) .AND. (TEMP .LT. 300.0)) THEN
      TABLE1(1,4) =  -0.0764095*TEMP + 105.9726364
     ELSEIF ((TEMP .GE. 300.0) .AND. (TEMP .LT. 350.0)) THEN
      TABLE1(1,4) = -0.3001800*TEMP + 173.1038000
     ELSEIF ((TEMP .GE. 350.0) .AND. (TEMP .LT. 400.0)) THEN
      TABLE1(1,4) =-0.1801080*TEMP + 131.0786000
     ELSE
      TABLE1(1,4) =59.0354
     ENDIF
C
     IF (TEMP .LT. 25.0) THEN
      TABLE1(1,5) =110.088
     ELSEIF ((TEMP .GE. 25.0) .AND. (TEMP .LT. 300.0)) THEN
      TABLE1(1,5) =  -0.0764247*TEMP + 111.9986182
     ELSEIF ((TEMP .GE. 300.0) .AND. (TEMP .LT. 350.0)) THEN
      TABLE1(1,5) =-0.2602080*TEMP + 167.1336000
     ELSEIF ((TEMP .GE. 350.0) .AND. (TEMP .LT. 400.0)) THEN
      TABLE1(1,5) = -0.1801440*TEMP + 139.1112000
     ELSE
      TABLE1(1,5) =67.0536
     ENDIF
C
     IF (TEMP .LT. 25.0) THEN
      TABLE1(1,6) =117.117
     ELSEIF ((TEMP .GE. 25.0) .AND. (TEMP .LT. 300.0)) THEN
      TABLE1(1,6) = -0.0800800*TEMP + 119.11900
     ELSEIF ((TEMP .GE. 300.0) .AND. (TEMP .LT. 350.0)) THEN
      TABLE1(1,6) = -0.2402400*TEMP + 167.1670000
     ELSEIF ((TEMP .GE. 350.0) .AND. (TEMP .LT. 400.0)) THEN
      TABLE1(1,6) =  -0.1801800*TEMP + 146.1460000
     ELSE
      TABLE1(1,6) =74.074
     ENDIF
C
     IF (TEMP .LT. 25.0) THEN
      TABLE1(1,7) =122.1464
     ELSEIF ((TEMP .GE. 25.0) .AND. (TEMP .LT. 300.0)) THEN
      TABLE1(1,7) = -0.0815523*TEMP + 124.1852073
     ELSEIF ((TEMP .GE. 300.0) .AND. (TEMP .LT. 350.0)) THEN
      TABLE1(1,7) =-0.2222664*TEMP + 166.399440
     ELSEIF ((TEMP .GE. 350.0) .AND. (TEMP .LT. 400.0)) THEN
      TABLE1(1,7) =-0.2102520*TEMP + 162.194400
     ELSE
      TABLE1(1,7) =78.0936
     ENDIF
C
     IF (TEMP .LT. 25.0) THEN
      TABLE1(1,8) =126.6771
     ELSEIF ((TEMP .GE. 25.0) .AND. (TEMP .LT. 300.0)) THEN
      TABLE1(1,8) =  -0.0819327*TEMP + 128.7254182
     ELSEIF ((TEMP .GE. 300.0) .AND. (TEMP .LT. 350.0)) THEN
      TABLE1(1,8) =  -0.2203080*TEMP + 170.238000
     ELSEIF ((TEMP .GE. 350.0) .AND. (TEMP .LT. 400.0)) THEN
      TABLE1(1,8) =  -0.2042856*TEMP + 164.630160
     ELSE
      TABLE1(1,8) =82.91592
     ENDIF
C
     IF (TEMP .LT. 25.0) THEN
```

```
      TABLE1(1,9) =130.7088
     ELSEIF ((TEMP .GE. 25.0) .AND. (TEMP .LT. 300.0)) THEN
      TABLE1(1,9) = -0.0826775*TEMP + 132.7757382
     ELSEIF ((TEMP .GE. 300.0) .AND. (TEMP .LT. 350.0)) THEN
      TABLE1(1,9) = -0.2163456*TEMP + 172.876160
     ELSEIF ((TEMP .GE. 350.0) .AND. (TEMP .LT. 400.0)) THEN
      TABLE1(1,9) = -0.2203520*TEMP + 174.278400
     ELSE
      TABLE1(1,9) =86.1376
     ENDIF
C
     IF (TEMP .LT. 25.0) THEN
      TABLE1(1,10) =134.7421
     ELSEIF ((TEMP .GE. 25.0) .AND. (TEMP .LT. 300.0)) THEN
      TABLE1(1,10) =  -0.083423*TEMP + 136.827665
     ELSEIF ((TEMP .GE. 300.0) .AND. (TEMP .LT. 350.0)) THEN
      TABLE1(1,10) = -0.242436*TEMP + 184.53156
     ELSEIF ((TEMP .GE. 350.0) .AND. (TEMP .LT. 400.0)) THEN
      TABLE1(1,10) = -0.198356*TEMP + 169.103840
     ELSE
      TABLE1(1,10) =89.76128
     ENDIF
C
     IF (TEMP .LT. 25.0) THEN
      TABLE1(1,11) =138.276
     ELSEIF ((TEMP .GE. 25.0) .AND. (TEMP .LT. 300.0)) THEN
      TABLE1(1,11) = -0.083804*TEMP + 140.371091
     ELSEIF ((TEMP .GE. 300.0) .AND. (TEMP .LT. 350.0)) THEN
      TABLE1(1,11) = -0.230460*TEMP + 184.368000
     ELSEIF ((TEMP .GE. 350.0) .AND. (TEMP .LT. 400.0)) THEN
      TABLE1(1,11) = -0.224448*TEMP + 182.2638
     ELSE
      TABLE1(1,11) =92.4846
     ENDIF
C
     IF (TEMP .LT. 25.0) THEN
      TABLE1(1,12) =140.8091
     ELSEIF ((TEMP .GE. 25.0) .AND. (TEMP .LT. 300.0)) THEN
      TABLE1(1,12) =  -0.081998*TEMP + 142.859055
     ELSEIF ((TEMP .GE. 300.0) .AND. (TEMP .LT. 350.0)) THEN
      TABLE1(1,12) =-0.240528*TEMP + 190.41800
     ELSEIF ((TEMP .GE. 350.0) .AND. (TEMP .LT. 400.0)) THEN
      TABLE1(1,12) = -0.200440*TEMP + 176.387200
     ELSE
      TABLE1(1,12) =96.2112
     ENDIF
C
     IF (TEMP .LT. 25.0) THEN
      TABLE1(1,13) =143.8444
     ELSEIF ((TEMP .GE. 25.0) .AND. (TEMP .LT. 300.0)) THEN
      TABLE1(1,13) = -0.085660*TEMP + 145.985891
     ELSEIF ((TEMP .GE. 300.0) .AND. (TEMP .LT. 350.0)) THEN
      TABLE1(1,13) =-0.230552*TEMP + 189.45360
     ELSEIF ((TEMP .GE. 350.0) .AND. (TEMP .LT. 400.0)) THEN
      TABLE1(1,13) = -0.220528*TEMP + 185.94520
     ELSE
      TABLE1(1,13) =97.734
     ENDIF
C
     IF (TEMP .LT. 25.0) THEN
      TABLE1(1,14) =146.3796
     ELSEIF ((TEMP .GE. 25.0) .AND. (TEMP .LT. 300.0)) THEN
      TABLE1(1,14) = -0.085677*TEMP + 148.521518
     ELSEIF ((TEMP .GE. 300.0) .AND. (TEMP .LT. 350.0)) THEN
      TABLE1(1,14) = -0.230598*TEMP + 191.997900
     ELSEIF ((TEMP .GE. 350.0) .AND. (TEMP .LT. 400.0)) THEN
      TABLE1(1,14) = -0.220572*TEMP + 188.48880
     ELSE
      TABLE1(1,14) =100.26
     ENDIF
C
     IF (TEMP .LT. 25.0) THEN
      TABLE1(1,15) =148.4144
     ELSEIF ((TEMP .GE. 25.0) .AND. (TEMP .LT. 300.0)) THEN
      TABLE1(1,15) = -0.087517*TEMP + 150.602327
     ELSEIF ((TEMP .GE. 300.0) .AND. (TEMP .LT. 350.0)) THEN
      TABLE1(1,15) = -0.210588*TEMP + 187.523600
     ELSEIF ((TEMP .GE. 350.0) .AND. (TEMP .LT. 400.0)) THEN
```

```
        TABLE1(1,15) =-0.240672*TEMP + 198.053000
       ELSE
        TABLE1(1,15) =101.7842
       ENDIF
C
       IF (TEMP .LT. 25.0) THEN
        TABLE1(1,16) =151.453
       ELSEIF ((TEMP .GE. 25.0) .AND. (TEMP .LT. 300.0)) THEN
        TABLE1(1,16) = -0.093005*TEMP + 153.778136
       ELSEIF ((TEMP .GE. 300.0) .AND. (TEMP .LT. 350.0)) THEN
        TABLE1(1,16) =-0.200600*TEMP + 186.056500
       ELSEIF ((TEMP .GE. 350.0) .AND. (TEMP .LT. 400.0)) THEN
        TABLE1(1,16) = -0.230690*TEMP + 196.588000
       ELSE
        TABLE1(1,16) =104.312
       ENDIF
C
       IF (TEMP .LT. 25.0) THEN
        TABLE1(1,17) =153.4896
       ELSEIF ((TEMP .GE. 25.0) .AND. (TEMP .LT. 300.0)) THEN
        TABLE1(1,17) = -0.092294*TEMP + 155.796960
       ELSEIF ((TEMP .GE. 300.0) .AND. (TEMP .LT. 350.0)) THEN
        TABLE1(1,17) =-0.204653*TEMP + 189.504480
       ELSEIF ((TEMP .GE. 350.0) .AND. (TEMP .LT. 400.0)) THEN
        TABLE1(1,17) = -0.250800*TEMP + 205.656000
       ELSE
        TABLE1(1,17) =105.336
       ENDIF
C
       IF (TEMP .LT. 25.0) THEN
        TABLE1(1,18) =155.0253
       ELSEIF ((TEMP .GE. 25.0) .AND. (TEMP .LT. 300.0)) THEN
        TABLE1(1,18) = -0.091218*TEMP + 157.305755
       ELSEIF ((TEMP .GE. 300.0) .AND. (TEMP .LT. 350.0)) THEN
        TABLE1(1,18) =-0.220748*TEMP + 196.164700
       ELSEIF ((TEMP .GE. 350.0) .AND. (TEMP .LT. 400.0)) THEN
        TABLE1(1,18) = -0.234796*TEMP + 201.081360
       ELSE
        TABLE1(1,18) =107.16312
       ENDIF
C
       IF (TEMP .LT. 25.0) THEN
        TABLE1(1,19) =156.5616
       ELSEIF ((TEMP .GE. 25.0) .AND. (TEMP .LT. 300.0)) THEN
        TABLE1(1,19) =  -0.091236*TEMP + 158.842509
       ELSEIF ((TEMP .GE. 300.0) .AND. (TEMP .LT. 350.0)) THEN
        TABLE1(1,19) = -0.210756*TEMP + 194.698400
       ELSEIF ((TEMP .GE. 350.0) .AND. (TEMP .LT. 400.0)) THEN
        TABLE1(1,19) =-0.240864*TEMP + 205.236200
       ELSE
        TABLE1(1,19) =108.8906
       ENDIF

      TABLE1(2,1)=0.0
      TABLE1(2,2)=0.0002
      TABLE1(2,3)=0.0004
      TABLE1(2,4)=0.0006
      TABLE1(2,5)=0.0008
      TABLE1(2,6)=0.0010
      TABLE1(2,7)=0.0012
      TABLE1(2,8)=0.0014
      TABLE1(2,9)=0.0016
      TABLE1(2,10)=0.0018
      TABLE1(2,11)=0.0020
      TABLE1(2,12)=0.0022
      TABLE1(2,13)=0.0024
      TABLE1(2,14)=0.0026
      TABLE1(2,15)=0.0028
      TABLE1(2,16)=0.0030
      TABLE1(2,17)=0.0032
      TABLE1(2,18)=0.0034
      TABLE1(2,19)=0.0036



CCCCCCCCCCCCCCCCCCCCCCCCCCCCCCCCCCCCCCCCCCC
   IF (HYDRO .LE. 0.0) THEN
```

```
C   SET YIELD STRESS TO LAST VALUE OF TABLE, HARDENING TO ZERO
    SYIELDD=TABLE(1,NVALUE)
    HARDD=0.0
C
C   IF MORE THAN ONE ENTRY, SEARCH TABLE
C
    IF(NVALUE.GT.1) THEN
     DO 410 K1=1,NVALUE-1
       EQPL1=TABLE(2,K1+1)
       IF(IN_X  LT. EQPL1) THEN
        EQPL0=TABLE(2,K1)
        IF(EQPL1 LE.EQPL0) THEN
          WRITE(6,1)
 1         FORMAT(//,30X,'***ERROR - PLASTIC STRAIN MUST BE ',
     1          'ENTERED IN ASCENDING ORDER')
          CALL XIT
        ENDIF
C
C       CURRENT YIELD STRESS AND HARDENING
C
        DDDEQPL=EQPL1-EQPL0
        SYIEL00=TABLE(1,K1)
        SYIEL11=TABLE(1,K1+1)
        DSYIEL=SYIEL11-SYIEL00
        HARDD=DSYIEL/DDDEQPL
        SYIELDD=SYIEL00+(IN_X-EQPL0)*HARDD
        GOTO 420
        ENDIF
 410      CONTINUE
 420      CONTINUE
    ENDIF

C   SET ENDIF FOR DIFFERENT YIELD SURFACE IN TENSION
    ENDIF
CCCCCCCCCCCCCCCCCCCCCCCCCCCCCCCCCCCCCCCCCCCCCCC
CCCCCCCCCCCCCCCCCCCCCCCCCCCCCCCCCCCCCCCCCCCCCCC
    IF (HYDRO .GE. 30.0) THEN

C   SET YIELD STRESS TO LAST VALUE OF TABLE, HARDENING TO ZERO
    SYIELDD=TABLE1(1,NVALUE1)
    HARDD=0.0
C
C   IF MORE THAN ONE ENTRY, SEARCH TABLE
C
    IF(NVALUE1.GT.1) THEN
     DO 430 K1=1,NVALUE1-1
       EQPL1=TABLE1(2,K1+1)
       IF(IN_X .LT. EQPL1) THEN
        EQPL0=TABLE1(2,K1)
        IF(EQPL1.LE.EQPL0) THEN
          WRITE(6,1)
          CALL XIT
        ENDIF
C
C       CURRENT YIELD STRESS AND HARDENING
C
        DDDEQPL=EQPL1-EQPL0
        SYIEL00=TABLE1(1,K1)
        SYIEL11=TABLE1(1,K1+1)
        DSYIEL=SYIEL11-SYIEL00
        HARDD=DSYIEL/DDDEQPL
        SYIELDD=SYIEL00+(IN_X-EQPL0)*HARDD
        GOTO 440
        ENDIF
 430      CONTINUE
 440      CONTINUE
    ENDIF

C   SET ELSEIF FOR TENSION YIELD SURFACE BEYOND TRANSIENT
    ENDIF
CCCCCCCCCCCCCCCCCCCCCCCCCCCCCCCCCCCCCCCCCCCCCCC
CCCCCCCCCCCCCCCCCCCCCCCCCCCCCCCCCCCCCCCCCCCCCCC
    IF (HYDRO  GT. 0.0 .AND. HYDRO  LT. 30.0) THEN

C   FIND COMPRESSION STRESS FROM IN_Y
C   SET YIELD STRESS TO LAST VALUE OF TABLE, HARDENING TO ZERO
    YIELDD=TABLE(1,NVALUE)
```

```
      YHARDD=0.0
C
C  IF MORE THAN ONE ENTRY, SEARCH TABLE
C
      IF(NVALUE.GT.1) THEN
       DO 450 K1=1,NVALUE-1
         YEQPL1=TABLE(2,K1+1)
         IF(IN_Y .LT. YEQPL1) THEN
          YEQPL0=TABLE(2,K1)
          IF(YEQPL1.LE.YEQPL0) THEN
            WRITE(6,1)
           CALL XIT
          ENDIF
C
C         CURRENT YIELD STRESS AND HARDENING
C
         YDDEQPL=YEQPL1-YEQPL0
         YYIEL00=TABLE(1,K1)
         YYIEL11=TABLE(1,K1+1)
         YDSYIEL=YYIEL11-YYIEL00
         YHARDD=YDSYIEL/YDDEQPL
         YIELDD=YYIEL00+(IN_Y-YEQPL0)*YHARDD
         GOTO 460
         ENDIF
 450       CONTINUE
 460       CONTINUE
       ENDIF
CCCCCCCCCCCCCCCCCCCCCCCCCCCCCC
C   SET YIELD STRESS TO LAST VALUE OF TABLE, HARDENING TO ZERO
      XIELDD=TABLE1(1,NVALUE1)
      XHARDD=0.0
C
C  IF MORE THAN ONE ENTRY, SEARCH TABLE
C
      IF(NVALUE1.GT.1) THEN
       DO 470 K1=1,NVALUE1-1
         XEQPL1=TABLE1(2,K1+1)
         IF(IN_X .LT. XEQPL1) THEN
          XEQPL0=TABLE1(2,K1)
          IF(XEQPL1 LE.XEQPL0) THEN
            WRITE(6,1)
            CALL XIT
          ENDIF
C
C         CURRENT YIELD STRESS AND HARDENING
C
         XDDEQPL=XEQPL1-XEQPL0
         XYIEL00=TABLE1(1,K1)
         XYIEL11=TABLE1(1,K1+1)
         XDSYIEL=XYIEL11-XYIEL00
         XHARDD=XDSYIEL/XDDEQPL
         XIELDD=XYIEL00+(IN_X-XEQPL0)*XHARDD
         GOTO 480
         ENDIF
 470       CONTINUE
 480       CONTINUE
       ENDIF
CCCCCCCCCCCCCCCCCCCCCCCCCCCCCC
      SYIELDD = (XIELDD-YIELDD)*HYDRO/30.0+YIELDD
C       HARDD = XHARDD*HYDRO/100.0
       HARDD = XHARDD
CCCCCC SET ENDIF FOR TRANSIENT SECTION CCCCCC
      ENDIF
CCCCCCCCCCCCCCCCCCCCCCCCCCCCCCCCCCCCCCCCCCCCCCCCCCCCCCCCCCCCCCCCCCCCCCCCC
      RETURN
```